

STUDIES OF HIGH-PERFORMANCE CATHODE MATERIALS FOR LITHIUM-
ION BATTERIES

A Dissertation

Presented to the Faculty of the Graduate School

of Cornell University

In Partial Fulfillment of the Requirements for the Degree of

Doctor of Philosophy

by

Dong Ren

May 2018

© 2018 Dong Ren

STUDIES OF HIGH-PERFORMANCE CATHODE MATERIALS FOR LITHIUM- ION BATTERIES

Dong Ren, Ph. D.

Cornell University 2018

The drive to lower the consumption of fossil fuels in transportation has reached unprecedented levels due to both energy and environmental concerns. A global effort has been undertaken to develop advanced lithium-ion battery (LIB) technologies for the electrification of transportation, with the goal of significantly reducing fossil fuel consumption. In current LIBs, energy density is mainly limited by the capacity and thermodynamics of cathode materials. So improvements in cathode materials are critically needed, particularly for demanding electric vehicle applications. The studies have focused on a series of high-performance cathode materials for LIBs. Key synthesis parameters including pH, stirring rate and calcination temperature have been fully optimized for the $\text{LiNi}_{0.6}\text{Mn}_{0.2}\text{Co}_{0.2}\text{O}_2$ cathode material using a co-precipitation-calcination two-step scalable process. A high-rate performance $\text{LiNi}_{0.33}\text{Mn}_{0.33}\text{Co}_{0.33}\text{O}_2$ cathode material with preferentially orientated lithium-diffusing channels also successfully developed. In addition, the carbon fiber decorated Ni-rich $\text{LiNi}_{0.88}\text{Mn}_{0.06}\text{Co}_{0.06}\text{O}_2$ composites, exhibited enhanced rate capability and stability due to the faster ionic/electronic diffusion and shorter diffusion path benefited from the carbon fiber network structure. Finally, a class of high-energy phenothiazine-derived redox-active polymers that deliver high capacities at ultrafast discharge rates have been studied.

BIOGRAPHICAL SKETCH

Born in Shengli Oilfield, the second largest oilfield in China, Dong Ren has been exposed to petrochemical processing since childhood. After having witnessed how his father studied on improving the performance of petrochemical catalysts, Dong became fascinated with the concept of chemistry, where it is the origin of his interests in science. When he studied at Shengli No.1 High School, Dong won the first prize in 2008 Chinese Chemistry Olympiad (Shandong Province). And because of that honor, he received an offer from Fudan University without taking National College Entrance Examination. Dong's research career started in his sophomore year at Fudan University, when he joined Professor Yong Cao's group that specializes on green catalysis. His undergraduate research focused on chemo-selective hydrogenation of quinolines using supported gold nanoparticles. Since coming to Cornell University, Dong has benefited a lot from productive interactions with his PhD advisor, Professor Héctor D. Abruña, as well as with other researchers in the Cornell community. His research in Professor Abruña's group mainly focused on developing high-performance cathode materials for lithium-ion batteries, with a heavy emphasis on electric vehicle applications. Dong and his wife Minghui got married in 2015. They enjoy traveling, eating good food, and watching TV shows together.

To my wife and my parents, I couldn't have done this without you. Thank you for all
your love and support along the way.

ACKNOWLEDGEMENTS

I would like to express the deepest gratitude to Professor Héctor D. Abruña, for providing me an opportunity to work in his research group, and introducing me to the research field of lithium-ion batteries. He has allowed me to pursue the research that has interested me the most and is truly concerned about my personal growth. He always gives me the strongest support and warmest encouragement. I hope that wherever I end up, I continue to enjoy the science and the people I work with just as he does.

I would also like to thank Professor Francis J. DiSalvo and Professor Tobias Hanrath, for being my committee members, and all their support and advice. Special thanks to Dr. Yingchao Yu for getting me started in the lab, and the following communications and collaborations during these years. I am also great thankful to Luxi Shen, Yao Yang, Elliot Padgett, Dr. Barnaby D.A. Levin, and Brian M. Peterson for all the collaborative research projects. Thanks to all my colleagues from Abruña's group over the past years: Dr. Jie Gao, Dr. Hongsen Wang, Dr. Ryo Wakabayashi, Dr. Li Xiao, Dr. Yi Shi, Dr. Peng Zhang, Dr. Kenneth Hernández, Na Zhang, Yin Xiong, and Xinran Feng. Also thanks to my friends and collaborators from Lionano, Inc.: Dr. Yun Shen and Dr. Peishen Huang.

My parents, Zhijiang Ren and Chunhui Liu, provided the intellectual, spiritual, and physical foundation of all of this. I will always be grateful for their unconditional love and support. Finally, I would like to thank Minghui Li, my wife and best friend, for everything she has done for me. Words cannot express my thankfulness and I hope that for years to come, my actions will show my appreciation.

TABLE OF CONTENTS

BIOGRAPHICAL SKETCH.....	IV
DEDICATION	V
ACKNOWLEDGEMENTS	VI
TABLE OF CONTENTS.....	VII
LIST OF FIGURES	X
LIST OF TABLES	XXII

CHAPTER ONE: INTRODUCTION

1.1 History of Lithium-Ion Batteries	1
1.2 Working Principle of and Components of Lithium-Ion Batteries.....	2
1.2.1 Cathode	4
1.2.2 Anode	7
1.2.3 Electrolyte	8
1.2.4 Separator	11
1.3 Layered LiCoO ₂ Cathode Material	12
1.3.1 Structure and Electrochemical Performance	12
1.3.2 Challenges and Developments of LiCoO ₂	17
1.4 Layered LiNiO ₂ Cathode Material	21
1.4.1 Structure and Electrochemical Performance	21
1.4.2 Challenges and Developments of LiNiO ₂	23
1.5 Spinel Lithium Manganate (LiMn ₂ O ₄)	26
1.5.1 Structure and Electrochemical Performance	26

1.5.2 Challenges and Developments of LiMn_2O_4	27
1.6 Ternary Cathode Material	34
1.6.1 Structure of Ternary $\text{Li}(\text{NiMnCo})\text{O}_2$ Cathode Material.....	36
1.6.2 Electrochemical Performance of Ternary $\text{Li}(\text{NiMnCo})\text{O}_2$ Cathode Material	40
1.7 Challenges and Developments of Ternary Cathode Material	48
1.7.1 Challenges of $\text{Li}(\text{NiMnCo})\text{O}_2$	48
1.7.2 Development of $\text{Li}(\text{NiMnCo})\text{O}_2$	54
1.8 Future Developments of Ternary Cathode Material	66

CHAPTER TWO: KEY PARAMETER OPTIMIZATION OF UNIFORM, HIGH-ENERGY AND HIGH STABILITY LITHIUM NICKEL MANGANESE COBALT OXIDE CATHODE MATERIAL FOR LITHIUM-ION BATTERIES

2.1 Introduction.....	76
2.2 Experimental Section	78
2.3 Results and Discussion	80
2.4 Conclusions.....	110

CHAPTER THREE: HIGH RATE PERFORMANCE OF LITHIUM NICKEL MANGANESE COBALT OXIDE CATHODE WITH PREFERENTIALLY ORENTATED LI-DIFFUSING CHANNELS

3.1 Introduction.....	116
3.2 Experimental Section	118
3.3 Results and Discussion.....	121
3.4 Conclusions.....	141

CHAPTER FOUR: Ni-RICH $\text{LiNi}_{0.88}\text{Mn}_{0.06}\text{Co}_{0.06}\text{O}_2$ CATHODE INTERWOVEN BY
CARBON FIBER WITH IMPROVED RATE CAPABILITY AND STABILITY

4.1 Introduction.....	148
4.2 Experimental Section	150
4.3 Results and Discussion.....	152
4.4 Conclusions.....	166

CHAPTER FIVE: HIGH RATE ELECTROCHEMICAL PERFORMNACE OF
PHENOTHIAZINE-BASED POLYMER CATHODE MATERIALS FOR LITHIUM-
ION BATTERIES

5.1 Introduction.....	169
5.2 Experimental Section	169
5.3 Results and Discussion.....	171
5.4 Conclusions.....	181

CHAPTER FIVE: HIGH RATE ELECTROCHEMICAL PERFORMNACE OF
PHENOTHIAZINE-BASED POLYMER CATHODE MATERIALS FOR LITHIUM-
ION BATTERIES

6.1 Overview.....	185
6.2 Future Work	186

LIST OF FIGURES

- Figure 1.1 A representative schematic of how Li-ion batteries work via Li ion intercalation processes. 3
- Figure 1.2 Voltage and capacity of the main cathode materials for lithium-ion batteries. 6
- Figure 1.3 Structural formulas of solvents and additives used in LIB electrolytes. 11
- Figure 1.4 Schematic illustrations of crystal structures for LiCoO₂ polymorphs: O2-, O3-, and O4-type LiCoO₂ (a). The O4-phase is prepared from OP4-type [Li, Na]CoO₂ by ion-exchange. Half of the CoO₂-Li-CoO₂ blocks in the OP4-phase glide toward the (2/3, 1/3, z) direction, forming the O4-phase as shown in (b). Na ions are located at trigonal prismatic sites (P-site), whereas Li ions are located at octahedral sites (O-site). After ion-exchange, Li ions (LiO₆ octahedra) share a face (denoted as “F”) with CoO₆ octahedra on one side. In contrast, in the O3-phase (or O3- domains), Li ions (LiO₆ octahedra) only share edges (denoted as “E”) with CoO₆ octahedra. 14
- Figure 1.5 (a) Galvanostatic oxidation/reduction curves of Li cells with different LiCoO₂ polymorphs, and (b) differential dx/dV plots. Dotted lines are guides to the eye. 16

Figure 1.6	Specific capacity vs. cycle number for (a) LiCoO_2 010301 before coating, (b) sample A with ZrO_2 -coating, (c) sample B with SiO_2 -coating, and (d) sample C with Al_2O_3 -coating.	18
Figure 1.7	Specific capacity vs. cycle number for different treated materials.	19
Figure 1.8	Schematic view of the formation of the solid solution at the coating/core material interface.	20
Figure 1.9	Schematic representation of the ideal and actual structures of LiNiO_2 .	22
Figure 1.10	Rate capability of Ni-rich $\text{Li}(\text{Ni}_{1-x}\text{Mn}_x)\text{O}_2$ ($0.1 \leq x \leq 0.5$) electrodes in a voltage window of 2.7–4.3 V.	25
Figure 1.11	Crystal structure of spinel LiMn_2O_4 .	27
Figure 1.12	Cycling data of $\text{Li}(\text{Co}_{1/6}\text{Mn}_{11/6})\text{O}_4$ at 2C and 5C. Voltage: 3.5-4.3V at room temperature.	30
Figure 1.13	The discharge capacity vs. cycle number at various charge–discharge rates.	31
Figure 1.14	the effects of AlF_3 coating to the electrochemical performance of $\text{Li}_{1.1}\text{Al}_{0.05}\text{Mn}_{1.85}\text{O}_4$.	33

Figure 1.15	The relation of capacity, thermal stability and cycling performance with the various Ni content.	36
Figure 1.16	d orbitals of each elements in $\text{LiNi}_x\text{Co}_{1-2x}\text{Mn}_x\text{O}_2$.	37
Figure 1.17	C/NCM full cell performance under 1C at room temperature. A: NCM523, B: NCM433, C: NCM433.	42
Figure 1.18	Simplified DOS profiles of uncharged (a) and charged (b) $\text{LiNi}_{0.64}\text{Co}_{0.25}\text{Mn}_{0.1}\text{O}_2$.	44
Figure 1.19	C/ $\text{Li}(\text{Ni}_{1/3}\text{Mn}_{1/3}\text{Co}_{1/3})\text{O}_2$ full cell in R18650 module (2.3A h). Discharge under different rates (a) 430mA, (b) 2150mA, (c) 4300mA at 20 °C. Constant current charge with 1500mA to cut-off voltage of 4.2V. Constant voltage charge at 4.2V to cut-off current of 110mA.	45
Figure 1.20	Hot-pot study of C/ $\text{Li}(\text{Ni}_{1/3}\text{Co}_{1/3}\text{Mn}_{1/3})\text{O}_2$ (Charged at 4.2V) and C/ $\text{Li}_{1-x}\text{CoO}_2$ (Charged at 4.7V) full cell. (a) $\text{Li}_{1-x}(\text{Ni}_{1/3}\text{Mn}_{1/3}\text{Co}_{1/3})\text{O}_2$ charged to 4.4V; (b) $\text{Li}_{1-x}(\text{Ni}_{1/3}\text{Mn}_{1/3}\text{Co}_{1/3})\text{O}_2$ charged to 4.7V; (c) $\text{Li}_{1-x}\text{CoO}_2$ charged to 4.2V; (d) $\text{Li}_{1-x}\text{CoO}_2$ charged to 4.7V.	47
Figure 1.21	Initial charge-discharge curves of $\text{Li} \text{Li}(\text{Ni}_x\text{Co}_y\text{Mn}_z)\text{O}_2$ ($x=1/3, 0.5, 0.6, 0.7, 0.8, \text{ and } 0.85$) and corresponding capacity vs. voltage curves for (b) $x=1/3$, (c) $x=0.5$, (d) $x=0.6$, (e) $x=0.7$, and (f) $x=0.8$. The applied current density across the positive	50

electrode was 20 mA g^{-1} (0.1 C) at $25 \text{ }^\circ\text{C}$ over the voltage range $3.0 \text{ V} \sim 4.3 \text{ V}$.

- Figure 1.22 DSC curves of $\text{Li}_{1-\delta}[\text{Ni}_x\text{Co}_y\text{Mn}_z]\text{O}_2$ cathode materials ($x=1/3, 0.5, 0.6, 0.7, 0.8, 0.85$). 52
- Figure 1.23 Phase changes in NCA materials during charging process. 54
- Figure 1.24 Discharge capacity-cycle number of $\text{LiNi}_{0.6-y}\text{Co}_{0.25}\text{Mn}_{0.15}\text{Mg}_y\text{O}_2$. ($y = 0, 0.01, 0.03, 0.05, \text{ and } 0.08$) Discharged at $55 \text{ }^\circ\text{C}$ between $3 \sim 4.5 \text{ V}$. 56
- Figure 1.25 (a) Thermogravimetry and (b) differential thermogravimetry curves of delithiated $\text{Li}[\text{Ni}_{0.8}\text{Mn}_{0.1-x-y}\text{Co}_{0.1}\text{Al}_x\text{Mg}_y]\text{O}_2$. 57
- Figure 1.26 Differential scanning calorimetry of $\text{Li}[\text{Ni}_{0.8}\text{Mn}_{0.1-y}\text{Co}_{0.1}\text{Mg}_y]\text{O}_2$ and $\text{Li}[\text{Ni}_{0.8}\text{Mn}_{0.1-x}\text{Co}_{0.1}\text{Al}_x]\text{O}_2$ as a function of Al doping. 58
- Figure 1.27 Capacity retention of $\text{LiNi}_{1/3}\text{Mn}_{(1/3-x)}\text{Co}_{1/3}\text{Al}_x\text{O}_2$. 59
- Figure 1.28 Power capability of uncoated and Li_3PO_4 coated $\text{Li}[\text{Ni}_{0.4}\text{Co}_{0.3}\text{Mn}_{0.3}]\text{O}_2$ in the voltage range of $3.0 \text{ V} \sim 4.6 \text{ V}$ at 0.5, 1, 2, 3, and 6C rates. 63
- Figure 1.29 Composition analysis of $\text{Li}[\text{Ni}_{0.67}\text{Co}_{0.15}\text{Mn}_{0.18}]\text{O}_2$ by cross section of a single particle by EPMA. 64
- Figure 1.30 DSC curves of core, concentration-gradient, and shell materials. 66

Figure 2.1	Schematic illustration of the synthesis procedure of $\text{LiNi}_{0.6}\text{Mn}_{0.2}\text{Co}_{0.2}\text{O}_2$.	81
Figure 2.2	Plot of particle size and tap density of precursor $\text{Ni}_{0.6}\text{Mn}_{0.2}\text{Co}_{0.2}(\text{OH})_2$ prepared at various pH values.	82
Figure 2.3	SEM images of precursor $\text{Ni}_{0.6}\text{Mn}_{0.2}\text{Co}_{0.2}(\text{OH})_2$ prepared at different stirring rates: (b) 600 rpm; (c) 800 rpm; (d) 1000 rpm; (e) 1200 rpm.	83
Figure 2.4	Tap density of precursors as a function of stirring rate.	84
Figure 2.5	Powder XRD patterns of the $\text{LiNi}_{0.6}\text{Mn}_{0.2}\text{Co}_{0.2}\text{O}_2$ materials prepared under different calcination temperatures.	86
Figure 2.6	Initial charge–discharge profiles at a rate of 0.5 C over the voltage range of 2.8 to 4.45 V of samples prepared under different calcination temperatures. (c) Cycling performance at 0.5 C over the voltage range of 2.8 to 4.45 V of samples prepared under different calcination temperatures.	88
Figure 2.7	Cycling performance at 0.5 C over the voltage range of 2.8 to 4.45 V of samples prepared under different calcination temperatures.	89
Figure 2.8	(a) Single particle SEM image and (b) overview SEM image of $\text{LiNi}_{0.6}\text{Mn}_{0.2}\text{Co}_{0.2}\text{O}_2$ particles.	90

Figure 2.9	Particle size distribution of $\text{LiNi}_{0.6}\text{Mn}_{0.2}\text{Co}_{0.2}\text{O}_2$ particles.	91
Figure 2.10	N_2 adsorption/desorption isotherm and pore size distribution for $\text{LiNi}_{0.6}\text{Mn}_{0.2}\text{Co}_{0.2}\text{O}_2$ sample.	92
Figure 2.11	(a) HAADF-STEM and (b) BF-TEM images of a small piece of a $\text{LiNi}_{0.6}\text{Mn}_{0.2}\text{Co}_{0.2}\text{O}_2$ particle. (c) HRTEM lattice images from the edge of the particle in (b) marked with red dashed box.	93
Figure 2.12	SEM image of partially broken $\text{LiNi}_{0.6}\text{Mn}_{0.2}\text{Co}_{0.2}\text{O}_2$ particles after sonication in ethanol for about 5min.	94
Figure 2.13	SAED pattern of $\text{LiNi}_{0.6}\text{Mn}_{0.2}\text{Co}_{0.2}\text{O}_2$.	95
Figure 2.14	XEDS spectrum of $\text{LiNi}_{0.6}\text{Mn}_{0.2}\text{Co}_{0.2}\text{O}_2$ sample.	96
Figure 2.15	EDX elemental maps of Co (a), Mn (b) and Ni (c) for the particle in Figure 2.11 (a).	96
Figure 2.16	Initial charge and discharge profiles at 0.1 C of our $\text{LiNi}_{0.6}\text{Mn}_{0.2}\text{Co}_{0.2}\text{O}_2$ and commercial c- $\text{LiNi}_{0.6}\text{Mn}_{0.2}\text{Co}_{0.2}\text{O}_2$ materials for different charging voltages.	99
Figure 2.17	Cyclability at 0.5 C up to 100 cycles of our $\text{LiNi}_{0.6}\text{Mn}_{0.2}\text{Co}_{0.2}\text{O}_2$ and commercial c- $\text{LiNi}_{0.6}\text{Mn}_{0.2}\text{Co}_{0.2}\text{O}_2$ materials for different charging voltages.	100

Figure 2.18	Cyclic voltammetry of $\text{LiNi}_{0.6}\text{Mn}_{0.2}\text{Co}_{0.2}\text{O}_2$ in a coin cell at 0.1 mV/s. Inset shows the integrated charge as a function of cycle number.	102
Figure 2.19	Cyclic voltammetry of $\text{LiNi}_{0.6}\text{Mn}_{0.2}\text{Co}_{0.2}\text{O}_2$ in a coin cell at 0.1 mV/s. Inset shows the integrated charge as a function of cycle number.	104
Figure 2.20	Rate performance of our $\text{LiNi}_{0.6}\text{Mn}_{0.2}\text{Co}_{0.2}\text{O}_2$ and a commercial sample of c- $\text{LiNi}_{0.6}\text{Mn}_{0.2}\text{Co}_{0.2}\text{O}_2$ cell from 0.1 C to 20 C.	106
Figure 2.21	(a) First charge and discharge profiles of a pouch-type full cell fabricated with our $\text{LiNi}_{0.6}\text{Mn}_{0.2}\text{Co}_{0.2}\text{O}_2$ cathode and a graphite anode and (b) Cycling performance of the cell in (a) at 0.5 C over the voltage range between 2.75 and 4.2 V.	108
Figure 3.1	XRD patterns of the HP-NMC material.	121
Figure 3.2	Size distribution of HP-NMC particles.	122
Figure 3.3	(a) Overview and (b) single particle SEM images of HP-NMC particles.	123
Figure 3.4	(a) STEM image of a cluster of primary particles, corresponding to the polycrystalline SAED pattern in (b). (c) SAED pattern from a single isolated grain, indicated in (a), oriented in the (001) direction. (d) STEM lattice image of a thin	125

specimen oriented in the (110) direction, showing layered crystal structure.

Figure 3.5 (a,b) SEM images of HP-NMC (left) and c-NMC (right) particles, showing plate-like and rounded surface morphologies, respectively. (c,d) SEM images of FIB-cut cross-sections of the particles in (a) and (b), showing interior structure and voids. (e,f) Grain structure maps derived from scanning transmission electron diffraction mapping of FIB thinned specimens. Each colored region represents a distinct crystallite. (f) shows grains that are plate-like, with edges oriented outward in HP-NMC, while (e) shows an isotropic grain structure in c-NMC. 128

Figure 3.6 STEM images of thin HP-NMC (top) and c-NMC (bottom) specimens, with inset STEM lattice images from indicated locations. Labels below each inset indicate crystalline zone axis. Specimens were tilted $<5^\circ$ to align on zone axis for each inset. In HP-NMC, the lattice is oriented with the c-axis parallel to the short direction of each plate-like grain, while in c-NMC, no trend is observed in the lattice orientation of each grain. 130

Figure 3.7 XEDS analysis of HP-NMC particles. (a) HAADF-STEM image of HP-NMC and (b, c, d) corresponding XEDS elemental maps of Co (b), Ni (c), Mn (d). (e) XEDS spectrum from this region. The intensities of the Mn, Co, and Ni $K\alpha$ peaks are consistent with equal concentrations of Mn, Co, and 131

Ni in the material.

- Figure 3.8 STEM EELS maps showing elemental distribution in regions indicated in overview images (top) of HP-NMC (left) and c-NMC (right). Maps show integrated signals from Ni L2,3, Mn L2,3, Co L2,3, Li K, and O K edges (top to bottom). 133
- Figure 3.9 (a) Initial charge–discharge curves of our HP-NMC and a commercial sample c-NMC cells at 0.2 C between 2.8 and 4.45 V. (b) Rate performances of HP-NMC and c- NMC cells from 0.1 C to 30 C over the voltage range between 2.8 and 4.45 V. 134
- Figure 3.10 (a) Discharge curves of commercial c-NMC cell from 0.1 C to 30 C. (b) Discharge curves of a HP-NMC cell from 0.1 C to 30 C. 136
- Figure 3.11 Cyclic voltammetric profiles of the HP-NMC material in a coin cell at various scan rates. Insert: I_p as a function of the square root of the sweep rate, indicating a diffusion limited process. 138
- Figure 3.12 (a) Cycling performance of HP-NMC and c-NMC cells, up to 150 cycles between 2.8 and 4.45 V at 1 C at room temperature (25 °C). (b) Cycling performance of HP-NMC cells at different current rates (1 to 20 C) up to 100 cycles. 139
- Figure 3.13 (a) Cycling performance of our HP-NMC and commercial c-NMC cells at 50 °C. (d) 1-20 C rate cycling performance of 140

HP-NMC and c-NMC cells up to 180 cycles.

- Figure 4.1 (a) XRD patterns of pristine NMC and CF-NMC composite, compared to the reference XRD of $\text{LiNi}_{0.33}\text{Mn}_{0.33}\text{Co}_{0.33}\text{O}_2$. (b) Particle Size Distribution of pristine NMC. (c) SEM image of pristine NMC. (d) SEM image of CF-NMC. 152
- Figure 4.2 (a) SEM image of a NMC cross section with a thickness of 1 μm made by FIB. (b, c, d): XEDS elemental mapping of Ni (b), Co (c), Mn (d), respectively for the NMC lamella in (a). 153
- Figure 4.3 XEDS spectrum corresponding to the XEDS elemental mapping in Figure 4.2. The intensities of the Mn, Co, and Ni $K\alpha$ peaks are consistent with the Ni-rich component shown by ICP-AES analysis. 154
- Figure 4.4 (a-b) HAADF-STEM image and the FFT of an ultrathin NMC cross section showing atom columns with (003) and (101) d-spacings with an angle of 79.5° on the [010] zone axis. (c) The corresponding crystal model shows the projection of layered structure of transition metals in the [010] direction of a hexagonal crystal structure. 156
- Figure 4.5 (a) Initial charge–discharge curves of CF-NMC and pristine NMC cells at 0.2 C between 2.8 and 4.3 V. (b) Rate performances of CF-NMC and pristine NMC cells from 0.1 C to 20 C. 158

Figure 4.6	(a) Discharge curves of the pristine NMC cell from 0.1 C to 20 C. (b) Discharge curves of the CF-NMC cell from 0.1 C to 20 C.	160
Figure 4.7	(a) CV of a lithium half cell using CF-NMC as cathode. I at 0.1 mV/s. CV of a lithium half cell using (b) pristine NMC and (c) CF-NMC as cathode, arrows indicate increasing scan rates of 0.1, 0.3, 0.5, 0.7, 0.9, 1.1, 1.3, 1.5, 1.7 and 1.9 mV/s.	162
Figure 4.8	(a) Cycling performance of CF-NMC and pristine NMC cells, up to 150 cycles between 2.8 and 4.3 V at 0.5 C at room temperature (25 °C). (b) Cycling performance of the CF-NMC and the pristine NMC cells at 50 °C.	164
Figure 5.1	Small molecule inspiration and material design.	170
Figure 5.2	(a) General synthetic strategy for PT-DMPD and PT-BZ polymers using Buchwald-Hartwig coupling. i: NaOtBu, RuPhos (3 mol%), RuPhos Pd G2 (3 mol%), Toluene, 80 °C. (b) Neutral and oxidized states of PT-DMPD (c) Slurry CV of PT-DMPD and PT-BZ in LiPF ₆ (1 M) in EC/DEC at 20 mV/s.	172
Figure 5.3	CV cycling the full potential window of 10% CL PT-DMPD in 1 M LiPF ₆ in EC/DEC in a coin cell at 0.2 mV/s	173
Figure 5.4	(a) Initial charge–discharge curves of PT-DMPD and PT-BZ coin cells at 1 C. (b) Cycling performance of the PT-DMPD	174

and PT-BZ cells at 1 C.

- Figure 5.5 (a) Cross-linker (CL) structure and material design. (b) Initial charge-discharge of PT-DMPD, PT-DMPD (5% CL), PT-DMPD (10% CL), and PT-DMPD (33% CL) at 5 C. 176
- Figure 5.6 Cycling performance of PT-DMPD, PT-DMPD (5% CL), PT-DMPD (10% CL), and PT-DMPD (33% CL) at 5 C. 177
- Figure 5.7 Discharge capacities of PT-DMPD (10% CL) and PT-DMPD (33% CL) at C-rates from 1 C to 120 C. 178
- Figure 5.8 Top panel: Equivalent circuit model for electrochemical impedance spectroscopy data. Middle panel: Electrochemical impedance spectroscopy performed on a typical coin cell using PT-DMPD (10% CL) as cathode material. Impedance of the device at 3.1, 3.3, 3.6 3.9 and 4.1 V was measured after 3600 s of potentiostatic pretreatment from 0.001 – 20000 Hz. Inset shows the charge transfer resistance (R_{ct}) as a function of potential of the device. 179

LIST OF TABLES

Table 2.1	Lattice parameters of $\text{LiNi}_{0.6}\text{Mn}_{0.2}\text{Co}_{0.2}\text{O}_2$ samples prepared at different temperatures.	86
Table 2.2	Secondary particle size information of $\text{LiNi}_{0.6}\text{Mn}_{0.2}\text{Co}_{0.2}\text{O}_2$ sample.	92
Table 2.3	Detailed analysis of the commercial sample (c- $\text{LiNi}_{0.6}\text{Mn}_{0.2}\text{Co}_{0.2}\text{O}_2$).	98
Table 2.4	Discharge capacities of a $\text{LiNi}_{0.6}\text{Mn}_{0.2}\text{Co}_{0.2}\text{O}_2$ and a commercial sample at different rates and the corresponding capacity retentions.	107
Table 3.1	Particle size information of HP-NMC sample.	122
Table 3.2	Particle size information of c-NMC sample.	129
Table 3.3	ICP-AES results our HP-NMC material.	132
Table 3.4	Discharge capacities of our HP-NMC sample and a commercial sample at different rates and the corresponding capacity retentions	136
Table 4.1	ICP-AES results of pristine NMC material.	154

CHAPTER 1

INTRODUCTION

1.1 History of Lithium-Ion Batteries

The primary manganese dioxide-zinc battery and the rechargeable lead acid battery, which have quite a long history and are continued to be among the major battery systems in use today. As the requirements for higher performance batteries continue, Lithium-ion batteries (LIBs) challenged the surprising of these established systems. Lithium has a low atomic number and a high electrode potential, which results in a significantly higher energy density for LIBs when compared to traditional lead and zinc batteries. However, the development of safe, high-energy and long-life lithium systems, has been neither simple nor easy. It requires the technological breakthroughs in cathode, anode, electrolyte and separator, as well as a system's approach to enable further improvements of lithium battery systems.

Some early concepts came when Matsuchita developed the lithium-carbon monofluoride $\text{Li}/(\text{CF})_x$ battery in 1973,¹ followed by Sanyo, one of the largest manufacturer of both lithium rechargeable batteries and nickel metal-hydride batteries, which commercialized primary lithium-manganese oxide, Li/MnO_2 , batteries in 1975.² These batteries were used, in LED fishing floats, and memory backup applications. Subsequent research efforts were focused on converting lithium primary batteries into secondary batteries with high energy density, with most efforts concentrated on inorganic cathode compounds. Goodenough recognized that lithium could be reversibly removed, electrochemically, from LiCoO_2 ,³ thus making it a viable cathode material. In 1991, Sony Co. combined the LiCoO_2 cathode with a carbon anode to make the first commercial LIB,⁴ which was immediately accepted because of its high energy density, good overall performance, and no memory effects as occurred with

nickel-cadmium batteries or nickel-hydride batteries. LIBs have been widely used in consumer electronics, and continue to dominate the secondary battery market. There is, currently, a high demand for LIBs from consumer electronics to large-scale applications including electric vehicles, hybrid electric vehicles, and stationary electrical energy storage.^{5,6} High performance LIBs are needed to address the exacting requirements of these applications.

1.2 Working Principle and Components of Lithium-Ion Batteries

Figure 1.1 illustrates the structure, components and operation modes of LIBs with LiCoO_2 as cathode and graphite as anode. A typical LIB is composed of a transition-metal oxide positive electrode (cathode) and a graphite negative electrode (anode), and which are electronically isolated from each other by means of a porous polyethylene or a polypropylene thin film separator and filled with a Li ion-conducting organic liquid electrolyte.⁷ The typical electrolyte is a solution of LiPF_6 dissolved in an organic carbonate solvent mixture, usually propylene carbonate (PC), ethylene carbonate (EC), dimethyl carbonate (DMC), diethyl carbonate (DEC), and ethylmethyl carbonate (EMC). In fact, the revolution in Li-ion battery technologies emerged when researchers discovered that reversible electrochemical intercalation of lithium into graphite at low potentials was possible, with relatively small volume changes.⁸

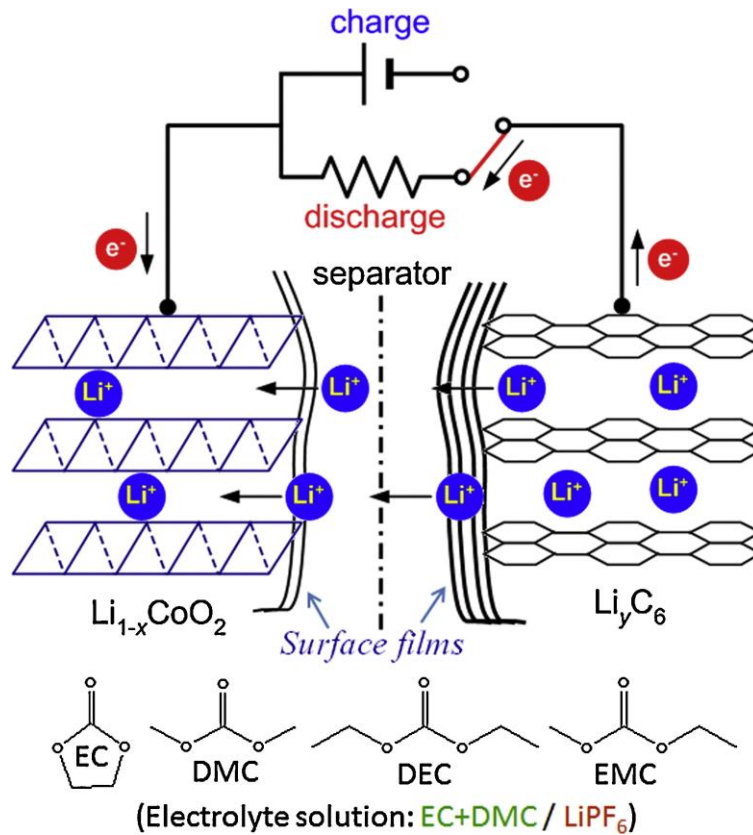
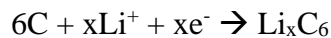


Figure 1.1 A representative schematic of how Li-ion batteries work via Li ion intercalation processes. (Reprinted from reference [8] with permission from Elsevier)

Cathode



Anode



Overall



During the discharge, electrons flow from the anode to the cathode through the

external circuit and, in the meantime, lithium ions flow from anode to cathode inside the cell to convert chemical energy into electrical energy. The current, I , in the external circuit generated by the electrochemical cell is matched by the ionic current within the cell. The charging process is the reverse where an electric current flows in the opposite direction by applying an external voltage, which converts electrical energy into chemical energy.

While a typical lithium ion battery usually contains cathode, anode, separator, electrolyte and packaging, the key components are cathode, anode, separator and electrolyte.

1.2.1 Cathode

Cathode materials play a critical role in the overall performance of lithium ion batteries. Since they are not only the active electrode material in the electrochemical reaction, but also the source of lithium ions. Therefore, specific capacity, cycling life, safety, cost and environmental effects are key factors in choosing a cathode material. The ideal cathode material, for lithium ion batteries, should meet the following requirements:

1. High specific capacity, which requires a low molecular weight and the ability to intercalate multiple lithium ions into its host structure.
2. High working voltage, which requires a high negative value of the Gibbs free energy of the discharging reaction.
3. High charging/discharging current rates, which requires rapid diffusion of the lithium ions inside and on the surface of the cathode material.
4. Long cycling performance, which requires a minimal structural change during lithiation/delithiation.

5. Safe, which requires that the material be thermally, chemically and electrochemically stable.
6. Low cost and environmentally friendly.

Generally, the cathode material for LIBs is a transition metal oxide or a polyanionic compound that contains lithium. Because of their multiple valence state, transition metals can remain electrically neutral during lithiation/delithiation. In addition, transition metal oxides usually have a high electrode potential vs. lithium when compared with transition metal sulfides, which leads to a higher voltage and consequently higher energy density. The order of electrode potential vs. lithium in transition metal oxides is: 3d transition metal oxides > 4d transition metal oxides > 5d transition metal oxides. More specially, in the 3d transition metal oxides, metal oxides of Co, Ni and Mn are dominant. LiCoO_2 is the most commonly used transition metal oxide cathode in commercial LIBs because of its high operating voltage, feasible synthesis, and good cycle life. Due to its highly ordered crystal structure, LiCoO_2 exhibits good lithium ion mobility and electrochemical performance. Although the theoretical capacity of LiCoO_2 is around 274 mAh/g, only half of it (ca. 145 mAh/g) can be utilized in practical lithium ion cells, due to the structural and chemical instability at low lithiation state. $\text{Li}(\text{NiMnCo})\text{O}_2$ material can have a theoretical capacity similar to LiCoO_2 . However, the practical capacity is depends on the specific composition. The theoretical capacity of LiMn_2O_4 is 148 mAh/g, and its practical capacity is 115 mAh/g. The theoretical capacity of LiFePO_4 is 170 mAh/g, with a practical capacity of 150 mAh/g.

Nowadays, various cathode materials are being developed based on LiCoO_2 , LiMn_2O_4 , LiFePO_4 , $\text{Li}(\text{NiMnCo})\text{O}_2$ and other cathode materials. Much effort on new cathode

materials has been exploited.⁹ For example, the high-voltage LiCoO₂, and ternary materials that are widely used in portable electronics, employ doping and coating methods to improve the structure stability at high voltage. Similarly, the structural stability, high temperature performance and working voltage of LiMn₂O₄ can also be significantly improved by doping. By controlling the morphology, particle size distribution, specific surface area and the impurities, the overall performance of the cathode material, including rate capability, cycling life, tapping density, electrochemical stability, chemical stability and thermal stability, can be enhanced. Still, the most critical issue is how to increase the energy density of the cathode material, which will require the improvement in capacity and working voltage.

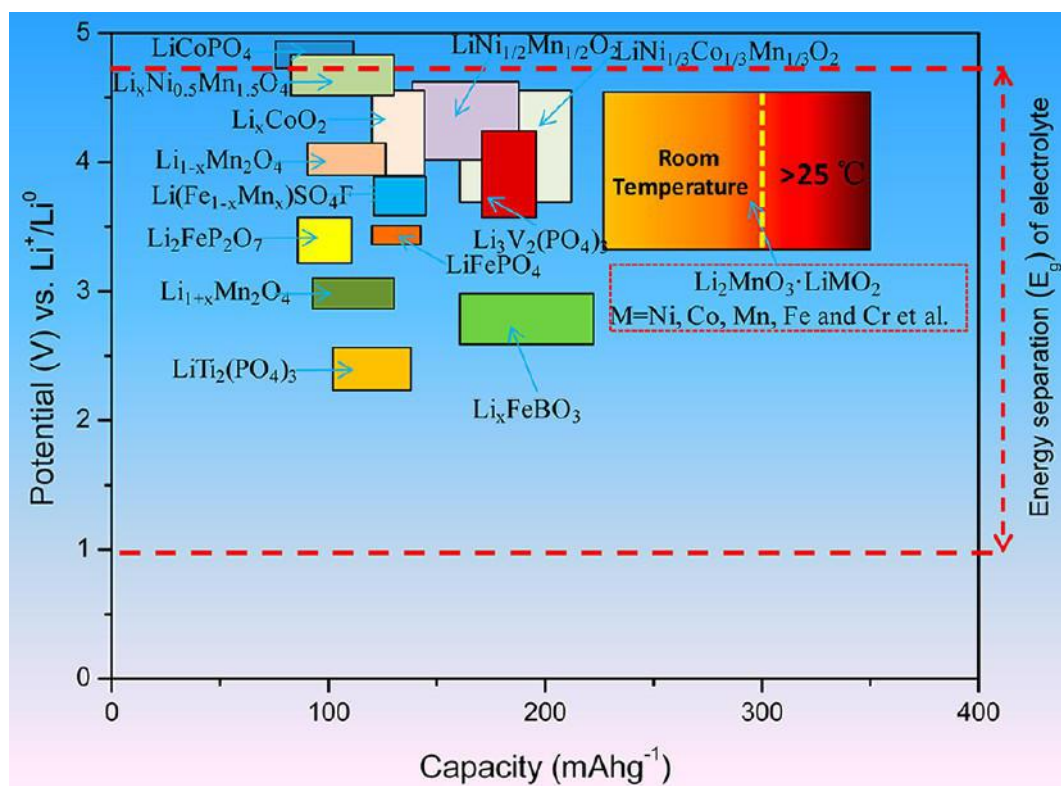


Figure 1.2 Voltage and capacity of the main cathode materials for lithium-ion batteries. (Reprinted with permission from reference [9]. Copyright 2018, American Chemical Society)

1.2.2 Anode

The anode is another key component of LIBs. The ideal anode material should meet the following requirements:

1. Delithiation should take place at a relative low oxidation potential, so that the entire cell can have a relative high output voltage.
2. There should only have a small change in the electrode potential during lithiation/delithiation processes in order to have a stable output voltage during charging and discharging.
3. Good structural stability and chemical stability during lithiation/delithiation, leading to a relative long cycle life and operational safety.
4. High reversible capacity.
5. High electronic and ionic conductivity, which are key factors for high rate capability at low temperatures and high current rates.
6. If the lithiation potential of lithiation is below 1.2 V, a dense and stable solid electrolyte layer (SEI) should be formed on the anode surface, to prevent the irreversible consumption of lithium from the cathode.
7. Low cost and environmental friendly.

There are two main anode types in commercialized LIBs. The first is carbon-based materials, such as graphite. The graphite anode has a theoretical specific capacity of 372 mAh/g, involving the transfer of one electron (or one equivalent of Li^+) per six carbon atoms. The actual capacity is typically around 300 mAh/g. All of the capacity can be accessed practically in a LIB. The types of graphite used as anode active materials in LIBs include natural graphite, synthetic graphite, meso-carbon microbead (MCMB) graphite, potato graphite, and graphite whose surface is modified with

poorly crystalline carbon.¹⁰ The graphite anode acquires stability in the LIB by forming an insoluble surface film, termed an SEI, from irreversible electrochemical reactions of the electrolyte. The SEI is impervious to electrons and protects the lithiated graphite electrode from extensive reactions with the electrolyte while allowing the transport of Li^+ , as in a solid electrolyte, to accomplish the electrode reactions. Thus, the SEI is ionically conducting, but electronically insulating.

The second one is a spinel structure base anode, $\text{Li}_4\text{Ti}_5\text{O}_{12}$, with a theoretical specific capacity of 175 mAh/g. The practical capacity can reach 160 mAh/g and the working voltage is 1.5 V. Although the working voltage of $\text{Li}_4\text{Ti}_5\text{O}_{12}$ is relatively high yielding a relatively low cell voltage, its cycling performance and rate capability are outstanding. When compared with carbon materials, it has a safety advantage. However, the lithiated $\text{Li}_4\text{Ti}_5\text{O}_{12}$ can react with the electrolyte and generate gas during the reaction, which is the most critical problem for this material.

The next generation high capacity anode material includes Si anodes and Sn-based alloys. The problem within these materials is their anisotropic volume changes during charging/discharging. To solve the electrode pulverization, caused by volume expansion, carbon/alloy composites have been used. However, composite anode materials also limit the capacity of alloys in practical cells. To some extent, the employment of carbon/alloy composite anodes can improve the energy density of current LIBs, but still cannot reach the theoretical expectations.

1.2.3 Electrolyte

Typical liquid electrolytes for LIBs are lithium salts dissolved in organic solvents. While there are many types of organic solvents and salts, not all are suitable for LIBs.

For liquid electrolytes to be useful in LIBs, they should have the following characteristics:

1. The electrolyte should have high ionic conductivity. Typically, around 3×10^{-3} to 2×10^{-2} S/cm at room temperature.
2. Good thermal stability. The electrolyte should be stable over a wide temperature range.
3. The electrolyte should have a wide electrochemical window and be stable up to 4.5V.
4. The electrolyte should exhibit high chemical and electrochemical stability towards two electrodes, current collectors, separator, binder and all cell components.
5. The electrolyte should have good solubility of the ions
6. The electrolyte should be non-toxic and have a low vapor pressure.
7. The electrolyte should be able to accelerate the reversible reaction between two electrodes.
8. The electrolyte should be easy to manufacture, and have a low cost.

Among these factors, the chemical stability, safety and reaction speed are the main factors.

The liquid electrolyte in LIBs is a mixture of organic solvents, lithium salts and some necessary additives. Cyclic carbonates such as ethylene carbonate (EC) and propylene carbonate (PC) have a high dielectric constant and high viscosity due to large mutual interactions within the solvent. Lithium dissociation is possible in EC, but it cannot be used alone, given its high melting point. In contrast, linear carbonates such as dimethyl carbonate (DMC) and diethyl carbonate (DEC) have a low dielectric constant and low viscosity. Thus, cyclic carbonates and linear carbonates are combined to obtain desirable characteristics, as organic solvents, for lithium secondary batteries.

Lithium hexafluorophosphate (LiPF_6) is the most widely used lithium salt in commercial LIBs. This salt is not the best option when single characteristics are compared, but it provides the optimal overall performance as an electrolyte- building salt in LIBs. LiPF_6 has a moderate Li transference number, good resistance to oxidation, reasonable dissociation constant, and good Al foil passivation capability. The major drawbacks of LiPF_6 are its chemical and thermal instabilities and sensitivity to moisture. The degradation products of LiPF_6 are HF, LiF and the gaseous Lewis acid PF_5 , which can easily react with the solvent. LiF can increase the surface resistance and reduce the battery cycling life. HF can corrode electrode materials and current collectors, which seriously affect overall battery performance.

To solve the problems associated with LiPF_6 , there are various options, including: 1. C-based lithium salts, such as $\text{LiC}(\text{CF}_3\text{SO}_2)_3$ and $\text{LiC}(\text{CF}_3\text{SO}_2)_2$. $\text{LiC}(\text{CF}_3\text{SO}_2)_3$ provides thermal stability and $\text{LiC}(\text{CF}_3\text{SO}_2)_2$ provides electrochemical stability. 2. N-based lithium salts, such as $\text{LiN}(\text{CF}_3\text{SO}_2)_2$ which has a comparable ionic conductivity to LiPF_6 . However, it will corrode the current collector when the voltage is higher than 3.6 V. 3. B-based lithium salts, such as Lithium bis-(oxalato)borate (LiBOB). A major advantage of LiBOB is its thermal stability. In addition, LiBOB has a better cycling stability at high temperatures. Moreover, LiBOB can form a lithium passivation film on aluminum during the first cycle, which passivates the aluminum current collector up to 5.75 V. LiBOB can also form a protective layer on graphite anodes, resulting in enhanced cycle life and shelf life.

Besides lithium salts and solvents, additives are also very important in electrolyte studies. Electrolyte additives, such as 1,3-propane sultone (PS), fluoroethylene

carbonate (FEC), vinylene carbonate (VC), and vinyl ethylene carbonate (VEC), have been identified to optimize the properties of the SEI layer on the electrode. The structural formulas of typical organic solvents and additives used in Li ion batteries are presented in Figure 1.3. Electrolyte additives are also used for deactivating the PF_5 produced by the dissociation of LiPF_6 ,¹¹ overcharge protection of Li cells,¹² as flame retardants,¹³ and for cell shutdown upon the initiation of a thermal runaway reactions.¹⁴

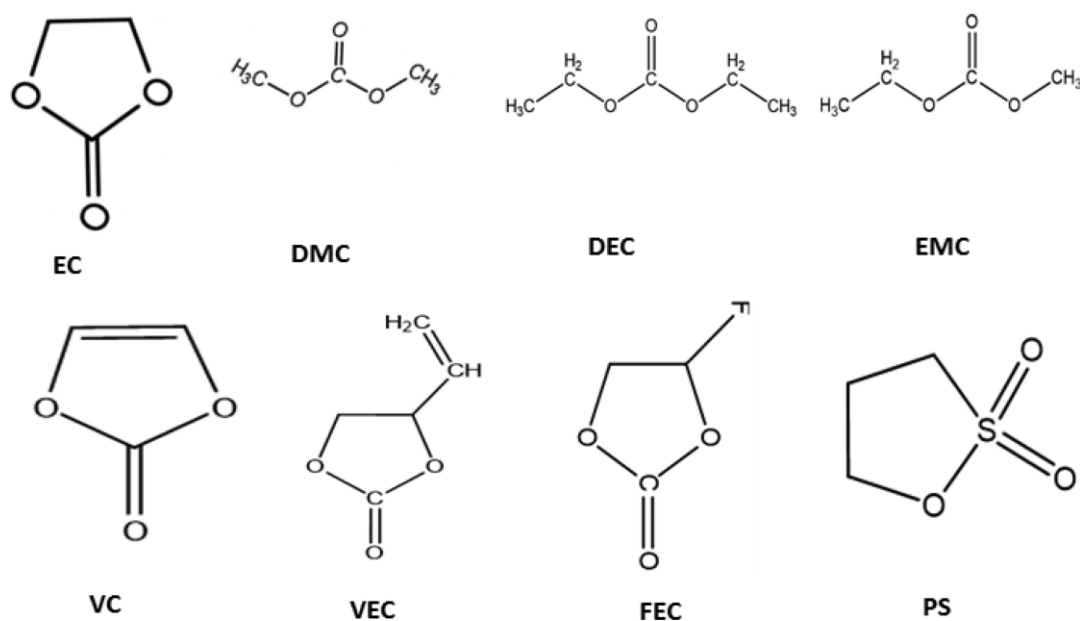


Figure 1.3 Structural formulas of solvents and additives used in LIB electrolytes. (Reprinted with permission from reference [9]. Copyright 2018, American Chemical Society)

1.2.4 Separator

Separators are electrochemically nonactive materials in LIBs. The fundamental function of separators is to provide a pathway for ion transport and separate physical contact between the anode and the cathode. Although separators do not participate in

the electrochemical reactions of batteries, they play a significantly role in determining battery performance and safety.

A common separator in lithium ion batteries is a microporous film made from polyolefins such as ultrahigh molecular weight polyethylene (PE) or polypropylene (PP). The advantages of these polyolefin films are good mechanical strength, excellent chemical stability and low cost. The pores in commercialized separators range from 0.03 to 1 μm , and the porosity is around 30% to 50%. Ceramic separators have a layer of inorganic nanoparticles (SiO_2 , TiO_2 , Al_2O_3 , ZrO_2 , etc.) and binder (polymer or inorganic) coated on the surface of a polyolefin or nonwoven film to form composite separators. Many separators based on new materials are being developing such as PMMA separators, and gel polymer electrolyte separators.

Al and Cu generally used as cathode and anode current collectors in LIBs, respectively. To make the cathode and anode powders into electrode sheets, binders (Polyvinylidene fluoride) and conducting additives (carbon black) are widely required.

1.3 Layered LiCoO_2 Cathode Material

1.3.1 Structure and Electrochemical Performance

LiCoO_2 has various crystal structures. In the early reports, LiCoO_2 was considered to have two kinds of layered structures: O3 and O2.³ The O3 structure of LiCoO_2 can be obtained by high temperature solid state reaction. LiCoO_2 with the O3 structure is thermally stable, and formed by LiO_6 and CoO_6 . O3- LiCoO_2 has the $\alpha\text{-NaFeO}_2$ layered structure, which belongs to the R3m rhombohedral structure, $a=2.8166 \text{ \AA}$, $c=14.0452 \text{ \AA}$. Li^+ and transition metal ions stay at 3a (000) and 3b(00 $\frac{1}{2}$) sites, and O^{2-} stays at 6c (00z) site. The O at 6c has cubic packing. The metal ions at 3b and Li at 3a

stay at the octahedral sites and are layered at (111). O2 type LiCoO_2 reported by Delmas¹⁵ is metastable which was synthesized by Na^+/Li^+ ion exchanged of $\text{P2-Na}_{0.70}\text{CoO}_2$. Recently, Naoaki Yabuuchi¹⁶ reported on a multi crystal structure LiCoO_2 has O4 structure. O4- LiCoO_2 is the third type of LiCoO_2 and is made via ion exchange in aqueous solution. The O4- LiCoO_2 structure was characterized by X-ray diffraction and neutron diffraction. The results showed that O4- LiCoO_2 has an O2 and O3 derived structure. The three types crystal structures are formed by packed CoO_2 (see Figure 1.4).

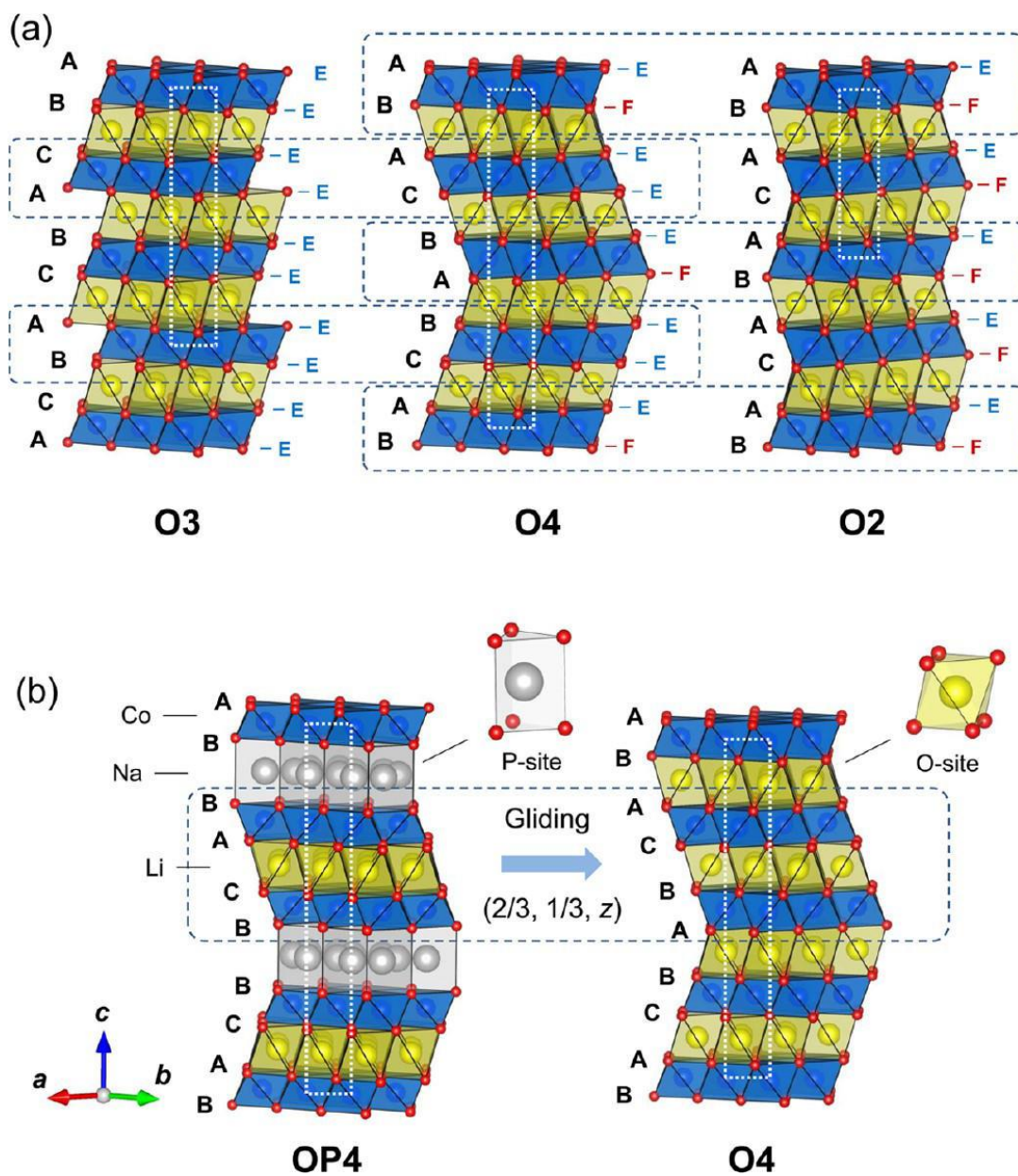


Figure 1.4 Schematic illustrations of crystal structures for LiCoO_2 polymorphs: O2-, O3-, and O4-type LiCoO_2 (a). The O4-phase is prepared from OP4-type $[\text{Li}, \text{Na}]\text{CoO}_2$ by ion-exchange. Half of the $\text{CoO}_2\text{-Li-CoO}_2$ blocks in the OP4-phase glide toward the $(2/3, 1/3, z)$ direction, forming the O4-phase as shown in (b). Na ions are located at trigonal prismatic sites (P-site), whereas Li ions are located at octahedral sites (O-site). After ion-exchange, Li ions (LiO_6 octahedra) share a face (denoted as "F") with CoO_6

octahedra on one side. In contrast, in the O3-phase (or O3- domains), Li ions (LiO_6 octahedra) only share edges (denoted as “E”) with CoO_6 octahedra. (Reprinted with permission from reference [16]. Copyright 2018, American Chemical Society)

In different layered structures. There is a rearrangement of Co and O with the changing concentration of Li during charging/discharging, which leads to the formation of new phases. Figure 1.5 presents galvanostatic charging/discharging curves and differential dx/dV plots for different LiCoO_2 polymorphs. Once the battery was charged to 4.8 V, almost all the lithium ions de-insert from O3. 80% of these lithium ions can re-insert into the O3 phase again. A capacity of 220 mAh/g can be achieved with a current rate of 20 mA/g. O3- LiCoO_2 has the highest reversible capacity among the three LiCoO_2 type. O3- LiCoO_2 has two voltage plateaus, around 3.9 V and 4.5 V. There is a minor peak at around 4.15V, which corresponds to a $\text{Li}_{0.5}\text{CoO}_2$ component. The lowest voltage plateaus of the three LiCoO_2 , are different, according to Figure 1.5 (b). The O3- LiCoO_2 is around 3.9V, the O2 is at 3.73V and the O4 is in between O2 and O3. In the O4 phase, lithium has two different positions: 2a and 2b. Although there is no evidence to show that lithium ions selectively de-insert from 2a or 2b, they are assumed to de-insert at the same time. Therefore, the voltage plateau of O4 is between of O2 and O3. However, further evidence is needed to prove this assumption.

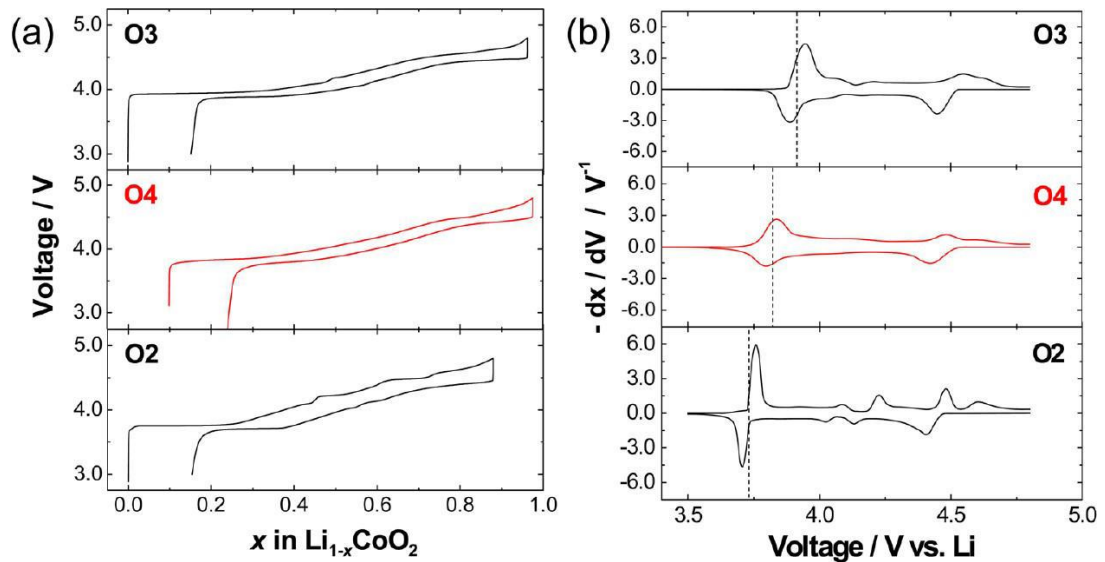


Figure 1.5 (a) Galvanostatic oxidation/reduction curves of Li cells with different LiCoO₂ polymorphs, and (b) differential dx/dV plots. Dotted lines are guides to the eye. (Reprinted with permission from reference [16]. Copyright 2018, American Chemical Society)

O3-LiCoO₂, with a R3m rhombohedral structure, is widely employed as a cathode material in commercial LIBs due to its suitability for mass production, despite its high cost. In commercial O3-LiCoO₂, lithium ion transport on the surface of the CoO₂ layers during charging/discharging in LiCoO₂. The diffusion coefficient of Li at room temperature is 10⁻¹¹ to 10⁻¹² cm²/s. The activation energy of lithium ion diffusion depends on the value of x in Li_{1-x}CoO₂, which depends on the state of charge or discharge.¹⁷ With the lithiation/dilatation, the length of the c axis of Li_{1-x}CoO₂ increases and then decreases, and after three phase transitions occur.¹⁸ The first phase transition (H1 to H2) occurs when 0.07 < x < 0.25. The c axis expands and conductivity increases. The other two phase transitions occur when x=0.5. At first, there is an order-disorder lithium ion transition, and then there is a transition from the hexagonal structure to a monoclinic structure.

1.3.2 Challenges and Developments of LiCoO₂

Currently, LiCoO₂ is mainly employed in traditional portable electronics. To achieve higher energy density, the main research directions have been aimed at high voltage (4.5 V) and high tapping density (4.1 g/cm³). More lithium ions can be de-insert from the crystal structure at high voltages, subsequent a high capacity of 180 mAh/g can be achieved. However, when more lithium ions are deintercalated, phase transitions may be irreversible, resulting the structural instability, thus, in fact, affect the cycling life and safety of the batteries.

Doping and coating are widely used to improve the structural stability and surfaces of LiCoO₂. By doping with element Mg, Al, Zr and Ti element or coating with ZrO₂, Al₂O₃ and SiO₂, the cut-off charging voltage of LiCoO₂ can be increased to 4.5 V vs Li/Li⁺ and better electrochemical performance can be achieved.

J. R. Dahn¹⁹ reported that clean a LiCoO₂ surface is critical for the stability of LiCoO₂ under high voltages. With a clean surface, LiCoO₂ can exhibit a discharge capacity of 180 mAh/g and relatively good cycling performance when charging to 4.5 V vs Li/Li⁺. If the surface of LiCoO₂ is not clean, the cycling performance rapidly degrades. The main reason is that LiPF₆ reacts with moisture and impurities during cycling, increasing the resistance of the battery. Impurities may include Li₂CO₃, which is stable at 4.2 V. But when charging to 4.2 – 4.5 V, Li₂CO₃ decomposes increasing the battery resistance and lowering the cycling performance. LiCoO₂ coated with ZrO₂, Al₂O₃ and SiO₂ can improve the surface and lower the surface resistance. Figure 1.6 shows the effect of different coating layers on the cycling performance. All three different coated-LiCoO₂ materials exhibited better cycling performance, but ZrO₂-coating

decreased the discharge capacity (Figure 1.6). Adding LiBOB into the electrolyte can also improve the cycling performance. A better cycling performance can be achieved by using a 800°C-treatment method and LiBOB as electrolyte, although the initial capacity was lower (Figure 1.7).

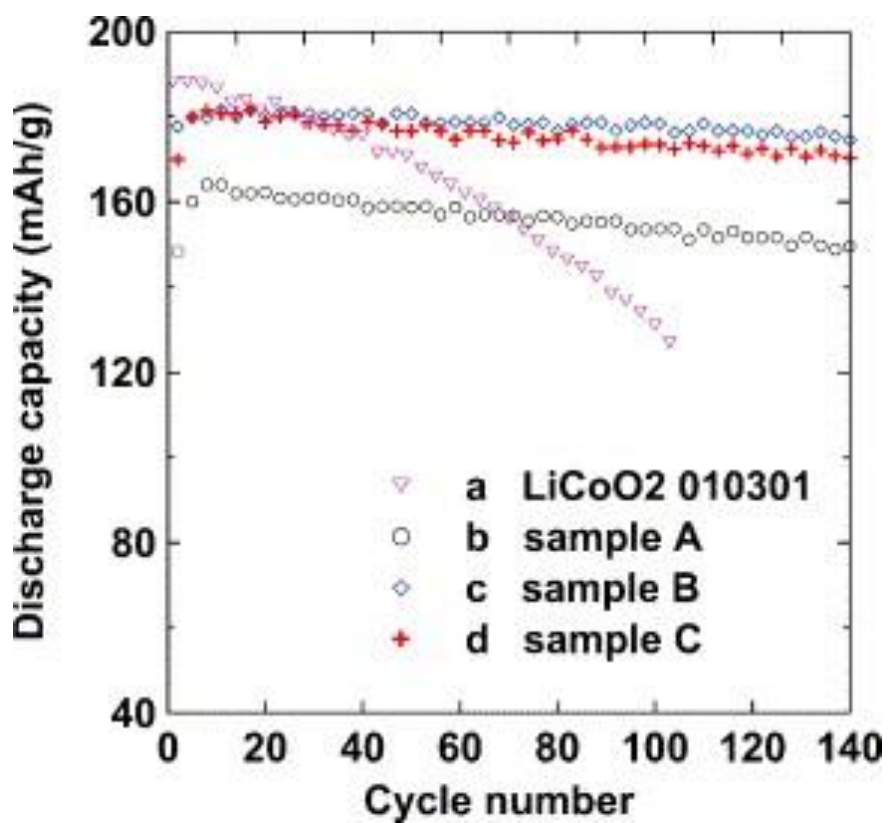


Figure 1.6 Specific capacity vs. cycle number for (a) LiCoO₂ 010301 before coating, (b) sample A with ZrO₂-coating, (c) sample B with SiO₂-coating, and (d) sample C with Al₂O₃-coating. (Reprinted from reference [19] with permission from Elsevier)

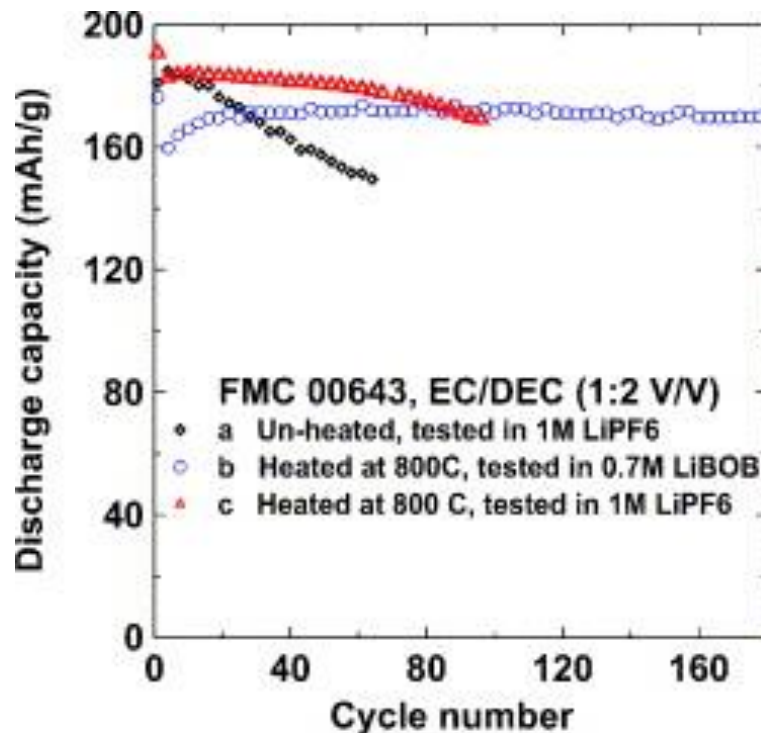


Figure 1.7 Specific capacity vs. cycle number for different treated materials. (Reprinted from reference [19] with permission from Elsevier)

L. Dahéron²⁰ used X-ray photoelectron spectroscopy (XPS) to study the Al_2O_3 coating on LiCoO_2 and found that the Al_2O_3 coating and LiCoO_2 form a layer of a solid solution of $\text{LiCo}_{1-x}\text{Al}_x\text{O}_2$. The surface acid–base properties of these materials were explored by adsorption of gaseous probe molecules followed by XPS analyses. The basic character of the $\text{LiCo}_{1-x}\text{Al}_x\text{O}_2$ surface strongly decreased when x increased, which makes these materials less reactive than LiCoO_2 towards acidic species (such as HF) that are present in LiPF_6 -based electrolytes. This is a possible explanation for the effectiveness of Al-based coatings to protect LiCoO_2 against cobalt dissolution in the electrolyte (See Figure 1.8).

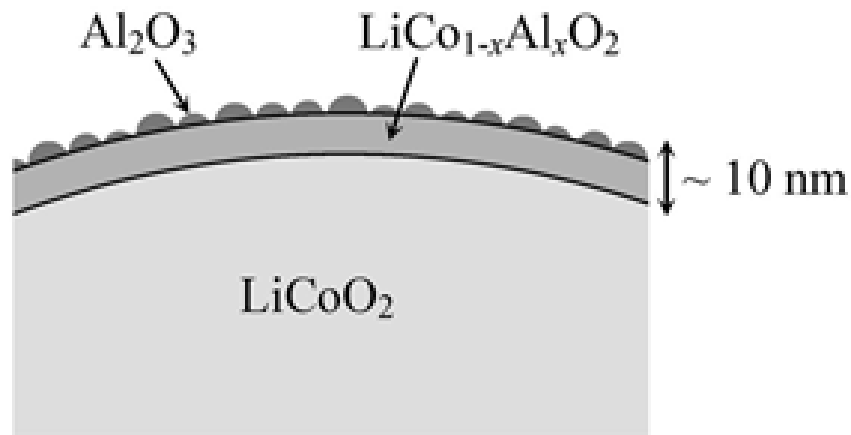


Figure 1.8 Schematic view of the formation of the solid solution at the coating/core material interface.²⁰

By doping with Al, Zr, Mg and F, Yang-kook Sun²¹ successfully developed $\text{LiMg}_{0.05}\text{Co}_{0.95}\text{O}_{1.95}\text{F}_{0.05}$ cathode materials via a solid-state reaction. XRD measurements showed that the cobalt and oxygen sites in LiCoO_2 were successfully substituted with metals (Mg, Al, Zr) and F, respectively. The co-substituted materials exhibited stable cycling performance, improved rate capability, and thermal stability compared to pristine LiCoO_2 . Furthermore, Co dissolution tests revealed that F substitution stabilizes the cathode surface and thus suppresses Co dissolution. Among the materials, $\text{LiMg}_{0.05}\text{Co}_{0.95}\text{O}_{1.95}\text{F}_{0.05}$ showed the best electrochemical and thermal properties. When charging to 4.5 V vs Li/Li^+ , the material exhibited a specific capacity of 185 mAh/g at 0.2 C, a specific capacity of 156 mAh/g at 3 C, and cycling performance with capacity retention of 88% after 50 cycles at 0.5 C.

1.4 Layered LiNiO₂ Cathode Material

1.4.1 Structure and Electrochemical Performance

LiNiO₂ has two types of structure: cubic LiNiO₂ (Fm3m) and hexagonal LiNiO₂ (R3m). Hexagonal LiNiO₂ has the same layered structure as O3-LiCoO₂. Only the hexagonal LiNiO₂ is electrochemically active. In hexagonal LiNiO₂ (R3m), the oxygen ions pack in 3 dimensions and occupy the 6c position, Ni and lithium ions occupy the octahedral interstitial sites formed by oxygen anions, and in position 3b and 3a (See Figure 1.9). C. Delmas²² named the NiO₆ as Slab and LiO₆ as interslab. As there are six d electrons in Ni³⁺, the influence of the octahedral field effect, causes a d electron split and twist of the NiO₆ octahedron, which leads to the formation of 2 long Ni-O (2.09 Å) and 4 short Ni-O (1.91 Å). The theoretical reversible capacity of LiNiO₂ is 275 mAh/g, which is comparable to LiCoO₂. The practical capacity can reach 180 mAh/g. The diffusion coefficient of Li in LiNiO₂ is around 10⁻¹¹ cm²/s at room temperature. Ni is more environmentally friendly and more abundant than Co. However, there is currently no commercialized battery application based on pure LiNiO₂, due to its numerous problems, including strict preparation conditions and poor reproducibility. Ni can also easily occupy lithium sites, which prevents the diffusion of lithium ions and decreases the specific capacity. In addition, LiNiO₂ is thermally unstable, decomposing at high temperatures, and leading to a dramatic decrease in reversible capacity. The problem of the capacity fade during charging and discharging is also severe and is due to cation mixing and structure collapse, after delithiation.

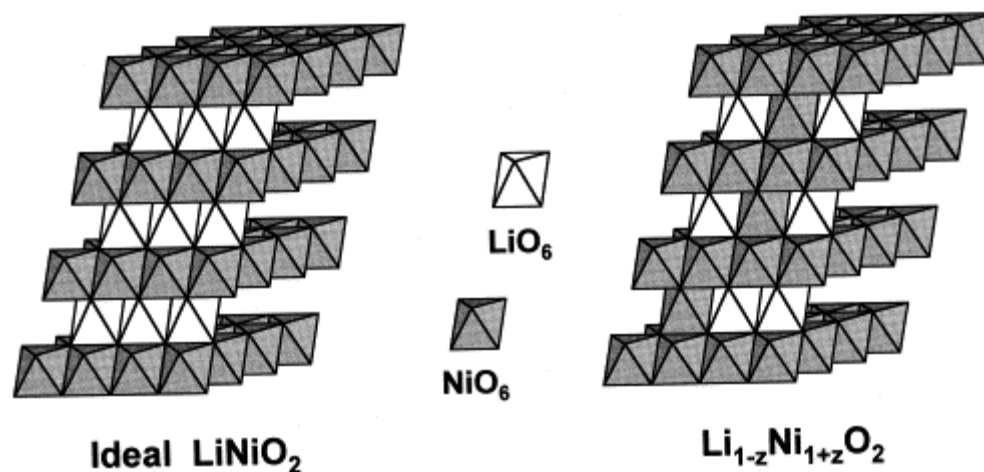


Figure 1.9 Schematic representation of the ideal and actual structures of LiNiO_2 . (Reprinted from reference [22] with permission from Elsevier)

LiNiO_2 has a theoretical capacity of 275 mAh/g. Due to the limitation of the structure, only part of the lithium ions can insert and de-insert reversibly. The overcharge may lead to damage of the structure and result in capacity decay and safety issues. Delmas²² used a constant current method to study the mechanism of Li/LiNiO_2 insert/de-insert. There are 4 pairs of oxidation and reduction peaks during lithiation and delithiation. They claimed that this reaction includes three single phase topotactic reactions and two hexagonal reactions. In the single-phase reaction region, the distance between each NiO_2 layer increased, and the reversibility was relatively good. However, the distance between NiO_2 layers dropped to 0.3 Å when continuously oxidized, leading to a decrease in the capacity. C. Delmas²³ reported that Ni^{2+} cannot be avoided during preparation. Half of the Ni^{2+} stays at NiO_2 layer, while the other half stays in the lithium ion position of 3a. During the first delithiation, only the Ni^{2+} in the NiO_2 layer oxidizes to Ni^{3+} , and then it does not affect the lithiation during the next discharge. The extra Ni^{2+} at 3a will oxidize to Ni^{3+} , which results in collapse of the layered structure, leading to high polarization.

1.4.2 Challenges and Developments of LiNiO₂

The difficulty in preparing stoichiometric LiNiO₂ remains as the main reason that has limited its communalization. Because stable Ni²⁺ tends to occupy Li⁺ sites, so LiNiO₂ tends to form non-stoichiometric Li_{1-x}Ni_{1+x}O₂. Therefore, it is virtually impossible to get stoichiometric LiNiO₂, and the actual formula should be Li_{1-x}Ni_{1+x}O₂ (0<x<0.20),²⁴ where x strongly depends on experimental conditions. To prepare the stoichiometric LiNiO₂ with good performance, researchers employed different lithium and nickel starting materials, as well as various synthesis conditions. In general, lower the temperatures trends to stabilize Ni³⁺. Li₂O, LiOH and LiNO₃ which are highly active, are chosen as sources of lithium, and NiO and Ni(OH)₂ as sources of nickel. The reaction temperature should be higher than 700°C to obtain the 2D structure. From the stand point of preparation, there are common methods including high temperature solid state reactions and low temperature reactions, such as sol-gel, co-precipitation and hydrothermal reactions.

Based on the DSC study of LiNiO₂ in electrolyte, LiNiO₂ was found to be stable even heated to 300 °C with the electrolyte. With decreasing amounts lithium ion in LiNiO₂, the exothermic reaction was enhanced and exhibited an exothermic peak around 180 °C. During the overcharge, there was a large amount of NiO₂ formed. The unstable Ni degraded and produced NiO and O₂. As a consequence, a lot of effects have focused on using dopants to solve these issues. For LiNi_{1-y}M_yO₂ (0<y<1) doping materials, the following factors need to be considered. 1. Solid solubility; 2. The uniformity in mirco-structure; 3. The stability of the doping component. The solubility of LiNi_{1-y}M_yO₂ relies on the differences in the phase structure of LiNiO₂ and LiMO₂. Among the common doping elements (M=CO, Mn, Al, Fe, Ga, Mg, Ti), only Co is fully soluble with LiNiO₂ to form LiNi_{1-x}Co_xO₂, though uniformity is hard to achieve. In

general, increasing the reaction temperature can improve uniformity, but there will also be partial reduction of Ni^{3+} and loss of lithium at high temperature.

$\text{LiNi}_{1-x}\text{Co}_x\text{O}_2$ has been the most studied doped compound. It was found that by doping suitable amounts of Co^{3+} the electrochemical performance can be significantly improved. This is due to the formation of $\text{Ni}_{1-x}\text{Co}_x\text{O}_2$ which stabilizes the hexagonal structure. The doping Co^{3+} prevents the phase transition of LiNiO_2 . The introduction of Co^{3+} reduces the $\text{Ni}^{2+}/\text{Li}^+$ mixing and leads to an ideal 2D structure. Therefore, lithium can insert freely so that the capacity will increase. In addition, by introducing Co^{3+} the crystal structure of $\text{LiNi}_{1-x}\text{Co}_x\text{O}_2$ changes very little during charging and discharging, which helps improve capacity retention.²⁴

Y-K Sun²⁵ studied the effects of Mn doping on the electrochemical performance of LiNiO_2 . They used a co-precipitation method to prepare the precursor of $\text{Li}(\text{Ni}_{1-x}\text{Mn}_x)\text{O}_2$ ($0.1 < x < 0.5$) and optimize the synthesis process. The result showed that among various compositions of $\text{Li}(\text{Ni}_{1-x}\text{Mn}_x)\text{O}_2$, when the concentration of Ni^{2+} in the lithium layer was 6.7%, the battery exhibited the best performance at high current rates (See Figure 1.10).

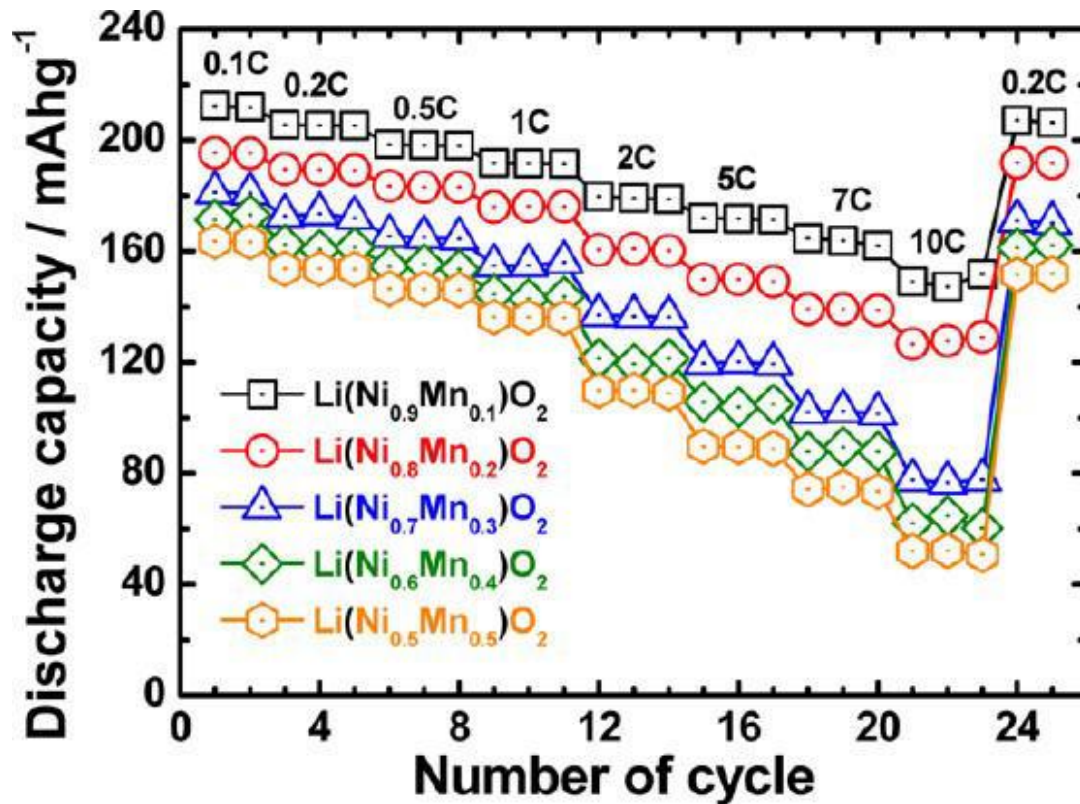


Figure 1.10 Rate capability of Ni-rich $\text{Li}(\text{Ni}_{1-x}\text{Mn}_x)\text{O}_2$ ($0.1 \leq x \leq 0.5$) electrodes in a voltage window of 2.7–4.3 V. (Reprinted with permission from reference [25]. Copyright 2018, American Chemical Society)

Al doping can also improve the performance of LiNiO_2 . Ohzuku²⁶ synthesized $\text{LiNi}_{3/4}\text{Al}_{1/4}\text{O}_2$, which can prevent its core structure from degradation when charging/discharge around 2.5 to 4.5 V. In addition, the layer distance of $\text{Li}_{1/4}\text{Ni}_{3/4}\text{Al}_{1/4}\text{O}_2$ remains 4.8 Å, and shows good cycling performance. Doping with Al inhibited extra delithiation, and stabilized the delithiated structure, makes it safer. C. Poullier²⁷ prepared $\text{LiNi}_{1-x}\text{Mg}_x\text{O}_2$. Mg doping improved the electrochemical performance of LiNiO_2 as well.

1.5 Spinel Lithium Manganate (LiMn₂O₄)

1.5.1 Structure and Electrochemical Performance

Due to the low cost of Mn, and easy of large scale manufacture, spinel lithium manganate (LiMn₂O₄) has been regarded as one of the most promising cathode materials for electric vehicle LIBs.

As shown in Figure 1.11, the space group of spinel lithium manganate (Li_xMn₂O₄) is Fd3m, and the sphere packing of oxygen atoms is face-centered cubic (fcc). The manganese atoms are located at the 16d positions of the 1/2 octahedron, while the lithium atoms are at the 8a positions of the 1/8 of the octahedron. The unoccupied tetrahedral and the octahedral sites shares side faces and edges, which form the lithium ion channels in 3D space. In the spinel structure, the lithium cation is a constant in the range of 10⁻¹² ~ 10⁻¹⁰ cm² s⁻¹. Its theoretical capacity is 148 mAh/g, and the actual capacity can reach 140 mAh/g. The charge-discharge processes can be divided into four major regions. When 0<x<0.1, the lithium cations intercalate into the single-phase A (γ-MnO₂); when 0.1<x<0.5, the compound forms two coexisting phases A and B (Li_{0.5}Mn₂O₄), which correlates with the charge-discharge plateau at high voltage (~4.15V); when x>0.5, the further intercalation of lithium cations leads to the formation of a new phase, C (LiMn₂O₄) which coexists with phase B. This region shows up at another charge-discharge plateau at lower voltages (4.03-3.9V).

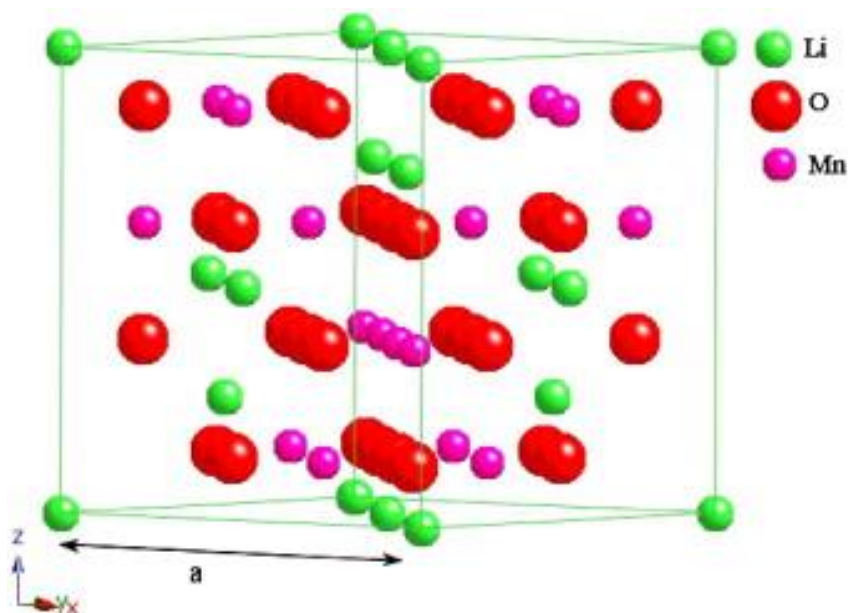


Figure 1.11 Crystal structure of spinel LiMn_2O_4 . (Reprinted from reference [28] with permission from Elsevier)

This material has a stable structure, but when discharged below 3V, the cubic crystal system is changed to a tetragonal crystal system due to the Jahn-Teller effect of Mn^{3+} cation, and the cyclability of the materials degraded. For this reason, the discharge voltage of LiMn_2O_4 is always set above 3V. Some other disadvantages of LiMn_2O_4 , besides the discharge voltage, are high temperature cycling and storage capability.²⁹

1.5.2 Challenges and Developments of LiMn_2O_4

There is a considerable capacity loss in LiMn_2O_4 at elevated temperature ($>55^\circ\text{C}$), which severely limits its practical application as the cathode material for LIBs. Researchers and scientists have carried broad studies to find the mechanisms of this decay. A widely accepted view focuses on Mn^{3+} . Mn^{3+} tends to have a redox disproportionation, which generates Mn^{4+} and Mn^{2+} . Mn^{2+} has a high solubility in electrolytes, and the dissolution process is accelerated under high temperature

condition. Loss of Mn eventually causes a structural decomposition. At the same time, Mn^{2+} migrates and plates at the anode. Uneven deposition of Mn at the anode surface also causes short circuits. Another important reason of the capacity decay is the Jahn-Teller effect of Mn, and this effect happens when the average valence is below +3.5. A twisted crystal structure is generated by the conversion of the cubic crystal system to the tetragonal crystal system. This change in the crystal structure generally leads to an enhanced polarization of the electrode, and finally causes the capacity decay.

After storage or cycling, the Mn in LiMn_2O_4 exhibits different oxidation states depending on location. In general, there is more Mn^{3+} on the surface than in the core. Thus, during discharge, a $\text{Li}_2\text{Mn}_2\text{O}_4$ or a defective spinel phase with an average valence below 3.5, will form on the surface. The crystal structure will be unstable resulting in capacity lost. Generally, LiMn_2O_4 only loses capacity at the discharge plateau at 4.2V. But, when the oxygen defective spinel lithium manganate is formed, the capacity loss will take place at two plateaus: 4.0V and 4.2V. Moreover, the defects caused by losing oxygen will further decrease the bond energy between oxygen and metal atoms, which causes the accelerated dissolution of Mn into the electrolyte. There are two main reasons that cause oxygen defects during the cycling of LiMn_2O_4 . First, LiMn_2O_4 can behave as a catalyst to decompose the electrolyte at elevated temperatures. The oxidation reaction of the electrolyte takes oxygen atoms from LiMn_2O_4 . Secondly, if the preparation of LiMn_2O_4 has an inaccurate stoichiometry, it may also cause insufficient oxygen in the material.

To improve the performance of LiMn_2O_4 , specifically its high temperature cycling and storage, researchers have employed different doping and coating methods. Surface modified LiMn_2O_4 will likely be one of the most promising cathode materials for

high-power lithium ion batteries, especially for EV applications.

Doping: The thermal stability and rate capability of LiMn_2O_4 can be improved through doping. The doping elements can be: Zn, Ce, La, Al, Sm, Co, Ti, Cr, Cr-V, Cr-Co, Cr-Al, F^- , Br^- and PO_4^{3-} in various degrees.

A. Sakunthala³⁰ studied the electrochemical properties of $\text{Co}_{1/6}$, $(\text{Co}_{1/12}\text{Cr}_{1/12})$, $(\text{Cr}_{1/12}\text{Al}_{1/12})$, $(\text{Co}_{1/12}\text{Al}_{1/12})$ doped LiMn_2O_4 . Among the listed elements, Co showed the optimal effects. As shown in Figure 1.12, the doped LiMn_2O_4 showed 94% capacity retention after 1000 cycles at 2C and at 5C. Co doping can effectively improve the electrochemical stability due to its 6 electrons at the lowest energy level in the t_{2g} orbitals. Its ligand field stabilizing energy is high enough to stabilize the structure, and improve cycling performance.

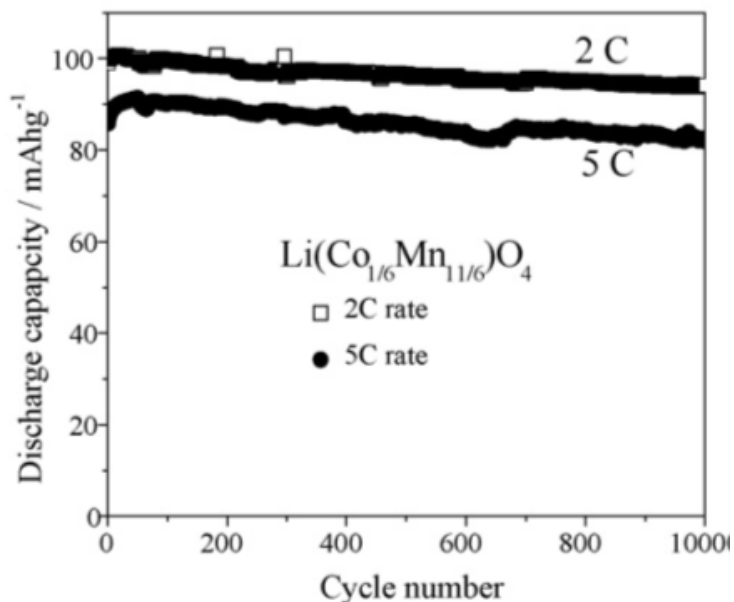


Figure 1.12 Cycling data of $\text{Li}(\text{Co}_{1/6}\text{Mn}_{11/6})\text{O}_4$ at 2C and 5C. Voltage: 3.5-4.3V at room temperature. (Reprinted from reference [30] with permission from Elsevier)

S. H. Ye³¹ prepared PO_4^{3-} doped LiMn_2O_4 through hydrothermal synthesis. The PO_4^{3-} is found at 1.5% in molar ratio to the LiMn_2O_4 . The doped materials showed improved cycling performance, with a capacity around 94 mAh/g when discharged at 20C (1 C=148 mAh/g), as shown in Figure 1.13. The AC impedance spectra demonstrated improved lithium ion diffusion coefficient, and a decreased ion migration impedance. These improvements are mainly due to the enlarged crystal cell volume after doping.

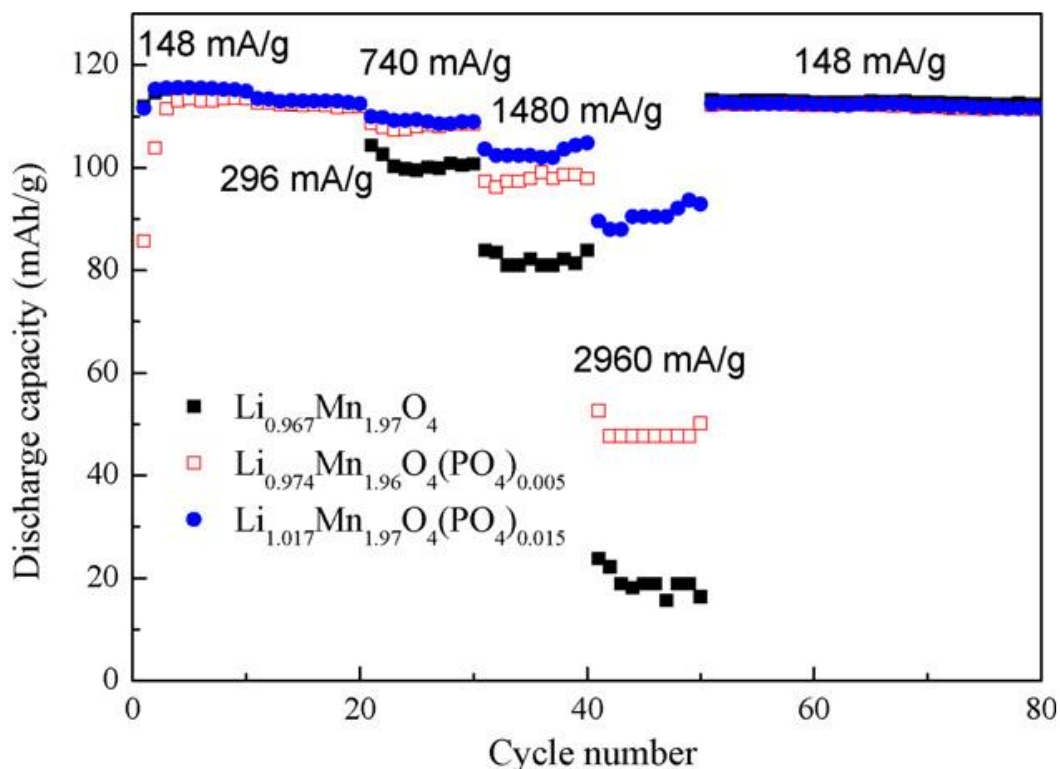


Figure 1.13 The discharge capacity vs. cycle number at various charge–discharge rates. (Reprinted from reference [31] with permission from Elsevier)

Lilong Xiong³² studied the effect of Ti doped LiMn_2O_4 in terms of its structure and electrochemical characters. The XPS and XRD analysis showed that Ti^{4+} can replace Mn^{4+} to improve the cycling and high current rate performance. The theoretical calculations showed an increase in the lattice energy with increasing Ti^{4+} as dopant. The structural stability of the spinel lithium manganate was enhanced by Ti doping. The current discharge tests showed a 135.7 mAh/g capacity for $\text{LiMn}_{1.97}\text{Ti}_{0.03}\text{O}_4$ at 0.5 C. The capacity after 70 cycles was the 95% of the original, which is higher than the 84.6 % of the un-doped material. In addition, when the charging rate was increased to 12 C, the discharge capacity was 107 mAh/g, which is also higher than the value of 82 mAh/g for the un-doped one. This is attribute to the high Ti-O bonding energy of 662

kJ/mol, which is higher than the value of 402 kJ/mol for Mn-O. An increased lithium ion diffusion coefficient and a decreased ion migration impedance were also observed with Ti doping. Ki-Soo Lee³³ prepared spinel $\text{Li}_{1.05}\text{Mn}_{0.05}\text{Mn}_{1.9}\text{O}_4$ via a precipitation methods. XRD analysis showed that the structure had an outstanding crystallinity with a $\text{Fd}3\text{m}$ 3D structure. The thermal stability was improved after doping with Al. With Al doping, the exo-thermal process was delayed by around 30 °C, and the released heat was less. This lead to a better high temperature stability, especially the cycling performance at 55 °C. The capacity was 91% of the original one.

The electrochemical reactions generally happen at the surface of the electrode. The electrochemical performance can be improved with surface structural modifications. Typical methods employed included: Al_2O_3 , AlF_3 , La_2O_3 , Cr_2O_3 , TiO_2 , ZrO_2 , SiO_2 , NiO , CeO_2 and others. D. Arumugam^{34,35} studied the effects of LiMn_2O_4 coating with CeO_2 and La_2O_3 . The XRD, SEM, TEM, XPS and electrochemical analysis methods prefer to an optimal thickness of 20 nm to effectively decrease the interfacial impedance and electron migration impedance, which further improved the cycling and high current performance of lithium ion batteries.

Yang-Kook Sun³⁶ studied the effects of AlF₃ coating on the electrochemical performance of Li_{1.1}Al_{0.05}Mn_{1.85}O₄. The cycling, high current and thermal behaviors after doping were also studied and shown in Figure 1.14. The AlF₃ can slow down the degradation of LiPF₆, and decrease the release of HF, which will slow down the dissolution of Mn.

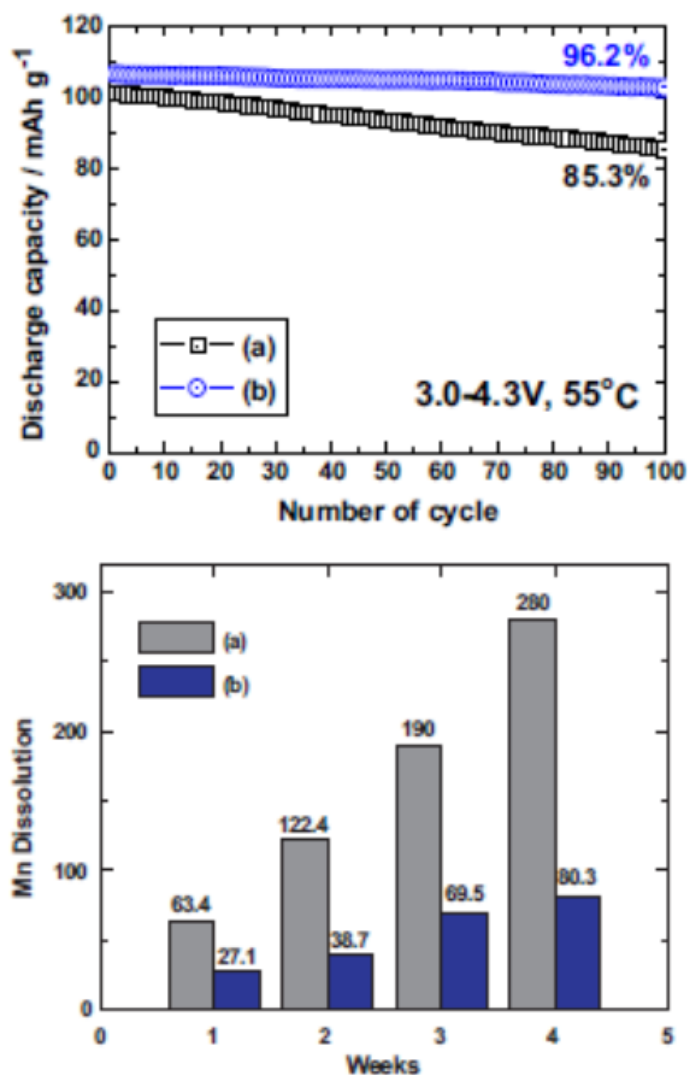


Figure 1.14 the effects of AlF₃ coating to the electrochemical performance of Li_{1.1}Al_{0.05}Mn_{1.85}O₄. (Reprinted from reference [36] with permission from Elsevier)

C. Y. Ouyang³⁷ estimated the potential mechanisms for the improvement effects provided by coating of LiMn_2O_4 . They posed that the stable state where the lithium ions stay in their lowest energy, and this can be achieved by an alternate arrangement of Li and MnO along the 001 directions of the crystal. The Al_2O_3 coating helps Mn maintain a high oxidation state, reduce the Mn at the surface, and thus, improve the overall performance of LiMn_2O_4 . Similarly, many other metal oxides have shown similar effects on LiMn_2O_4 .

1.6 Ternary Cathode Material

Layer-structured Ni-Mn-Co complex cathode materials have shown very promising performance in LIBs. Compared with LiCoO_2 , LiNiO_2 and LiMnO_2 , they show clear advantages in term of low-cost, high capacity, good cycling performance, high temperature performance and stable chemical structures. In 1999, Liu³⁸ first proposed a layered structure $\text{Li}(\text{NiMnCo})\text{O}_2$. The rations among Ni, Mn and Co were 712, 622 and 532. Later in 2001, Ohzuku and Makimura³⁹ synthesized a ternary complex with equal amounts of Ni, Co and Mn, with a the formula of $\text{Li}(\text{Ni}_{1/3}\text{Co}_{1/3}\text{Mn}_{1/3})\text{O}_2$. Because of the synergies among Ni-Mn-Co, ternary cathodes combined the advantages of the three cathode materials: long cycling life and high conductivity from LiCoO_2 ; high capacity from LiNiO_2 ; and safety and low-cost from LiMnO_2 .

By controlling the molar ratios among the Ni, Mn and Co, various properties can be developed and optimized. The main derivatives fall in two categories. The first one has an equal molar amounts of Ni and Mn, e.g. $\text{Li}(\text{Ni}_{1/3}\text{Mn}_{1/3}\text{Co}_{1/3})\text{O}_2$, (1 1 1), and $\text{Li}(\text{Ni}_{0.4}\text{Mn}_{0.4}\text{Co}_{0.2})\text{O}_2$ (442). In this type of material, the Co has a valence of +3, Ni is +2 and Mn is +4. The Mn^{4+} does not change its valence during the charge and discharge, and it works to keep the stability of the structure. Ni^{2+} loses two electrons

and is oxidized to Ni^{4+} during charging, and this is the main reason in the high capacity. The other type is a Ni-rich structure, e.g $\text{Li}(\text{Ni}_{0.5}\text{Mn}_{0.3}\text{Co}_{0.2})\text{O}_2$ (532) and $\text{Li}(\text{Ni}_{0.6}\text{Mn}_{0.2}\text{Co}_{0.2})\text{O}_2$ (622), and $\text{Li}(\text{Ni}_{0.8}\text{Mn}_{0.1}\text{Co}_{0.1})\text{O}_2$ (811). In these types of materials, Co has valence of +3, Ni is +2/+3 and Mn is +4. The valence of Mn does not change during the charge and discharge. For Co and Ni, oxidation happens along the charging process.

When the charging voltage is below 4.4 V vs Li/Li^+ , $\text{Ni}^{2+/3+}$ undergoes electrochemical reactions and forms Ni^{4+} . When the voltage goes above 4.4V, Co^{3+} can be oxidized to form Co^{4+} . Thus, when the charging voltage is below 4.4 V, cell can obtain higher reversible capacity with higher Ni content. Co affects the electron conductivity. The high rate performance can be improved by adding more elemented Co.⁴⁰ Lithium Nickel Co Aluminum (NCA) also belongs to the high-Ni ternary materials, Al^{3+} works in the same way with of Mn^{4+} . Its valence doesn't change during charging/discharging and also helps to stabilize the structure.

The theoretical capacity of ternary $\text{Li}(\text{NiMnCo})\text{O}_2$ materials can be slightly different, and is around 280 mAh/g. In Figure 1.15, the capacity of $\text{Li}(\text{NiMnCo})\text{O}_2$ materials increases, with Ni content, from 160 mAh/g to above 200 mAh/g. However, the thermal stability and cycling performance decrease accordingly.

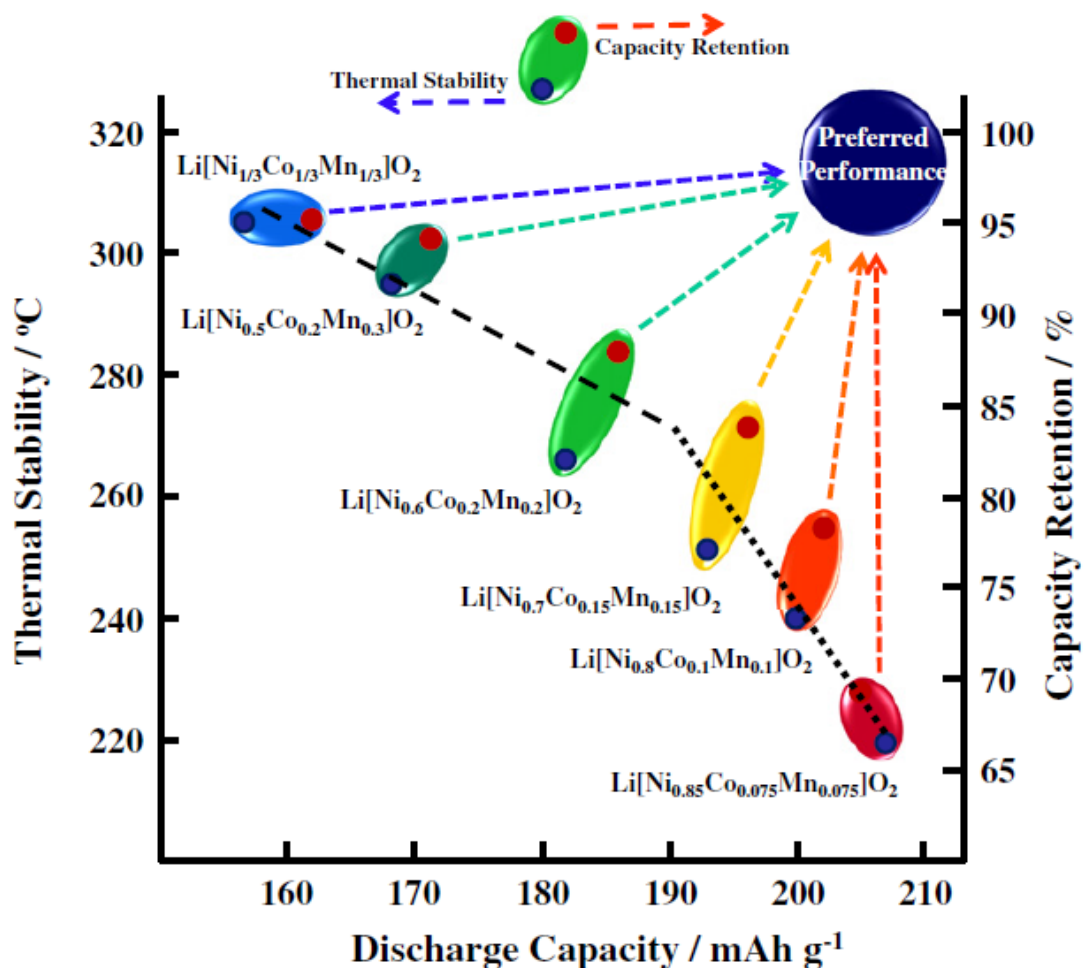


Figure 1.15 The relation of capacity, thermal stability and cycling performance with the various Ni content. (Reprinted from reference [41] with permission from Elsevier)

1.6.1 Structure of Ternary $\text{Li}(\text{NiMnCo})\text{O}_2$ Cathode Material

The structure of $\text{Li}(\text{Ni, Mn, Co})\text{O}_2$ materials belongs to hexagonal crystal system. It is an analogue of $\alpha\text{-NaFeO}_2$ with a layered structure in spatial group $R\bar{3}m$. In the crystal, Li ions and transition metals take the 3a (000) positions and 3b positions ($00\frac{1}{2}$). O^{2-} are located at the 6c position ($00z$) in the cubic compact packing. The transition metals at the 3b positions and the lithium ions at the 3a position alternate in the octahedron, and arrange in the (111) crystal face.

Using $\text{Li}(\text{Ni}_{1/3}\text{Co}_{1/3}\text{Mn}_{1/3})\text{O}_2$ as an example, Kim⁴² found its XANES is similar to $\text{LiNi}_{0.5}\text{Mn}_{0.5}\text{O}_2$ from Mn K-edge. This confirmed the valence of Mn at 4+, Ni at 2+ and Co at 3+. This experimental result matched the crystal model DOS calculation and XRD results from Koyama⁴³.

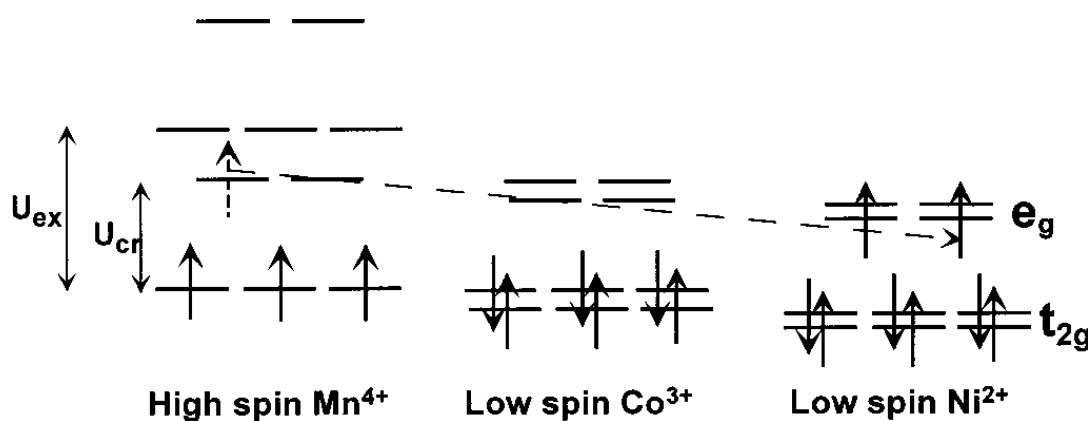


Figure 1.16 d orbitals of each elements in $\text{LiNi}_x\text{Co}_{1-2x}\text{Mn}_x\text{O}_2$. (Reprinted with permission from reference [44]. Copyright 2018, The Electrochemical Society.)

Mn^{4+} is in a high spin state ($t_{2g}^3e_g^0$) while Co^{3+} ($t_{2g}^6e_g^0$) and Ni^{2+} ($t_{2g}^6e_g^2$) are at low spin states. Mn^{4+} and Ni^{2+} are more stable than Mn^{3+} and Ni^{3+} . The electrons on the e_g orbitals of Mn tend to migrate to the e_g of Ni, and $\text{Mn}^{4+}/\text{Ni}^{2+}$ are formed. Ni^{2+} has a radius very similar to Li^+ , so it is easy for Ni^{2+} to take the 3a position of Li^+ . This results in a mixed arrangement of different cations, which directly changes the electrochemical performance.⁴⁵ For different ratios of Ni, Co and Mn, the cation mixing varies. The ratio of $I_{(003)}/I_{(104)}$ is used to quantify cation mixing. A lower ratio indicates a higher cation mixing. The Ni^{2+} at the Li^+ position generally lowers the capacity and hinders the migration of lithium ions. These disordered structures generate an undesirable decrease of electrochemical performance.

In the charging process, lithium ions are extracted from the layers of the cathode materials. The transition metals are oxidized to a higher valence state. From Koyama's calculation on $\text{Li}(\text{Ni}_{1/3}\text{Mn}_{1/3}\text{Co}_{1/3})\text{O}_2$ ($0 \leq x \leq 1$)⁴³, the redox reaction takes place on $\text{Ni}^{2+}/\text{Ni}^{3+}$ when $0 \leq x \leq 1/3$, $\text{Ni}^{3+}/\text{Ni}^{4+}$ when $1/3 \leq x \leq 2/3$, and $\text{Co}^{3+}/\text{Co}^{4+}$ when $2/3 \leq x \leq 1$. Kim⁴⁶ calculated the potential from ex situ XANES spectra, for each redox reaction in the ternary materials. The $\text{Ni}^{2+}/\text{Ni}^{3+}$ redox reaction happens at 3.8V, and the $\text{Ni}^{3+}/\text{Ni}^{4+}$ redox reaction happens in the range of 3.9-4.1V. After 4.1V, the Ni K-edge did not show any changes. The K-edge profile of Mn show small differences. They are due to changes of the surrounding environments, and Mn itself did not change. For Co, its K-edge profile changed with potential, so the redox reaction of $\text{Co}^{3+}/\text{Co}^{4+}$ happened throughout the entire potential changes. Ohzuku's calculations have shown a deviation from an ideal crystal structure. The conclusion is that the $\text{Co}^{3+}/\text{Co}^{4+}$ redox reaction happens at the 4.5V plateau.

From Koyam's calculation results, a comparison can be made between the average atomic distance in $\text{Li}(\text{Ni}_{1/3}\text{Mn}_{1/3}\text{Co}_{1/3})\text{O}_2$ and $\text{LiCoO}_2/\text{LiMnO}_2/\text{LiCoO}_2$. In the ternary materials, the Co-O bond length is similar to that in LiCoO_2 . However, the Ni-O bond length is longer than in LiNiO_2 , while the Mn-O bond distance is shorter than in LiMO_2 . This indicates a very different electronic environment around Ni and Mn compared to Co in the different compounds. During the discharge, the Mn-O bond length remains unchanged. Co-O bond is shortened slightly, but the Ni-O bond decreases dramatically. The metal oxygen bond length is closely related to the valence state of the metal. During the discharge, the $\text{Co}^{3+}/\text{Co}^{4+}$ redox reaction and the radius of Co remain almost the same ($r_{\text{Co}^{3+}}=0.545\text{\AA}$, $r_{\text{Co}^{4+}}=0.53\text{\AA}$). However, for the $\text{Ni}^{2+}/\text{Ni}^{3+}$ and $\text{Ni}^{3+}/\text{Ni}^{4+}$, the electrons are changing between t_{2g} and e_g orbitals, which causes a

considerable energy difference before and after. As a result, the radius of Ni changes to different valence states ($r_{\text{Ni}^{2+}}=0.69\text{\AA}$, $r_{\text{Ni}^{3+}}=0.56\text{\AA}$, $r_{\text{Ni}^{4+}}=0.48\text{\AA}$). MnO_6 with an octahedral structure, and its valence status does not change, so it plays the role of maintaining the structure.

In $\text{Li}(\text{Ni}, \text{Mn}, \text{Co})\text{O}_2$ system, when the three transition metals are the same mole percent, the lattice constants are $a=2.862\text{\AA}$, $c=14.227\text{\AA}$, and the volume of the unit cell is 100.6\AA^3 . Among LiMnO_2 , LiCoO_2 and LiNiO_2 , the LiCoO_2 has the smallest cell with lattice constants $a=2.819\text{\AA}$, $c=14.096\text{\AA}$, and a unit cell volume of 96.8\AA^3 . LiNiO_2 was the largest unit cell with a volume of 102.3\AA^3 . The cell volume of $\text{Li}(\text{Ni}, \text{Co}, \text{Mn})\text{O}_2$ changes with the ratio of the three metal elements. When the molar ratio of Co increases, the lattice constants a and c decrease. This is because that the larger Ni^{2+} ($r_{\text{Ni}^{2+}}=0.69\text{\AA}$) and Mn^{4+} ($r_{\text{Mn}^{4+}}=0.53\text{\AA}$) are replaced by the smaller Co^{3+} ($r_{\text{Co}^{3+}}=0.545\text{\AA}$). The c/a ratio is critical for identifying the structure. When c/a is larger than 4.9, the dominant structure in the crystal is the layered structure. When this value increases, the layered structure has a higher percentage. This indicates that a better layered structure can be obtained with a higher content of Co.

Before the charging voltage reaches 4.2V, the value of the lattice constant gets smaller due to the de-intercalation of lithium ions. A slight increase can be observed when the voltage gets close to 4.2V. The overall decreasing trends are due to the oxidation of Co and Ni. The c value keeps increasing during charging. This is because the force between oxygen atoms after the extraction of lithium ions. After 4.4V, the c value decreases rapidly, due to the accumulation of Ni^{4+} , which weakens the force between layers. During the charge and discharge cycles, the a value increases and the c value decreases in the ternary materials. The overall volume of the cell changes only by 2%.

This is smaller for both LiCoO_2 and LiNiO_2 . This experimental result matches well with Koyama's⁴³ calculation. In addition, no phase transition is observed for the charge and discharge of ternary materials. This helps the materials maintain their structure during the operation and prevent the crystals from cracking. As a result, the cathode particles can maintain good contact, and the internal resistance can be kept small after cycling. Then, the ternary materials can exhibit good capacity and long life time. Hence, when the molar ratio of Ni goes above 0.6, a phase transition will be observed, which leading to a shorter cycling life.

1.6.2 Electrochemical Performance of Ternary $\text{Li}(\text{NiMnCo})\text{O}_2$ Cathode Materials

Capacity-cycling performance is a key parameter for a material to be successfully employed in LIBs. The molar ratio of Ni-Mn-Co determines the capacity of the materials over the voltage range of 2.7-4.2V. A higher Ni content results in a higher capacity. Ni and Co have different redox potentials, and this causes the voltage plateau is not flat in the curve. Sun⁴¹ studied the capacity of $\text{Li}(\text{Ni}, \text{Mn}, \text{Co})\text{O}_2$ with different Ni content. The experiments were carried in half cells (Li metal anode) under 3 – 4.3 V at 25 °C. The Ni molar percentage varied as 1/3, 0.5, 0.6, 0.7, 0.8, and 0.85. The discharge capacities were 163, 175, 187, 194, 203, and 206 mAh/g, however the cycling performance decreased with high Ni content.

Liu⁴⁷ studied NMC-532 and NMC-433 in full cells with a carbon anode. As shown in Figure 1.17, NMC-433 displayed a lower capacity than NMC-532. However NMC-433 exhibited a much better cycling performance. Three different cells demonstrated 80% capacity retention after 2000 cycles. The capacity ratio between anode and cathode (optimal 1.19 in this case) is also very important for cycling performance. The reason for the better performance of NMC-433 is due to the limited cation mixing. The

impedance measurements showed that NMC-433 with 1.19 anode/cathode capacity ratio had the smallest interface impedance. Limited cathode dissolution and moderate SEI growth could be generated with relatively low Ni content.

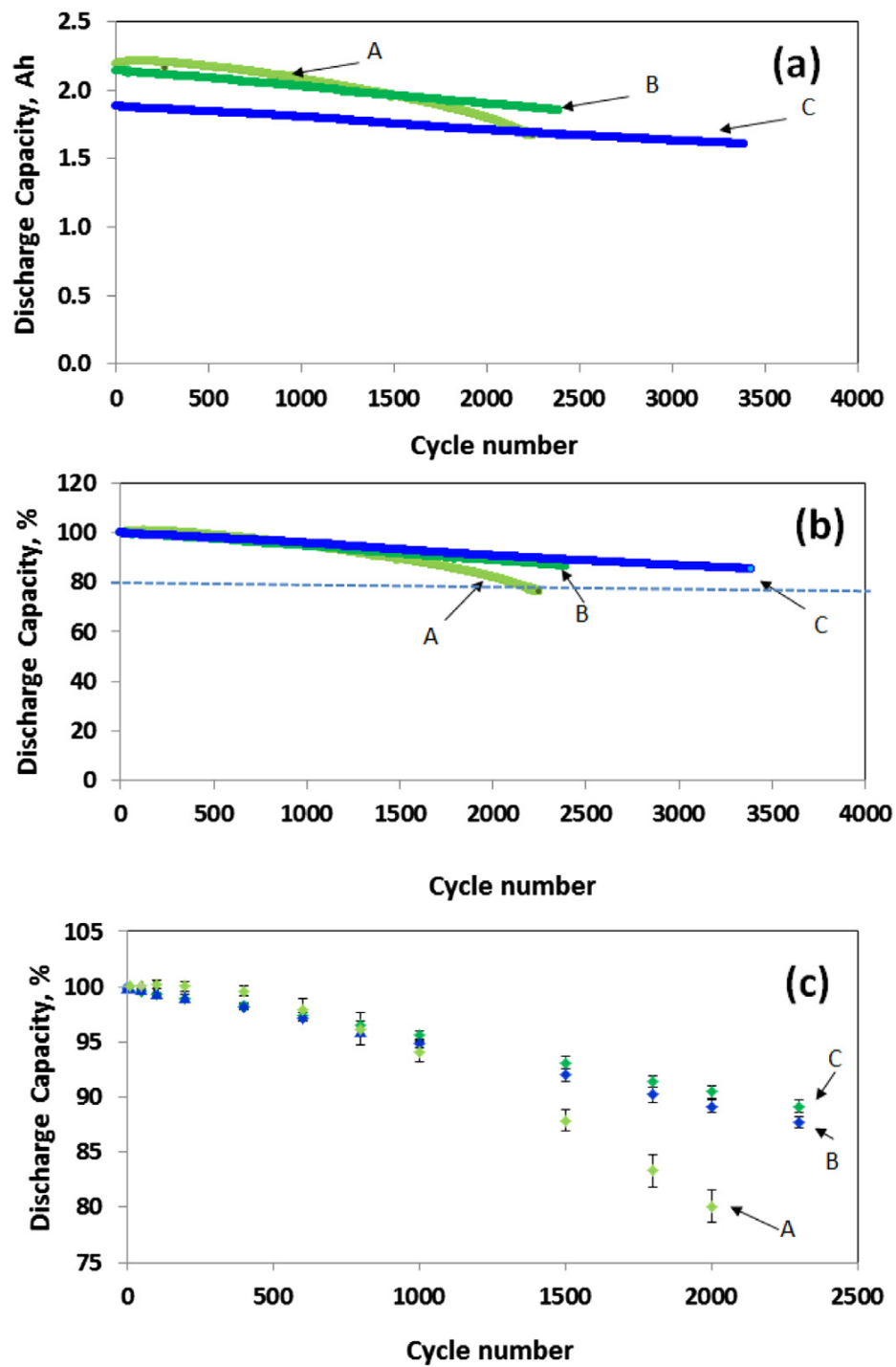


Figure 1.17 C/NCM full cell performance under 1C at room temperature. A: NCM523, B: NCM433, C: NCM433 (Reprinted from reference [47] with permission from Elsevier)

To improve the cycling performance of NMC-532, a fine tuning of the percentages of Co and Ni can be applied. Hyoung-Geun Kim⁴⁸ studied with the basic NMC-532 and added 0.04 more Mn and reduced 0.04 Co to improve the cycling performance and thermal stability. The non-active Mn helps to stabilize the layered structure of the ternary materials. Over the same voltage range, additional Ni increases the capacity. This is mainly due to the distribution of the energy levels in different ternary materials. Figure 1.18 shows a simplified DOS profile of uncharged and charged $\text{LiNi}_{0.64}\text{Co}_{0.25}\text{Mn}_{0.1}\text{O}_2$.⁴⁹ From Figure 1.18, the Co and oxygen have a larger overlap than Ni and oxygen. During charging, Ni^{2+} is first oxidized to Ni^{3+} , with Ni^{4+} forming earlier than Co^{4+} . Thus, the Ni rich ternary materials display higher capacity. At the same time, both $\text{Ni}^{3+}/\text{Ni}^{4+}$ and $\text{Co}^{3+}/\text{Co}^{4+}$ overlap with oxygen. This means that if a high percentage of lithium is extracted, the oxygen will extract from the crystal lattice. This will convert M^{4+} to M^{3+} eventually lowering the cycling performance.

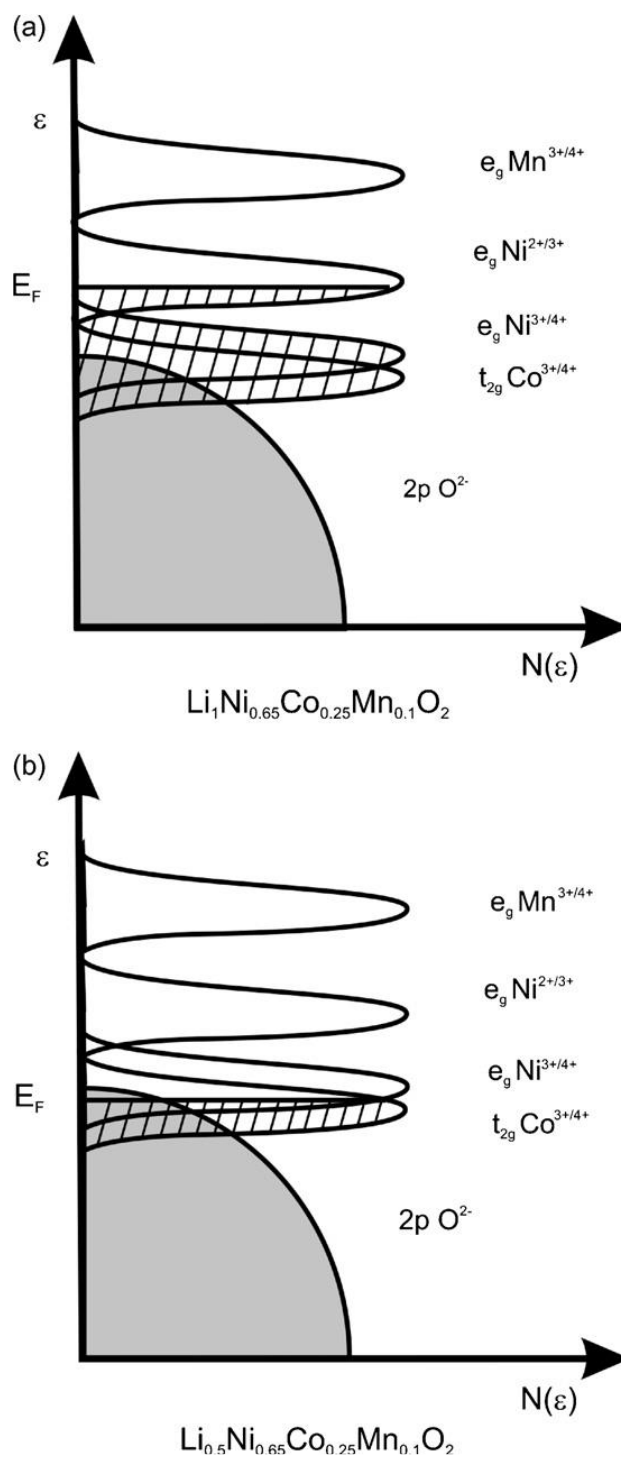


Figure 1.18 Simplified DOS profiles of uncharged (a) and charged (b) $\text{LiNi}_{0.64}\text{Co}_{0.25}\text{Mn}_{0.1}\text{O}_2$. (Reprinted from reference [49] with permission from Elsevier)

Ternary $\text{Li}(\text{Ni}, \text{Mn}, \text{Co})\text{O}_2$ materials have shown outstanding rate performance. Yoshizawa⁵⁰ compared the rate capability of $\text{Li}(\text{Ni}_{1/3}\text{Mn}_{1/3}\text{Co}_{1/3})\text{O}_2$ and LiCoO_2 . The former displayed both high discharge rate capability and long cycling life. In Figure 1.19, an R18650 cell with $\text{Li}(\text{Ni}_{1/3}\text{Mn}_{1/3}\text{Co}_{1/3})\text{O}_2$ achieved a capacity of 2.3Ah at 2C discharge and then caused a polarization of the cell, the capacity remained above 2.1Ah.

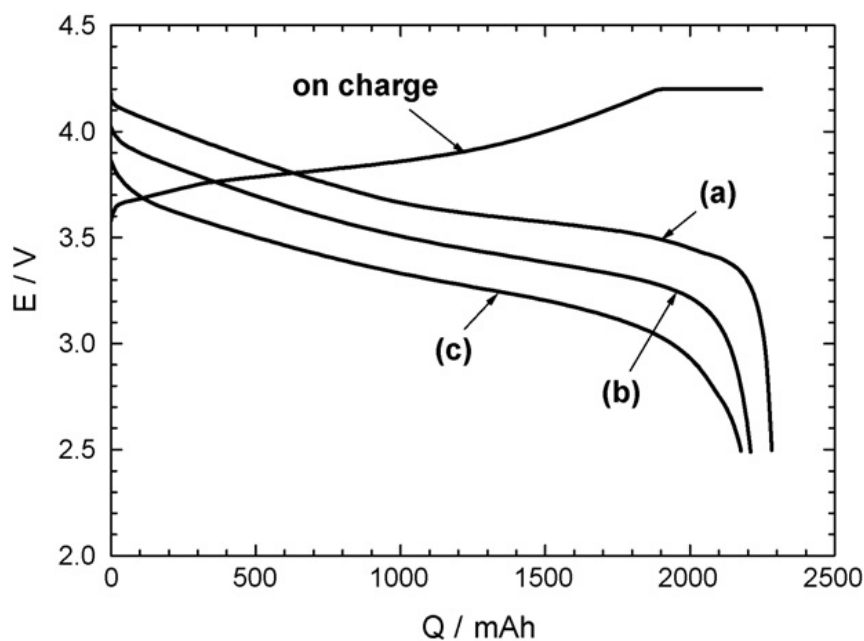


Figure 1.19 C/ $\text{Li}(\text{Ni}_{1/3}\text{Mn}_{1/3}\text{Co}_{1/3})\text{O}_2$ full cell in R18650 module (2.3A h). Discharge under different rates (a) 430mA, (b) 2150mA, (c) 4300mA at 20 °C. Constant current charge with 1500mA to cut-off voltage of 4.2V. Constant voltage charge at 4.2V to cut-off current of 110mA. (Reprinted from reference [50] with permission from Elsevier)

For different ratios of Ni, Mn, and Co, high Co content can improve rate capability. The transport of charges and diffusion of lithium ions are the rate determining steps of the charge/discharge performance. The NMC ternary materials have the layered structure as LiCoO_2 , but the covalency of O-M-O layers is weaker than in LiCoO_2 due

to the larger radius of Ni^{2+} and weaker polarizability of Mn^{4+} and Ni^{2+} related to Mn^{3+} and Ni^{3+} . This results in weakened M-O bonds, and Li-O bonds become stronger. This means a higher activation energy for lithium to migrate from different positions of the cathode particles. Using Ni^{3+} in LiNiO_2 as an example, its d electrons are in the orbitals $t_{2g}^6e_g^1$. The e_g orbital complexes with oxygen and forms σ bonds with oxygen's 2p orbitals. However, for the Co^{3+} , its t_{2g} orbital forms π -bonds with oxygen's 2p orbitals. This changes the overlap situation in different directions for $\text{Ni}^{4+}/\text{Ni}^{3+}$ and Co^{4+} and Co^{3+} . The $\text{Ni}^{4+}/\text{Ni}^{3+}$ provides an environment in which it is more difficult for Li^+ to migrate than $\text{Co}^{3+}/\text{Co}^{4+}$. As a result, LiCoO_2 has a higher current charge/discharge performance than LiNiO_2 . For the ternary materials, additional Ni will further degrade the high rate charge/discharge results. Additional studies have shown the importance of the charge transport processes in the overall electrochemical reactions and performance of the cathode materials. At higher temperatures, lithium ions can insert and de-insert from the materials more effectively and rapidly.

Venkatraman⁵¹ analyzed different parameters that influence the lithium insertion/extraction rates. The average lithium transport rate goes down with increasing Ni content. More importantly, the thickness of the Li-O layer (d_{LiO_2}) also determines the moving rate of lithium ions. A thicker d_{LiO_2} leads to a faster lithium ion movement. The bond strengths of Li-O and M-O also influence the electrochemical reaction rate. In ternary materials, Ni^{2+} , Co^{3+} , Mn^{4+} have similar electron energies. However, the Ni^{2+} has longer M-M bonds, fewer covalent electrons and lower overlap of d orbitals. This leads to a slow charge transporting behavior. Belharouak⁵² believes their $\text{Li}(\text{Ni}_{1/3}\text{Mn}_{1/3}\text{Co}_{1/3})\text{O}_2$ has promising high rate charge/discharge performance, and it has the potential to be applied to electric vehicles. Over the voltage range of 2.9 to

4.1 V, no capacity loss were observed, and only an 18% capacity loss was measured under 5 C discharge after 200 cycles.

The ternary Li(Ni, Mn, Co)O₂ materials have shown better thermal stability than LiCoO₂. The Ohzuku group⁵⁰ used mass spectrometry to analyze the gases which were generated by the thermal decomposition of Li_{1-x}CoO₂ (140 mAh/g) and Li_{1-x}(Ni_{1/3}Mn_{1/3}Co_{1/3})O₂ (185 mAh/g). As shown in Figure 1.20, the ternary starts to generate oxygen at higher temperatures than Li_{1-x}CoO₂. High temperature XRD indicated a spinel phase containing Ni, Co and Mn when the Li(Ni_{1/3}Mn_{1/3}Co_{1/3})O₂ was charged to 4.45V. A phase transition from layered structure to a spinel structure effectively stopped oxygen release from the crystal structure.

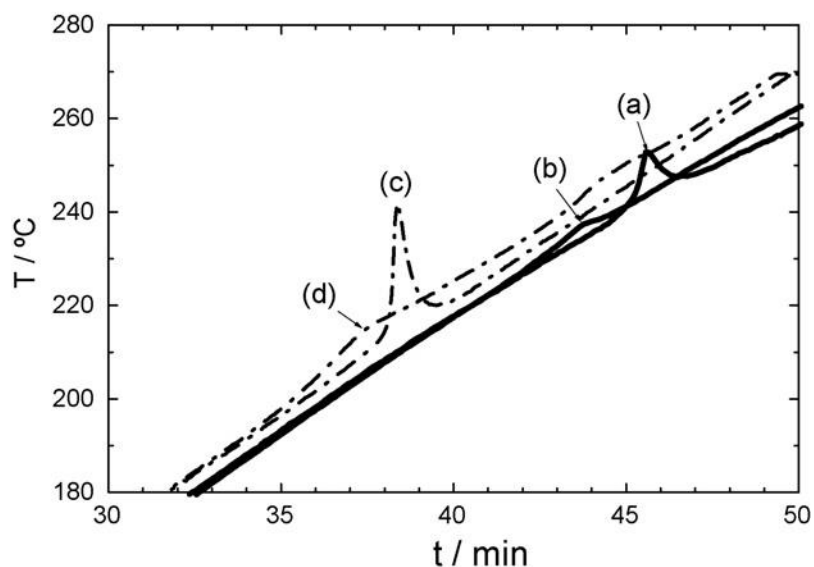


Figure 1.20 Hot-pot study of C/Li(Ni_{1/3}Co_{1/3}Mn_{1/3})O₂ (Charged at 4.2V) and C/Li_{1-x}CoO₂ (Charged at 4.7V) full cell. (a) Li_{1-x}(Ni_{1/3}Mn_{1/3}Co_{1/3})O₂ charged to 4.4V; (b) Li_{1-x}(Ni_{1/3}Mn_{1/3}Co_{1/3})O₂ charged to 4.7V; (c) Li_{1-x}CoO₂ charged to 4.2V; (d) Li_{1-x}CoO₂ charged to 4.7V. (Reprinted from reference [50] with permission from Elsevier)

For the ternary materials with different Ni content, the effect of each element on thermal stability is different. Konishi⁵³ studied the effects of Co and Mn on the $\text{Li}(\text{Ni}_x\text{Mn}_{(1-x)/2}\text{Co}_{(1-x)/2})\text{O}_2$ ($x=1/3, 0.6, \text{ and } 0.8$) thermal stability. XANES results confirmed changes in the oxidation states on Co and Ni. At high temperatures, Co ions relocates from the original octahedron to the tetrahedron. The position in the tetrahedron is more stable. Meanwhile, Mn stays at its original platform. The migration of Co ions slows down the beneficial phase change from layered structure to spinel structure.

Calendar life is also a very important performance of LIBs. Watanabe^{54,55} tested the calendar life of Ni-rich NCA. In 18650 cells, two cathodes, NCA (NCR18650) and LiCoO_2 (CGR18650E), were employed. The cells were fully charged and stored at 45 °C for two years. The NCR18650 showed a much better capacity retention than the NCR 18650E. After storage, the internal impedance increased, and the capacity dropped. The main reasons are the degradation of the electrodes. The SEI layer on both LCO and NCA were characterized by XPS. The elemental contents and the thickness were the same. For NCA, the Ni^{3+} was detected at 856.4 eV by electron energy loss near edge structure (ELNES), While the Co-L_{2,3} EXANES peaks decreased by ~1.5 eV in LCO. This confirmed that crystal structure degradation was severe in LCO, while the structure of NCA was maintained.

1.7 Challenges and Developments of Ternary Cathode Material

1.7.1 Challenges of $\text{Li}(\text{NiMnCo})\text{O}_2$

(1) Deterioration of cycle performance with increasing Ni content

Figure 1.21 presents the first cycle charge-discharge curve of a series of ternary

materials.⁴¹ The oxidation and reduction peaks of the first cycle were at 3.76 V and 3.72 V when $x=1/3$ (content of Ni in ternary material). An additional oxidation peak was observed at 3.64 V when the Ni content was increased. When $x=0.8$, four pairs of oxidation and reduction peaks were observed. The oxidation peaks were at 3.62 V, 3.78 V, 4.04 V, and 4.23 V, respectively. These peaks corresponded to phase changes from hexagonal H1 to monoclinic M, monoclinic M to hexagonal H2, and hexagonal H2 to hexagonal H3. The reduction peaks appeared at 3.58 V, 3.72 V, 3.98 V and 4.18 V. In the cycles, materials having $1/3$ of Ni showed stable redox behavior. However, increasing the Ni content led to a larger polarization of the redox peaks. The peak at 3.62 V shifted to 3.76 V after 100 cycles when the Ni content was 0.8. The capacity fade was mainly due to the volume shrinkage during the phase change from H2 to H3.⁵⁶ When the Ni content was lower, there was no phase change from H2 to H3, and the volume change occurred slightly during the cycles. Hence, the structure of ternary materials, having less Ni, was more stable, resulting in better reversibility. The better cyclability of low Ni content materials was ascribed to the controlled phase transition from H2 to H3.

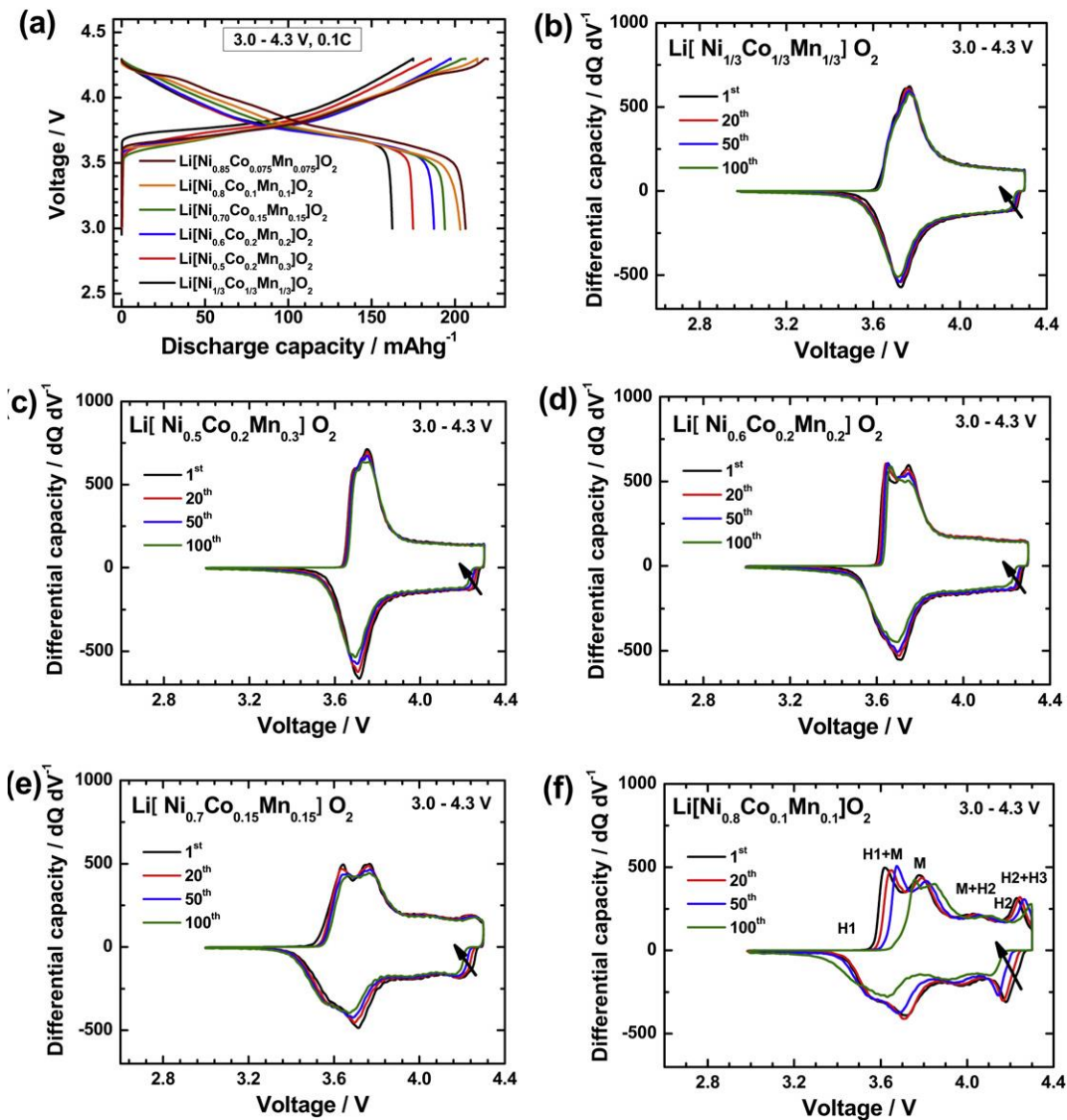


Figure 1.21 Initial charge-discharge curves of $\text{Li}[\text{Li}(\text{Ni}_x\text{Co}_y\text{Mn}_z)\text{O}_2$ ($x=1/3, 0.5, 0.6, 0.7, 0.8, \text{ and } 0.85$) and corresponding capacity vs. voltage curves for (b) $x=1/3$, (c) $x=0.5$, (d) $x=0.6$, (e) $x=0.7$, and (f) $x=0.8$. The applied current density across the positive electrode was 20 mA g^{-1} (0.1 C) at $25 \text{ }^\circ\text{C}$ over the voltage range $3.0 \text{ V} \sim 4.3 \text{ V}$. (Reprinted from reference [41] with permission from Elsevier)

(2) Residual amounts of LiOH and Li₂CO₃ on the cathode surface⁴¹

For high Ni content, Li[Ni_xMn_yCo_z]O₂ materials, especially when $x > 0.6$, Li₂CO₃ and LiOH are produced on the cathode surface once the materials are exposed to air. LiOH will react with LiPF₆ in the electrolyte to form HF, and Li₂CO₃ will cause severe inflation when stored at high temperature, particularly during charging of the battery. Table 1.1 shows that the total amount of Li₂CO₃ and LiOH on the cathode surface increases with increasing Ni contents in ternary materials. When $x > 0.7$, the residues increase, further impacting battery assembly and electrochemical properties.

(3) Thermal stability deterioration with increased Ni content

As shown in Figure 1.22, increasing the amount of Ni in ternary cathode materials, lowered the thermal degradation temperature and generated a higher heat generation. In other words, the thermal stability of the materials degraded when more Ni was present in the cathode. Figure 1.22 shows the DSC experiments for batteries charged to 4.3 V. In high Ni materials, more Li⁺ deintercalated, and yielded a larger amount of Ni⁴⁺ produced in the cathode. To balance the charges, oxygen was evolved worsening thermal stability.

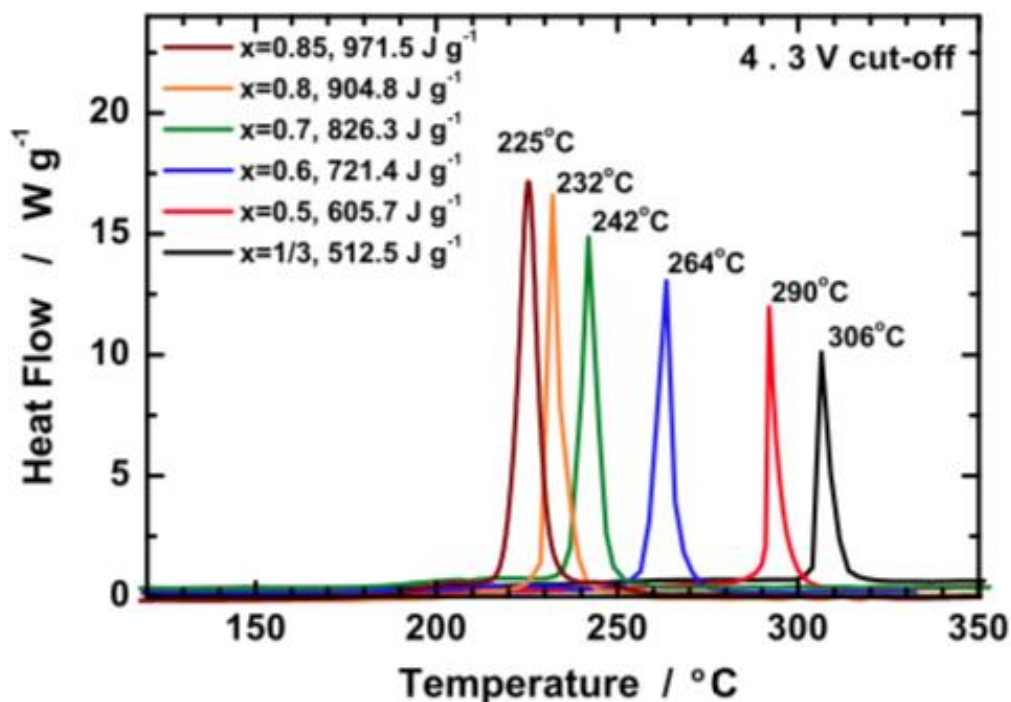


Figure 1.22 DSC curves of $\text{Li}_{1-\delta}[\text{Ni}_x\text{Co}_y\text{Mn}_z]\text{O}_2$ cathode materials ($x=1/3, 0.5, 0.6, 0.7, 0.8, 0.85$). (Reprinted from reference [41] with permission from Elsevier)

(4) Compatibility with electrolytes

The interfacial reaction and charge transfer between the electrolyte and cathode surface affect battery performance and stability. The corrosion of the active materials and electrolyte degradation significantly impacted the charge transfer between electrolytes and electrodes.⁵⁷ In terms of high Ni ternary materials, Li_2CO_3 and LiOH could easily react with the electrolyte at high temperatures. The produced HF caused the dissolution of Co and Ni ions, resulting in diminished storage life time.

(5) Influence by uneven surface reaction

Ni-rich ternary materials was then used to achieve high energy density batteries. In work by Hwang⁵⁸ the high discharge capacity (200 mAh/g) of NCA was considered as

one of the most promising cathode materials for batteries applied to electric vehicles. However, these materials exhibited fast capacity fade, increased in internal resistance, and thermal stability deterioration during cycling. From TEM characterization, the crystal and electron structures of the NCA surface were uneven during charging, as shown in Figure 1.23. Because of the dynamics, more Li^+ deintercalated from the particle surface, and led to structural instabilities. The instability caused the reduction of transition metal ions, and oxygen was lost to maintain electrical neutrality. At the same time, new phases produced on the material surface. For Ni rich materials, the structural instability is not favorable for the battery system. High temperature cycling experiments showed that the rapid power attenuation of NCA materials could be ascribed to the non-electrochemically active NiO , with similar rock-salt structure formed on the surface. Ni rich cathode materials formed complicated structures during charging. The nucleus is a layered $\text{R}\bar{3}\text{m}$ structure, and is covered by a spinel structure. The outer layer is a rock-salt structure. Oxygen released due to the phase transition caused react with combustible electrolyte and accelerate thermal runaway. Their research showed that certain coatings on the materials' surface could help increase the life time and improve the stability of the batteries. Since Li^+ is greatly influenced by dynamic factors, it is important to improve the dynamic properties and Li^+ diffusion of the materials by doping and surface modification.

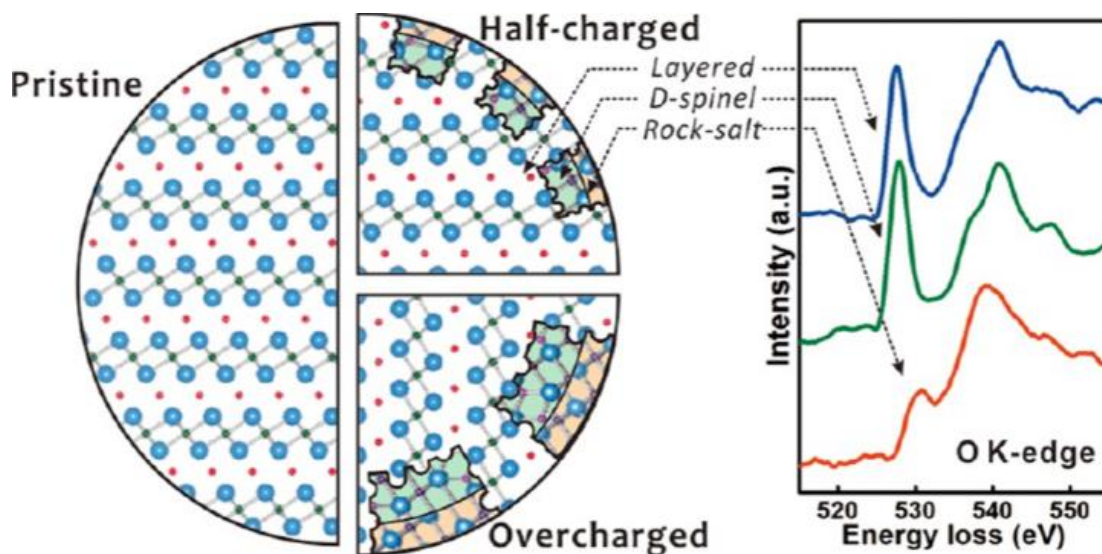


Figure 1.23 Phase changes in NCA materials during charging process. (Reprinted with permission from reference [58]. Copyright 2018, American Chemical Society)

1.7.2 Developments of $\text{Li}(\text{NiMnCo})\text{O}_2$

Ternary materials have some intrinsic disadvantages, such as instability caused by phase transitions during high voltage cycling, low electronic conductivity, low power rate due to Li/Ni mixing, inflation at high temperatures caused by Li_2CO_3 and LiOH , and low thermal stability due to strong oxidation of highly lithium-deintercalated materials. To address these problems, ion doping, surface protection and electrolyte additives have been employed to help improve the electrochemical properties of ternary cathode materials.

(1) Doping

Doping with metal and nonmetal ions can increase the electronic and ionic conductivity, improve output power density, and also the structural stability of ternary materials. The commonly used doping elements are Al, Mg, Ti, Zr, and F. Different doping elements have different roles.

When unequal valence charged cations are used for doping, the valence states of transition metals in the ternary materials will change, causing changes in electronic band structure, and affecting electronic conductivity. P. -Y. Liao⁵⁹ studied Mg doped $\text{LiNi}_{0.6-y}\text{Mn}_{0.15}\text{Co}_{0.25}\text{Mg}_y\text{O}_2$ and discussed the effect of Mg percentage on the structure and electrochemical properties of the materials. By increasing the amount of Mg^{2+} , parameters a and c of the unit cell increased. It also affected the oxidation states of Ni ($r_{\text{Ni}^{2+}} = 0.72 \text{ \AA}$, $r_{\text{Ni}^{3+}} = 0.56 \text{ \AA}$, $r_{\text{Mg}^{2+}} = 0.72 \text{ \AA}$), with the valence state of Co and Mn remained the same. The doping process significantly improved the cyclability of the battery and minimized polarization effects. The best performance was achieved when $x(\text{Mg}^{2+})=0.03$. The capacity retention of the batteries was improved from 77% and 63% to 93% after 30 cycles, respectively, either at room temperature or at 55 °C (Figure 1.24). The valence states and surrounding environment of the transition metals were investigated by high energy synchrotron X-ray absorption spectroscopy. The initial valence states of Ni, Co, and Mn were 2+/3+, 3+, and 4+ revealed by X-ray absorption near edge structure (XANES). When charged to 5.2 V, the main redox reaction was the oxidation of $\text{Ni}^{2+}/\text{Ni}^{3+}$ to Ni^{4+} . XANES results exhibited that Ni-O bond length dramatically decreased when Li deintercalated, while the bond length of Co-O and Mn-O only changed slightly. The results further explained that the distance change of M-M in the second layer was due to the oxidation of metal ions and the contraction of the a axis.

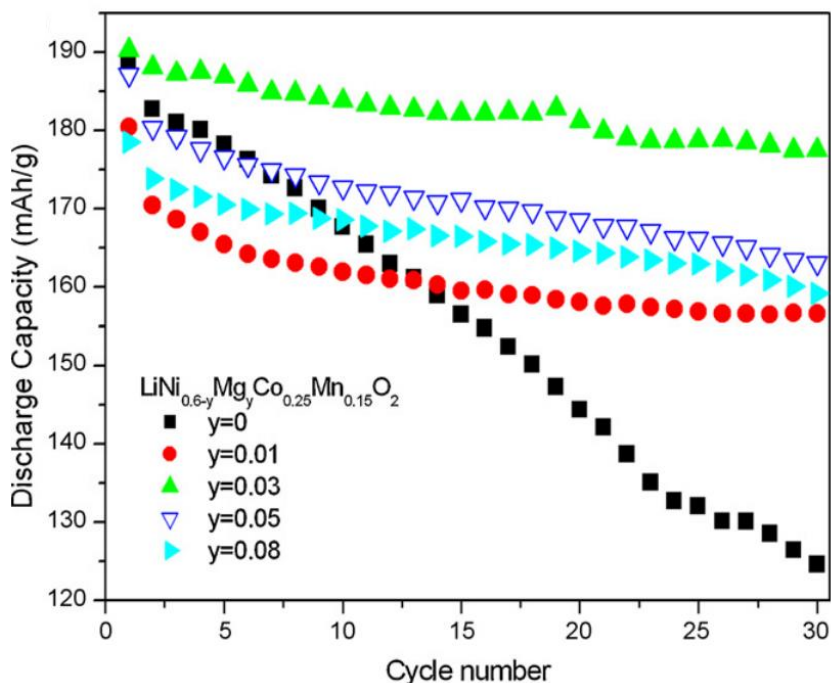


Figure 1.24 Discharge capacity-cycle number of $\text{LiNi}_{0.6-y}\text{Co}_{0.25}\text{Mn}_{0.15}\text{Mg}_y\text{O}_2$. ($y = 0, 0.01, 0.03, 0.05, \text{ and } 0.08$) Discharged at 55°C between $3 \sim 4.5$ V. (Reprinted from reference [59] with permission from Elsevier)

S. W. Woo⁶⁰ used Al and Mg to dope $\text{Li}[\text{Ni}_{0.8}\text{Mn}_{0.1-x-y}\text{Co}_{0.1}\text{Al}_x\text{Mg}_y]\text{O}_2$ and studied the influence of doping on the electrochemical properties of the materials. The mixing degree of cations in $\text{Li}[\text{Ni}_{0.8}\text{Mn}_{0.1-x-y}\text{Co}_{0.1}\text{Al}_x\text{Mg}_y]\text{O}_2$ was minimized with increasing amount of Al and Mg. The main reason is that Al and Mg engaged in the lattice and stabilized the lattice structure, which further improved the cyclability and thermal stability. Figure 1.25 presents TGA analysis of materials with different amounts of dopants. The generated oxygen was significantly reduced when Al/Mg mixtures were used as dopants. Figure 1.26 shows that the thermal stability of the materials was mostly impacted by Al doping resulting in an increase in degradation temperature with

increasing Al contents.

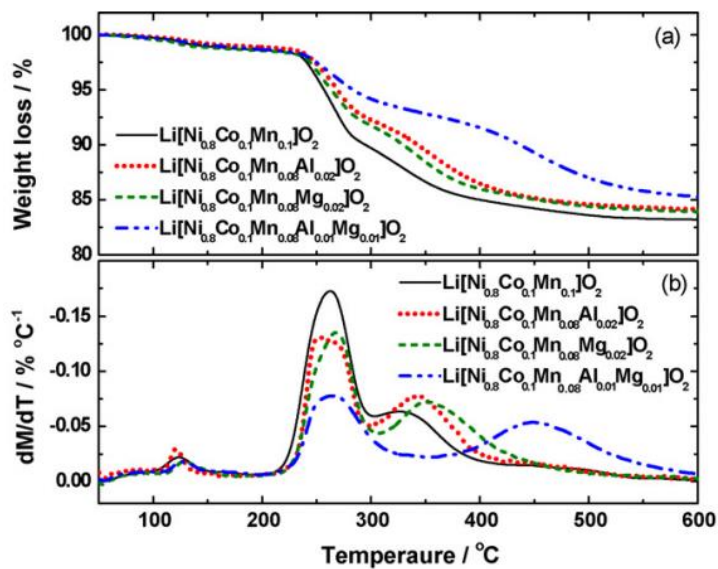


Figure 1.25 (a) Thermogravimetry and (b) differential thermogravimetry curves of delithiated $\text{Li}[\text{Ni}_{0.8}\text{Mn}_{0.1-x-y}\text{Co}_{0.1}\text{Al}_x\text{Mg}_y]\text{O}_2$. (Reprinted from reference [60] with permission from Elsevier)

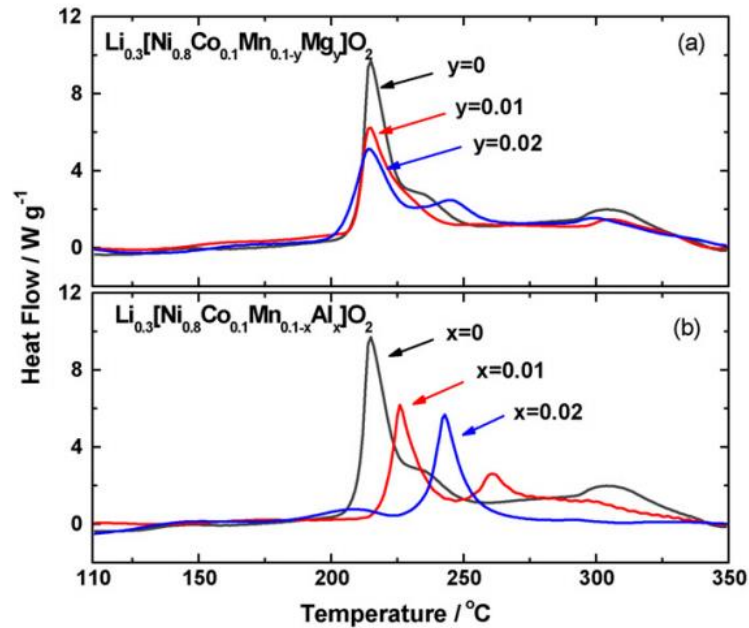


Figure 1.26 Differential scanning calorimetry of $\text{Li}[\text{Ni}_{0.8}\text{Mn}_{0.1-y}\text{Co}_{0.1}\text{Mg}_y]\text{O}_2$ and $\text{Li}[\text{Ni}_{0.8}\text{Mn}_{0.1-x}\text{Co}_{0.1}\text{Al}_x]\text{O}_2$ as a function of Al doping. (Reprinted from reference [60] with permission from Elsevier)

Zhou⁶¹ investigated the effects of replacing Co by Al in the delithiation process of $\text{LiNi}_{1/3}\text{Mn}_{1/3}\text{Co}_{(1/3-z)}\text{Al}_z\text{O}_2$ and reactions with the electrolyte at high temperatures. When more than 0.06 (molar ratio) of Al was used to replace Co, reactions with the electrolyte significantly decreased and were much less than in the spinel LiMn_2O_4 . When Al was about 0.1 (molar ratio), the cells showed enhanced safety. Ding⁶² found that when Mn was substituted by 0.06 molar ratio of Al, $\text{LiNi}_{1/3}\text{Mn}_{(1/3-x)}\text{Co}_{1/3}\text{Al}_x\text{O}_2$ exhibited better structural stability and cyclability as shown in Figure 1.27.

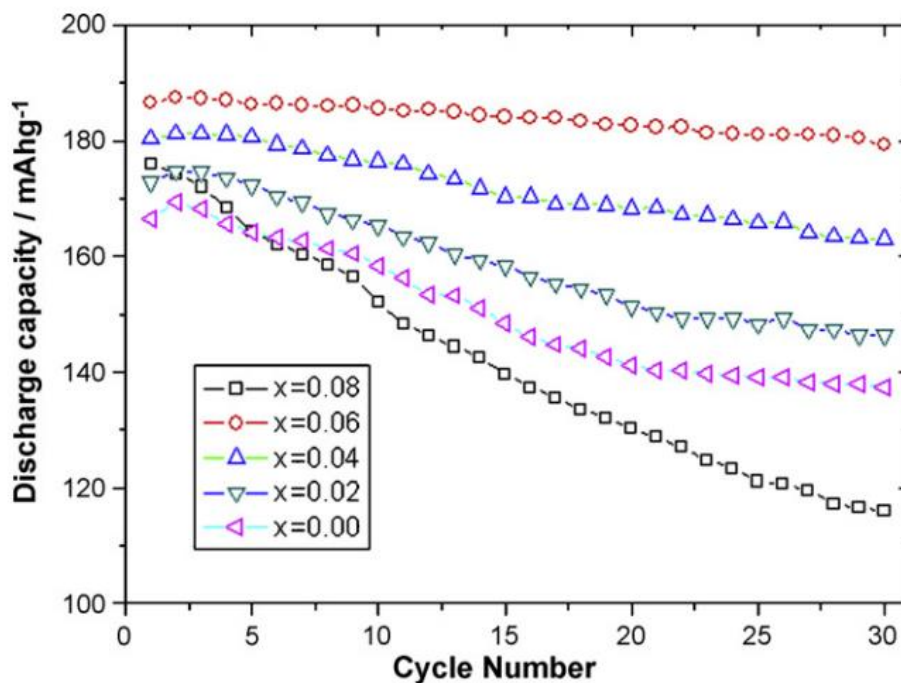


Figure 1.27 Capacity retention of $\text{LiNi}_{1/3}\text{Mn}_{(1/3-x)}\text{Co}_{1/3}\text{Al}_x\text{O}_2$. (Reprinted from reference [62] with permission from Elsevier)

(2) Coating

Since the redox reactions happen at the interface between the electrodes and electrolytes, surface coating is one of the most effective methods to improve the electrochemical properties of ternary materials. Coating could improve the reversible specific capacity, cyclability, rate capability and thermal properties. The impact of coating on electrode performance strongly depends on the properties, content, and thermal treatment of the coating. Commonly used coatings include metal oxides (Al_2O_3 , ZrO_2 , CeO_2 , TiO_2 , MgO , B_2O_3 , and ZnO), fluorinated compounds (LiF , and AlF_3), and phosphates (SnPO_4 , and Li_3PO_4).

Al_2O_3 is considered as the best oxide among oxide coatings. Al_2O_3 coats are insulating

to ions and electrons, and will form a layer of Li-Al-Co-O after thermal treatment preventing HF corrosion of the active materials. Al₂O₃ layers can also lower surface resistance and improve cyclability. Al₂O₃ layers can be obtained via precipitation, sol-gel, and deposition. Riley⁶³ used atomic layer deposition (ALD) to deposit Al₂O₃ on Li(Ni_{1/3}Mn_{1/3}Co_{1/3})O₂ and discussed the impact of coating thickness. No structural changes were observed for the treated materials revealed by XRD, Raman, and FTIR. Electrochemical impedance spectroscopy showed that 4 layers of Al₂O₃ (8.8 Å) could prevent HF corrosion and the cells could be charged up to 4.5V. In addition, only 2 layers of Al₂O₃ could improve the capacity retention from 65% to 91% after 100 cycles at C/2. Hence, surface coating also brought some negative impacts, such as lower specific capacity and large overpotentials. They speculated that Al-O-F and Al-F layers formed on the surface, from Al₂O₃, and acted as scavengers to control the content of HF in the electrolyte. The thickness of the Al₂O₃ coating greatly influenced battery performance and better electrochemical properties could be achieved by controlling the thickness below 8.8 Å using ALD method.

Kong⁶⁴ used ALD to deposit super thin ZnO layers on LiNi_{0.5}Co_{0.2}Mn_{0.3}O₂ cathode materials. The materials showed improved electrochemical properties after coating. The coating prevented dissolution of metal ions, HF corrosion, and enhanced structural stability under high voltages. Super thin layer of ZnO did not inhibit the diffusion of Li during charge and discharge, thus, it significantly increased the specific discharge capacity.

Surface modification using fluorinated compounds is also an effective method to improve the electrochemical properties of layered cathodes. Since Al₂O₃ will gradually changes to AlF₃ through Al-O-F, HF corrosion could be prevented to protect

the active materials. Myung⁶⁵ coated AlF_3 on the ternary materials and discussed the influence of AlF_3 coating in Li deintercalation and thermal stability of $\text{Li}[\text{Ni}_{1/3}\text{Mn}_{1/3}\text{Co}_{1/3}]\text{O}_2$ from room temperature to 600 °C. Thermogravimetric analysis indicated that less oxygen was produced after coating and there was an irreversible phase transition accompanied by a weight loss of uncoated powder. The phase changed from R3m to the cubic spinel structure Fd3m. High temperature XRD demonstrated that the AlF_3 coating delayed the phase transition. For the presence of electrolyte, the exothermic peak shifted to higher temperatures and less heat was generated. This was attributed to the formation of Li-Al-O on the surface.

Myung⁶⁶ studied the impact of Al_2O_3 , Nb_2O_5 , Ta_2O_5 , ZrO_2 and ZnO coatings on the electrochemical properties of $\text{Li}[\text{Li}_{0.05}\text{Ni}_{0.4}\text{Mn}_{0.4}\text{Co}_{0.15}]\text{O}_2$. The metal oxide coatings did not engage in the electrochemical reactions and greatly improved the cyclability of the batteries at 60 °C. The surface modified ternary materials showed higher specific capacity, better capacity retention, and reduced interfacial resistance. Al_2O_3 was the best coating materials among these metal oxides. The improved properties of the materials were mainly due to the M-F protection layer formed between coatings and electrolyte, which prevented dissolution of metal ions.

Anionic coatings are mainly based on phosphate. In the coatings, the P=O bond can improve the chemical stability of the materials, and protect the cathodes from being corroded. Also the strong PO_4 covalent bond could combine with metal ions to enhance thermal stability. AlPO_4 , $\text{Co}_3(\text{PO}_4)_2$, and SnPO_4 could improve the cyclability and thermal stability of cathodes, but they were also considered as prevention layers for Li^+ diffusion due to their low conductivity.⁶⁷ Li_3PO_4 was regarded as a Li conductor, and it could enhance electrochemical properties.

Han Gab Song et al⁶⁷ used Li_xPO_4 ($x = 0, 1.5, 3$), LiNiPO_4 and $\text{Li}_{0.5}\text{Ni}_{1.25}\text{PO}_4$ to coat $\text{Li}[\text{Ni}_{0.4}\text{Mn}_{0.3}\text{Co}_{0.3}]\text{O}_2$ and studied its impact on materials properties. Their results revealed that the properties were influenced by the coating composition. This was because of the diffusion of coating materials into the cathode surface, the high interfacial energy of nano-coating led to reactions with Li, Co, Ni and Mn. Also, Li_2O , produced during storage would react with the coating materials and produce different compounds. Li_3PO_4 , $\text{Li}_{1.5}\text{PO}_4$, and PO_4 coatings are amorphous, while LiNiPO_4 and $\text{Li}_{0.5}\text{Ni}_{1.25}\text{PO}_4$ are mixtures of amorphous and crystalline particles. Amorphous structures are more favorable for Li^+ diffusion. Li in coating materials does not engage in delithiation processes, but it can stabilize the structure, stop electrolytes-active materials reactions, and improve cyclability of the materials. After storing at 50 °C for 3 days, their Li_3PO_4 coating showed the best performance according to AC impedance experiments. Even for materials with same composition, preparation conditions made a difference. Figure 1.28 presents the influence of coatings prepared at different pH on power capability. It was found that a pH = 2 gave the best results.

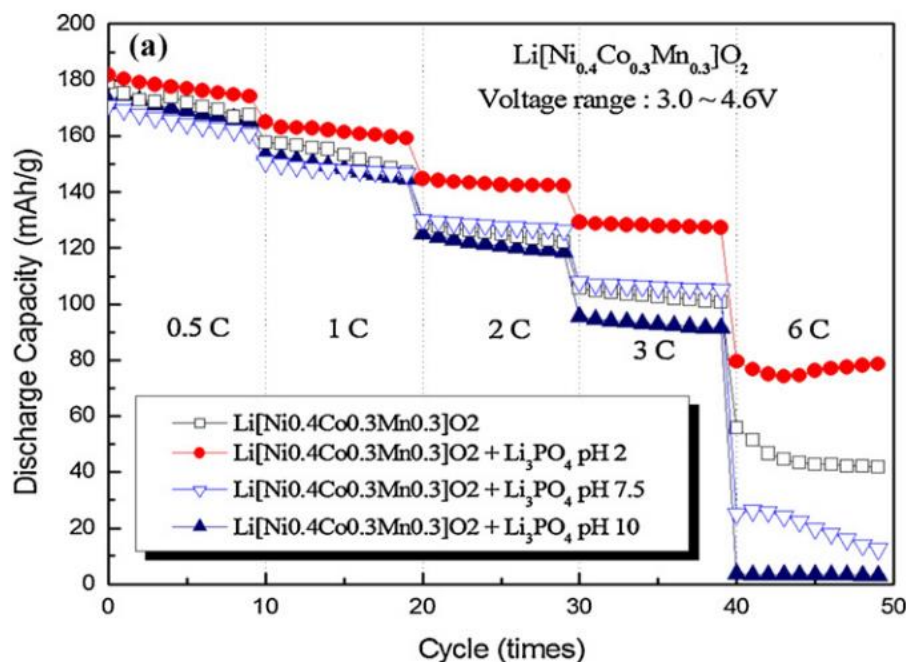


Figure 1.28 Power capability of uncoated and Li_3PO_4 coated $\text{Li}[\text{Ni}_{0.4}\text{Co}_{0.3}\text{Mn}_{0.3}]\text{O}_2$ in the voltage range of 3.0 V ~ 4.6 V at 0.5, 1, 2, 3, and 6C rates. (Reprinted from reference [67] with permission from Elsevier)

(3) Concentration-gradient materials

Electrochemical reactions take place at the interface between electrolytes and electrodes, thus the surface condition of materials is important. In general, high capacity Ni rich materials were used as core, while structurally stable Mn based materials, even when highly delithiated, were used as shell in core-shell structures, such as $\text{Li}[\text{Ni}_{0.5}\text{Mn}_{0.5}]\text{O}_2$. Due to the sudden change in transition metal composition and structural incompatibility between core and shell, the volume will change significantly during cycling. The volume change will further result in hindered Li^+ diffusion and degraded electrochemical performance. In contrast, shells having a Mn rich surface with concentration gradient can provide a gentle transition for Li^+ . This structure shows better specific capacity, cyclability, and thermal stability.

Sun⁶⁸ reported on the properties of $\text{Li}[\text{Ni}_{0.67}\text{Co}_{0.15}\text{Mn}_{0.18}]\text{O}_2$ prepared via a co-precipitation method. The material had $\text{Li}[\text{Ni}_{0.8}\text{Co}_{0.15}\text{Mn}_{0.05}]\text{O}_2$ as core and $\text{Li}[\text{Ni}_{0.57}\text{Co}_{0.15}\text{Mn}_{0.28}]\text{O}_2$ as shell with a gradient concentration. They observed improved performance and assumed it to the increased content of Mn^{4+} and decreased content of Ni in the outside shell. Concentration-gradient materials had better properties and this was due to uniform concentration distribution in the shell. Such uniform distribution avoided core-shell separation caused by large differences in composition during charge and discharge process. Figure 1.29 shows the cross section of a single particle, revealed by electron probe microanalysis (EPMA). A continuous change in composition was observed. The content of Ni, Co and Mn remained the same in the core, while the Ni content changed from 76% to 57% in the shell. In contrast, the Mn content increased from 7% to 28%.

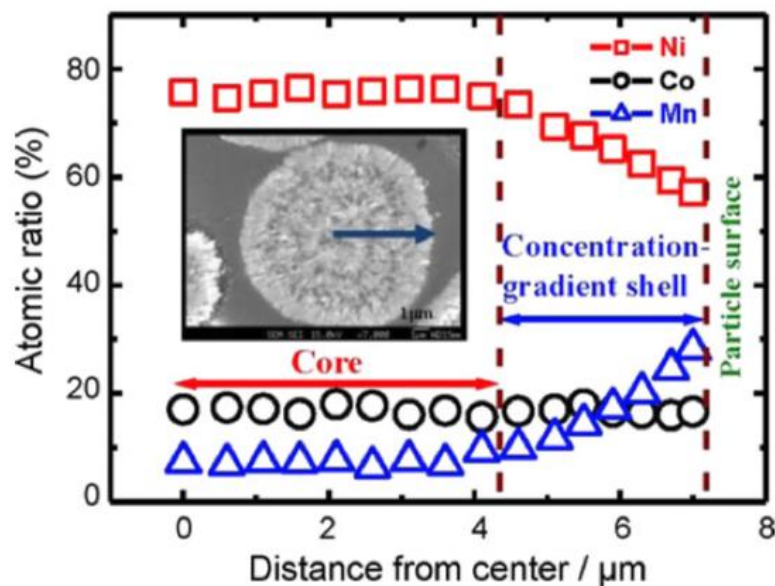


Figure 1.29 Composition analysis of $\text{Li}[\text{Ni}_{0.67}\text{Co}_{0.15}\text{Mn}_{0.18}]\text{O}_2$ by cross section of a single particle by EPMA. (Reprinted from reference [68] with permission from Elsevier)

Even though the core material had a high discharge capacity, it dropped dramatically with continued cycles. The poor performance could be explained by the phase change of the Ni rich core materials during charge and discharge. Increasing amount of Mn lowered the capacity, but suppressed the phase change, which improved cyclability of the batteries. In addition, the resistance of the surface film for concentration-gradient materials was twice that of the core material, but the former had a smaller charge-transfer resistance. Charge-transfer resistance of the concentration-gradient material was only 20% of the core material after 50 cycles. The differences in resistance also explained the improved performance.

Figure 1.30 presents a comparison of two materials in degradation temperatures and heat generation. For the core material, the degradation temperature was at 217 °C with 2632 J/g heat generated. A degradation temperature of 236 °C with 1530 J/g of heat generated were observed for the concentration-gradient material, while the shell material degraded at 271 °C and generated 858 J/g of heat. It indicated that thermally stable shell material prevented direct contact between the highly oxidized core materials and electrolyte, thus suppressing oxygen generation. The gradient, and continuous change, in Mn^{4+} concentration led to improved thermal stability and steady Li^+ intercalation.

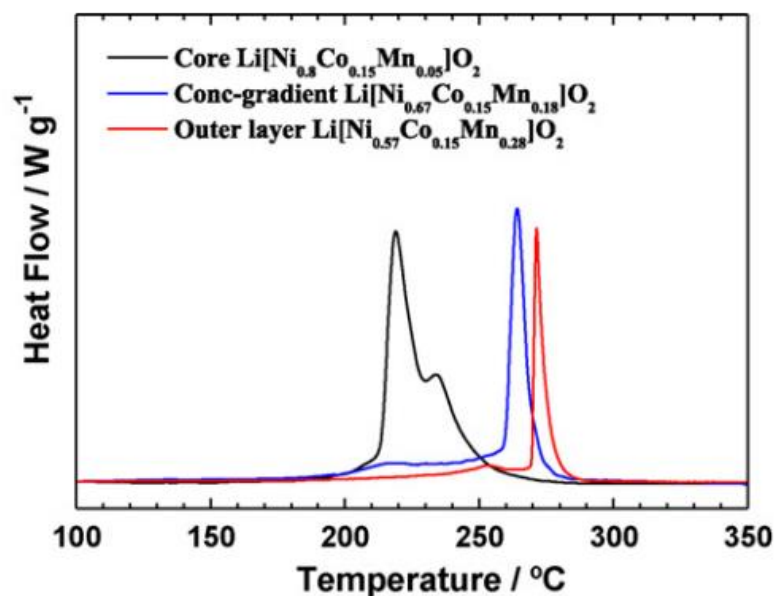


Figure 1.30 DSC curves of core, concentration-gradient, and shell materials. (Reprinted from reference [68] with permission from Elsevier)

1.8 Future Development of Ternary Cathode Material

To significantly boost the energy density of batteries for EV application, many countries have recently announced, medium-term, and long-term goals for EVs and EV batteries. For the cathode, the ternary transition metal oxides are more favorable when compared to other types in terms of enhancing the energy density.

(1) High capacity ternary materials

The cycle performance of $\text{LiAl}_{0.10}\text{Ni}_{0.76}\text{Co}_{0.14}\text{O}_2$ (NCA)/graphite at 25 °C and 60 °C over different charge-discharge voltages was investigated in Nakura group.⁶⁹ The deterioration in cycle performance was studied by XPS, annular dark-field imaging scanning transmission electron microscopy (HAADF-STEM), and scanning transmission electron microscope coupled with electron energy loss spectroscopy (STEM-EELS). They observed various fine cracks created between the primary

particles after cycling at 0 ~ 100% Δ DOD. Electrolyte could travel to the particle surface through those cracks and degraded to form a low conductivity passivating layer. However, this is not the main for poor cyclability. The main reason could be explained by the formation of a rock-salt structured NiO layer on the particle's surface. The cracks gave rise to a higher contact resistance among the particles and weakened cycle performance. Restricting the charge-discharge depth could greatly improve cycle performance. For instance, restricting Δ DOD to 10% ~ 70% significantly increased the number of cycles (at 60 °C) to 5000 without any microcracks being observed. However, the layer thickness of NiO depended on the operating temperatures (25 °C – 8 nm, 60 °C – 25 nm). However, the NiO layer only formed on the surface of secondary particles. Thus, even at 60 °C, the cyclability could be maintained by restricting the depth of discharge.

In addition to controlling the depth of discharge, avoiding the formation of microcracks and suppressing NiO layer formation can improve the performance of NCA batteries.

The thermal instability of NCA batteries is another major concern. The decomposition of NCA is exothermic when heated up to 200 ~ 300 °C and rises potential safety concerns. Battery safety is always related to exothermic reactions during charging since the heat generated can cause thermal runaway, and lead to catastrophic failure. When cathode materials are over charged, the generated oxygen species (O^{2-} , O^- , O_2^{2-} , and O_2) will actively react with the electrolyte and generate extensive heat.

In terms of NMC materials, especially those used at high voltages, the phase transition from layered structure to rock-salt like structure will happen at voltages higher than

4.5 V. Hence, studies on delaying or suppressing NiO formation is worth further attention.

(2) High power ternary materials

High power ternary materials have a bright future in numerous fields, such as electric tools, bikes and vehicles. Safety is still the major concern for ternary materials like NCA and NMC, when considering their applications in electric vehicles. In other words, improving safety is the focus on these materials, while rate capability and specific capacity are also important.

For ternary materials used as cathodes for high power batteries, the specific energy, thermal stability, and cycle performance are closely related to the ratio of Ni-Co-Mn. Aurbach et al⁷⁰ discussed the structure and electrochemical properties of three ternary materials, $\text{LiNi}_{0.50}\text{Mn}_{0.50}\text{O}_2$, $\text{LiNi}_{0.33}\text{Mn}_{0.33}\text{Co}_{0.33}\text{O}_2$, and $\text{LiNi}_{0.40}\text{Mn}_{0.40}\text{Co}_{0.20}\text{O}_2$, respectively. The first material had high capacity (190 mAh/g, 0.1 C, 2.5 – 4.5 V), but low rate capability. The capacity at 1 C are less than 100 mAh/g, and only 50 mAh/g was achieved at 3C. In contrast, the 111 material had a capacity of 170 mAh/g at 0.1 C, but it had good rate capability. A capacity above 100 mAh/g could be maintained at 3C. For 422 ternary materials, the capacity was around 180 mAh/g, 110 mAh/g, and 80 mAh/g at 0.1 C, 1 C, and 3 C, respectively. When the Co content increased from 0 to 0.33, the rate capability was improved. And capacity at 0.1C was enhanced from 170 mAh/g to 190 mAh/g when the Ni content was changed from 0.33 to 0.5. The research in Sun group⁴¹ also demonstrated a close relationship between materials composition and capacity retention and safety problems. Even though more Ni could increase discharge capacity, the capacity retention and battery safety are degraded.

Some other phenomena deserve attention. XPS revealed that the concentration of Ni at the surface is higher than inside. Also, the dissolution of Mn is twice that of Ni and Co in the electrolyte. Thus, research is needed to study Ni diffusion paths and control of Mn dissolution caused by the disproportionation reaction of Mn^{3+} at the surface. Battery safety, capacity, cyclability, rate capability, and price have to be considered when developing high power ternary materials. More effort has to be placed to study the relationships of structure and Ni/Co/Mn ratios, in order to establish conditions to achieve best overall performance.

Since Li^+ diffusion is affected by dynamic factors, increasing the diffusion coefficient through doping and surface modification is very important. According to numerous research results, doping can greatly improve the electrochemical properties of the cathode materials. Al, Zr, Mg, Cr, Ru, Zn, Ti, La, and F are the most studied doping elements. Since electrochemical reactions take place at the interface between electrodes and electrolytes, thermal degradation of Ni based cathode materials will be triggered and accelerated by reactions at the interface. Thus, the battery performance is greatly affected by electrode surface. There are many types of coating materials, such as oxides, fluorinated compounds, and phosphates.

Even though doping and coating can help mitigate the problems of uneven surface reactions, caused by slow ionic and electronic transport, the selection of dopant and coating need to favor their conductivity and structural stability.

(3) Electrolyte additive for ternary materials

Another important task in developing ternary cathode materials for LIBs is to explore compatible electrolytes. There are many reports regarding electrolytes, and additives

used for LiPF_6 in carbonate electrolytes to improve battery performance. The main purpose of additives is to improve the surface of the electrodes and prevent reactions between active materials and the electrolyte. This could be realized by electrolyte degradation at lower voltages and formation of compact films to protect the active materials. More research is needed to explore suitable electrolytes for ternary cathode material, such as electrolyte system for high voltage ternary cathode material, Ni-rich ternary cathode materials, and high power ternary cathode materials.

REFERENCE

- (1) Watanabe, N.; Fukuda, M. Primary cell for electric batteries. US3536532 A, October 27, 1970.
- (2) Whittingham, M. S. *Chem. Rev.* **2004**, *104* (10), 4271.
- (3) Mizushima, K.; Jones, P. C.; Goodenough, J. B. *Mater. Res. Bull.* **1980**, *15* (6), 783.
- (4) Ozawa, K. *Solid State Ionics* **1994**, *69* (3–4), 212.
- (5) Tarascon, J.-M.; Armand, M. *Nature* **2001**, *414* (6861), 359.
- (6) Armand, M.; Tarascon, J.-M. *Nature* **2008**, *451* (7179), 652.
- (7) Abraham, K. M. *J. Phys. Chem. Lett.* **2015**, 830.
- (8) Yoo, H. D.; Markevich, E.; Salitra, G.; Sharon, D.; Aurbach, D. *Mater. Today* **2014**, *17* (3), 110.
- (9) Yu, H.; Zhou, H. *J. Phys. Chem. Lett.* **2013**, *4* (8), 1268.
- (10) Winter, M.; Besenhard, J. O.; Spahr, M. E.; Novák, P. *Adv. Mater.* **1998**, *10* (10), 725.
- (11) Campion, C. L.; Li, W.; Euler, W. B.; Lucht, B. L.; Ravdel, B.; DiCarlo, J. F.; Gitzendanner, R.; Abraham, K. M. *Electrochem. Solid-State Lett.* **2004**, *7* (7), A194.
- (12) Abraham, K. M.; Pasquariello, D. M.; Willstaedt, E. B. *J. Electrochem. Soc.* **1990**, *137* (6), 1856.
- (13) Yoshimoto, N.; Niida, Y.; Egashira, M.; Morita, M. *J. Power Sources* **2006**, *163* (1), 238.
- (14) Feng, J. K.; Ai, X. P.; Cao, Y. L.; Yang, H. X. *Electrochem. Commun.* **2007**, *9* (1), 25.
- (15) Carlier, D.; Van der Ven, A.; Delmas, C.; Ceder, G. *Chem. Mater.* **2003**, *15* (13), 2651.
- (16) Yabuuchi, N.; Kawamoto, Y.; Hara, R.; Ishigaki, T.; Hoshikawa, A.;

- Yonemura, M.; Kamiyama, T.; Komaba, S. *Inorg. Chem.* **2013**, *52* (15), 9131.
- (17) Reimers, J. N.; Dahn, J. R. *J. Electrochem. Soc.* **1992**, *139* (8), 2091.
- (18) Ohzuku, T.; Ueda, A. *J. Electrochem. Soc.* **1994**, *141* (11), 2972.
- (19) Chen, Z.; Dahn, J. R. *Electrochim. Acta* **2004**, *49* (7), 1079.
- (20) Dahéron, L.; Dedryvère, R.; Martinez, H.; Flahaut, D.; Ménétrier, M.; Delmas, C.; Gonbeau, D. *Chem. Mater.* **2009**, *21* (23), 5607.
- (21) Jung, H.-G.; Gopal, N. V.; Prakash, J.; Kim, D.-W.; Sun, Y.-K. *Electrochim. Acta* **2012**, *68*, 153.
- (22) Delmas, C.; Menetrier, M.; Croguennec, L.; Saadoune, I.; Rougier, A.; Pouillier, C.; Prado, G.; Grüne, M.; Fournes, L. *Electrochim. Acta* **1999**, *45* (1–2), 243.
- (23) Delmas, C.; Peres, J.P.; Rougier, A.; Demourgues, A.; Weill, F.; Chadwick, A.; Broussely, M.; Perton, F.; Biensan, P.; Willmann, P. *J. Power Sources* **1997**, *68* (1), 120.
- (24) Rougier, A.; Saadoune, I.; Gravereau, P.; Willmann, P.; Delmas, C. *Solid State Ionics* **1996**, *90* (1–4), 83.
- (25) Sun, Y.-K.; Lee, D.-J.; Lee, Y. J.; Chen, Z.; Myung, S.-T. *ACS Appl. Mater. Interfaces* **2013**, *5* (21), 11434.
- (26) Ohzuku, T.; Ueda, A.; Kouguchi, M. *J. Electrochem. Soc.* **1995**, *142* (12), 4033.
- (27) Pouillier, C.; Croguennec, L.; Biensan, P.; Willmann, P.; Delmas, C. *J. Electrochem. Soc.* **2000**, *147* (6), 2061.
- (28) Xia, H.; Luo, Z.; Xie, J. *Prog. Nat. Sci.: Mater. Int.* **2012**, *22* (6), 572.
- (29) Wang, Z.; Chen, L.; Huang, X. *Progress in Chemistry* **2011**, *23*(2/3), 284.
- (30) Sakunthala, A.; Reddy, M. V.; Selvasekarapandian, S.; Chowdari, B. V. R.; Selvin, P. C. *Electrochim. Acta* **2010**, *55* (15), 4441.

- (31) Ye, S. H.; Bo, J. K.; Li, C. Z.; Cao, J. S.; Sun, Q. L.; Wang, Y. L. *Electrochim. Acta* **2010**, *55* (8), 2972.
- (32) Xiong, L.; Xu, Y.; Zhang, C.; Zhang, Z.; Li, J. *J. Solid State Electrochem.* **2011**, *15* (6), 1263.
- (33) Lee, K.-S.; Myung, S.-T.; Bang, H. J.; Chung, S.; Sun, Y.-K. *Electrochim. Acta* **2007**, *52* (16), 5201.
- (34) Arumugam, D.; Paruthimal Kalaignan, G. *Mater. Res. Bull.* **2010**, *45* (12), 1825.
- (35) Arumugam, D.; Kalaignan, G. P. *Electrochim. Acta* **2010**, *55* (28), 8709.
- (36) Lee, D.-J.; Lee, K.-S.; Myung, S.-T.; Yashiro, H.; Sun, Y.-K. *J. Power Sources* **2011**, *196* (3), 1353.
- (37) Ouyang, C. Y.; Zeng, X. M.; Šljivancanin, Ž.; Baldereschi, A. *J. Phys. Chem. C* **2010**, *114* (10), 4756.
- (38) Liu, Z.; Yu, A.; Lee, J.Y. *J. Power Sources* **1999**, *81–82*, 416.
- (39) Ohzuku, T.; Makimura, Y. *Chem. Lett.* **2001**, *30* (7), 642.
- (40) Venkatraman, S.; Choi, J.; Manthiram, A. *Electrochem. Commun.* **2004**, *6* (8), 832.
- (41) Noh, H.-J.; Youn, S.; Yoon, C. S.; Sun, Y.-K. *J. Power Sources* **2013**, *233*, 121.
- (42) Kim, J.-M.; Chung, H.-T. *Electrochim. Acta* **2004**, *49* (6), 937.
- (43) Koyama, Y.; Tanaka, I.; Adachi, H.; Makimura, Y.; Ohzuku, T. *J. Power Sources* **2003**, *119–121*, 644.
- (44) MacNeil, D. D.; Lu, Z.; Dahn, J. R. *J. Electrochem. Soc.* **2002**, *149* (10), A1332.
- (45) Whitfield, P.; Davidson, I.; Cranswick, L.; Swainson, I.; Stephens, P. *Solid State Ionics* **2005**, *176* (5–6), 463.
- (46) Kim, J.-M.; Chung, H.-T. *Electrochim. Acta* **2004**, *49* (21), 3573.

- (47) Liu, S.; Xiong, L.; He, C. *J. Power Sources* **2014**, *261*, 285.
- (48) Kim, H.-G.; Myung, S.-T.; Lee, J. K.; Sun, Y.-K. *J. Power Sources* **2011**, *196* (16), 6710.
- (49) Molenda, J.; Milewska, A. *J. Power Sources* **2009**, *194* (1), 88.
- (50) Yoshizawa, H.; Ohzuku, T. *J. Power Sources* **2007**, *174* (2), 813.
- (51) Venkatraman, S.; Choi, J.; Manthiram, A. *Electrochem. Commun.* **2004**, *6* (8), 832.
- (52) Belharouak, I.; Sun, Y.-K.; Liu, J.; Amine, K. *J. Power Sources* **2003**, *123* (2), 247.
- (53) Konishi, H.; Yoshikawa, M.; Hirano, T.; Hidaka, K. *J. Power Sources* **2014**, *254*, 338.
- (54) Watanabe, S.; Kinoshita, M.; Nakura, K. *J. Power Sources* **2014**, *247*, 412.
- (55) Watanabe, S.; Kinoshita, M.; Nakura, K. *J. Power Sources* **2011**, *196* (16), 6906.
- (56) Li, W.; Reimers, J.N.; Dahn, J.R. *Solid State Ionics* **1993**, *67* (1–2), 123.
- (57) Hausbrand, R.; Becker, D.; Jaegermann, W. *Prog. Solid State Chem.* **2014**, *42* (4), 175.
- (58) Hwang, S.; Chang, W.; Kim, S. M.; Su, D.; Kim, D. H.; Lee, J. Y.; Chung, K. Y.; Stach, E. A. *Chem. Mater.* **2014**, *26* (2), 1084.
- (59) Liao, P.-Y.; Duh, J.-G.; Lee, J.-F. *J. Power Sources* **2009**, *189* (1), 9.
- (60) Woo, S.-W.; Myung, S.-T.; Bang, H.; Kim, D.-W.; Sun, Y.-K. *Electrochim. Acta* **2009**, *54* (15), 3851.
- (61) Zhou, F.; Zhao, X.; Lu, Z.; Jiang, J.; Dahn, J. R. *Electrochem. Commun.* **2008**, *10* (8), 1168.
- (62) Ding, Y.; Zhang, P.; Long, Z.; Jiang, Y.; Xu, F. *J. Alloys Compd.* **2009**, *487* (1–2), 507.

- (63) Riley, L. A.; Van Atta, S.; Cavanagh, A. S.; Yan, Y.; George, S. M.; Liu, P.; Dillon, A. C.; Lee, S.-H. *J. Power Sources* **2011**, *196* (6), 3317.
- (64) Kong, J.-Z.; Ren, C.; Tai, G.-A.; Zhang, X.; Li, A.-D.; Wu, D.; Li, H.; Zhou, F. *J. Power Sources* **2014**, *266*, 433.
- (65) Myung, S.-T.; Lee, K.-S.; Yoon, C. S.; Sun, Y.-K.; Amine, K.; Yashiro, H. *J. Phys. Chem. C* **2010**, *114* (10), 4710.
- (66) Myung, S.-T.; Izumi, K.; Komaba, S.; Yashiro, H.; Bang, H. J.; Sun, Y.-K.; Kumagai, N. *J. Phys. Chem. C* **2007**, *111* (10), 4061.
- (67) Song, H. G.; Kim, J. Y.; Kim, K. T.; Park, Y. J. *J. Power Sources* **2011**, *196* (16), 6847.
- (68) Sun, Y.-K.; Kim, D.-H.; Jung, H.-G.; Myung, S.-T.; Amine, K. *Electrochim. Acta* **2010**, *55* (28), 8621.
- (69) Watanabe, S.; Kinoshita, M.; Hosokawa, T.; Morigaki, K.; Nakura, K. *J. Power Sources* **2014**, *258*, 210.
- (70) Martha, S. K.; Sclar, H.; Szmuk Framowitz, Z.; Kovacheva, D.; Saliyski, N.; Gofer, Y.; Sharon, P.; Golik, E.; Markovsky, B.; Aurbach, D. *J. Power Sources* **2009**, *189* (1), 248.

CHAPTER 2

KEY PARAMETER OPTIMIZATION OF UNIFORM, HIGH-ENERGY AND HIGH STABILITY LITHIUM NICKEL MANGANESE COBALT OXIDE CATHODE MATERIAL FOR LITHIUM-ION BATTERIES¹

2.1 Introduction

The drive to lower the consumption of fossil fuels in transportation has reached unprecedented levels in recent years due to both energy and environmental concerns. A global effort has been undertaken to develop advanced renewable energy generation and storage technologies for the electrification of transportation, with the goal of significantly reducing fossil fuel consumption.²⁻³ Among electrical energy storage technologies, lithium-ion batteries (LIBs) are among the most promising for plug-in hybrid and electric vehicles (EVs).³⁻⁶ For EV applications, significant improvements in energy density, safety, and cost are required. In current LIBs, energy density is mainly limited by the capacity and thermodynamics of the cathode material.⁷ Improvements in cathode materials are critically needed, particularly for demanding EV applications. Currently, there are four main types of cathode materials used for EV applications: lithium nickel cobalt aluminium oxide (NCA), lithium iron phosphate (LFP), lithium manganese oxide (LMO) and lithium nickel manganese cobalt oxide (NMC). The characteristics of each material along with their advantages and disadvantages can be summarized as follows: NCA can deliver high capacity (around 200 mAh/g) but suffers from severe safety problems; LFP is safe and offers a long cycle life, but has the lowest energy density; LMO offers high thermal stability but has a relatively low capacity and suffers from manganese dissolution at elevated temperatures.⁸ Since the current cathode materials cannot meet all the performance metrics for the emerging EV market, the development of an advanced cathode material with high energy density, low cost, good cycling stability and superior rate capability

is critically needed.

NMC materials offer a balance of performance metrics, and are regarded as promising candidates for future EV applications. The need for the three transition metal ions is predicated on: Ni provides superior capacity but exhibits poor thermal stability, Mn provides excellent cycling and safety but low capacity, and Co provides increased electronic conductivity but at increased cost.^{9,10}

Recently Ni-rich $\text{LiNi}_x\text{Mn}_y\text{Co}_{1-x-y}\text{O}_2$ ($x>0.5$) materials have received a great deal of attention¹¹⁻¹³ due to their high capacity and relatively low cost.¹⁴⁻¹⁹ Various methods have been employed in the synthesis of $\text{LiNi}_{0.6}\text{Mn}_{0.2}\text{Co}_{0.2}\text{O}_2$ cathode materials including hydroxide co-precipitation,^{10,11,20-22} carbonate co-precipitation,²³⁻²⁵ spray-drying,^{26,27} and solid state methods.^{12,28,29} However, few studies have addressed synthesis conditions systematically or paid attention to particle morphology and tap density of the material. Tap density, a measure of the material's mass/volume after taps, is well correlated to the pressing density that can be achieved in coated electrodes in practical LIBs.³⁰ To our knowledge, none of the previously reported $\text{LiNi}_{0.6}\text{Mn}_{0.2}\text{Co}_{0.2}\text{O}_2$ materials have delivered unprecedented electrochemical performance in capacity, cycling stability and rate capability. In addition, the long cycling performance of $\text{LiNi}_{0.6}\text{Mn}_{0.2}\text{Co}_{0.2}\text{O}_2$ materials at the industrially-relevant pouch cell level, which has far more significant practical implications and applications, has yet to be reported.

Herein, we report on a facile and highly scalable co-precipitation-calcination two-step synthesis of a $\text{LiNi}_{0.6}\text{Mn}_{0.2}\text{Co}_{0.2}\text{O}_2$ cathode material. We studied the optimum synthesis parameters including pH, stirring rate and calcination temperature in detail,

and we systematically investigated the structural properties, particle morphology, and electrochemical performance of the $\text{LiNi}_{0.6}\text{Mn}_{0.2}\text{Co}_{0.2}\text{O}_2$ cathode material. To demonstrate the potential for scalability, we fabricated and extensively tested a full pouch cell with a graphite anode and a $\text{LiNi}_{0.6}\text{Mn}_{0.2}\text{Co}_{0.2}\text{O}_2$ based cathode as electrodes.

2.2 Experimental Section

Sample preparation $\text{Ni}_{0.6}\text{Mn}_{0.2}\text{Co}_{0.2}(\text{OH})_2$, used as a precursor, was synthesized by a co-precipitation method. Appropriate amounts of $\text{NiSO}_4 \cdot 6\text{H}_2\text{O}$, $\text{CoSO}_4 \cdot 7\text{H}_2\text{O}$ and $\text{MnSO}_4 \cdot \text{H}_2\text{O}$ were used as starting materials and were dissolved in distilled water in molar ratios of Ni: Co: Mn = 6: 2: 2. A 2 M aqueous solution of the transition metal sulfates was slowly pumped into a continuously stirred tank reactor. Concomitantly, a 6 M NaOH solution (aq) and a 3 M NH_4OH solution (aq) were also separately pumped into the reactor. After reaction, the precipitate was filtered and washed several times with water to remove residual ions (Na^+ , SO_4^{2-} or other ions). The precipitate was then dried at 100 °C overnight. The resulting precursor and a 4.5% of excess $\text{LiOH} \cdot \text{H}_2\text{O}$ were mixed thoroughly in an agate mortar. The mixture was calcined for 12 h in air at 860 °C to obtain $\text{LiNi}_{0.6}\text{Mn}_{0.2}\text{Co}_{0.2}\text{O}_2$ powders.

Sample characterization X-ray diffraction patterns were obtained with a Rigaku Ultima VI powder X-ray diffractometer with CuK radiation ($K\alpha_1$, $\lambda = 1.5406 \text{ \AA}$ and $K\alpha_2$, $\lambda = 1.5444 \text{ \AA}$). Diffraction patterns were collected at a scanning rate of 5 °/min, and with a step of 0.02 °. The tap density was measured using a Hylology HY-100 Tap Density Tester. Particle size and size distribution were measured using a Bettersize BT-9300ST Laser Particle Size Analyzer. SEM was performed with a LEO-1550 field emission SEM (FSEM). Electron microscopy imaging was carried out using a

Schottky-field-emission-gun Tecnai F20 scanning transmission electron microscope (STEM) operated at 200 keV. X-ray energy dispersive spectroscopy (XEDS) analysis was performed using an Oxford XMAX detector, with an electron beam current of about 1 nA.

Electrochemical tests Electrochemical measurements were carried out in CR 2032 coin cells assembled in an argon filled glove box (residual water and oxygen were 0.5 ppm and 0.1 ppm, respectively) with lithium metal as the anode. The working cathodes were fabricated with 80 wt% active material, 10 wt% super P carbon, and 10 wt% poly(vinylidene fluoride) (PVDF) as binder. The resulting slurry was coated onto an Al foil current collector. The coated electrodes were dried for 12 h at 110 °C in a vacuum oven. The typical mass loading of the active material was 2 mg/cm². The counter electrode was Li metal. The two electrodes were separated by a polypropylene separator (Celgard 3501). The electrolyte was 1.2 M LiPF₆ in a 3:7 ratio of EC (ethylene carbonate) to EMC (ethyl methyl carbonate). Galvanostatic charge/discharge of the coin cells was carried out using an Arbin BT-2000 battery tester with a constant discharge/charge current rate of 0.1 C and a voltage range of 2.8 to 4.45 V vs. Li/Li⁺ at room temperature. Every experiment was carried out in triplicate (three parallel trials), and the error bar of the measured capacities, among the three trials, was less than 0.25%. We report the measured capacities rounded to the last integral digit; in which case, all results were identical. Thus we do not include error bars in these cases.

The long cycle-life tests were performed in a laminated-type full-cell wrapped with an Al pouch prepared at Lionano, Inc. The working cathodes were fabricated with 92 wt% active material, 4 wt% super P carbon, and 4 wt% PVDF as binder. The cathode loading of was 10.8 mg/cm² for single side and 21.6 mg/cm² for double side. Graphite

was used as the anode, with a composition of 92 wt% active material, 4 wt% super P carbon, and 4 wt% PVDF as binder. The anode loading was 7.45 mg/cm² for the single side and 14.9 mg/cm² for double side. The electrolyte was 1.2 M LiPF₆ in ethylene carbonate-ethyl methyl carbonate (3:7 by volume). The cells were cycled between 2.75 and 4.2 V at a rate of 0.1 C during the initial conditioning process. The cells were subsequently charged and discharged between 2.75 and 4.2 V by applying a constant 0.5 C current at room temperature.

2.3 Results and Discussion

A well-controlled co-precipitation method was employed for the synthesis of the LiNi_{0.6}Mn_{0.2}Co_{0.2}O₂ cathode material precursor. As illustrated in Figure 2.1, a continuous stirred tank reactor was used in the co-precipitation process. The reactor had a feedback control for both temperature and pH, enabling control of the kinetics of particle growth, leading to an optimal spherical morphology. Three stock solutions were employed: a mixture of the desired transition metal sulfate salts, ammonium hydroxide, used as the precipitation agent, and sodium hydroxide, used to control the pH. After precipitation, the complex metal hydroxide precursor Ni_{0.6}Mn_{0.2}Co_{0.2}(OH)₂ was mixed with lithium hydroxide and subsequently calcined in air. The described co-precipitation-calcination two-step synthesis was successfully scaled up to 50 kg per batch. We focused on the following key parameters, in detail, to obtain the optimized LiNi_{0.6}Mn_{0.2}Co_{0.2}O₂ cathode material: pH, stirring rate and calcination temperature.

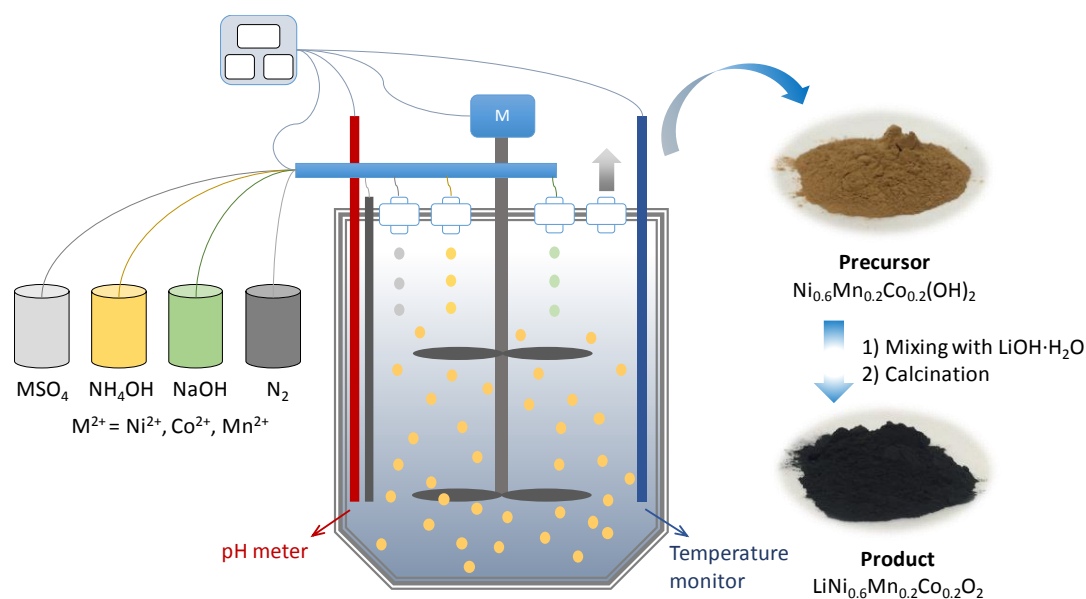


Figure 2.1 Schematic illustration of the synthesis procedure of $\text{LiNi}_{0.6}\text{Mn}_{0.2}\text{Co}_{0.2}\text{O}_2$

pH was identified as the most critical factor influencing precursor synthesis, as it affects the particle morphology and size distribution of the material, which in turn, are correlated to the volumetric capacity and energy density of practical LIBs. The tap density of materials with the same composition, is closely related to the particle morphology, particle size and size distribution. In general, materials composed of spherical particles have a higher tap density than those composed of irregularly shaped particles. The selected pH values were 10.2, 10.8, 11.4, and 12.0 for the co-precipitation process. Figure 2.2 presents a plot of particle size and tap density of precursor $\text{Ni}_{0.6}\text{Mn}_{0.2}\text{Co}_{0.2}(\text{OH})_2$ powders prepared at different pH values. Particle size was characterized by D50, which is defined as a particle diameter that is larger than fifty (50) percent of the total. With an increase in pH from 10.2 to 12.0, particle size tended to decrease. While at the low end of pH, the particle morphology became irregular, it was more regular when the pH was increased to 10.8. At a pH of 10.8, the tap density was higher than at pH 10.2. For pH values beyond 10.8, the particle size

decreased, resulting in an even lower tap density. At a pH value of 10.8, particles exhibited a well-controlled spherical morphology with smooth surfaces. These particles also showed the highest tap density. We found that only at a pH value of 10.8 was there a balance reached between crystal growth and nucleus formation, which allowed the particles to grow more densely in an orderly arrangement. Therefore, a pH value of 10.8 was identified as the optimal for precursor synthesis, as particles exhibited the most uniform spherical morphology resulting in the highest tap density.

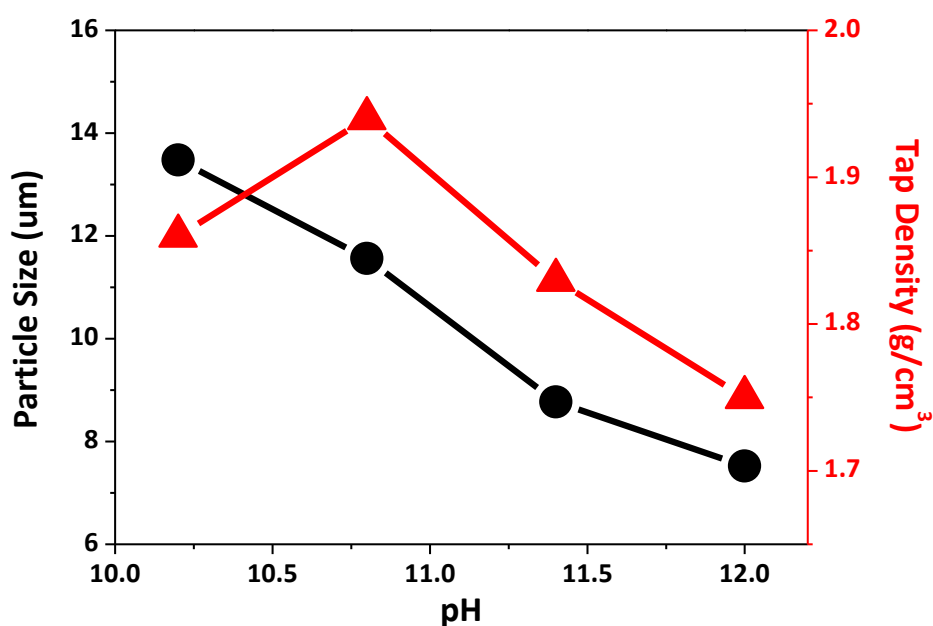


Figure 2.2 Plot of particle size and tap density of precursor $\text{Ni}_{0.6}\text{Mn}_{0.2}\text{Co}_{0.2}(\text{OH})_2$ prepared at various pH values.

In addition to pH, we also examined the role of stirring rate on the formation of regular spherical particles. Increasing the stirring rate intensified both inter-particle (particle/particle interactions) and intra-particle (particle and vessel-wall interactions) collisions, which facilitated homogeneous spherical particle formation.^{10,31} Stirring rates of 600, 800, 1000, and 1200 rpm were selected for studying the co-precipitation process. Figures 2.3 a–d show SEM images of precursor $\text{Ni}_{0.6}\text{Mn}_{0.2}\text{Co}_{0.2}(\text{OH})_2$

powders prepared at different stirring rates.

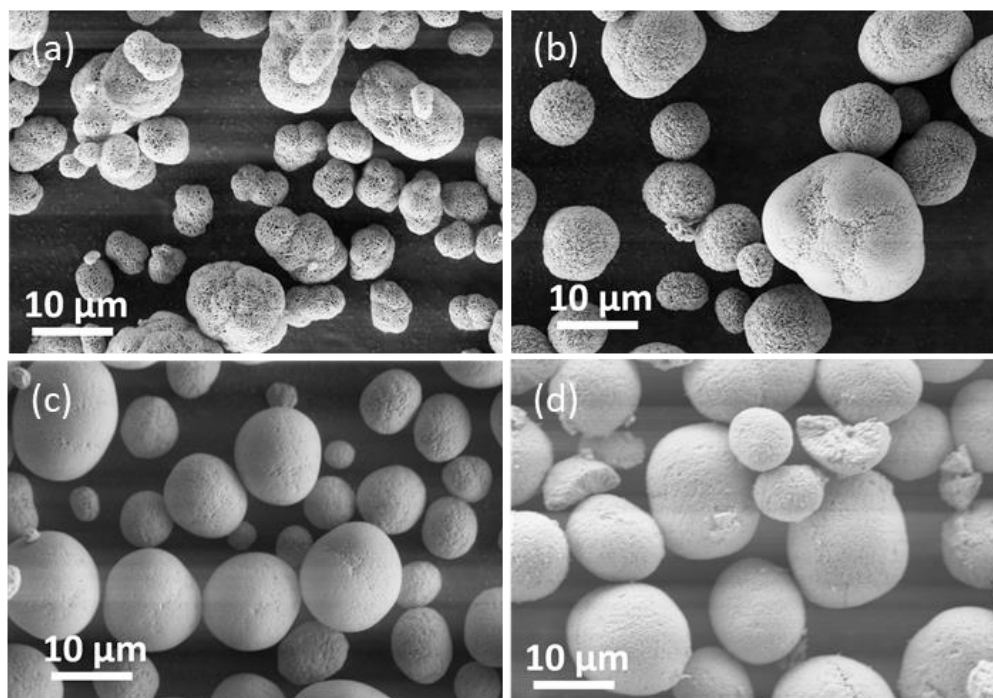


Figure 2.3 SEM images of precursor $\text{Ni}_{0.6}\text{Mn}_{0.2}\text{Co}_{0.2}(\text{OH})_2$ prepared at different stirring rates: (b) 600 rpm; (c) 800 rpm; (d) 1000 rpm; (e) 1200 rpm.

Figure 2.4 shows a plot of the tap density of the precursors versus stirring rate. At low stirring rates (600 rpm), the particles were agglomerated irregularly and loosely packed. As the stirring rate was increased to 1000 rpm, the primary particles packed closely, forming more densely-packed spherical particles. They also exhibited a smoother surface, and as a result, the tap density increased (See Figure 2.4). Although the particles remained dense and spherical when the stirring rate was further increased to 1200 rpm, the high stirring rate exceeded the tolerance level at which physical integrity was maintained, and some particles became cracked or deformed. Based on these observations, a stirring rate of 1000 rpm was deemed optimal for the precursor co-precipitation synthesis.

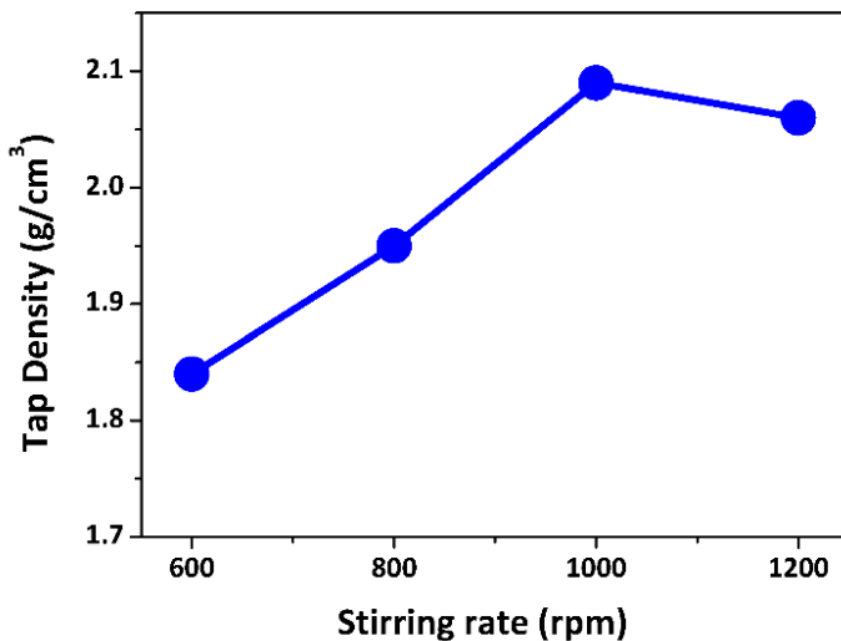


Figure 2.4 Tap density of precursors as a function of stirring rate.

The effect of calcination temperature was investigated, based on the previously optimized conditions of pH and stirring rate. The resultant precursor $\text{Ni}_{0.6}\text{Mn}_{0.2}\text{Co}_{0.2}(\text{OH})_2$ was mixed thoroughly with $\text{LiOH}\cdot\text{H}_2\text{O}$, and was subsequently calcined at four different temperatures (780, 820, 860, and 900 °C) in air to obtain the lithiated powders. X-ray powder diffraction (XRD) was used to characterize the crystal structure of the prepared materials. Figure 2.5 shows the XRD patterns of samples prepared at different calcination temperatures. All of the samples yielded a well-defined and impurity-free single phase material, which could be attributed to a hexagonal $\alpha\text{-NaFeO}_2$ type structure. With an increase in the calcination temperature, the XRD patterns showed a more clearly defined split between the (006)/(102) and (108)/(110) peaks, indicating that the materials had a better defined hexagonal structure.^{32,33} The lattice parameters (see Table 2.1) are similar to previously reported values.^{10,20,34} As the calcination temperature increased, the lattice constants *a*, *c* and

volume V increased from 2.867 Å, 14.229 Å, and 101.286 Å³ to 2.871 Å, 14.241 Å, and 101.654 Å³ respectively, which are in very good agreement with elemental crystal growth theory.²¹ Moreover, the intensity ratio of I(003)/I(104) is a reliable indicator for determining the cation distribution in the lattice of layered oxides. Cation mixing can be a direct indicator of Ni²⁺ occupancy on Li⁺ sites. The higher the intensity ratio, the lower the level of cation mixing. This is beneficial to the Li⁺ mobility upon charging, which in turn, may result in more intercalation of the material.³⁵ Note that as the intensity ratio of I(003)/I(104) increased upon increasing the temperature from 780 °C to 860 °C, cation mixing decreased (Table 2.1). However, when the temperature reached 900 °C the ratio was lower, likely due to vaporization of small amounts of lithium. Due to this volatile nature of lithium and its replacement by Ni²⁺ during calcination, the calcination temperature affects the discharge capacity of the materials.

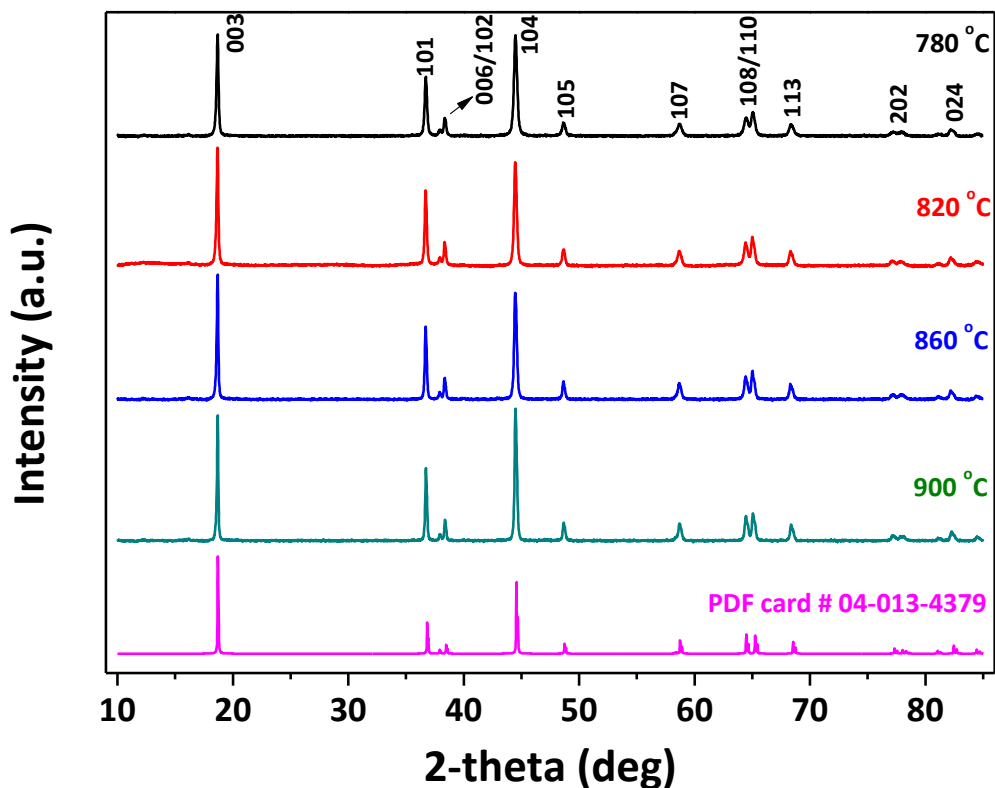


Figure 2.5 Powder XRD patterns of the $\text{LiNi}_{0.6}\text{Mn}_{0.2}\text{Co}_{0.2}\text{O}_2$ materials prepared under different calcination temperatures.

Table 2.1 Lattice parameters of $\text{LiNi}_{0.6}\text{Mn}_{0.2}\text{Co}_{0.2}\text{O}_2$ samples prepared at different temperatures.

Temperature (°C)	a (Å)	c(Å)	V(Å ³)	c/a	I(003)/I(104)
780	2.8672(2)	14.2289(4)	101.286	4.963	1.16
820	2.8679(3)	14.2313(2)	101.371	4.963	1.22
860	2.8683(3)	14.2381(5)	101.421	4.965	1.23
900	2.8712(2)	14.2412(4)	101.654	4.959	1.06

The electrochemical performance of the as-prepared materials was assessed in CR2032 coin cells with Li foil as the counter electrode. Figure 2.6 presents the cell voltage plotted against the specific capacity for the charge and discharge profiles between 2.8 and 4.45 V at a rate of 0.5 C at room temperature of the samples prepared under different calcination temperatures. Increasing the calcination temperature from 780 °C to 860 °C, increased the discharge capacity from 186 mAh/g to 195 mAh/g. However, further increasing the temperature to 900 °C led to a decreased capacity of 183 mAh/g. The capacity retention after 100 cycles was improved from 83.2% and 85.5% to 89.9%, by increasing the temperature from 780 °C to 820 °C and to 860 °C (Figure 2.7). However, it decreased to 78.0% after further increasing the temperature to 900 °C. While the effect of the replacement of Li⁺ by Ni²⁺ is known to have adverse effects on performance, the volatile nature of lithium should be considered as well.³² From these results, the optimal calcination temperature was determined to be 860 °C.

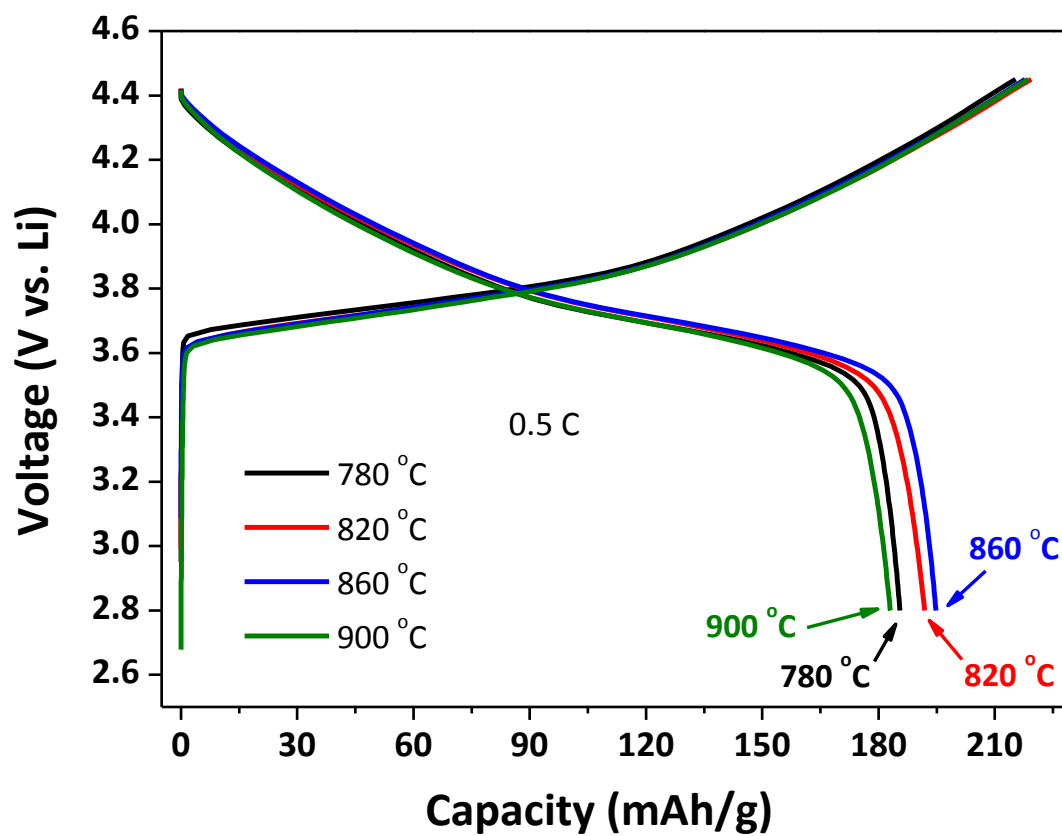


Figure 2.6 Initial charge–discharge profiles at a rate of 0.5 C over the voltage range of 2.8 to 4.45 V of samples prepared under different calcination temperatures. (c) Cycling performance at 0.5 C over the voltage range of 2.8 to 4.45 V of samples prepared under different calcination temperatures.

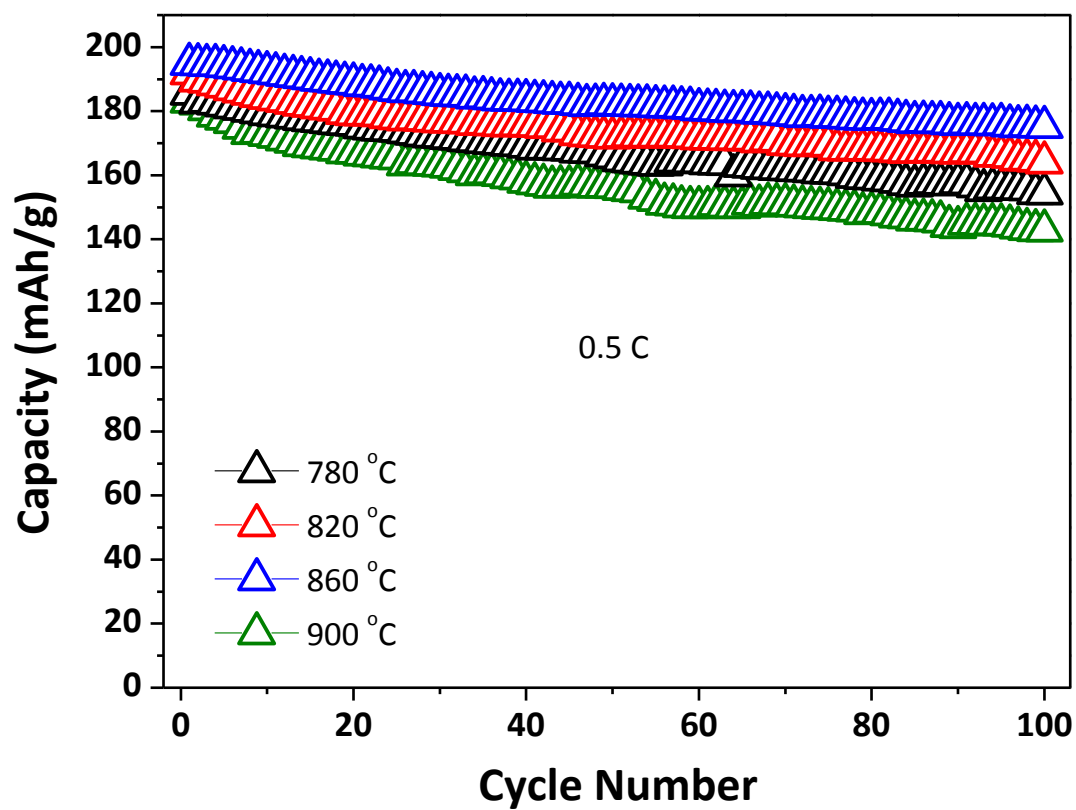


Figure 2.7 Cycling performance at 0.5 C over the voltage range of 2.8 to 4.45 V of samples prepared under different calcination temperatures.

Figures 2.8 a-b show Scanning Electron Microscopy (SEM) images of a single particle and a multi-particle overview of the optimized $\text{LiNi}_{0.6}\text{Mn}_{0.2}\text{Co}_{0.2}\text{O}_2$ cathode material. The particles consistently exhibited a spherical morphology, dense structures, and a homogenous size distribution, as illustrated in Figure 2.9. All of these aspects result in a high tap density, leading to a superior electrochemical performance of the material in both coin cells and full pouch cell testing. The tap density of our optimized material was 2.65 g/cm^3 . The surface area of the material, measured by N_2 BET, was $0.37 \text{ m}^2/\text{g}$ (See Figure 2.10). The particle size distribution, expressed in span, is defined as $(\text{D90}-\text{D10})/\text{D50}$, where D50 indicates a particle diameter that is larger than fifty percentile of the total particles (often denoted as the medium number), while D90 and D10 stand for particle diameters that are larger than ninety and ten percentile of the total particles, respectively. The particle size (D50) was $12.4 \mu\text{m}$ (see Table 2.2), and the span was 1.20, representing an optimal combination of energy density and power density.³⁴ This also implies that the particles were homogeneously and uniformly synthesized.

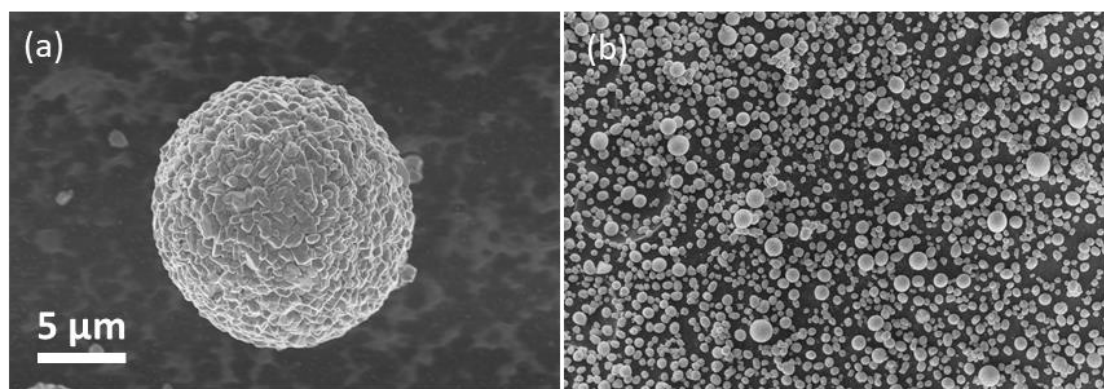


Figure 2.8 (a) Single particle SEM image and (b) overview SEM image of $\text{LiNi}_{0.6}\text{Mn}_{0.2}\text{Co}_{0.2}\text{O}_2$ particles.

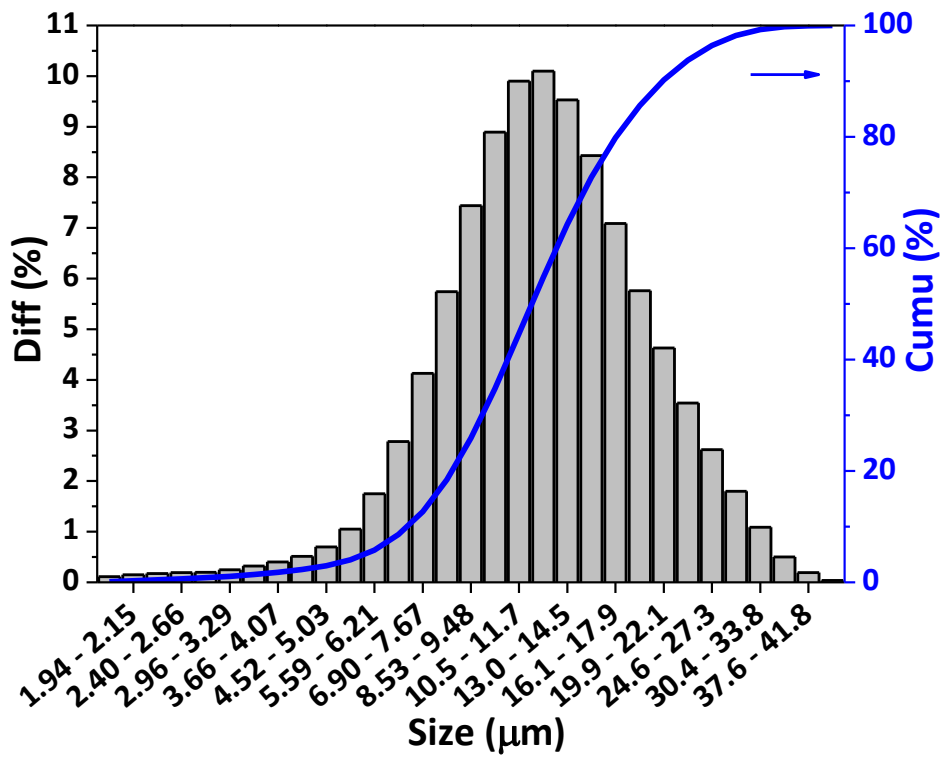


Figure 2.9 Particle size distribution of $\text{LiNi}_{0.6}\text{Mn}_{0.2}\text{Co}_{0.2}\text{O}_2$ particles.

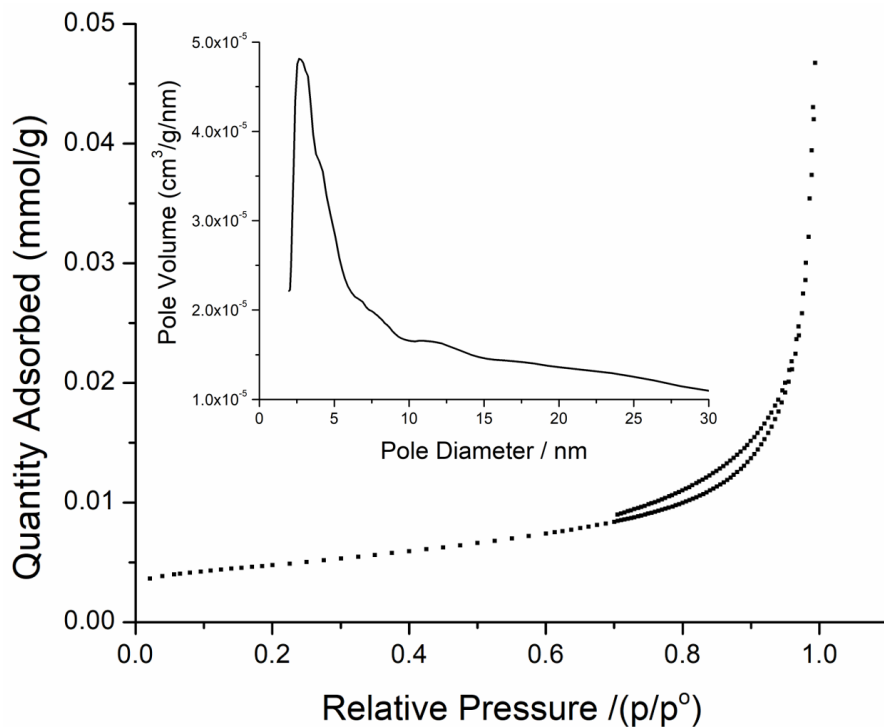


Figure 2.10 N₂ adsorption/desorption isotherm and pore size distribution for LiNi_{0.6}Mn_{0.2}Co_{0.2}O₂ sample

Table 2.2 Secondary particle size information of LiNi_{0.6}Mn_{0.2}Co_{0.2}O₂ sample.

Item	LiNi _{0.6} Mn _{0.2} Co _{0.2} O ₂ material
D03 (μm)	5.03
D10 (μm)	7.17
D50 (μm)	12.4
D90 (μm)	22.1
D97 (μm)	28.4
Span [(D90-D10)/D50]	1.20

To better understand the microstructure and morphology of the as-synthesized $\text{LiNi}_{0.6}\text{Mn}_{0.2}\text{Co}_{0.2}\text{O}_2$ material, we employed high-angle annular dark field scanning transmission electron microscopy (HAADF-STEM) and bright-field transmission electron microscopy (BF-TEM) to characterize the material. Figures 2.11a–b show a cluster of primary particles, which were exfoliated from secondary particles like those shown in Figure 2.8, due to sonication during TEM sample preparation, which was confirmed under SEM (Figure 2.12). In Figure 2.11c, a lattice resolution image from a smaller particle (red dashed box in Figure 2.11b) shows a d-spacing of $\sim 2.5 \text{ \AA}$, which matches well with the (101) d-spacing of $\text{LiNi}_{0.6}\text{Mn}_{0.2}\text{Co}_{0.2}\text{O}_2$ (2.44 \AA , PDF card # 04-013-4379).

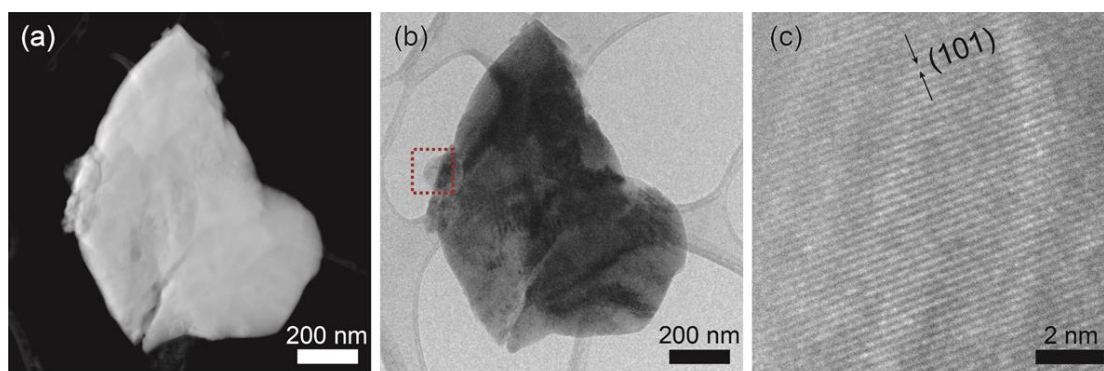


Figure 2.11 (a) HAADF-STEM and (b) BF-TEM images of a small piece of a $\text{LiNi}_{0.6}\text{Mn}_{0.2}\text{Co}_{0.2}\text{O}_2$ particle. (c) HRTEM lattice images from the edge of the particle in (b) marked with red dashed box.

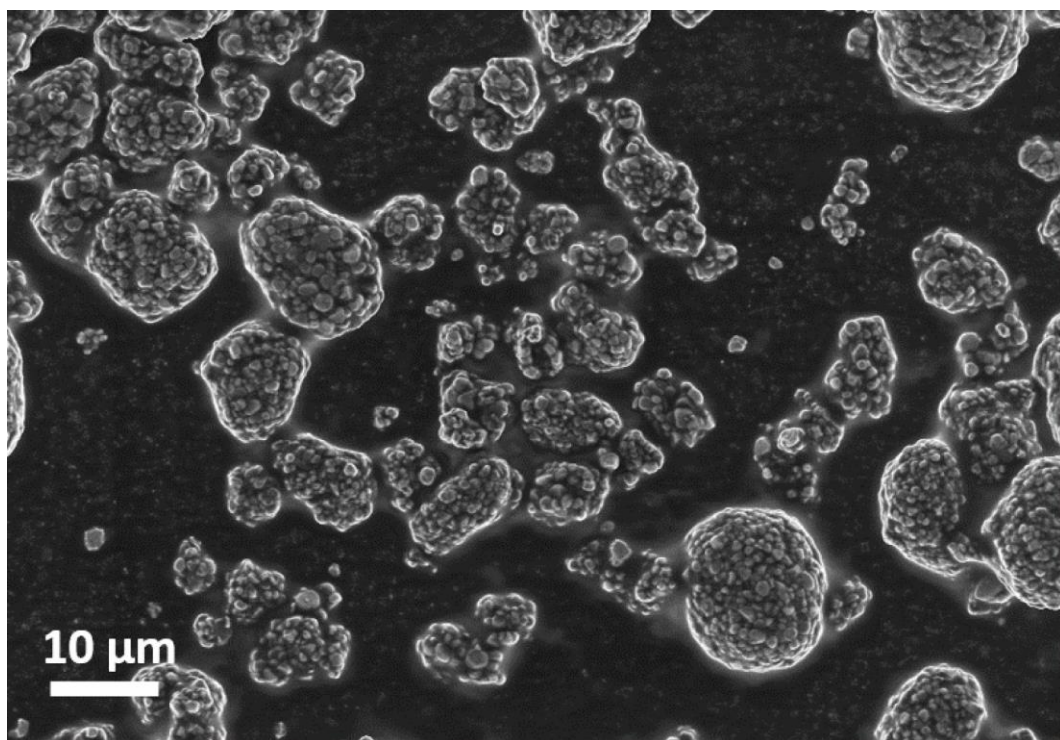


Figure 2.12 SEM image of partially broken $\text{LiNi}_{0.6}\text{Mn}_{0.2}\text{Co}_{0.2}\text{O}_2$ particles after sonication in ethanol for about 5min.

Selected area electron diffraction (SAED) from the whole particle cluster was used to determine the crystal structure of the particles (Figure 2.13). The diffraction pattern shows some intense diffraction spots, as well as fainter polycrystalline rings, suggesting that a range of different sized crystal grains are present in the field of view. The diffraction rings, from the smaller crystal grains, and diffraction spots, from the larger grains, all index to the d-spacings of $\text{LiNi}_{0.6}\text{Mn}_{0.2}\text{Co}_{0.2}\text{O}_2$, in good agreement with our XRD results (Figure 2.5). X-ray energy dispersive spectroscopy (XEDS) was used to establish the distribution of Mn, Co and Ni in the particles. Elemental maps of Mn, Co and Ni were obtained by integrating the peaks corresponding to the metal K-edges as shown in Figure 2.14. The elemental maps showed a uniform distribution of Mn, Co, and Ni in the particle (Figures 2.15a–c), confirming the

successful, uniform synthesis of the $\text{LiNi}_{0.6}\text{Mn}_{0.2}\text{Co}_{0.2}\text{O}_2$ material

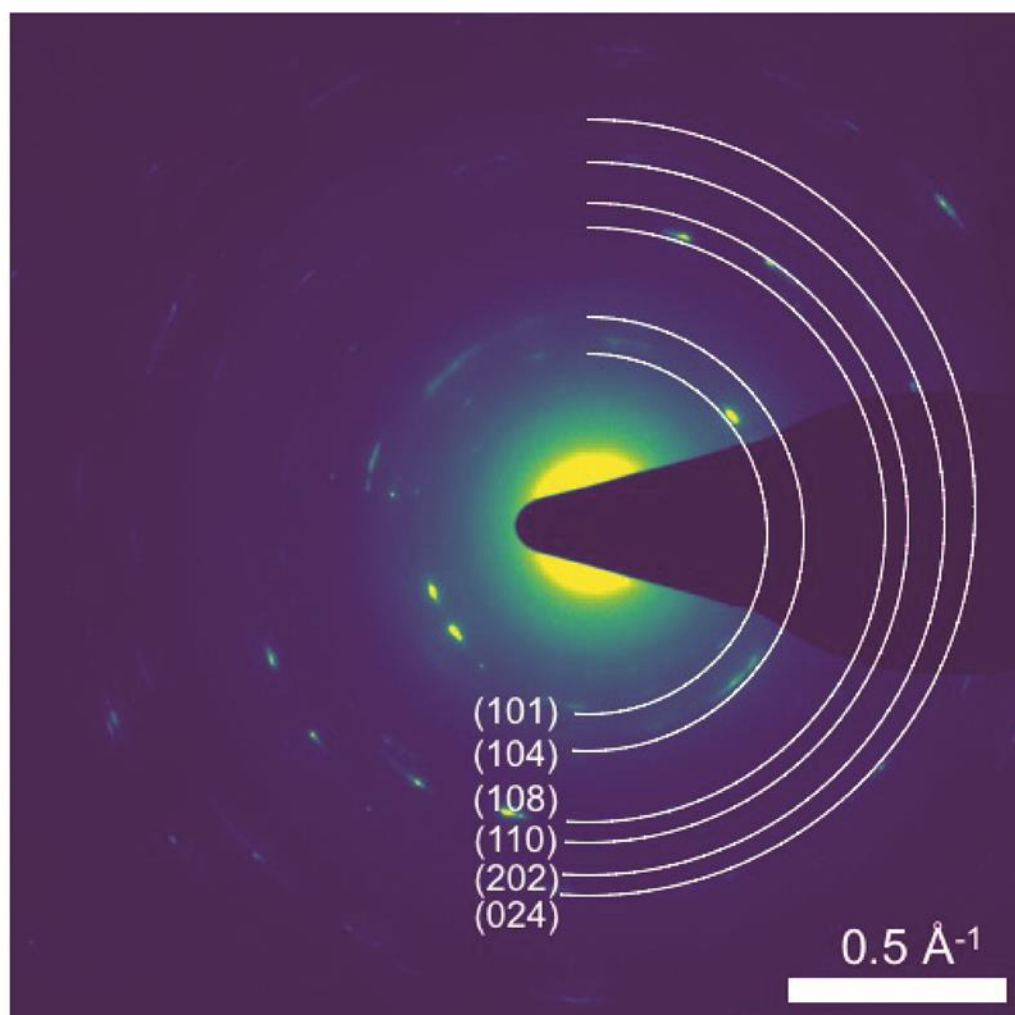


Figure 2.13 SAED pattern of $\text{LiNi}_{0.6}\text{Mn}_{0.2}\text{Co}_{0.2}\text{O}_2$.

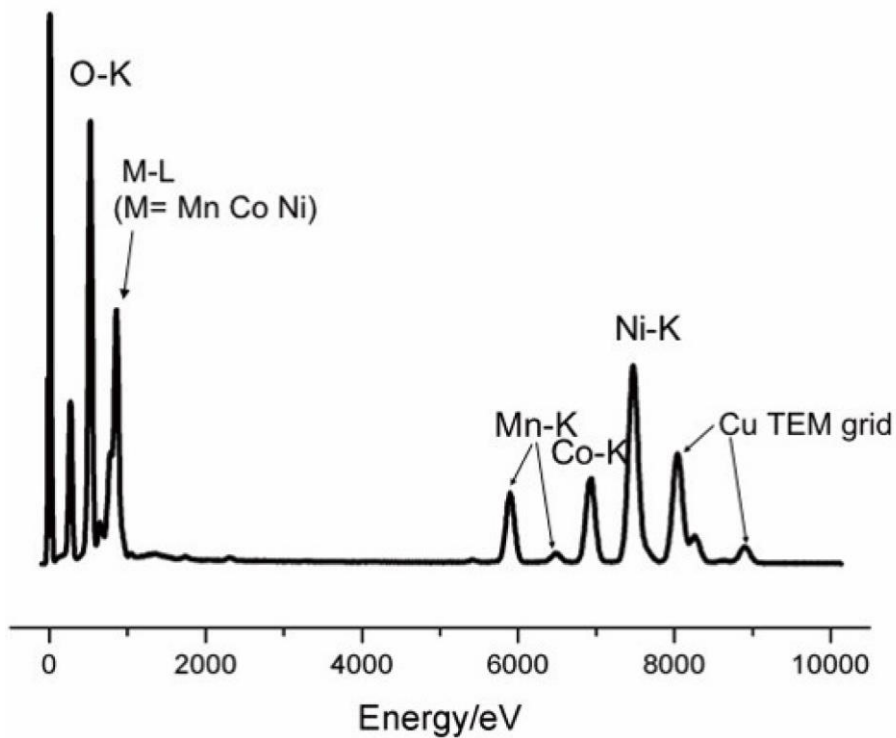


Figure 2.14 XEDS spectrum of $\text{LiNi}_{0.6}\text{Mn}_{0.2}\text{Co}_{0.2}\text{O}_2$ sample.

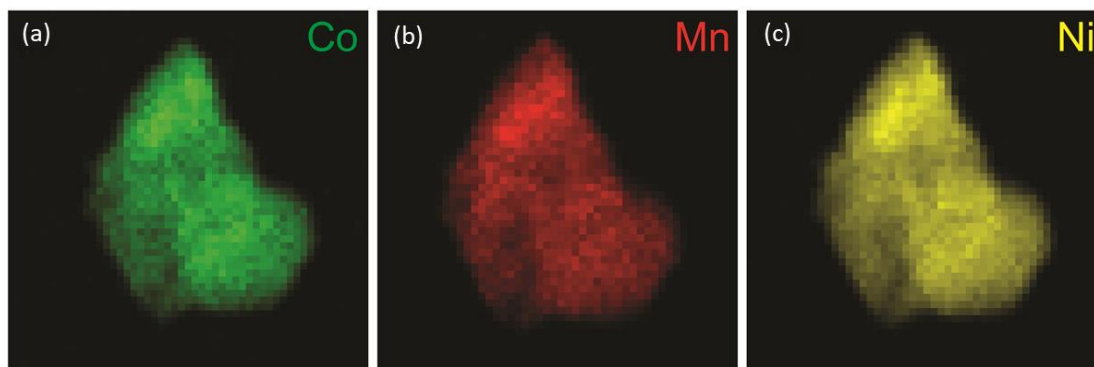


Figure 2.15 EDX elemental maps of Co (a), Mn (b) and Ni (c) for the particle in Figure 2.11 (a).

Having established the optimal conditions for synthesis, the electrochemical properties and performance of the as-prepared materials were tested. The difference in capacity for different charging voltage limits for our $\text{LiNi}_{0.6}\text{Mn}_{0.2}\text{Co}_{0.2}\text{O}_2$, and a commercial $\text{LiNi}_{0.6}\text{Mn}_{0.2}\text{Co}_{0.2}\text{O}_2$ material (see Table 2.3 for detailed analysis), provided by Lionano, Inc. (labelled as c- $\text{LiNi}_{0.6}\text{Mn}_{0.2}\text{Co}_{0.2}\text{O}_2$) are presented in Figure 2.16. By raising the charging voltage limit to 4.45 volts, the discharge capacities of our $\text{LiNi}_{0.6}\text{Mn}_{0.2}\text{Co}_{0.2}\text{O}_2$ electrodes increased from 189 mAh/g to 205 mAh/g. These results are superior to those obtained on the commercial sample of c- $\text{LiNi}_{0.6}\text{Mn}_{0.2}\text{Co}_{0.2}\text{O}_2$, which exhibited capacities of 177 mAh/g and 190 mAh/g at charging voltages of 4.25 V and 4.45 V, respectively. Our $\text{LiNi}_{0.6}\text{Mn}_{0.2}\text{Co}_{0.2}\text{O}_2$ also exhibited exceptional charge-discharge cycling stability as illustrated in Figure 2.17. Its capacity retention under 4.45 V charging was 89.9 % after 100 cycles, which is higher than that of the commercial material (84.0% after 100 cycles). Cobalt dissolution, observed at higher voltages (>4.3 V), has been found to result in detrimental effects on the high voltage operation of cobalt-containing cathode materials. However, our $\text{LiNi}_{0.6}\text{Mn}_{0.2}\text{Co}_{0.2}\text{O}_2$ material exhibited a comparable cycling performance at 4.45 V when compared with that under 4.25 V (89.9% vs. 90.1% after 100 cycles), suggesting that cobalt dissolution is greatly mitigated by the dense and homogeneous characteristics of our fully-optimized $\text{LiNi}_{0.6}\text{Mn}_{0.2}\text{Co}_{0.2}\text{O}_2$ material.³⁶

Table 2.3 Detailed analysis of the commercial sample (c-LiNi_{0.6}Mn_{0.2}Co_{0.2}O₂)

Item	c-LiNi_{0.6}Mn_{0.2}Co_{0.2}O₂ sample
D03 (μm)	2.56
D10 (μm)	5.85
D50 (μm)	11.71
D90 (μm)	24.74
D97 (μm)	33.36
Span [(D90-D10)/D50]	1.61
Surface Area (m ² /g)	0.37
Tap Density (g/cm ³)	2.46

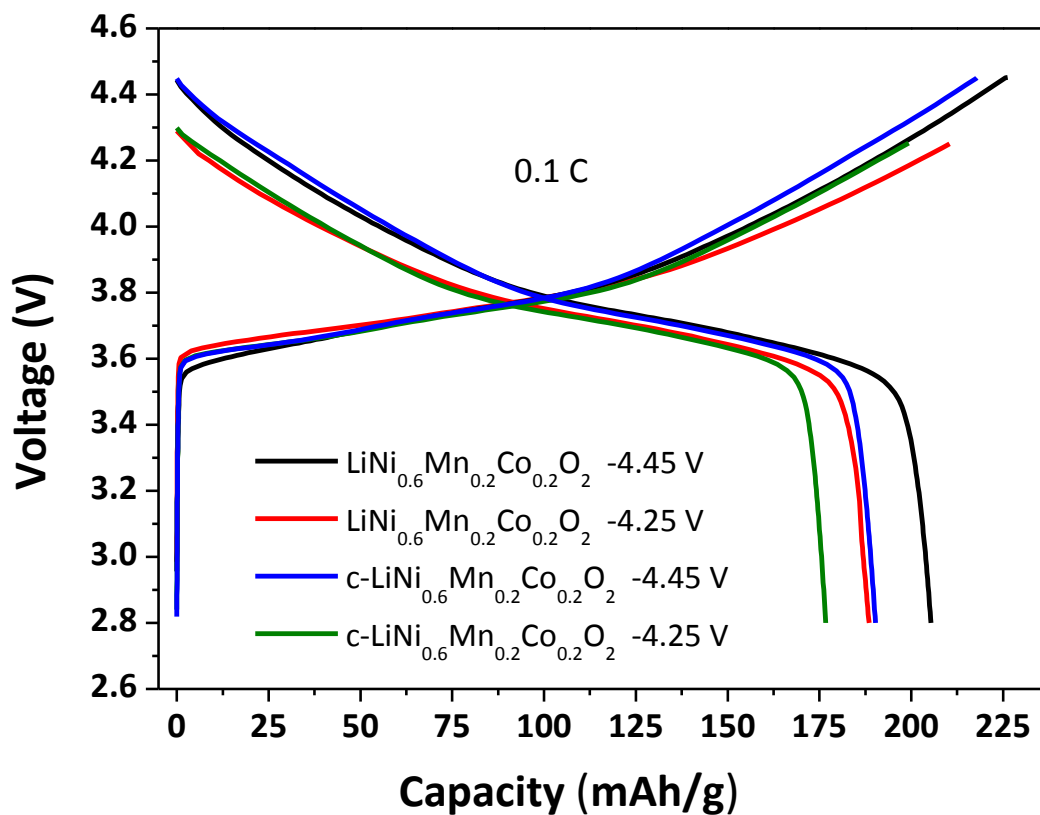


Figure 2.16 Initial charge and discharge profiles at 0.1 C of our $\text{LiNi}_{0.6}\text{Mn}_{0.2}\text{Co}_{0.2}\text{O}_2$ and commercial $\text{c-LiNi}_{0.6}\text{Mn}_{0.2}\text{Co}_{0.2}\text{O}_2$ materials for different charging voltages.

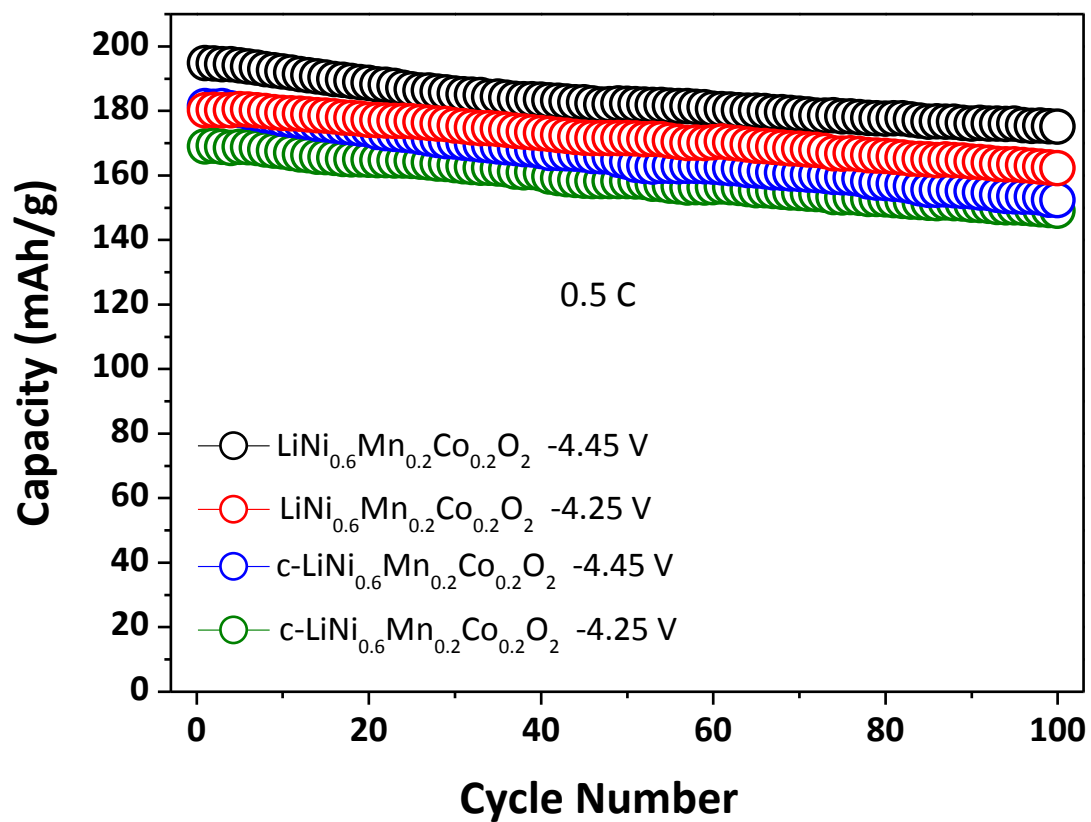


Figure 2.17 Cyclability at 0.5 C up to 100 cycles of our $\text{LiNi}_{0.6}\text{Mn}_{0.2}\text{Co}_{0.2}\text{O}_2$ and commercial c- $\text{LiNi}_{0.6}\text{Mn}_{0.2}\text{Co}_{0.2}\text{O}_2$ materials for different charging voltages.

Cyclic voltammetry (CV) was performed on a coin cell to probe the redox behavior of our $\text{LiNi}_{0.6}\text{Mn}_{0.2}\text{Co}_{0.2}\text{O}_2$ cathode as the battery underwent charge and discharge cycles (See Figure 2.18). The CV was obtained at 0.1 mV/s between 2.8 and 4.45 V vs. Li/Li^+ . Over the voltage window studied, one redox process was observed, consistently, at E_o of 3.75 V vs. Li/Li^+ over twenty cycles. This process was highly chemically and electrochemically reversible when compared to other NMC materials of different composition.³⁷ Upon closer inspection, one can note that the anodic peak potential ($E_{a,\text{pk}}$) and the cathodic peak potential ($E_{c,\text{pk}}$) gradually shifted to more negative and more positive potentials, respectively. In fact, $E_{a,\text{pk}}$ decreased by as much as 66 mV and $E_{c,\text{pk}}$ increased by 42 mV. This change in peak potentials, over the first ten cycles, gave rise to a decrease in ΔE_{pk} , which indicates a lower resistance in the charge and discharge process, potentially due to an enhanced wetting of the electrode material during the initial cycles. The large double layer observed at 4.45 V compared to that at 2.8 V is indicative of a material, with good conductivity, that was initially neutral, hence with minimal double layer at 2.8 V, and which becomes charged when oxidized, giving rise to a much enhanced double layer at 4.45 V. The integrated areas of the cycles correspond to the charge stored and released over the cycles. As shown in the inset to Figure 2.18, there is only a slight decrease in the integrated areas corresponding to a minimal fade in capacity with cycling.

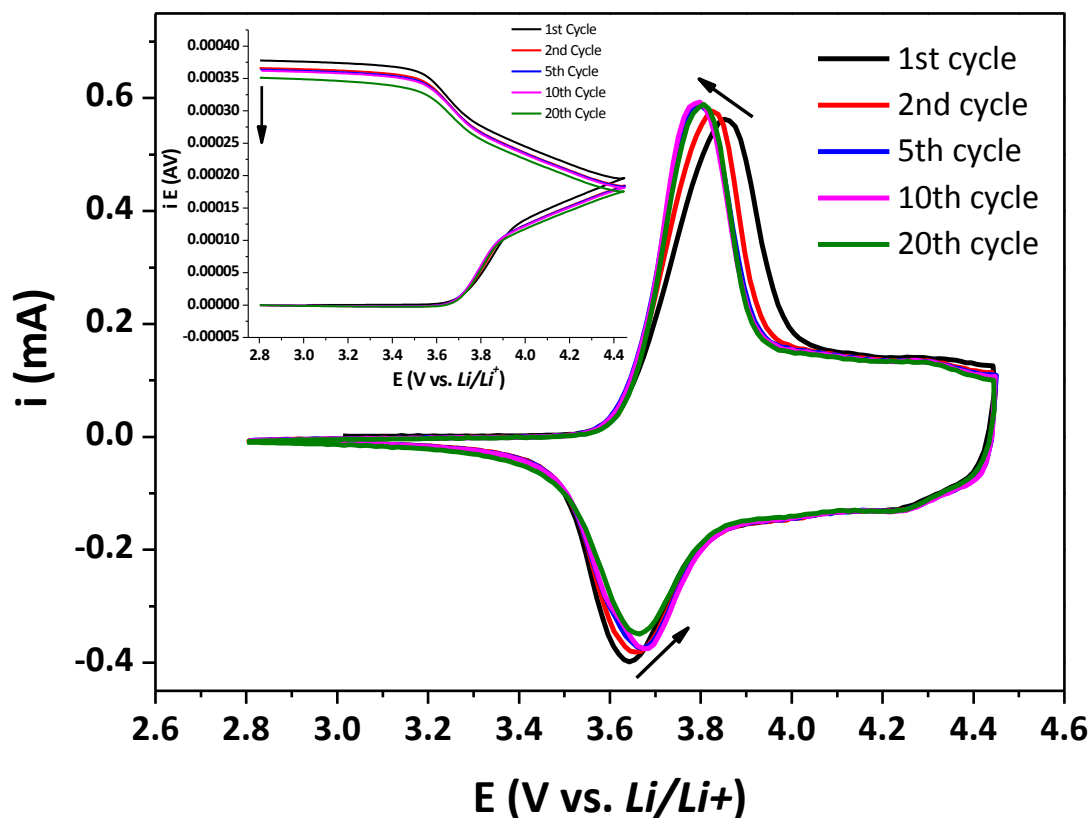


Figure 2.18 Cyclic voltammetry of $\text{LiNi}_{0.6}\text{Mn}_{0.2}\text{Co}_{0.2}\text{O}_2$ in a coin cell at 0.1 mV/s. Inset shows the integrated charge as a function of cycle number.

One of the biggest concerns for Ni-rich NMC cathode materials is their stability in air. Residual lithium on the surface of the cathode can react with moisture and CO_2 , in air, to produce residual LiOH and Li_2CO_3 . The presence of residual lithium compounds can be a serious problem because they may cause gas release through oxidative decomposition at high voltages, and degrade the battery performance in terms of cycling stability and rate capability.³⁸ The effect of air-storage on the cyclability of our $\text{LiNi}_{0.6}\text{Mn}_{0.2}\text{Co}_{0.2}\text{O}_2$ material was examined and the results are presented in Figure 2.19. The freshly synthesized $\text{LiNi}_{0.6}\text{Mn}_{0.2}\text{Co}_{0.2}\text{O}_2$ materials were exposed to air for 12 weeks at ambient temperature, in conditions that simulated the battery industry's typical storage practices. The air-stored materials were then dried in a vacuum oven at

130 °C for 5 h. As shown in Figure 2.19, the initial discharge capacity dropped only slightly from 195 mAh/g for the fresh material to 191 mAh/g for the air-stored one. Moreover, the air-stored material showed promising cycling stability performance with an 88.6% capacity retention after 100 cycles, while the fresh material maintained 89.9% capacity retention under the same conditions. This indicates that the prepared $\text{LiNi}_{0.6}\text{Mn}_{0.2}\text{Co}_{0.2}\text{O}_2$ materials are stable in air, which means that only a small amount of residual lithium existed on the surface, likely due to the well-controlled synthesis process.

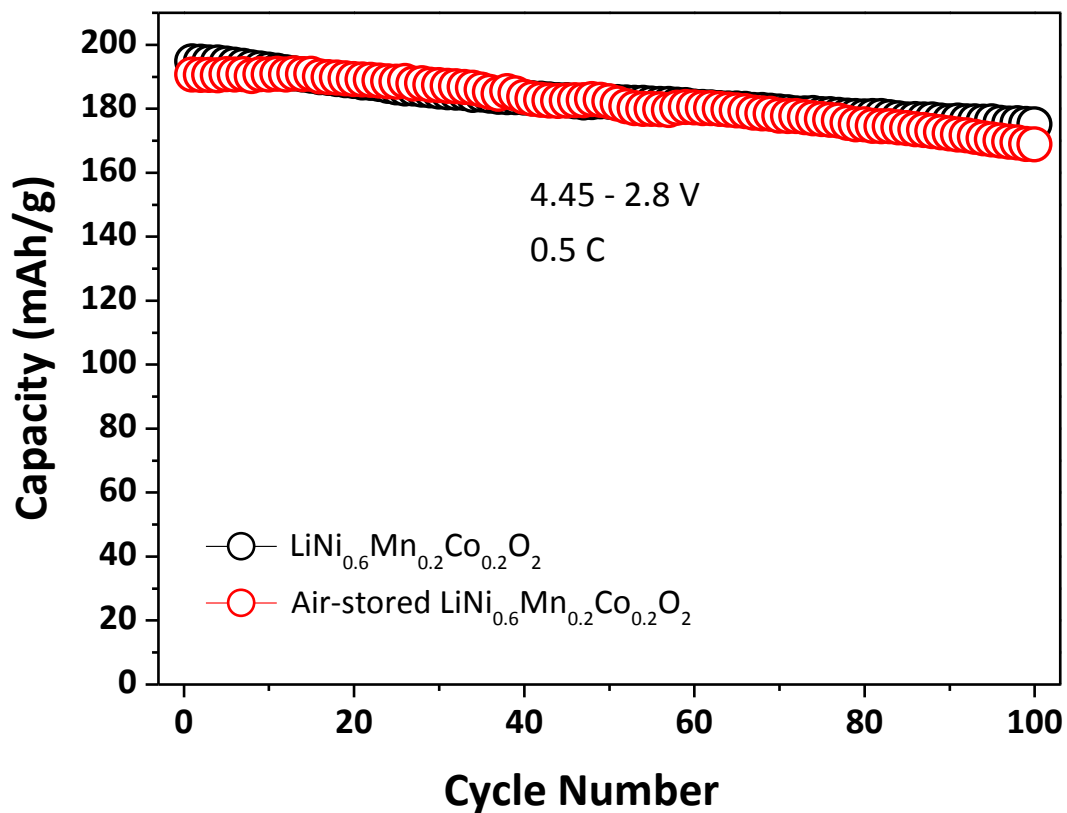


Figure 2.19 Cyclic voltammetry of $\text{LiNi}_{0.6}\text{Mn}_{0.2}\text{Co}_{0.2}\text{O}_2$ in a coin cell at 0.1 mV/s. Inset shows the integrated charge as a function of cycle number.

The rate capabilities of our $\text{LiNi}_{0.6}\text{Mn}_{0.2}\text{Co}_{0.2}\text{O}_2$ and commercial samples were investigated between 2.8 and 4.45 V at various current rates as shown in Figure 2.20. The cells were charged and discharged at C-rates of 0.1, 0.2, 0.5, 1, 2, 5, 10 and 20 for five cycles, respectively. As shown in Figure 2.20, our $\text{LiNi}_{0.6}\text{Mn}_{0.2}\text{Co}_{0.2}\text{O}_2$ sample delivered improved discharge capacities at all rates when compared to a commercial sample. Remarkably, our $\text{LiNi}_{0.6}\text{Mn}_{0.2}\text{Co}_{0.2}\text{O}_2$ material achieved capacities of 168, 157 and 137 mAh/g at C-rates of 5, 10 and 20, respectively. This result indicates that our

material, has the best discharge capacity reported to date for $\text{LiNi}_{0.6}\text{Mn}_{0.2}\text{Co}_{0.2}\text{O}_2$.^{10,11,20–23,25,28,29,34,39} In comparison, the commercial material only delivered a maximal discharge capacity of 190 mAh/g at 0.1 C, and faded rapidly to 54 mAh/g at 20 C. To clearly compare the rate capabilities of the two samples, their discharge capacities at different C-rates and the corresponding capacity retentions, relative to 0.1 C (retention at 0.1 C is 100%) are presented in Table 2.4. It is notable that our $\text{LiNi}_{0.6}\text{Mn}_{0.2}\text{Co}_{0.2}\text{O}_2$ material delivers a significantly better capacity retention than that of the commercial material, especially at ultrahigh current rates.

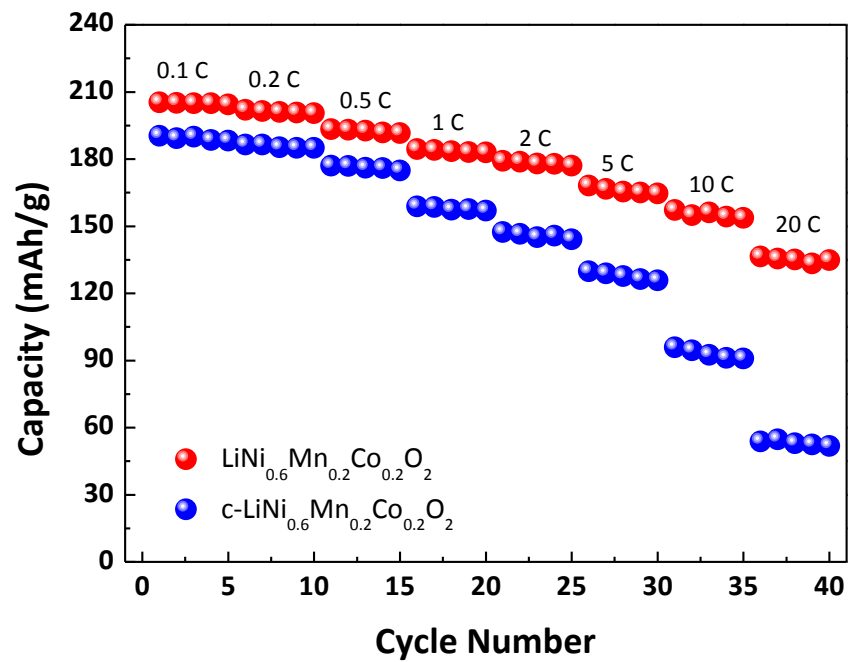


Figure 2.20 Rate performance of our LiNi_{0.6}Mn_{0.2}Co_{0.2}O₂ and a commercial sample of c- LiNi_{0.6}Mn_{0.2}Co_{0.2}O₂ cell from 0.1 C to 20 C.

Table 2.4 Discharge capacities of a $\text{LiNi}_{0.6}\text{Mn}_{0.2}\text{Co}_{0.2}\text{O}_2$ and a commercial sample at different rates and the corresponding capacity retentions (Note: the voltage range was 2.8 – 4.45 V; the cells were charged and discharged at C-rates of 0.1, 0.2, 0.5, 1, 2, 5, 10, and 20 for five cycles, respectively; a charging rate of 1 C was used when the discharging rate was higher than 1 C; retention at 0.1 C is defined as 100%).

Rates	$\text{LiNi}_{0.6}\text{Mn}_{0.2}\text{Co}_{0.2}\text{O}_2$		c- $\text{LiNi}_{0.6}\text{Mn}_{0.2}\text{Co}_{0.2}\text{O}_2$	
	Discharge capacity (mAh/g)	Capacity retention (%)	Discharge capacity (mAh/g)	Capacity retention (%)
0.1 C	205	100	190	100
0.2 C	202	98.5	187	98.4
0.5 C	193	94.1	177	93.2
1 C	184	89.8	159	83.7
2 C	179	87.3	147	77.4
5 C	168	82.0	130	68.4
10 C	157	76.6	96	50.5
20 C	137	66.9	54	28.4

After the electrochemical characterization of our $\text{LiNi}_{0.6}\text{Mn}_{0.2}\text{Co}_{0.2}\text{O}_2$ material in half cells, we incorporated our material into an Al-pouch cell paired with a graphite anode to obtain a more comprehensive assessment of the performance and reliability of our material. Passing the more rigorous full-cell tests, where one uses a lithium-molar-matched counter-electrode, would reveal the real characteristics of our $\text{LiNi}_{0.6}\text{Mn}_{0.2}\text{Co}_{0.2}\text{O}_2$ cathode material, and demonstrate that it has a great potential for

practical use.⁴⁰ Therefore, we assembled an Al pouch cell with a capacity of approximately 4.7 Ah using our $\text{LiNi}_{0.6}\text{Mn}_{0.2}\text{Co}_{0.2}\text{O}_2$ as cathode with a high loading of 21.6 mg/cm^2 , and a graphite anode. The fabricated battery was charged and discharged for 500 cycles at a rate of 0.5 C between 2.75 and 4.2 V (See Figure 2.21a–b). The cell exhibited exceptional cyclability with a capacity retention of 96% after 500 cycles, which is promising for EV applications that require long cycle life with high capacity retention, especially at high C-rates.

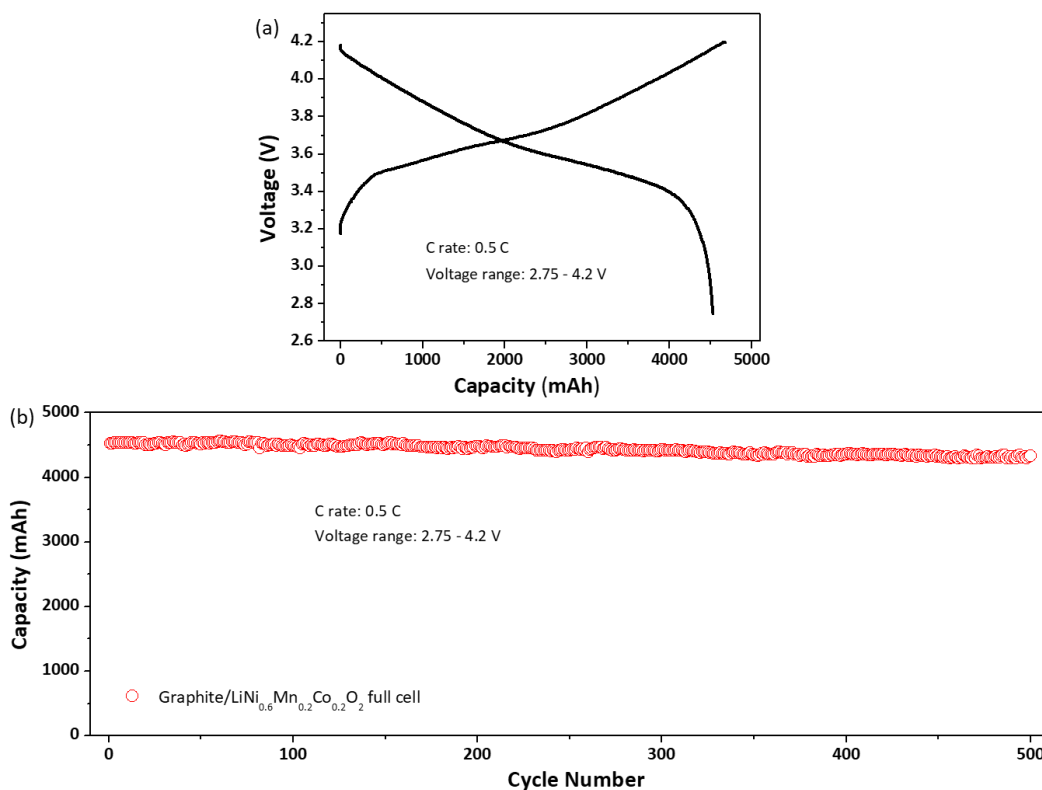


Figure 21. (a) First charge and discharge profiles of a pouch-type full cell fabricated with our $\text{LiNi}_{0.6}\text{Mn}_{0.2}\text{Co}_{0.2}\text{O}_2$ cathode and a graphite anode and (b) Cycling performance of the cell in (a) at 0.5 C over the voltage range between 2.75 and 4.2 V.

2.4 Conclusions

In summary, we have successfully developed a high-performance $\text{LiNi}_{0.6}\text{Mn}_{0.2}\text{Co}_{0.2}\text{O}_2$ cathode material using a co-precipitation-calcination two-step scalable synthesis process, by fully optimizing the synthesis parameters, including pH, stirring rate and calcination temperature. The particles exhibited a spherical morphology and uniform size distribution, with a well-defined crystal structure and homogeneous transition metal distribution pursuant to the well-controlled synthesis process. The materials exhibited superior electrochemical performances when compared with a commercial $\text{LiNi}_{0.6}\text{Mn}_{0.2}\text{Co}_{0.2}\text{O}_2$ sample, with an initial discharge capacity of 205 mAh/g at 0.1 C under a high cut-off voltage, and excellent rate capability with discharge capacities of 157 mAh/g and 137 mAh/g at 10 C and 20 C, respectively, as well as high air-stored stability. In order to demonstrate the applicability of this material to large-scale device applications such as EVs, a 4.7 Ah Al-pouch cell was fabricated with our $\text{LiNi}_{0.6}\text{Mn}_{0.2}\text{Co}_{0.2}\text{O}_2$ cathode with a high loading of 21.6 mg/cm² and a graphite anode, and tested under standard industry conditions. The cell exhibited superior cyclability with a capacity retention of 96% after 500 cycles. Our $\text{LiNi}_{0.6}\text{Mn}_{0.2}\text{Co}_{0.2}\text{O}_2$ cathode material, which was obtained by a fully-optimized synthesis, delivered a combined electrochemical performance that, has not yet been matched in any published report. To the best of our knowledge, we feel confident that the remarkable overall performance presented here comprehensively demonstrate that our $\text{LiNi}_{0.6}\text{Mn}_{0.2}\text{Co}_{0.2}\text{O}_2$ cathode material is practical and ready to use in EV applications which demand low cost, high energy density, and long cycling performance.

REFERENCE

- (1) Reprinted with permission from Ren, D.; Shen, Y.; Yang, Y.; Shen, L.; Levin, B. D. A.; Yu, Y.; Muller, D. A.; Abruña, H. D. *ACS Appl. Mater. Interfaces* **2017**, *9* (41), 35811. Copyright 2018 American Chemical Society.
- (2) Abruña, H. D.; Kiya, Y.; Henderson, J. C. Batteries and Electrochemical Capacitors. *Phys. Today* **2008**, *61*, 43.
- (3) Aricò, A. S.; Bruce, B.; Scrosati, B.; Tarascon, J. M.; van Schalkwijk, W. Nanostructured Materials for Advanced Energy Conversion and Storage Devices. *Nat. Mater.* **2005**, *4*, 366.
- (4) Tarascon, J. M.; Armand, M. Issues and Challenges Facing Rechargeable Lithium Batteries. *Nature* **2001**, *414*, 359.
- (5) Dunn, B.; Kamath, H.; Tarascon, J. M. Electrical Energy Storage for the Grid: A Battery of Choices. *Science* **2011**, *334*, 928.
- (6) Lee, J. H.; Yoon, C. S.; Hwang, J.-Y.; Kim, S.-J.; Maglia, F.; Lamp, P.; Myung, S.-T.; Sun, Y.-K. High-Energy-Density Lithium-Ion Battery Using a Carbon-nanotube–Si Composite Anode and a Compositionally Graded $\text{Li}[\text{Ni}_{0.85}\text{Co}_{0.05}\text{Mn}_{0.10}]\text{O}_2$ Cathode. *Energy Environ. Sci.* **2016**, *9*, 2152.
- (7) Xu, B.; Qian, D.; Wang, Z.; Meng, Y. S. Recent Progress in Cathode Materials Research for Advanced Lithium Ion Batteries. *Mater. Sci. Eng., R* **2012**, *73*, 51.
- (8) Etacheri, V.; Marom, R.; Elazari, R.; Salitra, G.; Aurbach, D. Challenges in the Development of Advanced Li-Ion Batteries: A Review. *Energy Environ. Sci.* **2011**, *4*, 3243.
- (9) Sun, H.-H.; Choi, W.; Lee, J. K.; Oh, I.-H.; Jung, H.-G. Control of Electrochemical Properties of Nickel-Rich Layered Cathode Materials for Lithium Ion Batteries by Variation of the Manganese to Cobalt Ratio. *J. Power Sources* **2015**, *275*, 877.
- (10) Liang, L.; Du, K.; Peng, Z.; Cao, Y.; Duan, J.; Jiang, J.; Hu, G. Co-precipitation

Synthesis of $\text{Ni}_{0.6}\text{Co}_{0.2}\text{Mn}_{0.2}(\text{OH})_2$ Precursor and Characterization of $\text{LiNi}_{0.6}\text{Co}_{0.2}\text{Mn}_{0.2}\text{O}_2$ Cathode Material for Secondary Lithium Batteries. *Electrochim. Acta* **2014**, *130*, 82.

(11) Liu, Z.; Yu, A.; Lee, J. Y. Synthesis and Characterization of $\text{LiNi}_{1-x-y}\text{Co}_x\text{Mn}_y\text{O}_2$ as the Cathode Materials of Secondary Lithium Batteries. *J. Power Sources* **1999**, *81–82*, 416.

(12) Yoshio, M.; Noguchi, H.; Itoh, J.; Okada, M.; Mouri, T. Preparation and Properties of $\text{LiCo}_y\text{Mn}_x\text{Ni}_{1-x-y}\text{O}_2$ as a Cathode for Lithium Ion Batteries. *J. Power Sources* **2000**, *90*, 176.

(13) Manthiram, A.; Knight, J. C.; Myung, S.-T.; Oh, S.-M.; Sun, Y.-K. Nickel-Rich and Lithium-Rich Layered Oxide Cathodes: Progress and Perspectives. *Adv. Energy Mater.* **2016**, *6*, 1501010.

(14) Zheng, J.; Kan, W. H.; Manthiram, A. Role of Mn Content on the Electrochemical Properties of Nickel-Rich Layered $\text{LiNi}_{0.8-x}\text{Co}_{0.1}\text{Mn}_{0.1+x}\text{O}_2$ ($0.0 \leq X \leq 0.08$) Cathodes for Lithium-Ion Batteries. *ACS Appl. Mater. Interfaces* **2015**, *7*, 6926.

(15) Sun, Y.-K.; Kim, D.-H.; Yoon, C. S.; Myung, S.-T.; Prakash, J.; Amine, K. A Novel Cathode Material with a Concentration-Gradient for High-Energy and Safe Lithium-Ion Batteries. *Adv. Funct. Mater.* **2010**, *20*, 485.

(16) Arai, H.; Okada, S.; Sakurai, Y.; Yamaki, J.-I. Electrochemical and Thermal Behavior of $\text{LiNi}_{1-z}\text{M}_z\text{O}_2$ ($\text{M} = \text{Co}, \text{Mn}, \text{Ti}$). *J. Electrochem. Soc.* **1997**, *144*, 3117.

(17) Jung, S.-K.; Gwon, H.; Hong, J.; Park, K.-Y.; Seo, D.-H.; Kim, H.; Hyun, J.; Yang, W.; Kang, K. Understanding the Degradation Mechanisms of $\text{LiNi}_{0.5}\text{Co}_{0.2}\text{Mn}_{0.3}\text{O}_2$ Cathode Material in Lithium Ion Batteries. *Adv. Energy Mater.* **2014**, *4*, 1300787.

(18) Liu, W.; Oh, P.; Liu, X.; Lee, M.-J.; Cho, W.; Chae, S.; Kim, Y.; Cho, J. Nickel-Rich Layered Lithium Transition-Metal Oxide for High-Energy Lithium-Ion Batteries.

Angew. Chem., Int. Ed. **2015**, *54*, 4440.

(19) Park, K.-J.; Lim, B.-B.; Choi, M.-H.; Jung, H.-G.; Sun, Y.-K.; Haro, M.; Vicente, N.; Bisquert, J.; Garcia-Belmonte, G. A High-Capacity $\text{Li}[\text{Ni}_{0.8}\text{Co}_{0.06}\text{Mn}_{0.14}]\text{O}_2$ Positive Electrode with a Dual Concentration Gradient for next-Generation Lithium-Ion Batteries. *J. Mater. Chem. A* **2015**, *3*, 22183.

(20) Yue, P.; Wang, Z.; Li, X.; Xiong, X.; Wang, J.; Wu, X.; Guo, H. The Enhanced Electrochemical Performance of $\text{LiNi}_{0.6}\text{Co}_{0.2}\text{Mn}_{0.2}\text{O}_2$ Cathode Materials by Low Temperature Fluorine Substitution. *Electrochim. Acta* **2013**, *95*, 112.

(21) Cao, H.; Zhang, Y.; Zhang, J.; Xia, B. Synthesis and Electrochemical Characteristics of Layered LiNiCoMnO Cathode Material for Lithium Ion Batteries. *Solid State Ionics* **2005**, *176*, 1207.

(22) Chen, Y.; Wang, G. X.; Konstantinov, K.; Liu, H. K.; Dou, S. X. Synthesis and Characterization of $\text{LiCo}_x\text{Mn}_y\text{Ni}_{1-x-y}\text{O}_2$ as a Cathode Material for Secondary Lithium Batteries. *J. Power Sources* **2003**, *119–121*, 184.

(23) Zhang, Y.; Cao, H.; Zhang, J.; Xia, B. Synthesis of $\text{LiNi}_{0.6}\text{Co}_{0.2}\text{Mn}_{0.2}\text{O}_2$ Cathode Material by a Carbonate Co-Precipitation Method and Its Electrochemical Characterization. *Solid State Ionics* **2006**, *177*, 3303.

(24) Zheng, Z.; Guo, X.-D.; Chou, S.-L.; Hua, W.-B.; Liu, H.-K.; Dou, S. X.; Yang, X.-S. Uniform Ni-Rich $\text{LiNi}_{0.6}\text{Co}_{0.2}\text{Mn}_{0.2}\text{O}_2$ Porous Microspheres: Facile Designed Synthesis and Their Improved Electrochemical Performance. *Electrochim. Acta* **2016**, *191*, 401.

(25) Zhong, S.; Li, W.; Zuo, Z.; Tang, X.; Li, Y. Synthesis and Electrochemical Performances of $\text{LiNi}_{0.6}\text{Co}_{0.2}\text{Mn}_{0.2}\text{O}_2$ Cathode Materials. *Trans. Nonferrous Met. Soc. China* **2009**, *19*, 1499.

(26) Yue, P.; Wang, Z.; Peng, W.; Li, L.; Chen, W.; Guo, H.; Li, X. Spray-Drying Synthesized $\text{LiNi}_{0.6}\text{Co}_{0.2}\text{Mn}_{0.2}\text{O}_2$ and Its Electrochemical Performance as Cathode

Materials for Lithium Ion Batteries. *Powder Technol.* **2011**, *214*, 279.

(27) Yue, P.; Wang, Z.; Peng, W.; Li, L.; Guo, H.; Li, X.; Hu, Q.; Zhang, Y. Preparation and Electrochemical Properties of Submicron $\text{LiNi}_{0.6}\text{Co}_{0.2}\text{Mn}_{0.2}\text{O}_2$ as Cathode Material for Lithium Ion Batteries. *Scr. Mater.* **2011**, *65*, 1077.

(28) Yue, P.; Wang, Z.; Guo, H.; Wu, F.; He, Z.; Li, X. Effect of Synthesis Routes on the Electrochemical Performance of $\text{Li}[\text{Ni}_{0.6}\text{Co}_{0.2}\text{Mn}_{0.2}]\text{O}_2$ for Lithium Ion Batteries. *J. Solid State Electrochem.* **2012**, *16*, 3849.

(29) Gan, C.; Hu, X.; Zhan, H.; Zhou, Y. Synthesis and Characterization of $\text{Li}_{1.2}\text{Ni}_{0.6}\text{Co}_{0.2}\text{Mn}_{0.2}\text{O}_{2+\delta}$ as a Cathode Material for Secondary Lithium Batteries. *Solid State Ionics* **2005**, *176*, 687.

(30) Chen, Z.; Dahn, J. R. Reducing Carbon in LiFePO_4/C Composite Electrodes to Maximize Specific Energy, Volumetric Energy, and Tap Density. *J. Electrochem. Soc.* **2002**, *149*, A1184.

(31) Chang, S. M.; Lee, M.; Kim, W.-S. Preparation of Large Monodispersed Spherical Silica Particles Using Seed Particle Growth. *J. Colloid Interface Sci.* **2005**, *286*, 536.

(32) Jiang, D.; Zhao, L.; Shao, Y.; Wang, D. Preparation and Characterization of Layered $\text{LiNi}_{0.9}\text{Co}_{0.05}\text{Mn}_{0.025}\text{Mg}_{0.025}\text{O}_2$ Cathode Material by a Sol-gel Method for Lithium-Ion Batteries. *RSC Adv.* **2015**, *5*, 40779.

(33) Rougier, A.; Gravereau, P.; Delmas, C. Optimization of the Composition of the $\text{Li}_{1-z}\text{Ni}_{1+z}\text{O}_2$ Electrode Materials: Structural, Magnetic, and Electrochemical Studies. *J. Electrochem. Soc.* **1996**, *143*, 1168.

(34) Li, J.; Wang, L.; Zhang, Q.; He, X. Synthesis and Characterization of $\text{LiNi}_{0.6}\text{Mn}_{0.4-x}\text{Co}_x\text{O}_2$ as Cathode Materials for Li-Ion Batteries. *J. Power Sources* **2009**, *189*, 28.

(35) Kang, K.; Ceder, G. Factors That Affect Li Mobility in Layered Lithium

Transition Metal Oxides. *Phys. Rev. B* **2006**, *74*, 94105.

(36) Lee, M.-H.; Kang, Y.-J.; Myung, S.-T.; Sun, Y.-K. Synthetic Optimization of $\text{Li}[\text{Ni}_{1/3}\text{Co}_{1/3}\text{Mn}_{1/3}]\text{O}_2$ via Co-Precipitation. *Electrochim. Acta* **2004**, *50*, 939.

(37) Wu, Z.; Ji, S.; Hu, Z.; Zheng, J.; Xiao, S.; Lin, Y.; Xu, K.; Amine, K.; Pan, F. Pre-Lithiation of $\text{Li}(\text{Ni}_{1-x-y}\text{Mn}_x\text{Co}_y)\text{O}_2$ Materials Enabling Enhancement of Performance for Li-Ion Battery. *ACS Appl. Mater. Interfaces* **2016**, *8*, 15361.

(38) Cho, D.-H.; Jo, C.-H.; Cho, W.; Kim, Y.-J.; Yashiro, H.; Sun, Y.-K.; Myung, S.-T. Effect of Residual Lithium Compounds on Layer Ni-Rich $\text{Li}[\text{Ni}_{0.7}\text{Mn}_{0.3}]\text{O}_2$. *J. Electrochem. Soc.* **2014**, *161*, A920.

(39) Dahbi, M.; Wikberg, J. M.; Saadoune, I.; Gustafsson, T.; Svedlindh, P.; Edström, K. Electrochemical Behavior of $\text{LiNi}_{1-y-z}\text{Co}_y\text{Mn}_z\text{O}_2$ Probed through Structural and Magnetic Properties. *J. Appl. Phys.* **2012**, *111*, 23904.

(40) Liao, J.-Y.; Oh, S.-M.; Manthiram, A. Core/Double-Shell Type Gradient Ni-Rich $\text{LiNi}_{0.76}\text{Co}_{0.10}\text{Mn}_{0.14}\text{O}_2$ with High Capacity and Long Cycle Life for Lithium-Ion Batteries. *ACS Appl. Mater. Interfaces* **2016**, *8*, 24543.

CHAPTER 3
HIGH RATE PERFORMANCE OF LITHIUM NICKEL MANGANESE COBALT
OXIDE CATHODE WITH PREFERENTIALLY ORENTATED LI-DIFFUSING
CHANNELS¹

3.1 Introduction

There is, currently, a demand for high performance lithium-ion batteries (LIBs) from consumer electronics to large-scale applications including electric vehicles, hybrid electric vehicles, and stationary electrical energy storage.^{2,3} LIBs with higher power density, combined with longer cycling life, are needed to address the exacting requirements of these applications.⁴⁻⁸ It is generally accepted that the limitation for achieving higher energy densities in LIBs arises from the capacity imbalance between cathode and anode.⁹ In the past few years, layered Li transition metal oxides, with their large theoretical capacities (~280 mAh/g), have served as the most important family of cathode materials for high-energy density batteries, compared with olivine or spinel based materials.¹⁰⁻¹³ Lithium cobalt oxide (LCO) delivers a high working voltage (~3.9 V) with excellent rate capability and has been the most widely used material for consumer electronics batteries.¹⁴ However, the limitations of LCO, including a small practical capacity (~150 mAh/g), safety concerns, and the high cost of cobalt, have led researchers to focus on other layered materials containing less Co. Among candidate cathode materials, layered lithium nickel manganese cobalt oxides (NMCs) have attracted much attention since the introduction of Ohzuku's $\text{LiNi}_{0.33}\text{Mn}_{0.33}\text{Co}_{0.33}\text{O}_2$.^{15,16} In NMC cathodes, Mn provides cycling and safety but has a low capacity, while Co increases the electrical conductivity to improve the rate capability but at increased cost, while Ni provides superior capacity but exhibits poor thermal stability.^{17,18} The lower quantity of Co in NMC materials, compared with LCO, has contributed to a reduction in cost and improved safety for the new battery

systems. NMC materials have been successfully applied to commercial LIBs with the expectation of delivering high performance.

To date, two representative NMC materials have been successfully adopted into commercial LIBs: $\text{LiNi}_{0.33}\text{Mn}_{0.33}\text{Co}_{0.33}\text{O}_2$ and $\text{LiNi}_{0.5}\text{Mn}_{0.3}\text{Co}_{0.2}\text{O}_2$. However, the practical use of NMC cathodes, particularly in electric vehicles and plug-in hybrid electric vehicles, has been severely delayed because of their limited power performance (rate capability) and dramatic capacity losses during cycling at high operating temperatures (45-60 °C) and high voltages (>4.3 V).^{19,20} The cycling and thermal characteristics of these materials, especially at high voltages and high temperatures, necessitate further exploration because of the intrinsic thermal instability in the delithiated state, and unsatisfactory cycle life due to structural instabilities. Thus, it is imperative to develop high-rate capable and robust NMC cathode materials for high power applications.

Many strategies have been pursued in an effort to overcome the aforementioned limitations. It is well known that the electrochemical performance of cathodes (cycling stability, power density, and reversibility) critically depend on the morphological and compositional characteristics of the electrode materials. Thus, tight control of the synthesis parameters of $\text{LiNi}_{0.33}\text{Mn}_{0.33}\text{Co}_{0.33}\text{O}_2$ cathodes and morphological design have been regarded as very promising venues to improve electrochemical performance. Reducing the average particle size can greatly shorten the diffusional distances of lithium ions, increase electrode-electrolyte contact, and effectively improve the high-rate charge/discharge performance.²¹⁻²⁴ Numerous methods such as solid-state synthesis,²⁵⁻²⁷ sol-gel,²⁸ spray drying processes,²⁹⁻³¹ combustion methods,³² and co-precipitation methods,³³⁻³⁵ have been developed to prepare morphologically uniform

high performance $\text{LiNi}_{0.33}\text{Mn}_{0.33}\text{Co}_{0.33}\text{O}_2$ cathodes. However, to date, none of these materials exhibit high-rate capability while maintaining long cycling life, especially at high operating temperatures.

In this paper, we report on the exceptional high-rate performance of our $\text{LiNi}_{0.33}\text{Mn}_{0.33}\text{Co}_{0.33}\text{O}_2$ (HP-NMC) cathode material with high stability at high temperatures for lithium-ion batteries. We studied the structural properties, composition and particle morphology of the HP-NMC. The electrochemical performance, including the discharge capacity, columbic efficiency, rate capability and cycling life were systemically investigated.

3.2 Experimental Section

Sample preparation The $\text{Ni}_{0.33}\text{Mn}_{0.33}\text{Co}_{0.33}(\text{OH})_2$ precursor was synthesized via coprecipitation of $\text{NiSO}_4 \cdot 6\text{H}_2\text{O}$, $\text{CoSO}_4 \cdot 7\text{H}_2\text{O}$ and $\text{MnSO}_4 \cdot \text{H}_2\text{O}$ as starting materials, dissolved in distilled water in molar ratios of Ni: Co: Mn = 1:1:1.⁸ A 2 M aqueous solution of the transition metal sulfates was slowly pumped into a continuously stirred tank reactor. Concomitantly, a 6 M NaOH solution (aq) and a 3 M NH_4OH solution (aq) were also separately pumped into the reactor. After reaction, the precipitate was filtered and washed several times with water to remove residual ions (Na^+ , SO_4^{2-} or other ions). The precipitate was then dried at 100 °C overnight. The resulting hydroxide precursor $\text{Ni}_{0.33}\text{Mn}_{0.33}\text{Co}_{0.33}(\text{OH})_2$ was mixed with $\text{LiOH} \cdot \text{H}_2\text{O}$ and calcined at 900 °C for 12 h in air to obtain the $\text{LiNi}_{0.33}\text{Mn}_{0.33}\text{Co}_{0.33}\text{O}_2$ (HP-NMC) cathode material.

Sample characterization X-ray diffraction patterns were obtained with a Rigaku Ultima VI powder X-ray diffractometer with CuK radiation ($\text{K}\alpha_1$, $\lambda = 1.5406 \text{ \AA}$ and

$K\alpha_2$, $\lambda = 1.5444 \text{ \AA}$). Diffraction patterns were collected at a scanning rate of $5^\circ/\text{min}$, and with a step of 0.02° (Figure 3.1). Particle size and size distribution were measured using a Bettersize BT-9300ST Laser Particle Size Analyzer (Figure 3.2). SEM imaging (Figure 3.3) was performed with a LEO-1550 field emission SEM (FSEM). Low magnification STEM imaging, SAED, and XEDS analysis were carried out using a FEI Tecnai F20 (S)TEM with a Schottky field emission gun operated at 200 kV. XEDS analysis was performed using an Oxford XMAX detector, with an electron beam current of about 1 nA.

Particle cross-section milling, SEM imaging (Figure 3.3), and thin TEM specimen preparation were performed in a FEI Strata 400 Dual Beam FIB SEM. To prepare for FIB milling, NMC particles were dispersed on a piece of silicon wafer and carbon coated to improve the sample conductivity and protect the NMC surface. Additional protective layers of platinum-carbon composite were subsequently deposited first with the electron beam and then with the ion beam. NMC particles were attached to a copper TEM half-grid using an OmniProbe nanomanipulator and ion-beam deposited platinum. A 30kV gallium ion beam was used to expose the particle interiors imaged in Figure 3.3 and remove material to produce a $\sim 1 \text{ \mu m}$ thick disk from each particle. The specimen was then thinned to a wedge with a 5kV ion beam and smoothed with a 2kV ion beam to minimize ion-beam damage to the newly exposed surfaces.⁴¹

Atomic resolution STEM imaging and scanning transmission electron diffraction were performed in a probe-corrected FEI Titan Themis (S)TEM operated at 300kV. The convergence semi-angle was set to 21 mrad for atomic resolution imaging, and 0.5 mrad for scanning diffraction. Scanning transmission electron diffraction maps were acquired using the electron microscope pixel array detector (EMPAD) with a 1 ms

acquisition time per diffraction pattern.⁴¹ The camera length was chosen to capture all visible diffraction spots. To improve recognition of the underlying lattice orientation and reduce the influence of defects and small crystal tilts, PCA analysis was calculated using the logarithm of the magnitude of the fast Fourier transform of the logarithm of each diffraction pattern ($\log[\text{abs}[\text{fft}[\log[D]]]$). The first 20 PCA components (excluding simple intensity components) were combined into a color visualization of the grain structure by mapping the principal angle of each component's intensity onto a color wheel to assign it a color, and then summing the resulting color images into a single composite image.

STEM EELS mapping was performed in a fifth-order aberration-correction NION UltraSTEM with a cold field emission electron gun operating at 100kV with a 30mrad convergence angle. Dual EELS acquisition of the zero loss peak was used to correct for the energy drift in the spectrum due to the large field of view used for mapping. The Li K edge signal was extracted from a separate spectrum image at the same location as the signal for the O K, Mn L_{2,3}, Co L_{2,3}, and Ni L_{2,3} edges.

Electrochemical tests Electrochemical measurements were carried out in CR 2032 coin cells assembled in an argon filled glove box (residual water and oxygen were 0.5 ppm and 0.1 ppm, respectively) with lithium metal as the anode. The working cathode was fabricated with 80 wt% active material, 10 wt% super P carbon, and 10 wt% poly(vinylidene fluoride) (PVDF) as binder. The resulting slurry was coated onto an Al foil current collector. The coated electrode was dried for 12 h at 110 °C in a vacuum oven. The typical mass loading of the active material was 2.0 mg/cm². The counter electrode was Li metal. The two electrodes were separated by a polypropylene separator (Celgard 3501). The electrolyte was 1.2 M LiPF₆ in a 3:7 ratio of EC

(ethylene carbonate) to EMC (ethyl methyl carbonate). Galvanostatic charge/discharge of the coin cells was carried out using an Arbin BT-2000 battery tester with a constant discharge/charge current rate of 0.1 C and a voltage range of 2.8 to 4.45 V vs. Li/Li⁺ at room temperature. Every experiment was carried out in triplicate (three parallel trials), and the error bar of the measured capacities, among the three trials, was less than 0.25%. We report the measured capacities rounded to the last integral digit; in which case, all results were identical. Thus we do not include error bars in these cases.

3.3 Results and Discussion

Figure 3.1 presents the XRD pattern of our HP-NMC cathode material. The synthesis yielded a well-defined and impurity-free single-phase material, and all reflections could be indexed on the basis of a hexagonal α -NaFeO₂ type structure (space group R-3m). In addition, a split between the (006)/(102) and (108)/(110) peaks, respectively, was clearly observed, indicating that the structure had good layering.^{12,36} The intensity ratio of I(003)/I(104) is a reliable indicator for determining the cation distribution in the lattice of the layered oxide. Cation mixing can be a direct indicator of Ni²⁺ occupancy on Li⁺ sites. Generally, when the intensity ratio is higher than 1.2, the degree of cation mixing is low, and the sample has a more well-defined layered structure with a lower level of cation mixing.³⁷ Our HP-NMC sample had a high value (1.21) of the I(003)/I(104) intensity ratio and, thus, a low value of cation mixing. This is beneficial to Li ion mobility upon charging, which in turn, may result in more Li intercalation into the material and higher rate performance.

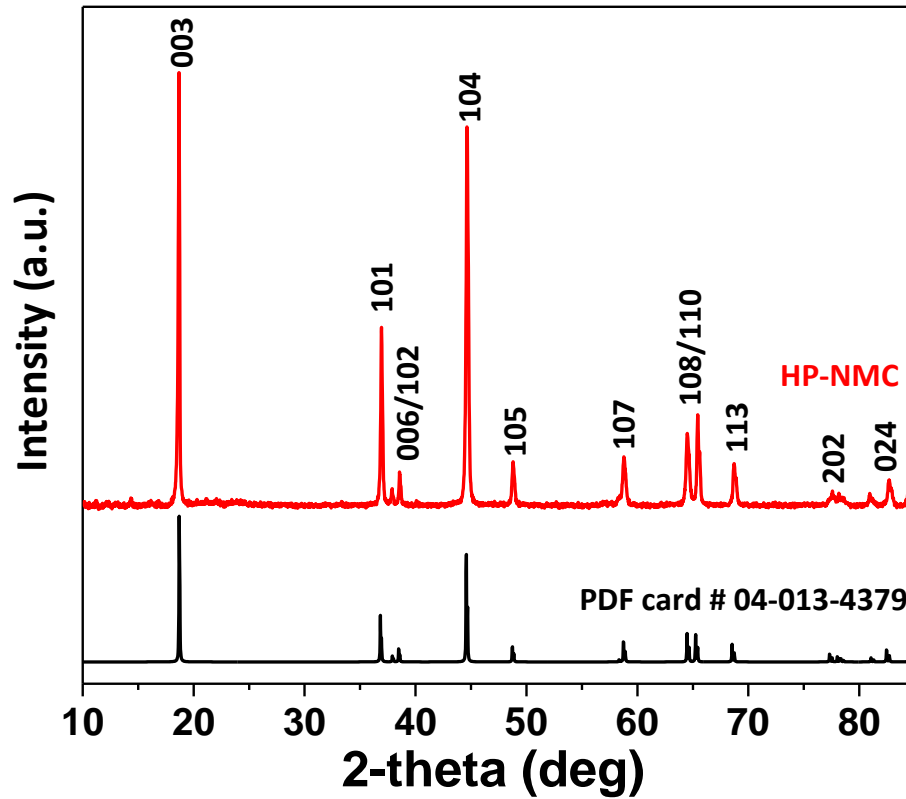


Figure 3.1 XRD patterns of the HP-NMC material.

The size distribution of our HP-NMC particles (see Figure 3.2), expressed in span, defined as $(D_{90}-D_{10})/D_{50}$, where D_{50} indicates a particle diameter that is larger than fifty percentile of the total particles (often denoted as the medium number), while D_{90} and D_{10} indicate particle diameters that are larger than ninety and ten percentile of the total particles, respectively. The particle size, D_{50} , was measured to be 6.26 μm , and the span was measured to be 1.42 for a sample of NMC particles (see Table 3.1). Our HP-NMC particles have an advantageously small average particle size, which is likely to result in greater capacity at high current rates. Figures 3.3a-b present SEM images of an overview of particles (a) and a single particle (b) of the prepared HP-NMC

material. The particles exhibited a roughly spherical morphology, where each of the larger particles contain a large number of smaller primary particles or grains that are hundreds of nanometers in size.

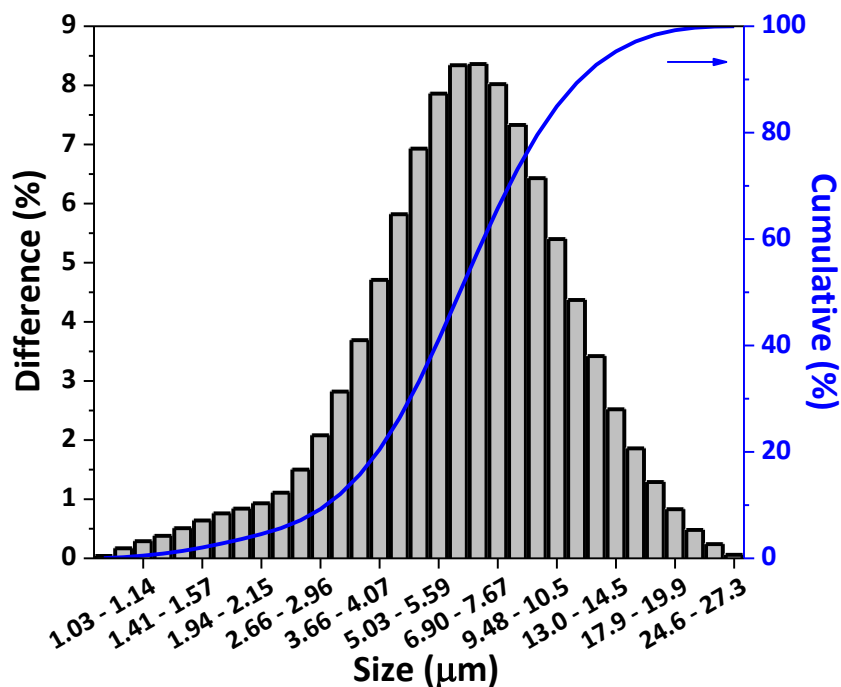


Figure 3.2 Size distribution of HP-NMC particles.

Table 3.1 Particle size information of HP-NMC sample.

Item	LiNi _{0.6} Mn _{0.2} Co _{0.2} O ₂ material
D03 (µm)	1.79
D10 (µm)	3.05
D50 (µm)	6.26
D90 (µm)	11.97
D97 (µm)	15.98
Span [(D90-D10)/D50]	1.42

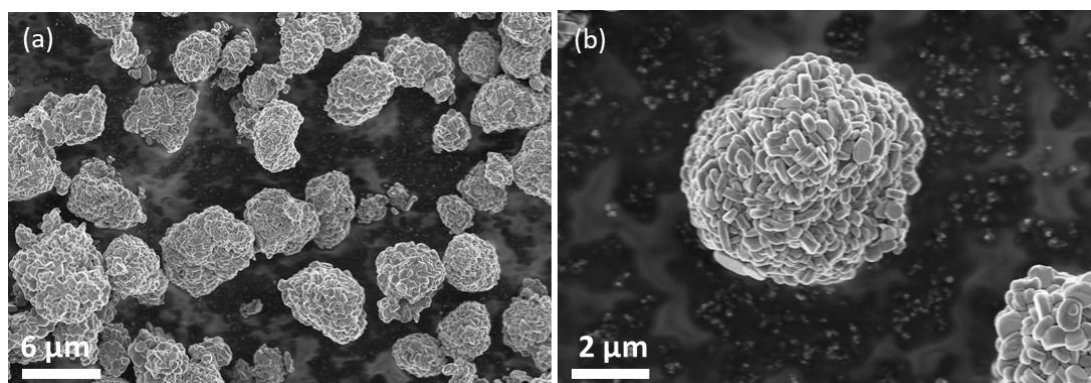


Figure 3.3 (a) Overview and (b) single particle SEM images of HP-NMC particles.

To better understand the microstructure of our HP-NMC material, we employed (scanning) transmission electron microscopy ((S)TEM). Typical multi-micron sized NMC particles cannot be characterized directly by (S)TEM, as they are too large to allow electron beam transmission. Instead, we employed two different methods to prepare thinner specimens for (S)TEM characterization. In the first method, crude specimens were prepared by ultrasonication, which causes some primary particles or clusters of primary particles to break off from the larger NMC particles. These specimens are suitable for low-resolution characterization and electron diffraction. In the second method, thin specimens were prepared using focused ion beam (FIB) milling, producing thinned cross-sections from full-sized NMC particles. This approach offers the advantages of high-resolution characterization, as well as allowing us to study the intact interior structure of a typical particle.

Figure 3.4 shows selected area electron diffraction (SAED) and high angle annular dark field (HAADF) STEM imaging carried out to characterize the crystal structure of the HP-NMC particles. Figure 3.4a shows a low resolution (HAADF) STEM image of a cluster of primary particles with a typical diameter of $\sim 300 - 700$ nm. A SAED

pattern from a cluster of HP-NMC particles (Figures 3.3b) was polycrystalline, with rings of spots corresponding to typical reflections of NMC materials such as (101), (104) and (108), consistent with the powder XRD results (Figure 3.1). The SAED pattern from one isolated primary particle (Figure 3.4c) exhibited a single-crystal SAED pattern, indicating that each primary particle corresponds to a single crystalline grain. The diffraction pattern showed hexagonal symmetry, with the {110} family of diffraction spots, indicated with a white dashed hexagon in Figure 3.4c, corresponding to the R-3m space group of trigonal crystals. These prominent diffraction spots (e.g., C, D in Figure 3.4c) are surrounded by additional, faint diffraction spots (e.g., A, B in Figure 3.4c), that also have hexagonal symmetry. The distance of these faint spots to the (0,0) beam in reciprocal space is one third of that of the prominent spots, indicating that the superlattice ordering has a d-spacing three times as large as the regular (110) spacing. These spots have previously been observed by Yabuuchi et al.,³⁸ and indicate a $\sqrt{3} \times \sqrt{3}$ R30°-type superlattice ordering in the transition-metal layers of NMC layered materials. Yabuuchi et. al. proposed that the superlattice structure is due to in-plane ordering of Ni, Mn and Co, and that the associated diffraction spots are faint due to the small difference in the atomic scattering factors among Ni, Mn and Co. The NMC crystal structure was further studied using atomic resolution HAADF STEM imaging in a FIB thinned specimen. Figure 3.4d shows an image of the specimen oriented along the (110) direction, providing a clear illustration of the layered crystal structure. The layers of transition metal atoms, which appear bright in HAADF STEM due to their relatively high atomic number, are separated by layers of oxygen and lithium atoms, which do not appear due to their low atomic numbers. The lattice in a ~1 nm layer near the crystal surface also shows a reconstruction, with a high degree of cation mixing, visible as bright transition metal atoms filling the lithium channels. This surface reconstruction layer is known to

expand upon contact with the electrolyte and electrochemical cycling.³⁹

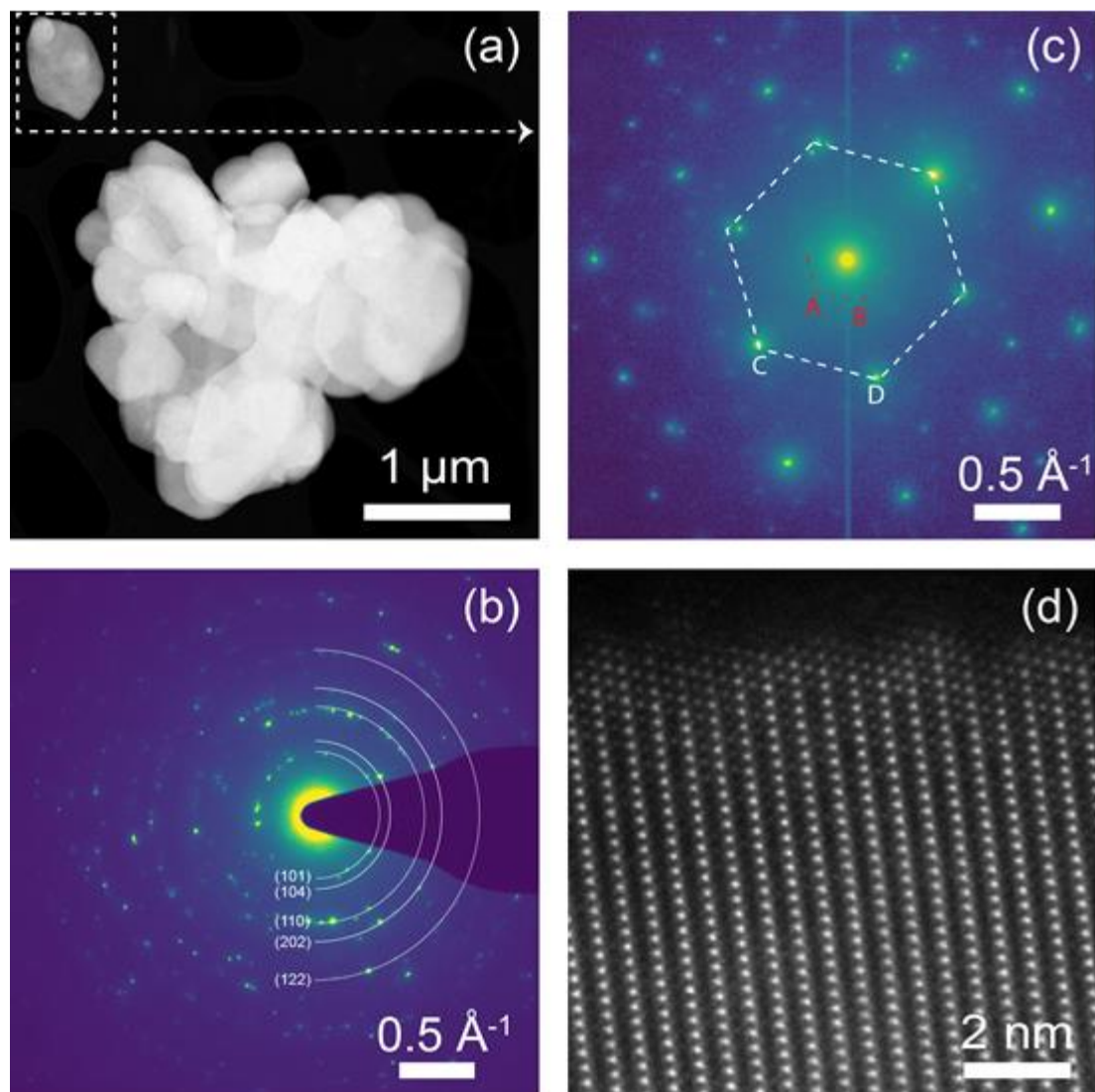


Figure 3.4 (a) STEM image of a cluster of primary particles, corresponding to the polycrystalline SAED pattern in (b). (c) SAED pattern from a single isolated grain, indicated in (a), oriented in the (001) direction. (d) STEM lattice image of a thin specimen oriented in the (110) direction, showing layered crystal structure.

The overall microstructure of a representative HP-NMC particle was also

characterized and compared to that of a representative commercial NMC (c-NMC) particle using a combination of SEM imaging, FIB cross-sectioning, and STEM scanning diffraction (Figure 3.5). SEM images of the representative HP-NMC and c-NMC particles (Figures 3.5a, b respectively) show differing surface texturing between the two materials. Individual grains in HP-NMC appear to have a plate-like morphology, with edges frequently protruding out from the particle exterior, while grains in c-NMC typically appear more rounded in shape at the particle surface. The particle size of the c-NMC particles was 11.40 μm , significantly larger than the HP-NMC particles (See Table 3.2). To observe the interior morphology of each particle, SEM images were acquired during the preparation of thin TEM specimens after half of the particle was removed with the FIB. These images (Figures 3.5c, d) show that both particles have a hollow core surrounded by a relatively dense shell of material. The thickness of the dense shell was observed to be 1-1.5 μm in the HP-NMC particle and 3-4 μm in the c-NMC particle. The thinner shell thickness in HP-NMC, due to both a slightly larger hollow core and an overall smaller total diameter of the particle, is expected to reduce the distance over which lithium ions must diffuse as the material is charged and discharged.

STEM diffraction mapping was employed to characterize the crystal grain structure of the materials and its potential impact on battery performance. Principal component analysis (PCA) was performed on the 4D diffraction maps to produce false-color grain maps (Figures 3.5e-f) for each thin specimen, where grains with distinct crystal orientations appear in different colors (see methods section for details). The grain map of HP-NMC (Figure 3.5e) shows that the grains have a predominantly plate-like geometry, indicating that the surface structure observed in Figure 3.5a extends into the particle interior. Furthermore, the plate-like grains show a preferential alignment, with

the long axes oriented radially outward from the center of the particle. By contrast, the c-NMC grain map (Figure 3.5f) shows grains with a much more isotropic structure, not showing any clear preferred geometry or orientation. The typical grain size also appears to be significantly larger in c-NMC than in HP-NMC.

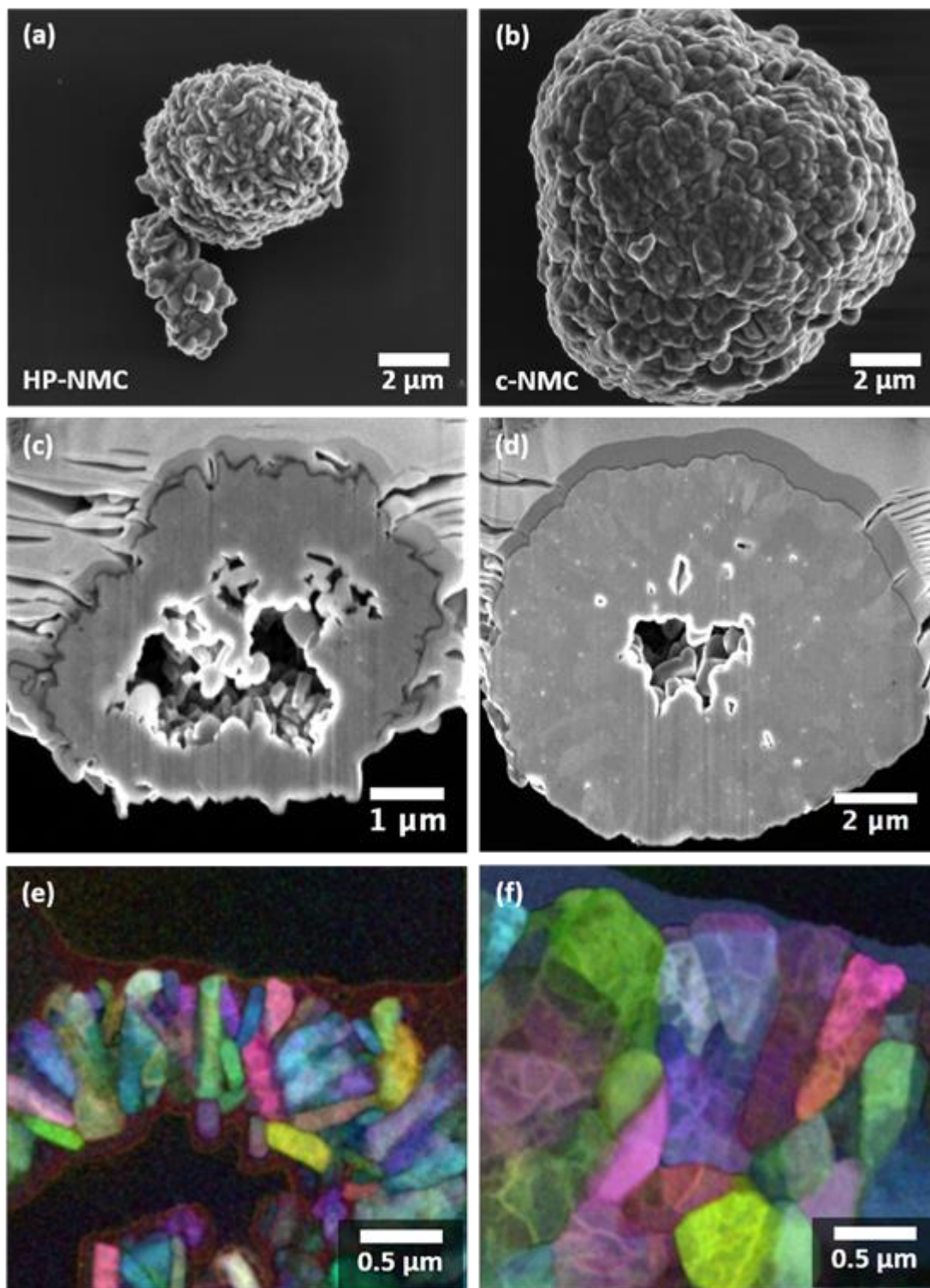


Figure 3.5 (a,b) SEM images of HP-NMC (left) and c-NMC (right) particles, showing plate-like and rounded surface morphologies, respectively. (c,d) SEM images of FIB-

cut cross-sections of the particles in (a) and (b), showing interior structure and voids. (e,f) Grain structure maps derived from scanning transmission electron diffraction mapping of FIB thinned specimens. Each colored region represents a distinct crystallite. (f) shows grains that are plate-like, with edges oriented outward in HP-NMC, while (e) shows an isotropic grain structure in c-NMC.

Table 3.2. Particle size information of c-NMC sample.

Item	LiNi_{0.6}Mn_{0.2}Co_{0.2}O₂ material
D03 (μm)	3.75
D10 (μm)	5.57
D50 (μm)	11.40
D90 (μm)	22.04
D97 (μm)	28.38
Span [(D90-D10)/D50]	1.44

The relationship between the grain geometry and orientation of the layered crystal lattice was further explored using atomic resolution HAADF STEM imaging (Figure 3.6). In HP-NMC, the lattice is observed to be oriented with the c-axis corresponding to the thin dimension of the plate-like grains. The Li channels between the transition metal oxide layers are parallel to the long dimension of each plate. Thus, the HP-NMC microstructure is arranged with the Li channels preferentially orientated radially outward from the center of the particle. This is expected to greatly enhance the rate of Li diffusion in HP-NMC particles during battery operation. The c-NMC particle, by contrast, shows no discernible relationship between the lattice orientation and the grain geometry.

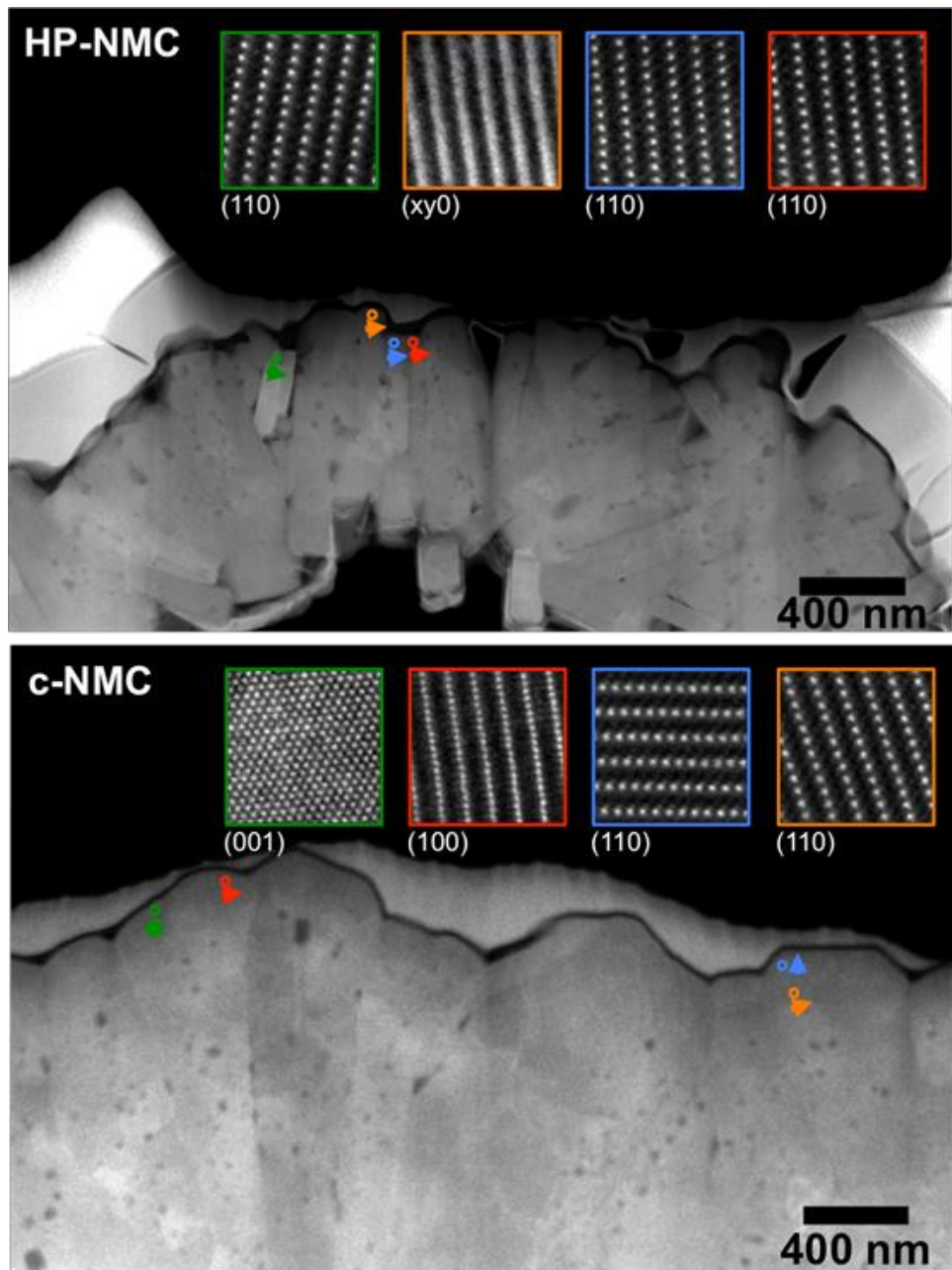


Figure 3.6 STEM images of thin HP-NMC (top) and c-NMC (bottom) specimens, with inset STEM lattice images from indicated locations. Labels below each inset indicate crystalline zone axis. Specimens were tilted $<5^\circ$ to align on zone axis for each inset. In HP-NMC, the lattice is oriented with the c-axis parallel to the short direction of each plate-like grain, while in c-NMC, no trend is observed in the lattice orientation of each grain.

The distribution of elements in the NMC samples was investigated using both X-ray energy dispersive spectroscopy (XEDS) in the ultrasonically dispersed specimen and electron energy loss spectroscopy in the FIB-thinned specimens. Figure 3.7 shows XEDS analysis of dispersed HP-NMC particles. XEDS maps of the distribution of Ni, Mn and Co (Figures 3.7a-d) show that the distribution of Ni, Mn and Co is uniform throughout the material, confirming the successful chemical synthesis of homogenous HP-NMC particles. Furthermore, the associated XEDS spectrum (Figure 3.7e) shows that the intensities of the Ni, Mn, and Co K α peaks are very similar, confirming that approximately equal concentrations of Ni, Mn, and Co are present in the particles, which is consistent with ICP elemental analysis (Table 3.3) and anticipated stoichiometry.

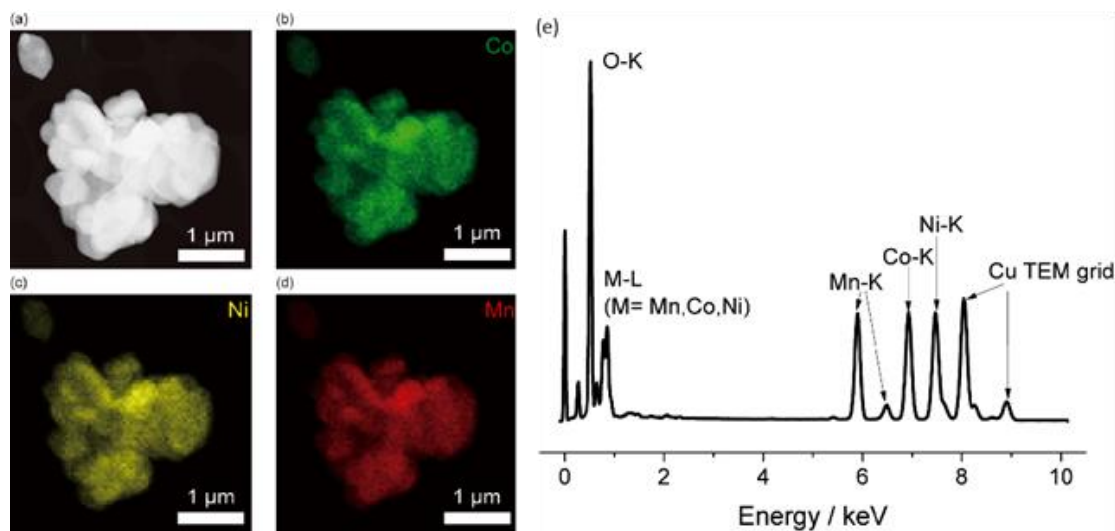


Figure 3.7 XEDS analysis of HP-NMC particles. (a) HAADF-STEM image of HP-NMC and (b, c, d) corresponding XEDS elemental maps of Co (b), Ni (c), Mn (d). (e) XEDS spectrum from this region. The intensities of the Mn, Co, and Ni K α peaks are consistent with equal concentrations of Mn, Co, and Ni in the material.

Table 3.3 ICP-AES results our HP-NMC material.

Element	Content (mg/L)	Molar percentage in (Ni+Mn+Co) (%)
Ni 231.604	2.137	33.76
Mn 294.921	1.963	33.14
Co 228.616	2.103	33.10

The elemental distribution was examined in finer detail using EELS composition mapping of the thin specimens of HP-NMC, and c-NMC for comparison. Elemental maps of Ni, Mn, and Co were produced using their respective L_{2,3} edges, in addition to maps of O and Li, using their respective K edges (Figure 3.8). A large field of view was mapped in order to minimize potential electron beam-induced delithiation of the crystal, and to provide elemental maps that were as representative as possible. These elemental maps show a generally homogeneous distribution of Ni, Mn, and Co across the HP-NMC grains, in addition to a uniform distribution of Li and O. In the c-NMC specimen, however, some inhomogeneity of the transition metals was observed, as a 20-60 nm layer of Co-enriched material is present at the particle surface. The Li and O content appear uniform and consistent between this surface layer and the interior, suggesting that the inhomogeneity is merely substitution of Co for Mn and Ni within the same crystal structure. The relatively homogeneous chemical composition of the HP-NMC material compared to the c-NMC material demonstrates the benefits of our highly controlled synthesis.

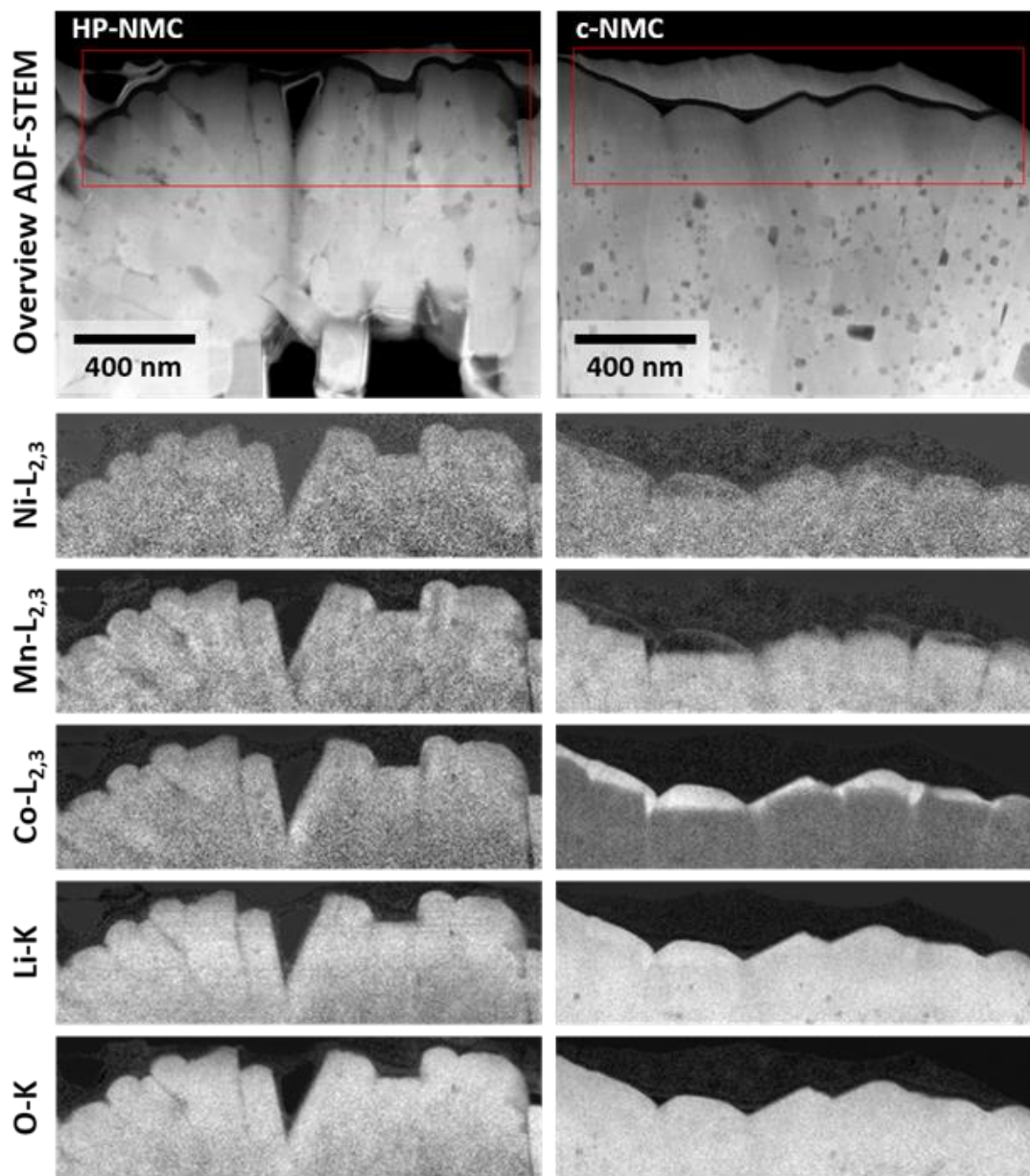


Figure 3.8 STEM EELS maps showing elemental distribution in regions indicated in overview images (top) of HP-NMC (left) and c-NMC (right). Maps show integrated signals from Ni L_{2,3}, Mn L_{2,3}, Co L_{2,3}, Li K, and O K edges (top to bottom).

To characterize the electrochemical properties of the synthesized HP-NMC materials, coin cell tests were carried out using the synthesized HP-NMC samples and c-NMC as cathode materials, and Li metal as an anode. Figure 3.9a presents the initial charge/discharge curves at 0.2 C for the two cathode materials over the voltage range of 2.8 and 4.45 V. Our HP-NMC exhibited a virtually identical discharge capacity (175 mAh/g vs. 176 mAh/g) and a slightly better first cycle coulombic efficiency (89.9 % vs. 88.4 %) when compared to a commercial NMC sample. The rate capabilities of our HP-NMC and commercial samples were investigated between 2.8 and 4.45 V at various current (“C”) rates as shown in Figure 3.9b. The cells were charged and discharged at C-rate values of 0.2, 0.5, 1, 2, 5, 10, 20 and 30 for five cycles, respectively (a charging rate of 1 C was used when the discharging rate was higher than 1 C).

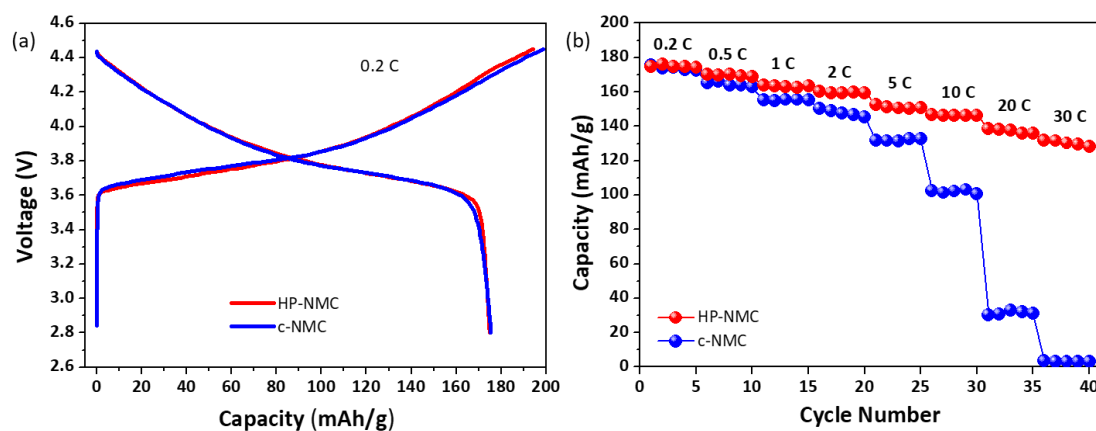


Figure 3.9 (a) Initial charge–discharge curves of our HP-NMC and a commercial sample c-NMC cells at 0.2 C between 2.8 and 4.45 V. (b) Rate performances of HP-NMC and c- NMC cells from 0.1 C to 30 C over the voltage range between 2.8 and 4.45 V.

Figures 3.10a-b present the discharge profiles at different current rates of our HP-NMC material and a commercial c-NMC material, respectively. While similar capacities are observed at the lower rates for both materials, clear capacity differences became evident at higher rates, and these increased with increasing rate. The HP-NMC cathode material exhibited a stable high capacity at both low and high current rates, while the commercial c-NMC cathode material exhibited a rapid decay in capacity with increasing current rate. Remarkably, our HP-NMC material retained capacities of 147 and 138 mAh/g at C-rates of 10 and 20 C, respectively. In comparison, the commercial material only delivered discharge capacities of 103 mAh/g at 10 C, and 31 mAh/g at 20 C. To our surprise, the HP-NMC cathode still had a capacity of 131 mAh/g at the ultrahigh C-rate of 30 C, while the commercial c-NMC cathode had lost almost all of its capacity (4 mAh/g). To clearly compare the rate capabilities of the two samples, their discharge capacities, at different C-rates, and the corresponding capacity retentions, relative to 0.2 C (retention at 0.2 C is 100%) are presented in Table 3.4. It is notable that our HP-NMC material delivered an exceptionally better capacity retention than the commercial material, especially at high current rates. At 30 C, the capacity retention of our HP-NMC material was 74.9%, which represents the best rate capability reported to date for NMC materials. In light of the microstructural characterization presented above, these significant differences in performance at high rate are most likely related to the shorter migration paths and faster ionic diffusion in the HP-NMC materials. Because the Li-diffusing channels of the layered NMC material are preferentially oriented radially outward from the particle center, much higher ionic diffusion is expected than for a material with isotropic grain orientations. This is complemented by the relatively small particle size, which requires a shorter overall migration path for Li.

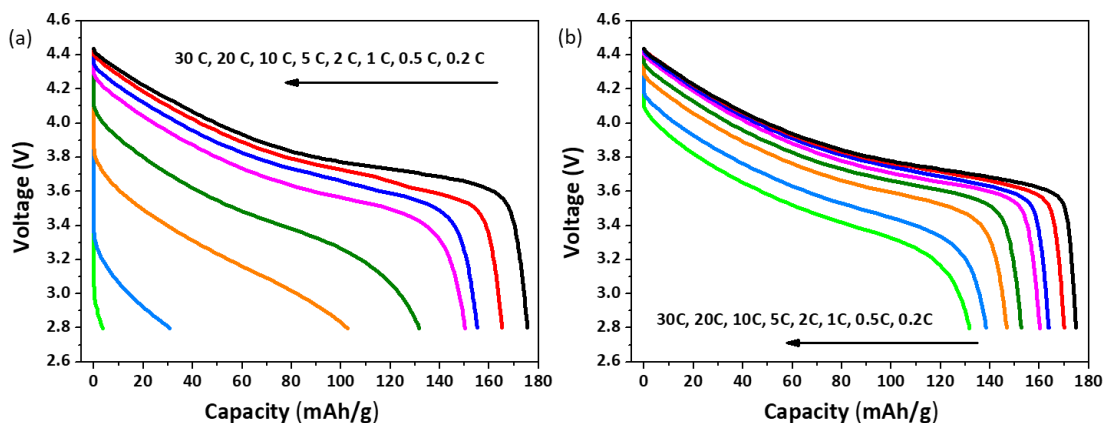


Figure 3.10 (a) Discharge curves of commercial c-NMC cell from 0.1 C to 30 C. (b) Discharge curves of a HP-NMC cell from 0.1 C to 30 C.

Table 3.4 Discharge capacities of our HP-NMC sample and a commercial sample at different rates and the corresponding capacity retentions (Note: retention at 0.2 C is defined as 100%).

Rates	HP-NMC		c-NMC	
	Discharge capacity (mAh/g)	Capacity retention (%)	Discharge capacity (mAh/g)	Capacity retention (%)
0.2 C	175	100	176	100
0.5 C	170	97.1	165	93.8
1 C	164	93.7	155	88.1
2 C	160	91.4	150	85.2
5 C	153	87.4	132	75.0
10 C	147	84.0	103	58.5
20 C	138	78.9	31	17.6
30 C	131	74.9	4	2.3

In a coin cell, two-electrode cyclic voltammetry was performed on the cell at various scan rates to probe the redox activity and diffusion behavior of the HP-NMC cathode material (Figure 3.11). The voltage range scanned was set between 2.8 and 4.45 V vs. Li/Li⁺, to ensure that the redox activity of the cathode materials would be studied exclusively. From the cyclic voltammogram, a highly chemically reversible redox couple was observed with a formal potential, E° , of 3.75 V vs. Li/Li⁺, at the slowest scan rate. The peak current, i_p , was proportional to the square root of the sweep rate, consistent with a diffusion-controlled process. This behavior likely originates from the diffusion of Li⁺ entering and exiting the thick and dense electrode matrix, which would be diffusive in nature. The E° shifted to more positive values as the scan rate increased, over a series of equivalent C-rates from 0.2 C to 5 C, indicating that $E_{pk, a}$ shifted more positively than $E_{pk, c}$ shifted negatively as a result of diffusion in the electrode. This observation suggests that the diffusion of Li ion de-insertion (oxidation of cathode) is slower than the diffusion of Li ion insertion (reduction of cathode). This suggests that, as the scan rate or charging rate increases, the high limit of charging will likely be limited by Li⁺ de-insertion.

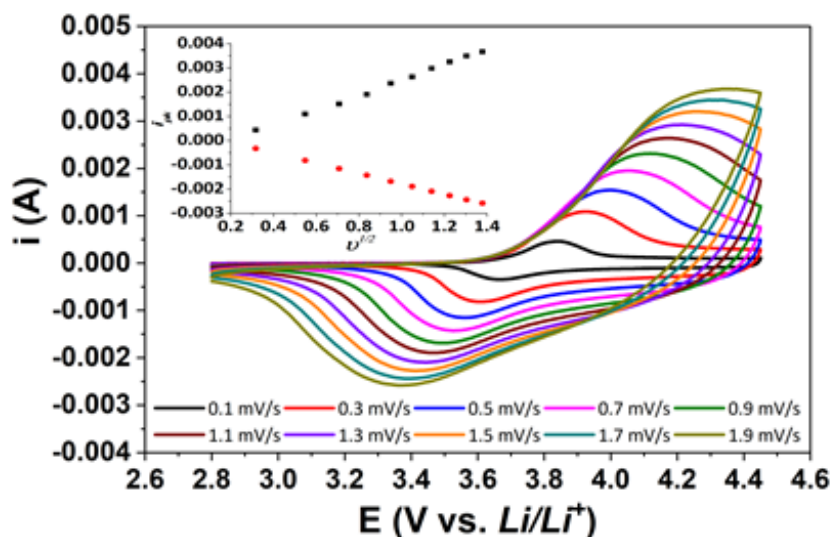


Figure 3.11 Cyclic voltammetric profiles of the HP-NMC material in a coin cell at various scan rates. Insert: I_p as a function of the square root of the sweep rate, indicating a diffusion limited process.

The cycling performances of our HP-NMC cathode and commercial c-NMC cathode are shown in Figure 3.12a. The cells were charge-discharge cycled at 25 °C over the voltage range of 2.8 and 4.45 V at 1 C. The first discharge capacities of our HP-NMC material and commercial c-NMC material were 165 and 157 mAh/g with Coulombic efficiencies of 89.1 % and 88.9 %, respectively. The capacity retention of our HP-NMC material was 81.6% after 150 cycles, which is significantly higher than that of the commercial c-NMC material (59.4% after 150 cycles). The cycling stability of our HP-NMC material, at C-rates of 1, 2, 5, 10 and 20 is also shown in Figure 3.12b. Our material retained a high discharge capacity at all the current rates. The discharge capacity retentions were 88.3%, 89.7%, 88.2%, 87.4% and 87.8% at C-rates of 1, 2, 5, 10 and 20, respectively.

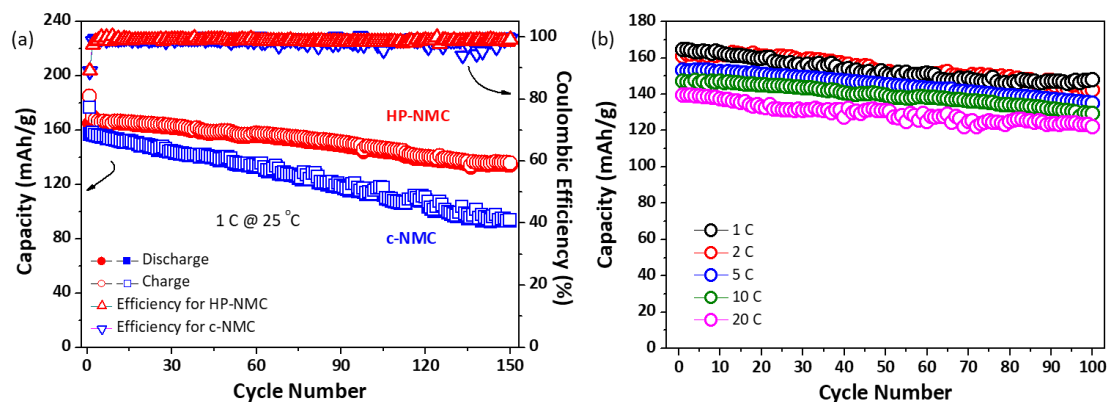


Figure 3.12 (a) Cycling performance of HP-NMC and c-NMC cells, up to 150 cycles between 2.8 and 4.45 V at 1 C at room temperature (25 °C). (b) Cycling performance of HP-NMC cells at different current rates (1 to 20 C) up to 100 cycles.

The cycling performances of our HP-NMC cathode and commercial c-NMC cathode at 50 °C were also studied. In Figure 3.13a the variation of discharge capacity vs. cycle number is plotted. It is clear that the capacity fade of electrodes containing our HP-NMC material (12.5% capacity loss after 50 cycles) is much less pronounced than that of electrodes comprising a commercial c-NMC cathode material (32.7% capacity loss after 50 cycles). A more detailed comparison of the rate-cycling performance of our HP-NMC material and commercial c-NMC material is presented in Figure 3.13b. For these tests, a 10-cycle 20 C discharge pulse was applied every 20 cycles to probe the structural resistance of the electrodes to high C-rates (A charging rate of 1 C was used). A discharge capacity of 142 mAh/g was obtained for the HP-NMC cell over 170 cycles. In contrast, the capacity retention for a commercial c-NMC cell was poor, namely 105 mAh/g remained, with significant deterioration under the high C-rate pulses. These results indicate that, in contrast to commercial c-NMC materials, our material is highly resistant not only to low current discharge but also to high current densities, validating the robustness of our HP-NMC material.

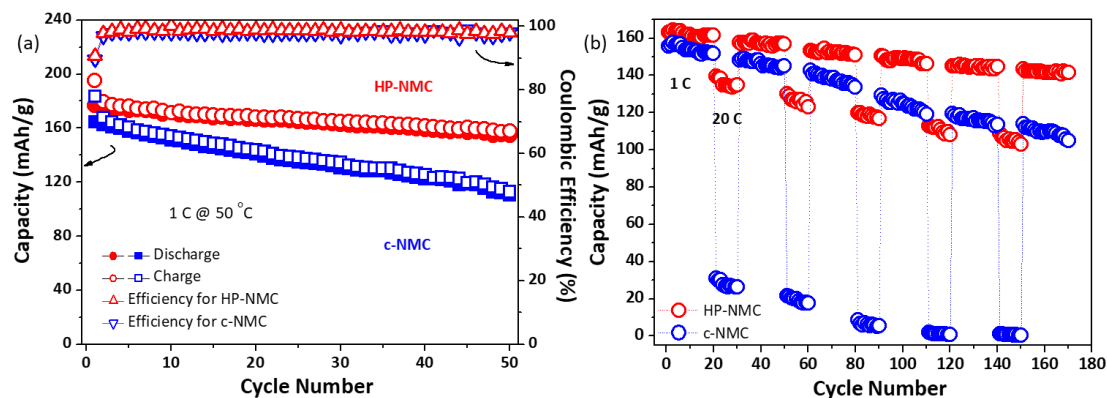


Figure 3.13 (a) Cycling performance of our HP-NMC and commercial c-NMC cells at 50 °C. (d) 1-20 C rate cycling performance of HP-NMC and c-NMC cells up to 180 cycles.

3.4 Conclusions

In summary, we have successfully developed a high-rate performance $\text{LiNi}_{0.33}\text{Mn}_{0.33}\text{Co}_{0.33}\text{O}_2$ cathode material with high stability. The particles exhibited a quasi-spherical morphology and uniform size distribution, with a well-defined crystal structure and homogeneous transition metal distribution pursuant to the well-controlled synthesis process. These materials exhibited superior electrochemical performance when compared with a commercial $\text{LiNi}_{0.33}\text{Mn}_{0.33}\text{Co}_{0.33}\text{O}_2$ sample, with an exceptional rate capability of 147 mAh/g and 138 mAh/g at 10 C and 20 C, respectively. Even at the ultrahigh C-rate of 30 C, our HP-NMC material delivered a discharge capacity of 131 mAh/g (capacity retention of 74.9% vs. 0.2 C). Our material also exhibited an enhanced cycling performance when compared to a commercial sample, under both room temperature and high temperature operation. The material also showed high stability at both low and high current densities. Our HP-NMC cathode material, delivered a combined electrochemical performance that has not yet been matched in any published report. The exceptionally high rate performance is

most likely attributable to the unique crystalline microstructure observed in (S)TEM characterization. The HP-NMC particles are composed of plate-like grains with a preferential stacking that results in the radially outward orientation of the high-Li-diffusivity channels of the crystal grains. This structure should allow a much higher rate lithium transport in the NMC material, especially when combined with shorter overall diffusion lengths from a uniformly smaller particle size. To the best of our knowledge, we feel confident that the remarkable overall performances presented here comprehensively demonstrate that our HP-NMC cathode material is practical and ready to use in plug-in hybrid electric vehicles and electric vehicles applications which demand high power, low cost, and long cycling performance especially at high operating temperatures.

REFERENCE

- (1) Reprinted with permission from the submitted manuscript.
- (2) Tarascon, J. M.; Armand, M. Issues and Challenges Facing Rechargeable Lithium Batteries. *Nature* **2001**, *414*, 359.
- (3) Armand, M.; Tarascon, J.M. Building Better Batteries. *Nature* **2008**, *451*, 652.
- (4) Kang, K. Electrodes with High Power and High Capacity for Rechargeable Lithium Batteries. *Science* **2006**, *311*, 977.
- (5) Kang, B.; Ceder, G. Battery Materials for Ultrafast Charging and Discharging. *Nature* **2009**, *458*, 190.
- (6) Dunn, B.; Kamath, H.; Tarascon, J. M. Electrical Energy Storage for the Grid: A Battery of Choices. *Science* **2011**, *334*, 928.
- (7) Cui, S.; Wei, Y.; Liu, T.; Deng, W.; Hu, Z.; Su, Y.; Li, H.; Li, M.; Guo, H.; Duan, Y.; Wang, W.; Rao, M.; Zheng, J.; Wang, X.; Pan, F. Optimized Temperature Effect of Li-Ion Diffusion with Layer Distance in $\text{Li}(\text{Ni}_x\text{Mn}_y\text{Co}_z)\text{O}_2$ Cathode Materials for High Performance Li-Ion Battery. *Adv. Energy Mater.* **2016**, *6*, 1501309.
- (8) Ren, D.; Shen, Y.; Yang, Y.; Shen, L.; Levin, B. D. A.; Yu, Y.; Muller, D. A.; Abruña, H. D. *ACS Appl. Mater. Interfaces* **2017**, *9*, 35811.
- (9) Xu, B.; Qian, D.; Wang, Z.; Meng, Y. S. Recent Progress in Cathode Materials Research for Advanced Lithium Ion Batteries. *Mater. Sci. Eng., R* **2012**, *73*, 51.
- (10) Reimers, J. N.; Dahn, J. R. Electrochemical and In Situ X - Ray Diffraction Studies of Lithium Intercalation in Li_xCoO_2 . *J. Electrochem. Soc.* **1992**, *139*, 2091.
- (11) Armstrong, A. R.; Bruce, P. G. Synthesis of Layered LiMnO_2 as an Electrode for Rechargeable Lithium Batteries. *Nature* **1996**, *381*, 499.
- (12) Rougier, A.; Gravereau, P.; Delmas, C. Optimization of the Composition of the $\text{Li}_{1-z}\text{Ni}_1+z\text{O}_2$ Electrode Materials: Structural, Magnetic, and Electrochemical Studies. *J. Electrochem. Soc.* **1996**, *143*, 1168.

- (13) He, P.; Yu, H.; Li, D.; Zhou, H. Layered Lithium Transition Metal Oxide Cathodes towards High Energy Lithium-Ion Batteries. *J. Mater. Chem.* **2012**, *22*, 3680.
- (14) Chen, Y.; CHEN, R.; Tang, Z.; Wang, L. Synthesis and Characterization of Zn-Doped $\text{LiCo}_0.3\text{Ni}_0.4(\text{xMn}_0.3\text{Zn}_x\text{O}_2$ Cathode Materials for Lithium-Ion Batteries. *J. Alloys Compd.* **2009**, *476*, 539.
- (15) Ohzuku, T.; Makimura, Y. Layered Lithium Insertion Material of $\text{LiCo}_{1/3}\text{Ni}_{1/3}\text{Mn}_{1/3}\text{O}_2$ for Lithium-Ion Batteries. *Chem. Lett.* **2001**, *30*, 642.
- (16) Ohzuku, T.; Makimura, Y. Layered Lithium Insertion Material of $\text{LiNi}_{1/2}\text{Mn}_{1/2}\text{O}_2$: A Possible Alternative to LiCoO_2 for Advanced Lithium-Ion Batteries. *Chem. Lett.* **2001**, *30*, 744.
- (17) Sun, H.-H.; Choi, W.; Lee, J. K.; Oh, I.-H.; Jung, H.-G. Control of Electrochemical Properties of Nickel-Rich Layered Cathode Materials for Lithium Ion Batteries by Variation of the Manganese to Cobalt Ratio. *J. Power Sources* **2015**, *275*, 877.
- (18) Liang, L.; Du, K.; Peng, Z.; Cao, Y.; Duan, J.; Jiang, J.; Hu, G. Co-precipitation Synthesis of $\text{Ni}_{0.6}\text{Co}_{0.2}\text{Mn}_{0.2}(\text{OH})_2$ Precursor and Characterization of $\text{LiNi}_{0.6}\text{Co}_{0.2}\text{Mn}_{0.2}\text{O}_2$ Cathode Material for Secondary Lithium Batteries. *Electrochim. Acta* **2014**, *130*, 82.
- (19) Amine, K.; Chen, Z.; Zhang, Z.; Liu, J.; Lu, W.; Qin, Y.; Lu, J.; Curtis, L.; Sun, Y.-K. Mechanism of Capacity Fade of MCMB/ $\text{Li}_{1.1}[\text{Ni}_{1/3}\text{Mn}_{1/3}\text{Co}_{1/3}]_{0.9}\text{O}_2$ Cell at Elevated Temperature and Additives to Improve Its Cycle Life. *J. Mater. Chem.* **2011**, *21*, 17754.
- (20) Chen, Z.; Sun, Y.-K.; Amine, K. Electrochemical Properties of Lithium-Rich $\text{Li}_{1+x}(\text{Mn}_{1/3}\text{Ni}_{1/3}\text{Co}_{1/3})_{1-x}\text{O}_2$ at High Potential. *J. Electrochem. Soc.* **2006**, *153*, A1818.
- (21) Li, L.; Meyer, W. H.; Wegner, G.; Wohlfahrt-Mehrens, M. Synthesis of Submicrometer-Sized Electrochemically Active Lithium Cobalt Oxide via a Polymer

Precursor. *Adv. Mater.* **2005**, *17*, 984.

(22) Kawamura, T.; Makidera, M.; Okada, S.; Koga, K.; Miura, N.; Yamaki, J. Effect of Nano-Size LiCoO₂ Cathode Powders on Li-Ion Cells. *J. Power Sources* **2005**, *146*, 27.

(23) Zhang, H.; Yu, X.; Braun, P. V. Three-Dimensional Bicontinuous Ultrafast-Charge and -Discharge Bulk Battery Electrodes. *Nature Nanotech.* **2011**, *6*, 277.

(24) Wang, J.; Yang, J.; Tang, Y.; Liu, J.; Zhang, Y.; Liang, G.; Gauthier, M.; Chen-Wiegart, Y. K.; Banis, M. N.; Li, X.; *et al.* Size-Dependent Surface Phase Change of Lithium Iron Phosphate during Carbon Coating. *Nat. Commun.* **2014**, *5*, 3415.

(25) Zhang, L.; Wang, X.; Muta, T.; Li, D.; Noguchi, H.; Yoshio, M.; Ma, R.; Takada, K.; Sasaki, T. The Effects of Extra Li Content, Synthesis Method, Sintering Temperature on Synthesis and Electrochemistry of Layered LiNi_{1/3}Mn_{1/3}Co_{1/3}O₂. *J. Power Sources* **2006**, *162*, 629.

(26) He, Y.-S.; Ma, Z.-F.; Liao, X.-Z.; Jiang, Y. Synthesis and Characterization of Submicron-Sized LiNi_{1/3}Co_{1/3}Mn_{1/3}O₂ by a Simple Self-Propagating Solid-State Metathesis Method. *J. Power Sources* **2007**, *163*, 1053.

(27) Liu, J.; Qiu, W.; Yu, L.; Zhang, G.; Zhao, H.; Li, T. Studies on the Low-Heating Solid-State Reaction Method to Synthesize LiNi_{1/3}Co_{1/3}Mn_{1/3}O₂ Cathode Materials. *J. Power Sources* **2007**, *174*, 701.

(28) Sathiya, M.; Prakash, A. S.; Ramesha, K.; Shukla, A. K. Rapid Synthetic Routes to Prepare LiNi_{1/3}Mn_{1/3}Co_{1/3}O₂ as a High Voltage, High-Capacity Li-Ion Battery Cathode Material. *Mater. Res. Bull.* **2009**, *44*, 1990.

(29) Li, D.-C.; Muta, T.; Zhang, L.-Q.; Yoshio, M.; Noguchi, H. Effect of Synthesis Method on the Electrochemical Performance of LiNi_{1/3}Mn_{1/3}Co_{1/3}O₂. *J. Power Sources* **2004**, *132*, 150.

(30) Li, D.; Sasaki, Y.; Kobayakawa, K.; Noguchi, H.; Sato, Y. Preparation,

Morphology and Electrochemical Characteristics of $\text{LiNi}_{1/3}\text{Mn}_{1/3}\text{Co}_{1/3}\text{O}_2$ with LiF Addition. *Electrochim. Acta* **2006**, 52, 643.

(31) Kim, J.-M.; Kumagai, N.; Kadoma, Y.; Yashiro, H. Synthesis and Electrochemical Properties of Lithium Non-Stoichiometric $\text{Li}_{1+x}(\text{Ni}_{1/3}\text{Co}_{1/3}\text{Mn}_{1/3})\text{O}_{2+\delta}$ Prepared by a Spray Drying Method. *J. Power Sources* **2007**, 174, 473.

(32) Patoux, S.; Doeff, M. M. Direct Synthesis of $\text{LiNi}_{1/3}\text{Co}_{1/3}\text{Mn}_{1/3}\text{O}_2$ from Nitrate Precursors. *Electrochem. Commun.* **2004**, 6, 767.

(33) He, P.; Wang, H.; Qi, L.; Osaka, T. Electrochemical Characteristics of Layered $\text{LiNi}_{1/3}\text{Co}_{1/3}\text{Mn}_{1/3}\text{O}_2$ and with Different Synthesis Conditions. *J. Power Sources* **2006**, 160, 627.

(34) Huang, Y.-J.; Gao, D.-S.; Lei, G.-T.; Li, Z.-H.; Su, G.-Y. Synthesis and Characterization of $\text{Li}(\text{Ni}_{1/3}\text{Co}_{1/3}\text{Mn}_{1/3})_{0.96}\text{Si}_{0.04}\text{O}_{1.96}\text{F}_{0.04}$ as a Cathode Material for Lithium-Ion Battery. *Mater. Chem. Phys.* **2007**, 106, 354.

(35) Li, X. Characterizations on the Structural and Electrochemical Properties of $\text{LiNi}_{1/3}\text{Mn}_{1/3}\text{Co}_{1/3}\text{O}_2$ Prepared by a Wet-Chemical Process. *Solid State Ionics* **2008**, 178, 1969.

(36) Jiang, D.; Zhao, L.; Shao, Y.; Wang, D. Preparation and Characterization of Layered $\text{LiNi}_{0.9}\text{Co}_{0.05}\text{Mn}_{0.025}\text{Mg}_{0.025}\text{O}_2$ Cathode Material by a Sol-gel Method for Lithium-Ion Batteries. *RSC Adv.* **2015**, 5, 40779.

(37) Kang, K.; Ceder, G. Factors That Affect Li Mobility in Layered Lithium Transition Metal Oxides. *Phys. Rev. B* **2006**, 74, 94105.

(38) Yabuuchi, N.; Koyama, Y.; Nakayama, N.; Ohzuku, T. Solid-State Chemistry and Electrochemistry of $\text{LiCo}_{1/3}\text{Ni}_{1/3}\text{Mn}_{1/3}\text{O}_2$ for Advanced Lithium-Ion Batteries II. Preparation and Characterization. *J. Electrochem. Soc.* **2005**, 152, A1434.

(39) Lin, F.; Markus, I. M.; Nordlund, D.; Weng, T.-C.; Asta, M. D.; Xin, H. L.; Doeff, M. M. *Nat. Commun.* **2014**, 5, 3529.

(40) Schaffer, M.; Schaffer, B.; Ramasse, Q. *Ultramicroscopy* **2012**, *114*, 62.

(41) Tate, M. W.; Purohit, P.; Chamberlain, D.; Nguyen, K. X.; Hovden, R.; Chang, C. S.; Deb, P.; Turgut, E.; Heron, J. T.; Schlom, D. G.; Ralph, D. C.; Fuchs, G. D.; Shanks, K. S.; Philipp, H. T.; Muller, D. A.; Gruner, S. M. *Microsc. Microanal.* **2016**, *22 (1)*, 237.

CHAPTER 4

Ni-RICH $\text{LiNi}_{0.88}\text{Mn}_{0.06}\text{Co}_{0.06}\text{O}_2$ CATHODE INTERWOVEN BY CARBON FIBER WITH IMPROVED RATE CAPABILITY AND STABILITY¹

4.1 Introduction

The demand for high-energy and high-power lithium-ion batteries (LIBs) is increasing dramatically for large-scale applications including hybrid electric vehicles and electric vehicles.^{2,3} However, the limited rate capability and modest cycling life, as well as the high cost of electrode materials has suppressed the development of LIBs for these applications. In general, high-energy and high-power LIBs can be achieved by using high-capacity and high-rate electrode materials and by increasing the working voltage, respectively. Lithium cobalt oxide (LCO), the most widely employed cathode material in consumer electronics with a small practical capacity of ~150 mAh/g, is restricted by the high cost of cobalt, safety issues and toxicity.⁴ Among the commercially available candidate cathode materials for LIBs, Ni and Mn substituted compounds layered lithium nickel manganese cobalt oxides (NMC) have been widely explored since the introduction of Ohzuku's $\text{LiNi}_{0.33}\text{Mn}_{0.33}\text{Co}_{0.33}\text{O}_2$.^{5,6} However, the instability of delithiated Li_xNiO_2 and LiMnO_2 limits their usage in electric vehicles and hybrid electric vehicles applications. The electronic conductivity and structural stability of NMC compounds are lower than these of LCO, thereby adversely affecting rate capability and cycling performance, respectively.^{7,8} Different compounds with variations in the ratio of the three transition metals have been studied, but it still has not been possible to demonstrate stable high rates with conventional electrodes.⁹

The discharge capacity of NMC is determined by the Ni content, as Ni is the major redox species ($\text{Ni}^{2+}/\text{Ni}^{4+}$).^{10,11} Thus higher Ni content ($\text{Ni}>0.8$) in cathode active materials, can guarantee, a high specific capacity, and consequently a high energy

density. NMC cathode materials with greater Ni content ($\text{Ni} > 0.8$) have shown poor rate capability, poor cycling life and poor thermal stability due to structural instabilities.¹² Numerous efforts to enhance the conductivity of layered structures, that improve the rate performance, have been undertaken. Carbon coatings have been shown to be a successful pathway to enhance electronic conductivity.^{13–15} Some nanoscale materials have also been used to improve rate performance by shortening the lithium diffusion paths.¹⁶ However, unanticipated side reactions are caused by the high surface area of nanomaterials, then impaired cycle life.¹⁷ Surface coatings with stable transition metal oxides have been employed to protect the surface resulting in a longer cycle performance.^{18–20} However, the electronic conductivity may be reduced if the coating is insulating. In an effort to overcome the issues of high capacity Ni-rich cathode, but maintain their excellent rate capability and long cycle life, rational design strategies are urgently needed. To our knowledge there is no prior literature of a simple application of bulk carbon fibers on high Ni content NMC cathodes, not on studies of how the composite affects the power, energy, and cycling performance.

Herein, for the first time, cathode composite of $\text{LiNi}_{0.88}\text{Mn}_{0.06}\text{Co}_{0.06}\text{O}_2$ interwoven in a carbon fiber network were prepared by a simple treatment. For comparison, pristine $\text{LiNi}_{0.88}\text{Mn}_{0.06}\text{Co}_{0.06}\text{O}_2$ particles were also synthesized by a co-precipitation method. We found that the carbon fiber decorated $\text{LiNi}_{0.88}\text{Mn}_{0.06}\text{Co}_{0.06}\text{O}_2$ composites displayed higher capacity retention, better rate capability and more stable cyclic performance when compared to the pristine counterpart. The results not only provide further insight into the reaction mechanism, but also a rational direction to synthesize high performance cathode materials for Li-ion batteries.

4.2 Experimental Section

Sample preparation The $\text{Ni}_{0.88}\text{Mn}_{0.06}\text{Co}_{0.06}(\text{OH})_2$ precursor was synthesized by a coprecipitation of $\text{NiSO}_4 \cdot 6\text{H}_2\text{O}$, $\text{CoSO}_4 \cdot 7\text{H}_2\text{O}$ and $\text{MnSO}_4 \cdot \text{H}_2\text{O}$ as starting materials, dissolved in distilled water in molar ratios of Ni: Co: Mn = 44:3:3. A 1.5 M aqueous solution of the transition metal sulfates was slowly pumped into a continuously stirred tank reactor. Concomitantly, a 4 M NaOH solution (aq) and a 2.5 M NH_4OH solution (aq) were also separately pumped into the reactor. After reaction, the precipitate was filtered and washed several times with water to remove residual ions (Na^+ , SO_4^{2-} or other ions). The precipitate was then dried at 100 °C overnight. The resulting hydroxide precursor $\text{Ni}_{0.88}\text{Mn}_{0.06}\text{Co}_{0.06}(\text{OH})_2$ was mixed with $\text{LiOH} \cdot \text{H}_2\text{O}$ and calcined at 700 °C for 15 h in oxygen to obtain the pristine $\text{LiNi}_{0.88}\text{Mn}_{0.06}\text{Co}_{0.06}\text{O}_2$ (pristine NMC) cathode material.

Pristine NMC interwoven with carbon fibers was achieved as follows. First, 0.5 g of carbon fibers were added to 50 mL of isopropanol with stirring for 15 min. Then 9.5 g of the pristine NMC powders were dispersed in the solution, with stirring, for 1 h under a nitrogen atmosphere. After removing the solvent by filtration, the materials were dried at 80 °C in a vacuum oven for 12 h and then heated at 200 °C for 3 h in a furnace under a nitrogen atmosphere, to obtain the carbon fiber interwoven NMC (CF-NMC) composite.

Sample characterization X-ray diffraction patterns were obtained on a Rigaku Ultima VI powder X-ray diffractometer with Cu K radiation ($K\alpha_1$, $\lambda = 1.5406 \text{ \AA}$ and $K\alpha_2$, $\lambda = 1.5444 \text{ \AA}$). Diffraction patterns were collected at a scanning rate of 2 °/min, and with a step of 0.02 °. Particle size and size distribution were measured using a Bettersize BT-9300ST Laser Particle Size Analyzer. SEM was performed with a LEO-

1550 field emission SEM (FSEM). FEI Strata 400 Focused Ion Beam (FIB) was used to mill the spherical NMC particles into a 1 μm cross section at a milling voltage of 30keV. The NMC spherical particles were mounted on Cu TEM grids by Pt deposition. The final ultrathin cross-sectional TEM specimens (< 20 nm) were prepared with a final milling step of 2 keV to minimize surface damage. X-ray energy dispersive spectroscopy (XEDS) elemental mapping was performed using an Oxford X-Max detector. High-resolution STEM images were acquired on a fifth-order aberration-corrected FEI Titan Themis STEM operated at 300 keV.

Electrochemical tests Electrochemical measurements were carried out in CR 2032 coin cells assembled in an argon filled glove box (residual water and oxygen were 0.1 ppm and 0.1 ppm, respectively) with lithium metal as the anode. The working cathode was fabricated with 90 wt% active material, 5 wt% super P carbon, and 5 wt% poly(vinylidene fluoride) (PVDF) as binder. For the CF-NMC composite, the mass percentage of carbon fibers was included in the 5% carbon source. The resulting slurry was coated onto an Al foil current collector. The coated electrode was dried for 12 h at 110 $^{\circ}\text{C}$ in a vacuum oven. The typical mass loading of the active material was 2.0 mg/cm^2 . The counter electrode was Li metal. The two electrodes were separated by a polypropylene separator (Celgard 3501). The electrolyte was 1.2 M LiPF_6 in a 3:7 ratio of EC (ethylene carbonate) to EMC (ethyl methyl carbonate). Galvanostatic charge/discharge of the coin cells was carried out using an Arbin BT-2000 battery tester with a constant discharge/charge current rate of 0.1 C and a voltage range of 2.8 to 4.3 V vs. Li/Li^+ at room temperature. Every experiment was carried out in triplicate (three parallel trials), and the error bar of the measured capacities, among the three trials, was less than 0.25%. We report the measured capacities rounded to the last integral digit; in which case, all results were identical. Thus we do not include error

bars in these cases.

4.3 Results and Discussion

Figure 4.1a presents the XRD patterns of our pristine NMC and the composite CF-NMC cathode materials. The sample yielded a well-defined and impurity-free single phase, and the reflections matched the reference on the basis of a hexagonal α -NaFeO₂ type structure (space group R-3mH)²¹. In addition, a split between the (006)/(102) and (108)/(110) peaks, respectively, was clearly observed, indicating that the structure had good layering.²² The particle size distribution (see Figure 4.1b), expressed in span, defined as (D90-D10)/D50, where D50 indicates a particle diameter that is larger than 50% of the total particle (often denoted as the medium number), while D90 and D10 refer to particle diameters that are larger than ninety and ten percentile of the total particles, respectively. The pristine NMC particle size (D50) was 11.69 μm with a span of 0.62. The pristine NMC materials had an advantageously narrow span, which is likely to result in greater capacity at high current rates. Figure 4.1c presents SEM images of the particle of the prepared pristine NMC material. Pursuant to the well-controlled synthesis process, the particles have an average size of about 12 μm , which is consistent with the D50 value. Figure 1d shows that the CF-NMC material is well embedded in the carbon fiber, which serve as a highly efficient conductive network and facilitates the lithiation/delithiation processes of NMC.

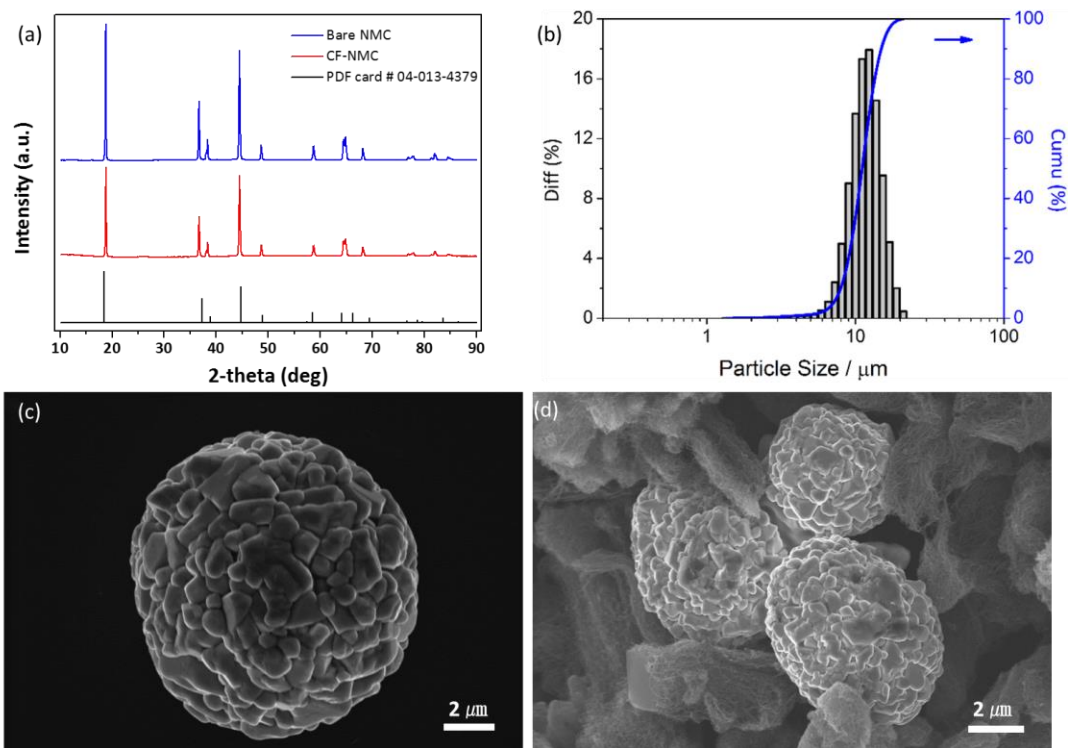


Figure 4.1 (a) XRD patterns of pristine NMC and CF-NMC composite, compared to the reference XRD of $\text{LiNi}_{0.33}\text{Mn}_{0.33}\text{Co}_{0.33}\text{O}_2$. (b) Particle Size Distribution of pristine NMC. (c) SEM image of pristine NMC. (d) SEM image of CF-NMC.

To better understand the microstructure of our NMC material, we employed a focused ion beam (FIB) to mill a spherical NMC particle into a thin cross section (Figure 4.2). Figure 4.2a show a NMC lamella, with a thickness of 1 μm, and a dense internal microstructure with multiple crystal grains and several small pores. This structure could generate from the fact that the crystal seeds grew along with some stacking pores at the beginning of the co-precipitation process of the transition metal hydroxide. The distribution of Ni, Mn and Co in the particle (Figures 4.2b-d) was examined by X-ray energy dispersive spectroscopy (XEDS). Compared with regular NMC spherical particles, XEDS mapping of NMC lamella could reveal both inner and outer elemental

distributions. The intensity maps of the Ni, Mn, and Co K α signals matched each other, suggesting that the distribution of Ni, Mn and Co (Figures 4.2b-d) is uniform throughout the material, confirming the successful chemical synthesis of homogenous NMC particles. The X-ray spectrum associated with the maps is shown in Figure 4.3. The atomic ratios of Ni: Mn: Co were calculated from the metal K α peaks to be 17.6:1:1, which is consistent with ICP elemental analysis (Ni: Mn: Co =88:6:6) in Table 4.1.

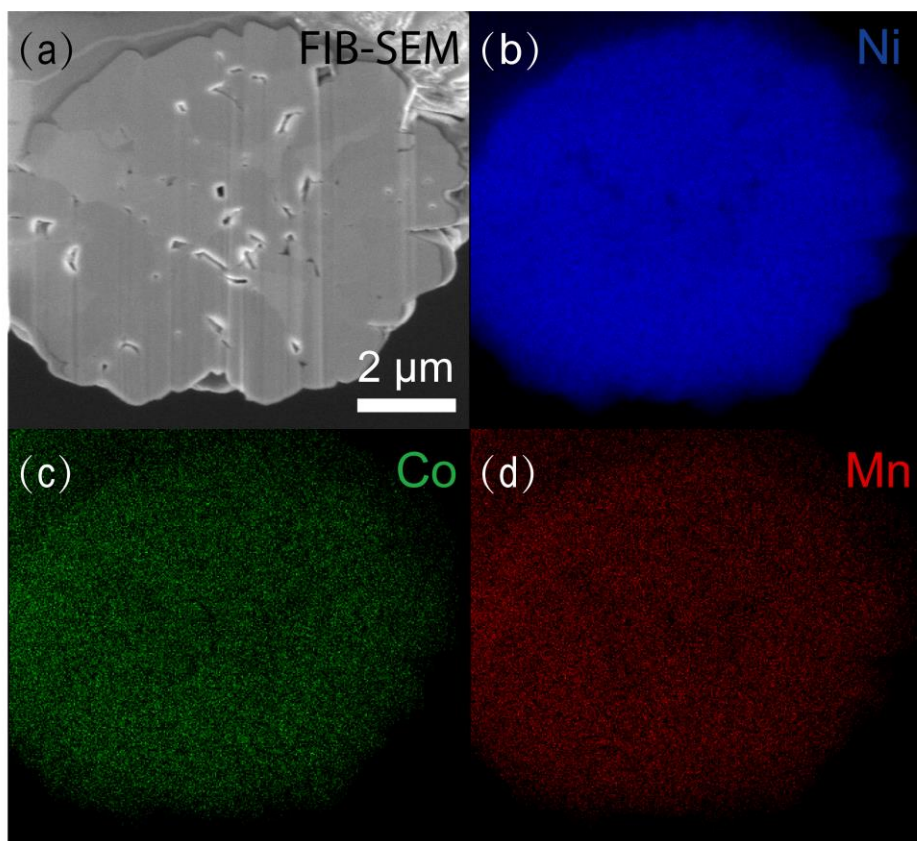


Figure 4.2 (a) SEM image of a NMC cross section with a thickness of 1 μm made by FIB. (b, c, d): XEDS elemental mapping of Ni (b), Co (c), Mn (d), respectively for the NMC lamella in (a).

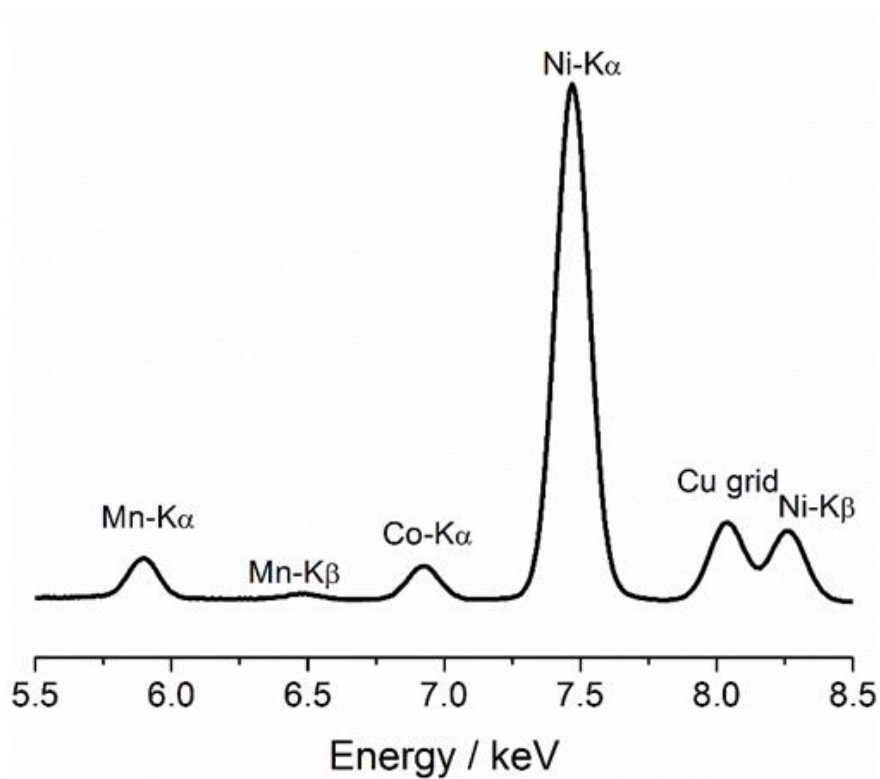


Figure 4.3 XEDS spectrum corresponding to the XEDS elemental mapping in Figure 4.2. The intensities of the Mn, Co, and Ni $K\alpha$ peaks are consistent with the Ni-rich component shown by ICP-AES analysis.

Table 4.1 ICP-AES results of pristine NMC material.

Element	Molar percentage in (Ni+Mn+Co) (%)
Ni 231.604	88.12
Mn 294.921	6.02
Co 228.616	5.86

The 1 μm NMC lamella was then milled to an ultrathin NMC cross section (< 20 nm) and used for acquiring atomic-scale STEM images. As shown in Figures 4.4a-b, the high-angle annular dark-field (HAADF) STEM image and its Fast Fourier Transform (FFT) clearly show a layered structure of transition metals in NMC at the atomic-scale. (003) and (101) planes were observed in two directions with an angle of 79.5° on the [010] zone axis, which is very consistent with the hexagonal $\alpha\text{-NaFeO}_2$ type structure.²¹ The (003) plane had a d-spacing of 4.8 Å, nearly same as that of reference NMC-111 (4.74 Å) whereas (101) has a d-spacing of 2.6 Å, slightly larger than that of the reference NMC-111 (2.44 Å). This (101) lattice expansion is likely due to the high Ni content and consistent with the left shift of (101) facet in the powder XRD pattern (Figure 4.1a). CrystalMaker software was used to construct the corresponding crystal model from the XRD data of a NMC-111 reference (Figure 4.4c) which shows the projection of the transition metals layers in the [010] direction and is consistent with the layered structure in the STEM image.

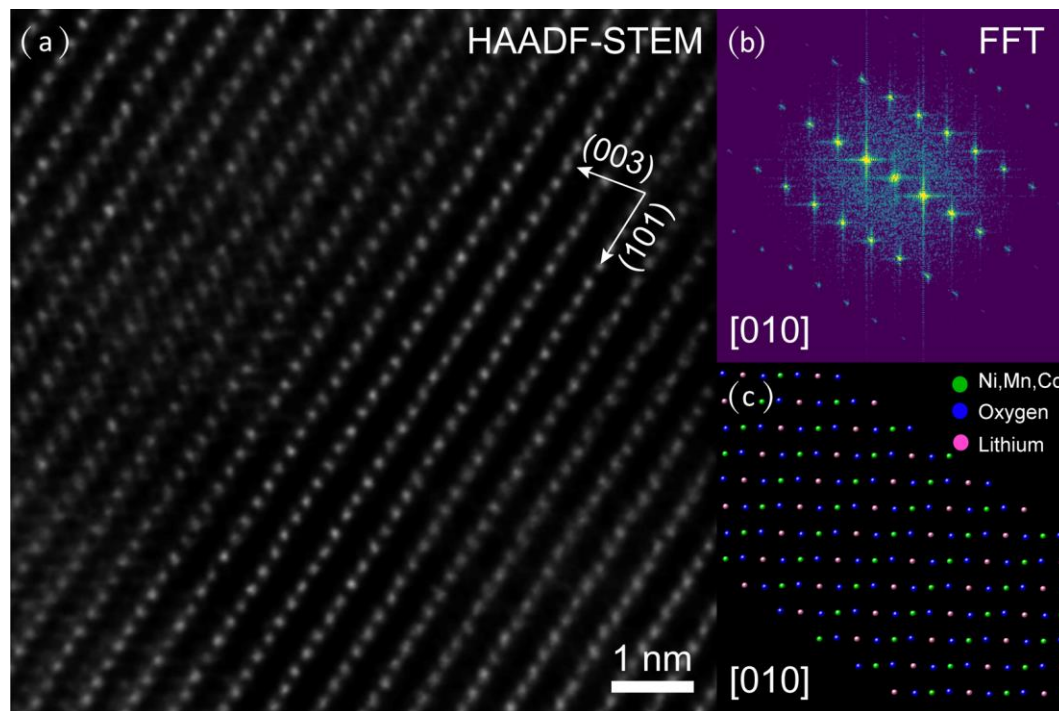


Figure 4.4 (a-b) HAADF-STEM image and the FFT of an ultrathin NMC cross section showing atom columns with (003) and (101) d-spacings with an angle of 79.5° on the [010] zone axis. (c) The corresponding crystal model shows the projection of layered structure of transition metals in the [010] direction of a hexagonal crystal structure.

The electrochemical evaluation of pristine NMC and CF-NMC materials was carried out in 2032 coin cells, which were carried out using pristine NMC and CF-NMC as cathodes, respectively, and Li metal as an anode. Figure 4.5a presents the initial charge/discharge curves at 0.2 C for the two cathode materials over the voltage range of 2.8 and 4.3 V. CF-NMC delivered a virtually identical discharge capacity (210 mAh/g vs. 212 mAh/g) and a slightly better first cycle coulombic efficiency (90.1 % vs. 89.8 %) when compared to pristine NMC cathode. To investigate the discharge

rate capability at various currents, the cells were always charged at 0.5 C first, and subsequently discharged at different rates. Figure 4.5b exhibits the capacity retentions as a function of discharge rates from 0.2 C to 20 C between 2.8 and 4.3 V. Similar discharge capacities were observed at lower rate for both samples, but clear capacity differences were evident with increasing discharging rate with CF-NMC consistently outperforming the pristine NMC materials.

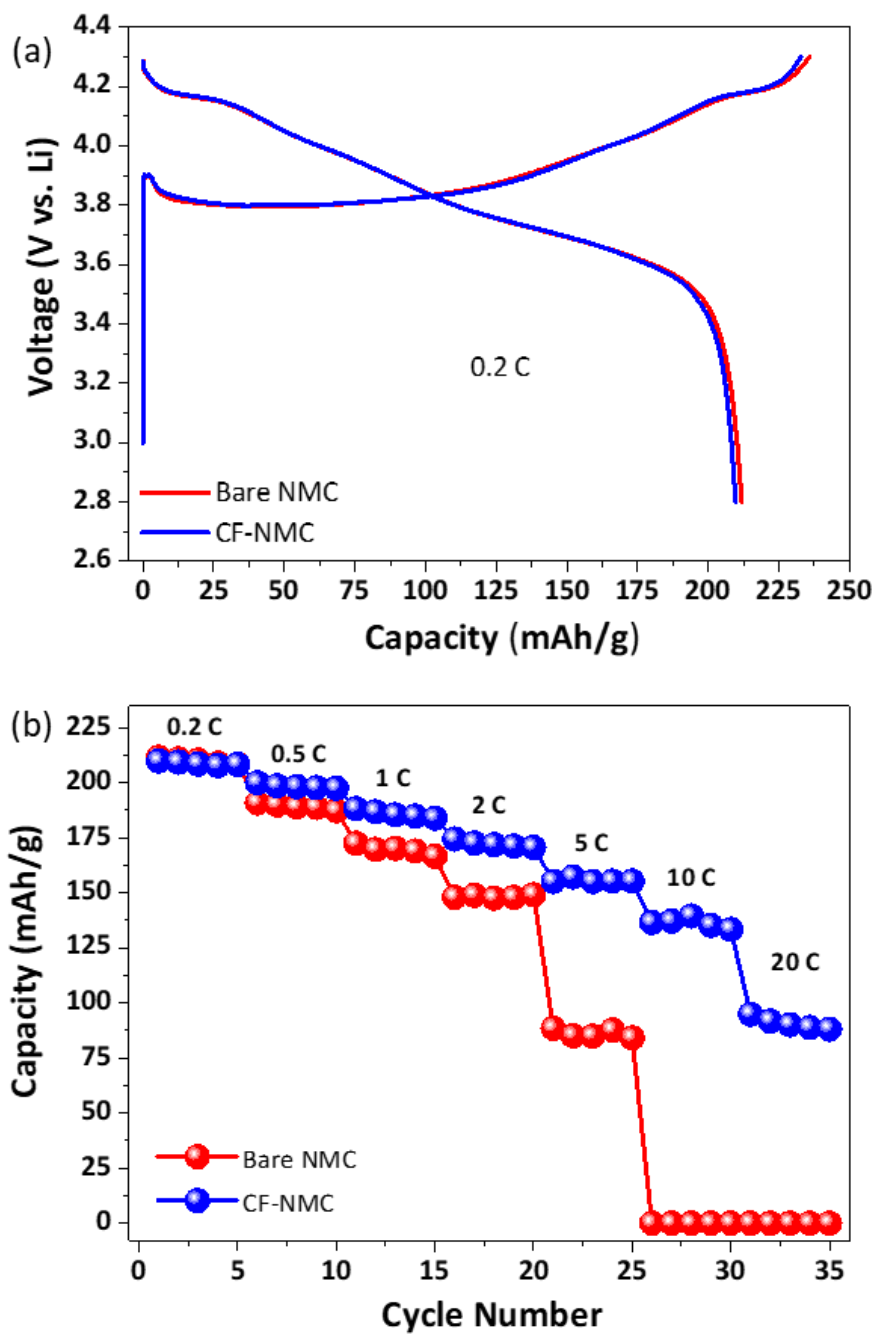


Figure 4.5 (a) Initial charge–discharge curves of CF-NMC and pristine NMC cells at 0.2 C between 2.8 and 4.3 V. (b) Rate performances of CF-NMC and pristine NMC cells from 0.1 C to 20 C.

Figures 4.6a-b present the discharge profiles at different current rates for CF-NMC and pristine NMC materials, respectively. While similar capacities are observed at the lower rates for both materials, clear capacity differences became evident at higher rates, and these differences increased with increasing rate. The CF-NMC cathode material exhibited a stable high capacity at both low and high current rates, while the pristine NMC cathode material exhibited a rapid decay in capacity with increasing current rate. Remarkably, the CF-NMC materials retained capacities of 155 at a C-rate of 5 C. In comparison, the pristine material only delivered a discharge capacity of 89 mAh/g at 5 C. To our surprise, the CF-NMC cathode still had a capacity of 137 mAh/g and 95 mAh/g at the ultrahigh C-rates of 10 and 20 C, respectively, while the pristine NMC cathode had lost all of its capacity. It is notable that the CF-NMC material delivered an exceptionally better capacity retention than the pristine material, especially at high current rates. Such behavior might be related to the faster ionic and/or electronic diffusion, and shorter migration paths at high rates, which were benefited from the network structures.

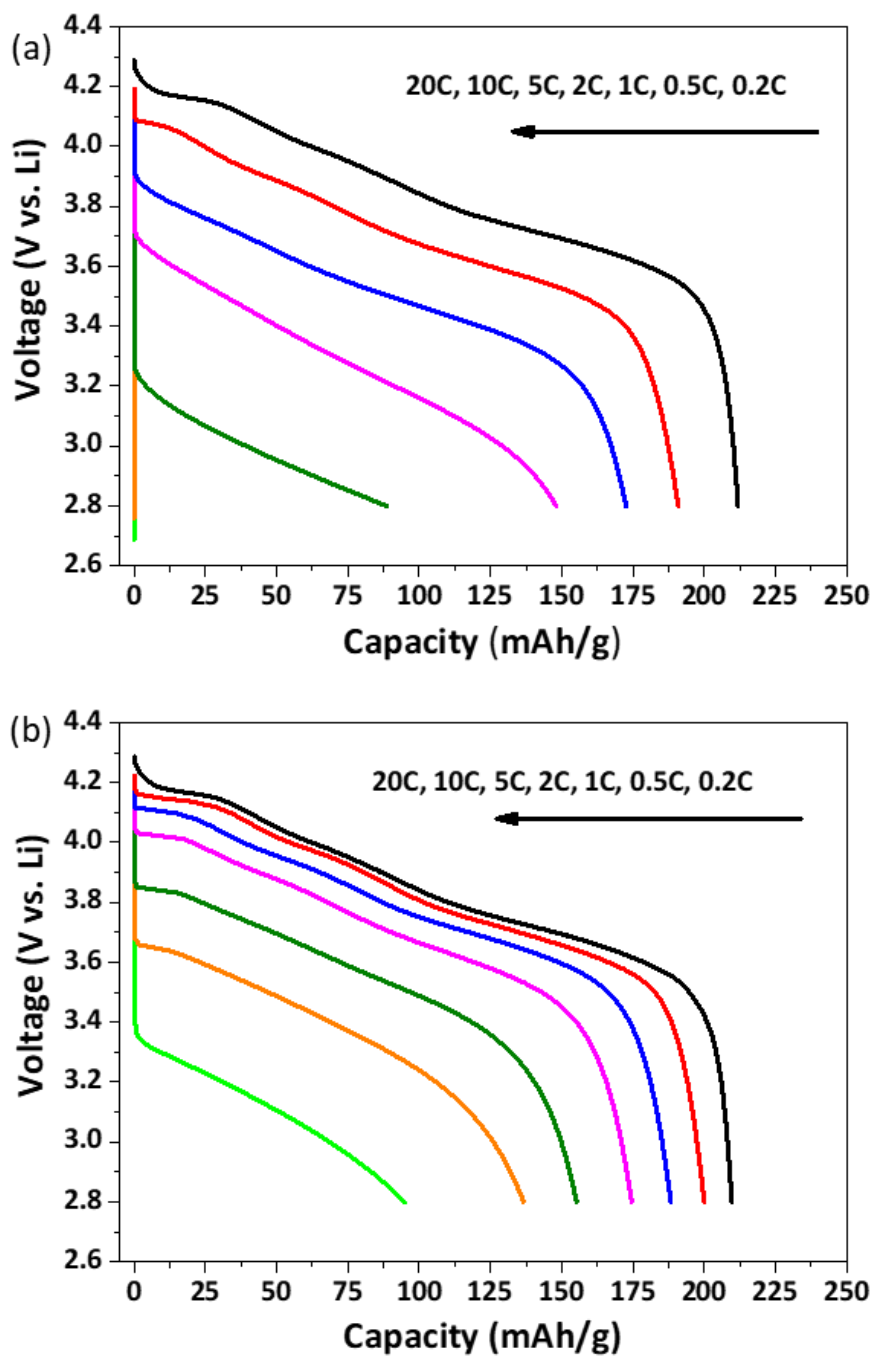


Figure 4.6 (a) Discharge curves of the pristine NMC cell from 0.1 C to 20 C. (b) Discharge curves of the CF-NMC cell from 0.1 C to 20 C.

Cyclic voltammetry (CV) of coin cells using CF-NMC as a cathode material in lithium half-cells was performed and insights of structural dynamics of the CF-NMC were suggested from the electrochemical behavior. Figure 4.7a presents a CV of a coin cell with CF-NMC as a cathode cycled from 2.8 to 4.3 V at 0.1 mV/s. Three redox couples conferred at 3.75, 3.99 and 4.17 V can be clearly be observed. Such redox behavior is characteristic of phase transitions, which have been extensively studied in LiNiO_2 ²³ and $\text{LiNi}_{1-x}\text{Co}_x\text{O}_2$ ($x = 0-0.3$).^{24,25} These redox couples indicate a series of phase transitions of CF-NMC from hexagonal (H_1) to monoclinic (M_1), monoclinic (M_1) to hexagonal (H_2) and hexagonal (H_2) to hexagonal (H_3), as the cell is charged from 2.8 to 4.3 V.²³ As shown in these studies and in this material, higher Ni content is associated with more evident phase transitions in both CV and charge/discharge curves, indicating that such structural transitions are dominated by a LiNiO_2 layered structure.

CVs at different scan rates were compared with and without the use of carbon fiber as the conducting additive. From 0.1 mV/s to 1.9 mV/s, the pristine NMC (Figure 4.7b) exhibited higher internal resistance when compare to the CF-NMC (Figure 4.7c), as indicated by the large slanting in the onset of oxidation in Figure 4.7b. As the scan rate increased, the carbon fiber could capture the phase transitions up to ca. 1.1 mV/s, while with super P, the transitions were barely visible at even the slowest scan rate, indicating superior electronic conductivity by the use of a carbon fiber conductive network.

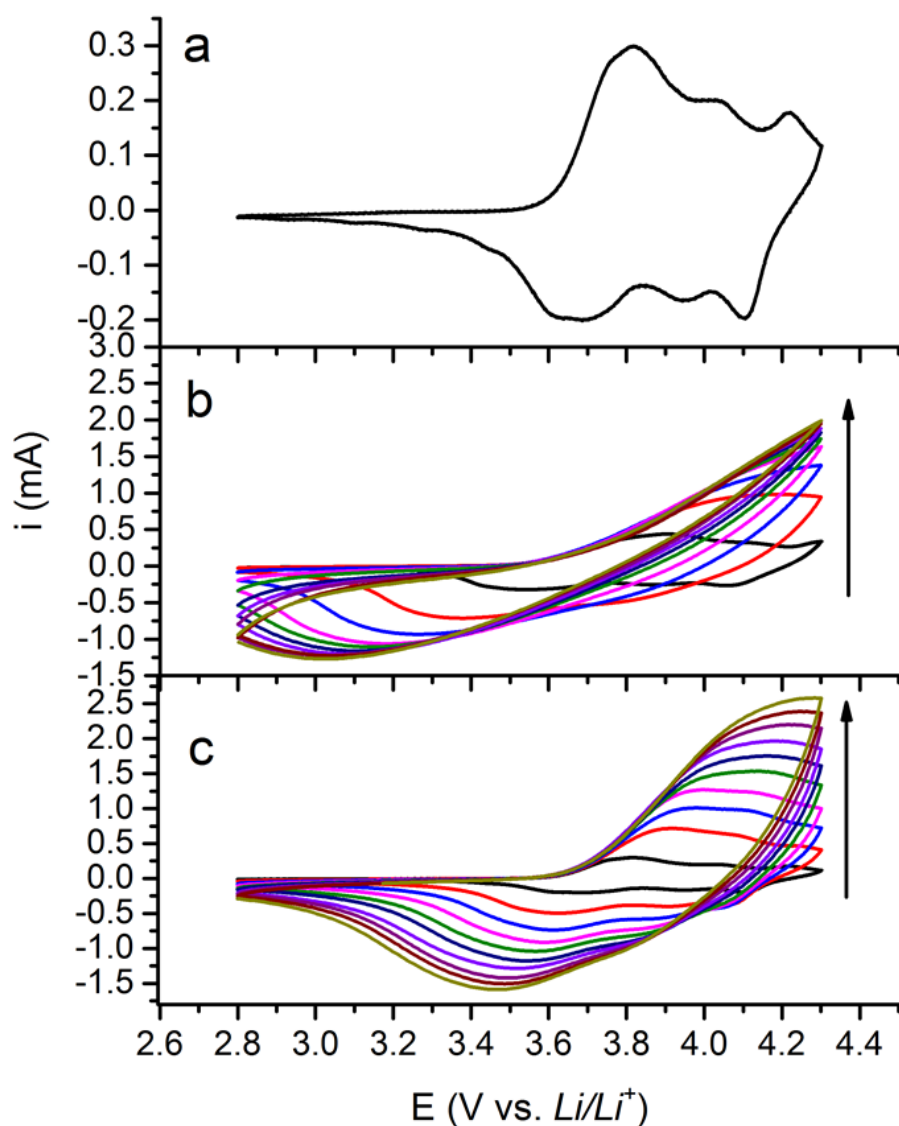


Figure 4.7 (a) CV of a lithium half cell using CF-NMC as cathode. I at 0.1 mV/s. CV of a lithium half cell using (b) pristine NMC and (c) CF-NMC as cathode, arrows indicate increasing scan rates of 0.1, 0.3, 0.5, 0.7, 0.9, 1.1, 1.3, 1.5, 1.7 and 1.9 mV/s.

The cycling performances of the CF-NMC cathode and the pristine NMC cathode are presented in Figure 4.8a. The cells were charge-discharge cycled at 25 °C over the voltage range of 2.8 and 4.3 V at 0.5 C. The first discharge capacities of the CF-NMC material and the pristine NMC material were 200 and 191 mAh/g, respectively. The

capacity retention of the CF-NMC material was 67.3% after 150 cycles, which is higher than that of the pristine NMC material (55.0% after 150 cycles). The cycling performances of the CF-NMC cathode and the pristine NMC cathodes at 50 °C were also studied. In Figure 4.8b the variation of the discharge capacity vs. cycle number is presented. It is clear that the capacity fade of electrodes containing the CF-NMC material (30.0% capacity loss after 100 cycles) is much less pronounced than that of electrodes comprising the pristine NMC cathode material (71.5% capacity loss after 100 cycles). The better cycling stability and capacity retention of the CF-NMC materials may be attributed at least in part to the synergistic effect of the larger specific surface area and the protection by the carbon fiber coating. Compared with the pristine samples, the larger specific surface area of carbon fibers provides more conductive paths for ions and/or electrons, and the carbon coating layer simultaneously prevents the inner oxide from reacting with HF in the electrolyte and mitigate agglomeration during electrochemical testing.

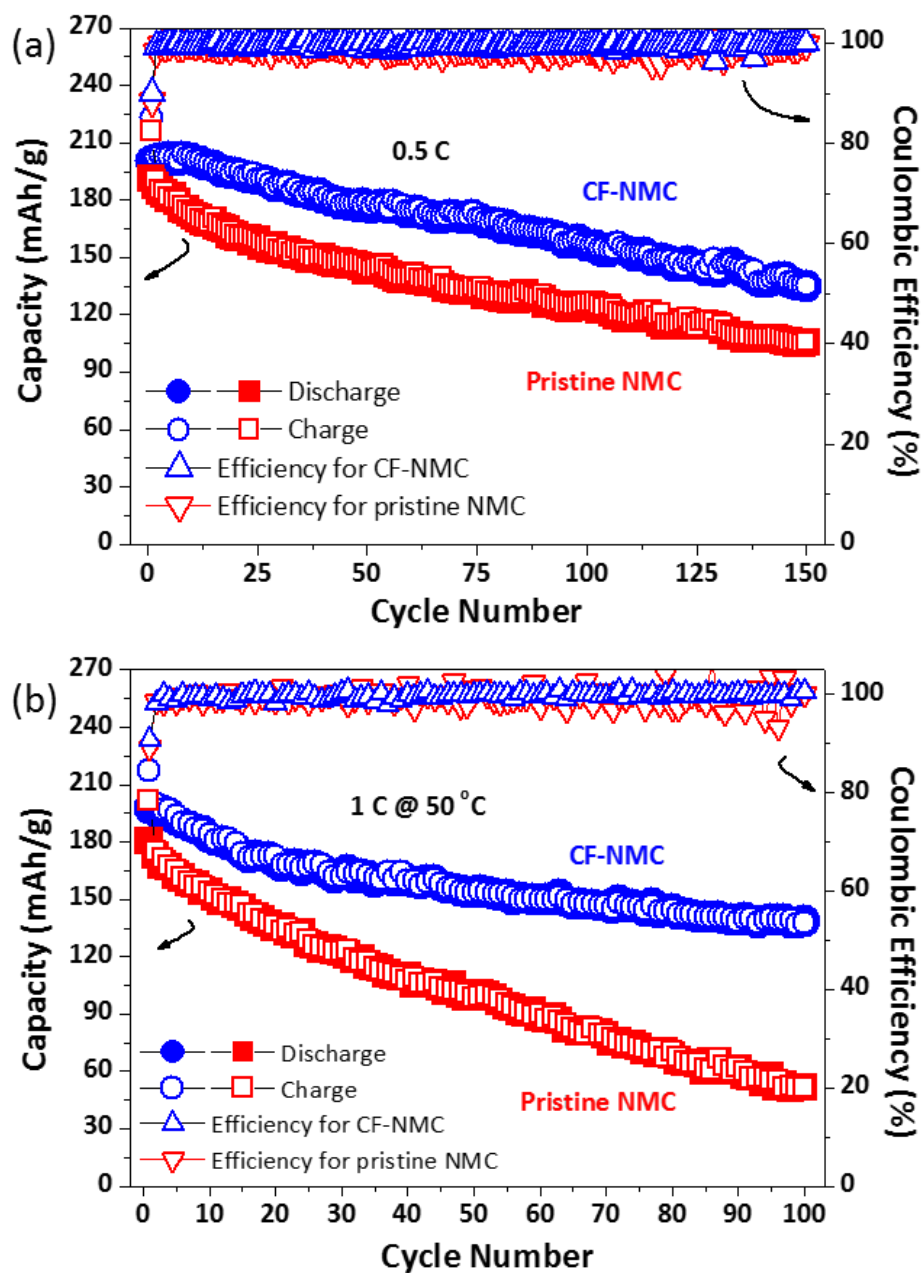


Figure 4.8 (a) Cycling performance of CF-NMC and pristine NMC cells, up to 150 cycles between 2.8 and 4.3 V at 0.5 C at room temperature (25 °C). (b) Cycling performance of the CF-NMC and the pristine NMC cells at 50 °C.

4.4 Conclusions

In summary, we have successfully developed a carbon fiber interwoven $\text{LiNi}_{0.88}\text{Mn}_{0.06}\text{Co}_{0.06}\text{O}_2$ cathode material with enhanced rate capability and stability. The particles exhibited a spherical morphology and uniform size distribution, with a well-defined crystal structure and homogeneous transition metal distribution. The CF-NMC material exhibited superior electrochemical performance when compared with the pristine sample, with an exceptional rate capability of 137 mAh/g and 95 mAh/g at 10 C and 20 C, respectively. The CF-NMC material also exhibited an improved cycling performance when compared to the pristine sample, under both room temperature and high temperature operation. The exceptionally high rate performance is most likely attributable to the faster ionic/electronic diffusion and shorter migration paths at high rate, which benefited from the carbon fiber network structure. We feel confident that the remarkable overall performances presented here comprehensively demonstrate that our CF-NMC cathode material is practical and ready to use in plug-in hybrid electric vehicles and electric vehicles applications which demand high power, low cost, and long cycling performance especially at high operating temperatures and current rates.

REFERENCE

- (1) Reprinted with permission from the submitted manuscript.
- (2) Etacheri, V.; Marom, R.; Elazari, R.; Salitra, G.; Aurbach, D. *Energy Environ. Sci.* **2011**, *4* (9), 3243.
- (3) Scrosati, B.; Garche, J. *Journal of Power Sources* **2010**, *195* (9), 2419–2430.
- (4) Ju, S. H.; Kang, I.-S.; Lee, Y.-S.; Shin, W.-K.; Kim, S.; Shin, K.; Kim, D.-W. *ACS Appl. Mater. Interfaces* **2014**, *6* (4), 2546.
- (5) Ohzuku, T.; Makimura, Y. *Chem. Lett.* **2001**, *30* (8), 744.
- (6) Ohzuku, T.; Makimura, Y. *Chem. Lett.* **2001**, *30* (7), 642.
- (7) MacNeil, D. D.; Lu, Z.; Dahn, J. R. *J. Electrochem. Soc.* **2002**, *149* (10), A1332.
- (8) Jouanneau, S.; MacNeil, D. D.; Lu, Z.; Beattie, S. D.; Murphy, G.; Dahn, J. R. *J. Electrochem. Soc.* **2003**, *150* (10), A1299.
- (9) Ngala, J. K.; Chernova, N. A.; Ma, M.; Mamak, M.; Zavalij, P. Y.; Whittingham, M. S. *J. Mater. Chem.* **2004**, *14* (2), 214.
- (10) Yoon, S.-J.; Myung, S.-T.; Sun, Y.-K. *J. Electrochem. Soc.* **2014**, *161* (10), A1514.
- (11) Ren, D.; Shen, Y.; Yang, Y.; Shen, L.; Levin, B. D. A.; Yu, Y.; Muller, D. A.; Abruña, H. D. *ACS Appl. Mater. Interfaces* **2017**, *9* (41), 35811.
- (12) Noh, H.-J.; Youn, S.; Yoon, C. S.; Sun, Y.-K. *Journal of Power Sources* **2013**, *233*, 121.
- (13) Ban, C.; Chernova, N. A.; Whittingham, M. S. *Electrochemistry Communications* **2009**, *11* (3), 522.
- (14) Liu, J.; Wang, Q.; Reeja-Jayan, B.; Manthiram, A. *Electrochemistry Communications* **2010**, *12* (6), 750.
- (15) Chen, Z.; Dahn, J. R. *J. Electrochem. Soc.* **2002**, *149* (9), A1184.

- (16) Jamnik, J.; Maier, J. *Physical Chemistry Chemical Physics* **2003**, *5* (23), 5215.
- (17) Aricò, A. S.; Bruce, P.; Scrosati, B.; Tarascon, J.-M.; Schalkwijk, W. van. *Nature Materials* **2005**, *4* (5), 366.
- (18) Riley, L. A.; Van Atta, S.; Cavanagh, A. S.; Yan, Y.; George, S. M.; Liu, P.; Dillon, A. C.; Lee, S.-H. *Journal of Power Sources* **2011**, *196* (6), 3317.
- (19) Myung, S.-T.; Izumi, K.; Komaba, S.; Yashiro, H.; Bang, H. J.; Sun, Y.-K.; Kumagai, N. *The Journal of Physical Chemistry C* **2007**, *111* (10), 4061.
- (20) Kong, J.-Z.; Ren, C.; Tai, G.-A.; Zhang, X.; Li, A.-D.; Wu, D.; Li, H.; Zhou, F. *Journal of Power Sources* **2014**, *266*, 433.
- (21) Yin, S.-C.; Rho, Y.-H.; Swainson, I.; Nazar, L. F. *Chem. Mater.* **2006**, *18* (7), 1901.
- (22) Rougier, A.; Gravereau, P.; Delmas, C. *J. Electrochem. Soc.* **1996**, *143* (4), 1168.
- (23) Li, W.; Reimers, J.N.; Dahn, J.R. *Solid State Ionics* **1993**, *67* (1–2), 123.
- (24) Cho, J.; Jung, H.; Park, Y.; Kim, G.; Lim, H. S. *J. Electrochem. Soc.* **2000**, *147* (1), 15.
- (25) Cho, J.; Kim, T.-J.; Kim, Y. J.; Park, B. *Electrochem. Solid-State Lett.* **2001**, *4* (10), A159.

CHAPTER 5

HIGH RATE ELECTROCHEMICAL PERFORMANCE OF PHENOTHIAZINE-BASED POLYMER CATHODE MATERIALS FOR LITHIUM-ION BATTERIES¹

5.1 Introduction

Organic and polymeric materials have been shown to be excellent candidates for next generation electrode materials in high-energy and high-power electrochemical energy storage applications, namely lithium-ion batteries.²⁻⁴ Organic materials that incorporate carbonyl-centered redox-active functionalities within covalent-organic frameworks (COFs)⁵ or conjugated backbones⁶⁻⁸ have yielded some of the highest capacities with stable cycling performance. Nonetheless, the crystalline nature of COFs hinders ion diffusion, limiting the material's power density.⁹⁻¹¹ Furthermore, the relatively negative reduction potentials of conjugated carbonyl motifs results in low working voltages.¹²⁻¹⁴ Amorphous polymers, incorporating redox active functionalities with high positive oxidation potentials, can improve upon current organic cathode candidates. Herein, we present a redox-active polymer with high operating voltages and unprecedented power densities.

5.2 Experimental Section

Electrochemical Tests Electrochemical measurements were carried out in CR 2032 coin cells assembled in an argon filled glove box (residual water and oxygen were 0.1 ppm and 0.1 ppm, respectively) with lithium metal as the anode. The working cathode was fabricated with 30 wt% active material, 60 wt% Super P carbon, and 10 wt% poly(vinylidene fluoride) (PVDF) as binder. A high loading cathode was fabricated with 75 wt% active material, 15 wt% Super P carbon, and 10 wt% poly(vinylidene fluoride) (PVDF) as binder. The resulting slurry was coated onto a carbon paper

current collector. The coated electrode was dried for 12 h at 100 °C in a vacuum oven. The counter electrode was Li metal. The two electrodes were separated by a polypropylene separator (Celgard 2300). The electrolyte was 1.0 M LiPF₆ in a 1:1 ratio of EC (ethylene carbonate) to DEC (diethyl carbonate). Galvanostatic charge/discharge of the coin cells was carried out using an Arbin BT-2000 battery tester with a constant charge-discharge current rate and a voltage range of 2.8 to 4.3 V vs. Li/Li⁺ at 25 °C.

Electrochemical Impedance Spectroscopy (EIS) Electrochemical impedance spectroscopy measurements using a Solartron 1280-B potentiostat, were performed on a lithium coin cell with PT-DMPD (10% cross linking) as cathode. Impedance measurements were taken at 3.1, 3.3, 3.6, 3.9 and 4.1 V vs. Li/Li⁺ after 3600 s of pretreatment at the respective potentials from 0.001 - 20000 Hz. AC amplitude of the measurements were 10 mV.

Slurry Preparation 2.0 mg of bulk polymer, 2.5 mg of carbon black and 0.5 mg of PVDF were mixed in a 5 mL vial with 1 mL N-Methyl-2-pyrrolidone. Such a composition yields a composite loading of 5 mg/mL. The mixture was sonicated for 1 h until the mixture was homogeneously dispersed in solvent. 10 µL of the ink were drop-casted onto the GC surface to create a polymer loading of 0.28 mg/cm². Even though the powdered polymers were insoluble in conventional organic solvents, when oxidized the polymers become slightly soluble in EC/DEC, as the slurry on the GC dissolved as the materials became oxidized. Since materials were lost during cycling, scan rate dependence and other quantitative analysis were not performed on CVs obtained from slurries.

5.3 Results and Discussion

In design, we sought to incorporate small molecules capable of multiple reversible oxidations at high potentials relative to Li/Li⁺. Specifically, three small molecules that exhibit oxidations at potentials greater than 3.3 V vs Li/Li⁺ garnered our attention: N-methyl phenothiazine (1), N, N, N', N'-tetramethyl-p-phenylenediamine (2), and N, N, N', N'-tetramethylbenzidine (3). Of these, the latter two exhibit two reversible oxidations to the quinoidal dication. We hypothesized that copolymerization of N-methylphenothiazine with either N, N'-dimethylphenylene diamine or N, N'-dimethylbenzidine would result in polymers exhibiting three reversible oxidation processes (Figure 5.1). All species generated through oxidation would be stabilized through resonance within the electron-rich polymer backbone. Moreover, implanting redox activity within the polymer main chain would eliminate any insulating polymeric backbone, which we anticipate would result in lowered ohmic resistance and high theoretical capacities (due to lower mass per electron transferred).

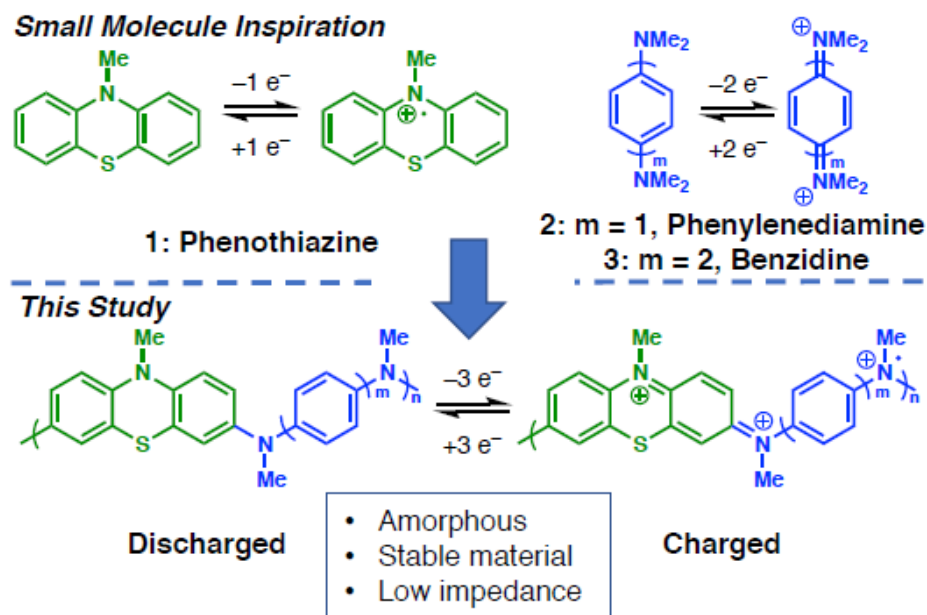


Figure 5.1 Small molecule inspiration and material design.

Poly(N-methylphenothiazine dimethylphenylenediamine) (PT-DMPD) and poly(N-methylphenothiazine benzidine) (PT-BZ) were synthesized from inexpensive starting materials using Buchwald-Hartwig cross-coupling of 3,7-dibromo-N-methylphenothiazine (1a) and dimethylphenylenediamine (2a) or dimethylbenzidine (3a) (Figure 5.2a).^{15,16} The resulting linear polymers were insoluble in their neutral state, and their electrochemical properties were probed using cyclic voltammetry (CV), measured as slurries in a solution of LiPF₆ (1M) in ethylene carbonate/diethyl carbonate (EC/DEC). The neutral and oxidized redox states of PT-DMPD are displayed in Figure 5.2b. The three discrete redox couples of each polymer were observed by CV (Figure 5.2c), occurring at 3.3, 3.6, and 4.3 V vs Li/Li⁺. These redox couples are among the highest, in organic electrodes, reported for electrical energy storage applications.

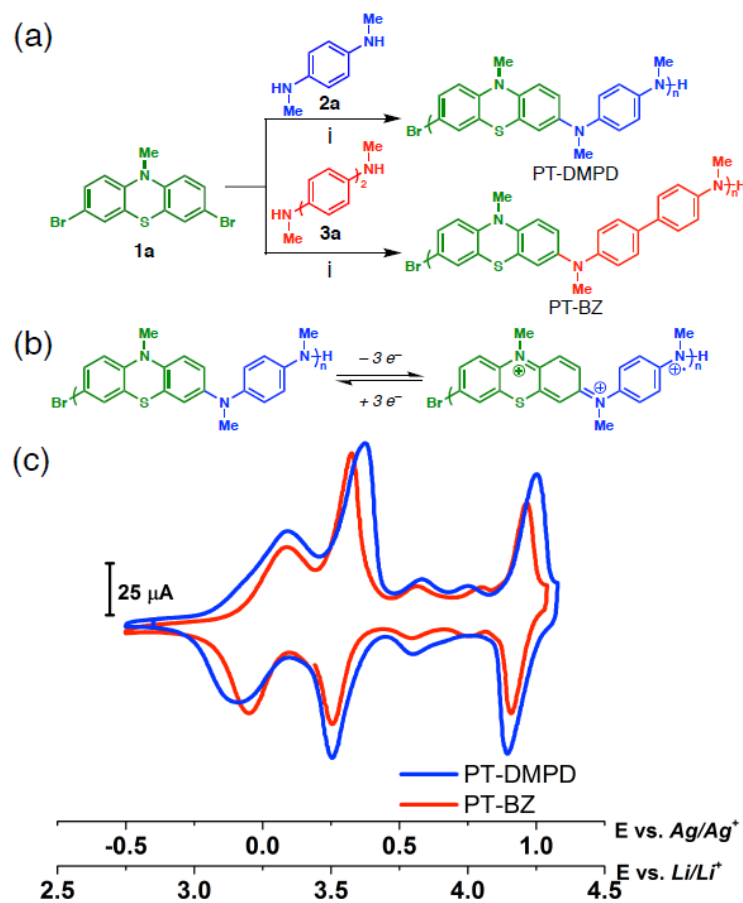


Figure 5.2 (a) General synthetic strategy for PT-DMPD and PT-BZ polymers using Buchwald-Hartwig coupling. i: NaOtBu, RuPhos (3 mol%), RuPhos Pd G2 (3 mol%), Toluene, 80 °C. (b) Neutral and oxidized states of PT-DMPD (c) Slurry CV of PT-DMPD and PT-BZ in LiPF₆ (1 M) in EC/DEC at 20 mV/s

Coin cells employing PT-DMPD or PT-BZ as the cathode and Li metal as the anode were assembled to explore the performance of the polymers in devices. Due to the limited stability window of the electrolyte medium (EC/DEC), only the first two redox couples were accessed in coin cell cycling (Figure 5.3).

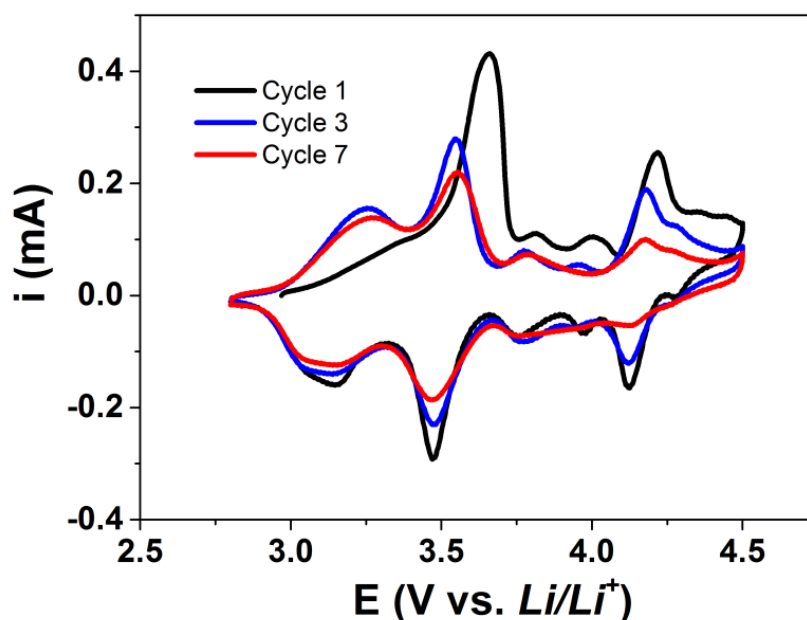


Figure 5.3 CV cycling the full potential window of 10% CL PT-DMPD in 1 M LiPF₆ in EC/DEC in a coin cell at 0.2 mV/s.

Figure 5.4a displays the first cycle charge/discharge curves of PT-DMPD and PT-BZ at 1 C over the voltage range from 2.8 to 4.3 V. Both exhibit reversible two-stage charge-discharge behavior, which is consistent with the two major redox couples observed in the CV. The discharge capacities of PT-DMPD and PT-BZ were 128 mAh/g and 97 mAh/g, representing 82 and 76% of theoretical capacity, respectively. However, both materials exhibited a relatively low coulombic efficiency (35% for PT-DMPD and 44% for PT-BZ). The cycling performances of the PT-DMPD and PT-BZ cathode materials are shown in Figure 5.4b. Both cells were cycled at 25 °C over the

same voltage range at 1 C. The discharge capacity of PT-DMPD was 82 mAh/g after 50 cycles (64% retention), while that of PT-BZ was 64 mAh/g after 50 cycles (66% retention). Since the PT-DMPD polymer exhibited higher capacity than PT-BZ polymer, further work focused on the former.

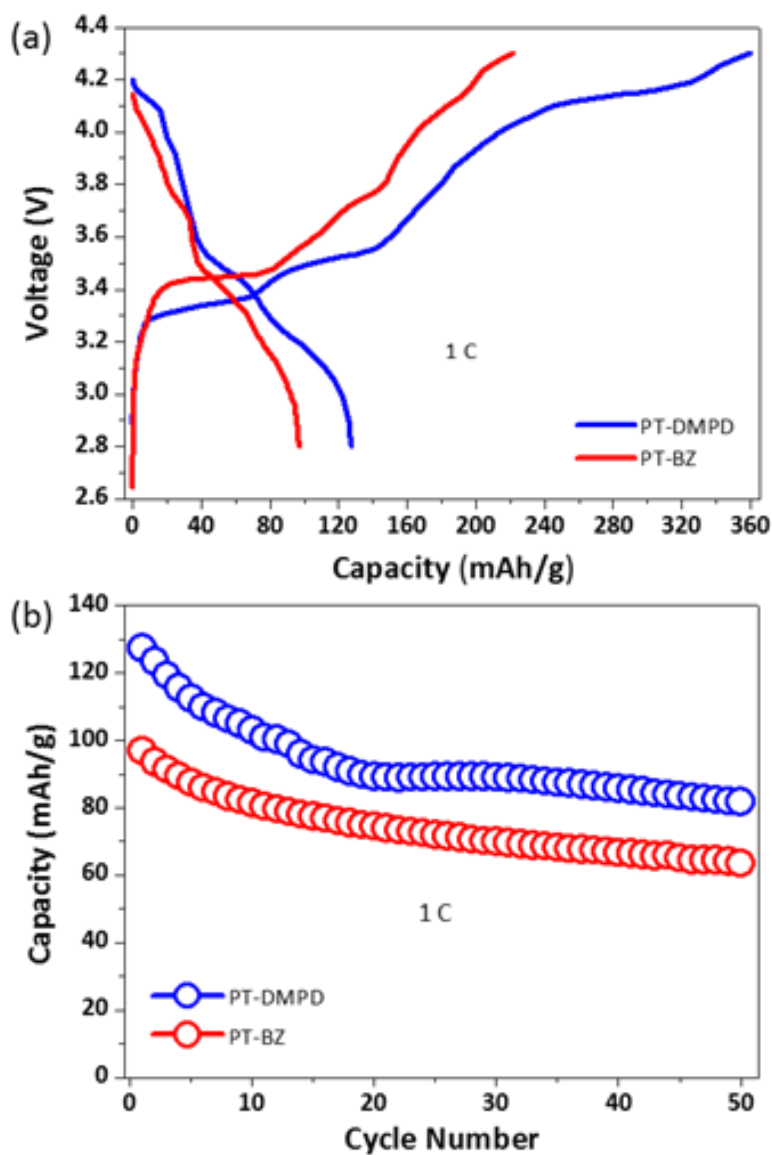


Figure 5.4 (a) Initial charge–discharge curves of PT-DMPD and PT-BZ coin cells at 1 C. (b) Cycling performance of the PT-DMPD and PT-BZ cells at 1 C.

We hypothesized that the low coulombic efficiency and capacity fade upon cycling were caused by dissolution of the polymer upon oxidation. This dissolution could be observed visually as green dissolved polymer that diffused away from the electrode during CV cycling. To address these limitations, a second class of crosslinked materials was synthesized to generate polymers with decreased solubility in the electrolyte medium (Figure 5.5a). The first charge-discharge cycle of PT-DMPD, PT-DMPD (5% cross-linked, 5% CL), PT-DMPD (10% CL), and PT-DMPD (33% CL) at 5 C are shown in Figure 5.5b. Increased discharge capacities were obtained as the mol percentage of cross-linker increased, with PT-DMPD (10% CL) exhibiting the highest discharge capacity of 150 mAh/g (97% of the theoretical value of PT-DMPD). Moreover, the coulombic efficiency significantly improved with increasing copolymerization of cross-linker. The coulombic efficiency at 5 C increases from 49% to 82% between linear (no cross-linker) and 33% cross-linked polymer. By eliminating dissolution through cross-linking, both the capacity and coulombic efficiency were greatly improved.

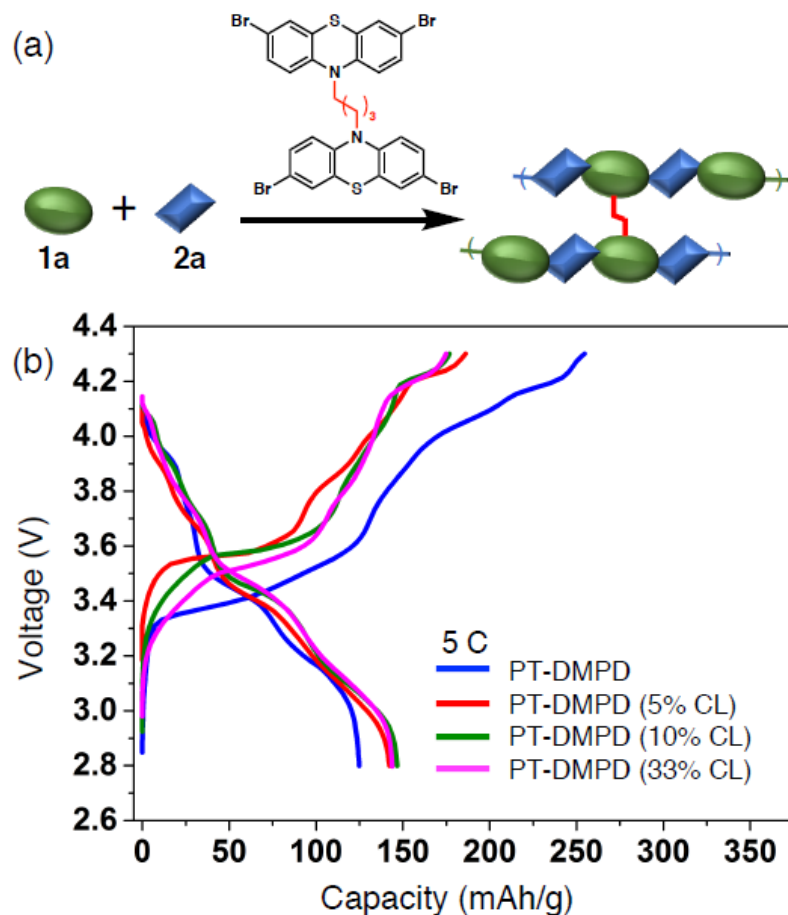


Figure 5.5 (a) Cross-linker (CL) structure and material design. (b) Initial charge-discharge of PT-DMPD, PT-DMPD (5% CL), PT-DMPD (10% CL), and PT-DMPD (33% CL) at 5 C.

The cycling performance of PT-DMPD, PT-DMPD (5% CL), PT-DMPD (10% CL) and PT-DMPD (33% CL) materials was investigated between 2.8 and 4.3 V at 5 C, as shown in Figure 5.6. Increasing the mol percentage of cross-linker resulted in materials exhibiting better cycling performance when compared to linear PT-DMPD. As the mol percentage of cross-linker increased from 0% to 5% to 10% to 33%, the capacity retention after 50 cycles increased from 65% to 73% to 74% to 82%, respectively. These results demonstrate that dissolution of the polymer from the

cathode was mitigated in the cross-linked materials.

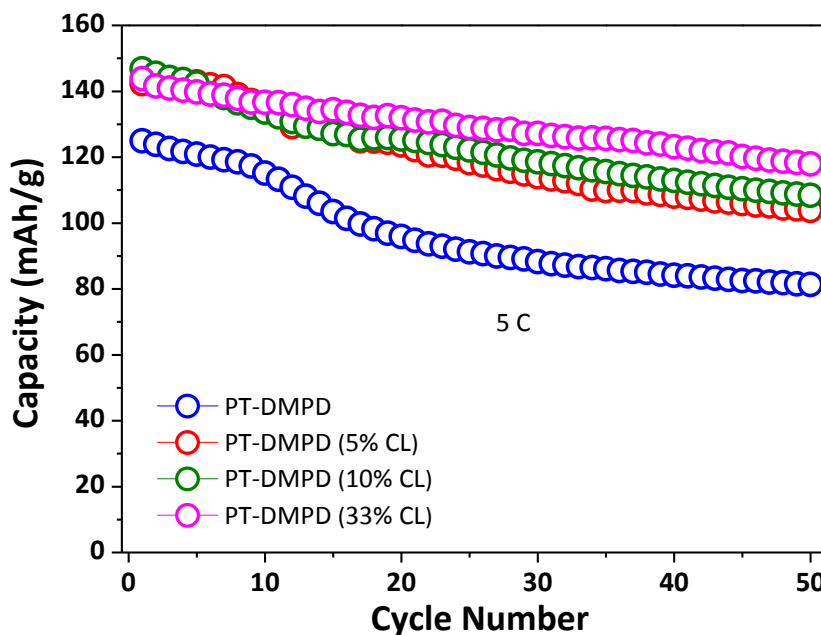


Figure 5.6 Cycling performance of PT-DMPD, PT-DMPD (5% CL), PT-DMPD (10% CL), and PT-DMPD (33% CL) at 5 C.

For use in high power applications, the proposed materials must be able to deliver high discharge capacities at fast discharge rates. To better understand the relationship between mol% cross-linker and the materials capacity retention at increasing discharge rates, the rate capabilities of PT-DMPD (10% CL) and PT-DMPD (33% CL), the two materials displaying the highest discharge capacities, were investigated between 2.8 and 4.3 V. Figure 5.7 compares the discharge capacities of these materials charged at 1 C and discharged at C-rates of 1, 5, 10, 20, 40, 60, and 120 C. Significantly, excellent capacity retention (82%) was observed in PT-DMPD (10% CL) between even the most extreme discharging rates, 1 C to 120 C. While similar capacities are observed at the lower rates for both materials, an apparent decrease in

capacity is evident in PT-DMPD (33% CL) at higher discharge rates. We attribute this to a decrease in the rate of counterion transport through the more densely cross-linked material. Notably, the PT-DMPD (10% CL) material retained a very high discharge capacity of 122.3 mAh/g at the ultrahigh C-rate of 120 C.

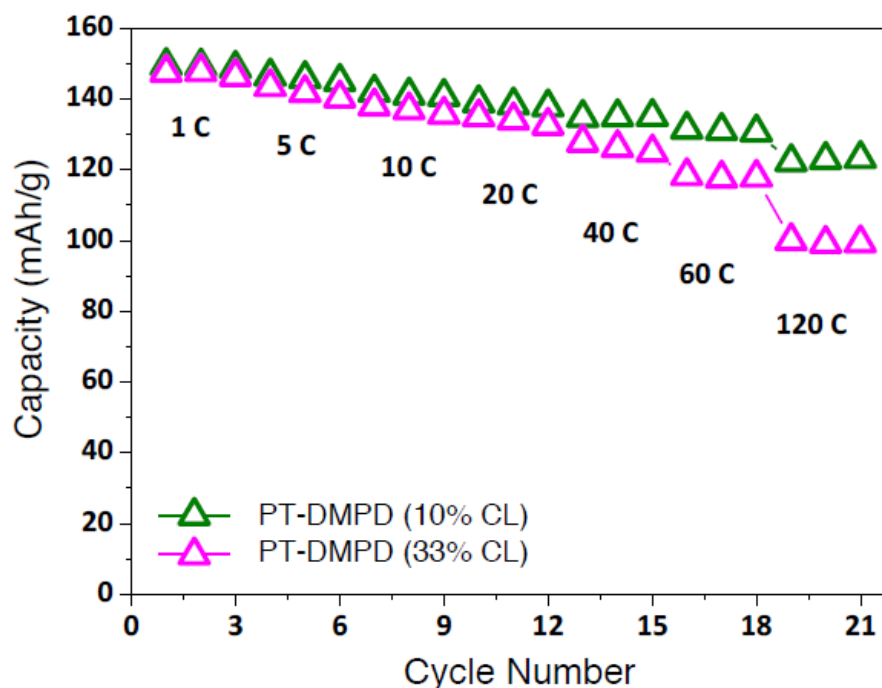


Figure 5.7 Discharge capacities of PT-DMPD (10% CL) and PT-DMPD (33% CL) at C-rates from 1 C to 120 C.

Encouraged by the fast discharge rates exhibited by these materials, electrochemical impedance spectroscopy (EIS) was used to measure the charge transfer resistance of PT-DMPD (10% CL) in a coin cell to explore the origin of the ultrahigh-rate behavior.¹⁷⁻¹⁹ In impedance measurements, a high frequency semicircle is attributed to the double layer and the kinetics of the active material (Figure 5.8). In addition, the low frequency behavior is attributed to transport effects. The high frequency semicircle was fit to a simplified Randles model, and the charge transfer resistances

obtained are given as an inset to Figure 5.8.

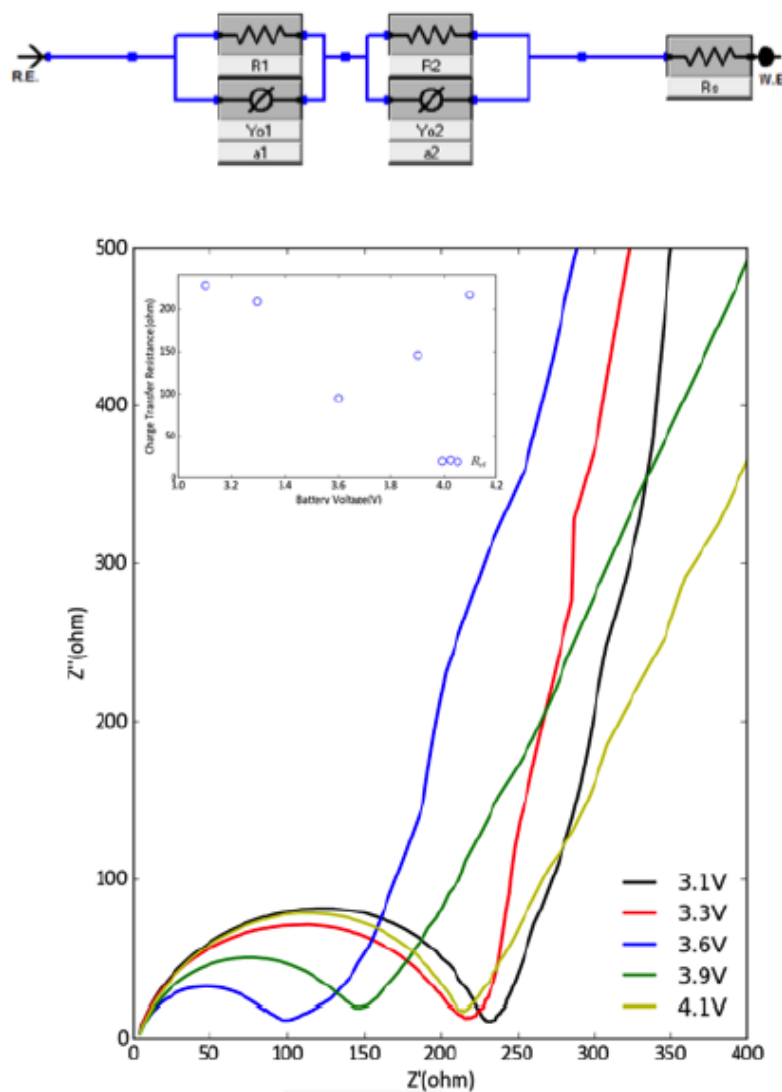


Figure 5.8 Top panel: Equivalent circuit model for electrochemical impedance spectroscopy data. Middle panel: Electrochemical impedance spectroscopy performed on a typical coin cell using PT-DMPD (10% CL) as cathode material. Impedance of the device at 3.1, 3.3, 3.6 3.9 and 4.1 V was measured after 3600 s of potentiostatic pretreatment from 0.001 – 20000 Hz. Inset shows the charge transfer resistance (R_{ct}) as a function of potential of the device.

As expected, the charge transfer resistance was a function of the oxidation state of the polymer. The charge transfer resistances near the redox couple around 3.6 V seem to be much lower than the charge transfer resistances near 4.1 V and 3.1 V. Overall, the charge transfer resistance was between 80 Ω and 230 Ω . When compared to literature reports, these values are similar or lower than comparable systems, reflecting fast charge transfer kinetics.^{5,19-21} This facile kinetic behavior allows the battery to operate at high C-rates without excessive overpotentials. The low overpotentials, in turn, are one of the reasons for the high rate cycling capability without significant loss of capacity.

5.4 Conclusions

In conclusion, we have designed, synthesized, and tested a class of high-energy phenothiazine-derived redox-active polymers that deliver high capacities at ultrafast discharge rates and high operating voltages in lithium ion batteries. The initial capacity fade, due to electrode dissolution, was largely mitigated through the use of cross-linked materials, which led to dramatically improved cycling performance, discharge capacity, and coulombic efficiency without compromising the material's rate capability. PT-DMPD (10% CL) retained 82% capacity at an unparalleled 120 C rating. These results validate our design principles, and are highly instructive for future design of high-energy and high-rate organic electrodes for electrical energy storage applications.

REFERENCE

- (1) Reprinted with permission from the submitted manuscript.
- (2) Novák, P.; Müller, K.; Santhanam, K. S. V.; Haas, O. Electrochemically Active Polymers for Rechargeable Batteries. *Chem. Rev.* **1997**, *97* (1), 207.
- (3) Liang, Y.; Tao, Z.; Chen, J. Organic Electrodes: Organic Electrode Materials for Rechargeable Lithium Batteries (Adv. Energy Mater. 7/2012). *Adv. Energy Mater.* **2012**, *2* (7), 702.
- (4) B. Schon, T.; T. McAllister, B.; Li, P.-F.; S. Seferos, D. The Rise of Organic Electrode Materials for Energy Storage. *Chemical Society Reviews* **2016**, *45* (22), 6345.
- (5) Wang, S.; Wang, Q.; Shao, P.; Han, Y.; Gao, X.; Ma, L.; Yuan, S.; Ma, X.; Zhou, J.; Feng, X.; et al. Exfoliation of Covalent Organic Frameworks into Few-Layer Redox-Active Nanosheets as Cathode Materials for Lithium-Ion Batteries. *J. Am. Chem. Soc.* **2017**, *139* (12), 4258.
- (6) Etori, H.; Kanbara, T.; Yamamoto, T. New Type of π -Conjugated Polymers Constituted of Quinone Units in the Main Chain. *Chem. Lett.* **1994**, *23* (3), 461.
- (7) Naka, K.; Uemura, T.; Chujo, Y. A Polymer with Two Different Redox Centers in the π -Conjugated Main Chain: Alternate Combinations of Ferrocene and Dithiafulvene. *Macromolecules* **2000**, *33* (19), 6965.
- (8) Liang, Y.; Chen, Z.; Jing, Y.; Rong, Y.; Facchetti, A.; Yao, Y. Heavily N-Dopable π -Conjugated Redox Polymers with Ultrafast Energy Storage Capability. *J. Am. Chem. Soc.* **2015**, *137* (15), 4956.
- (9) Xu, F.; Jin, S.; Zhong, H.; Wu, D.; Yang, X.; Chen, X.; Wei, H.; Fu, R.; Jiang, D. Electrochemically Active, Crystalline, Mesoporous Covalent Organic Frameworks on Carbon Nanotubes for Synergistic Lithium-Ion Battery Energy Storage. *Scientific Reports* **2015**, *5*, 8225.

- (10) Yang, H.; Zhang, S.; Han, L.; Zhang, Z.; Xue, Z.; Gao, J.; Li, Y.; Huang, C.; Yi, Y.; Liu, H.; et al. High Conductive Two-Dimensional Covalent Organic Framework for Lithium Storage with Large Capacity. *ACS Appl. Mater. Interfaces* **2016**, 8 (8), 5366.
- (11) Bai, L.; Gao, Q.; Zhao, Y. Two Fully Conjugated Covalent Organic Frameworks as Anode Materials for Lithium Ion Batteries. *J. Mater. Chem. A* **2016**, 4 (37), 14106.
- (12) Huang, W.; Zhu, Z.; Wang, L.; Wang, S.; Li, H.; Tao, Z.; Shi, J.; Guan, L.; Chen, J. Quasi-Solid-State Rechargeable Lithium-Ion Batteries with a Calix[4]Quinone Cathode and Gel Polymer Electrolyte. *Angew. Chem. Int. Ed.* **2013**, 52 (35), 9162.
- (13) Zhu, Z.; Hong, M.; Guo, D.; Shi, J.; Tao, Z.; Chen, J. All-Solid-State Lithium Organic Battery with Composite Polymer Electrolyte and Pillar[5]Quinone Cathode. *J. Am. Chem. Soc.* **2014**, 136 (47), 16461.
- (14) Zhao, Q.; Guo, C.; Lu, Y.; Liu, L.; Liang, J.; Chen, J. Rechargeable Lithium Batteries with Electrodes of Small Organic Carbonyl Salts and Advanced Electrolytes. *Ind. Eng. Chem. Res.* **2016**, 55 (20), 5795.
- (15) Maiti, D.; P. Fors, B.; L. Henderson, J.; Nakamura, Y.; L. Buchwald, S. Palladium-Catalyzed Coupling of Functionalized Primary and Secondary Amines with Aryl and Heteroaryl Halides: Two Ligands Suffice in Most Cases. *Chemical Science* **2011**, 2 (1), 57.
- (16) Kinzel, T.; Zhang, Y.; Buchwald, S. L. A New Palladium Precatalyst Allows for the Fast Suzuki–Miyaura Coupling Reactions of Unstable Polyfluorophenyl and 2-Heteroaryl Boronic Acids. *J. Am. Chem. Soc.* **2010**, 132 (40), 14073.
- (17) Bhosale, M. E.; Krishnamoorthy, K. Chemically Reduced Organic Small-Molecule-Based Lithium Battery with Improved Efficiency. *Chem. Mater.* **2015**, 27

(6), 2121.

(18) Zhang, K.; Guo, C.; Zhao, Q.; Niu, Z.; Chen, J. High-Performance Organic Lithium Batteries with an Ether-Based Electrolyte and 9,10-Anthraquinone (AQ)/CMK-3 Cathode. *Adv. Sci.* **2015**, *2* (5), 1500018.

(19) Wu, H.; Shevlin, S. A.; Meng, Q.; Guo, W.; Meng, Y.; Lu, K.; Wei, Z.; Guo, Z. Flexible and Binder-Free Organic Cathode for High-Performance Lithium-Ion Batteries. *Adv. Mater.* **2014**, *26* (20), 3338.

(20) Song, Z.; Qian, Y.; Gordin, M. L.; Tang, D.; Xu, T.; Otani, M.; Zhan, H.; Zhou, H.; Wang, D. Polyanthraquinone as a Reliable Organic Electrode for Stable and Fast Lithium Storage. *Angew. Chem.* **2015**, *127* (47), 14153.

(21) Song, Z.; Qian, Y.; Liu, X.; Zhang, T.; Zhu, Y.; Yu, H.; Otani, M.; Zhou, H. A Quinone-Based Oligomeric Lithium Salt for Superior Li-organic Batteries. *Energy Environ. Sci.* **2014**, *7* (12), 4077.

CHAPTER 6

CONCLUSION AND OUTLOOK

6.1 Overview

The research presented in this dissertation has focused on a series of high-performance cathode materials for lithium-ion batteries. Key synthesis parameters including pH, stirring rate and calcination temperature have been fully optimized for the $\text{LiNi}_{0.6}\text{Mn}_{0.2}\text{Co}_{0.2}\text{O}_2$ cathode material using a co-precipitation-calcination two-step scalable process. A high-rate performance $\text{LiNi}_{0.33}\text{Mn}_{0.33}\text{Co}_{0.33}\text{O}_2$ cathode material with high stabilities also successfully developed. The material exhibited superior rate capability which is most likely attributable to the unique crystalline microstructure observed in STEM characterization. The particles are composed of plate-like grains with a preferential stacking that results in the radially outward orientation of the high-Li-diffusivity channels of the crystal grains. This structure would allow a much higher rate of lithium transport in the NMC material, especially when combined with overall shorter diffusion lengths from a uniformly smaller particle size. What's more, a Ni-rich $\text{LiNi}_{0.88}\text{Mn}_{0.06}\text{Co}_{0.06}\text{O}_2$ interwoven by carbon fiber cathode material, exhibited enhanced rate capability and stability due to the faster ionic/electronic diffusion and shorter diffusion path which benefited from the carbon fiber network structure. Finally, a class of high-energy phenothiazine-derived redox-active polymers that deliver high capacities at ultrafast discharge rates have been studied. The initial capacity fade, due to electrode dissolution, was largely mitigated using cross-linked materials, which led to dramatically improved cycling performance, discharge capacity, and coulombic efficiency without compromising the material's rate capability.

6.2 Future Work

Ni-rich NMC/NCA cathode materials have been widely studied and will be dominate the cathode market for EV application in the near future. However, some intrinsic disadvantages will inhibit the fast development of these cathode materials. Surface modification methods, including coating and doping technologies, will be further developed to improve the electrochemical performance of these cathode materials.

Co-precipitation methods have been widely employed for the synthesis of precursors of ternary cathode materials including in this dissertation. But due to the different solubility product constants of Ni, Mn (Al) and Co, the segregation of Ni will occur if the synthesis conditions are not controlled well during the process. This will in turn affect the rate capability and cycling life of the material. Different preparation methods, including solid-state method and hydrothermal synthesis have also been developed to improve or assist the current synthesis process.^{1,2} The improvement of the reactor is also important to the performance of the cathode material. The continuous Couette–Taylor crystallizer has been experimentally studied to produce hydroxide precursors.³ A narrow size distribution and rough surface conditions can be obtained and the final cathode material exhibited enhanced rate capability and cycling performance.

Another critical future technology is solid-state electrolytes and solid-state batteries. Significant safety concerns are being raised by using combustible flammable organic liquids as electrolytes in current lithium-ion batteries. Several severe incidents including the recent fires of the LIBs of Samsung Note 7 and Tesla Model S have brought a new round of challenges to the safety of using LIBs for both consumer electronics and electric drive vehicle (EV) applications. Furthermore, the energy

density of current state-of-art LIBs is far below the requirements in the United States Advanced Battery Consortium Goals for Advanced Batteries for EVs.⁴ Precautionary systems have been developed to prevent thermal runaway and performance deterioration in battery systems, resulting in additional weight, volume, and cost. Solid electrolytes are nonflammable; consequently, batteries would be inherently resistant to thermal runaway failures, rather than needing to rely on bulky and expensive external systems to reactively suppress, or contain, combustion. A safe solid-state battery would allow the heavy steel shells currently used to minimize explosive hazards to be replaced with lightweight plastic containers,^{5,6} which would lessen overall EV material costs while unlocking all of the benefits of reduced vehicle weight.

Additionally, solid-state electrolytes can efficiently block lithium dendrite formation, which would enable the use of high-capacity lithium anodes that are prone to shorting cells featuring organic liquid electrolytes.⁷ As such, we believe that all-solid-state batteries and solid electrolytes are a promising avenue of exploration for the development of next-generation safe and high-energy density rechargeable batteries.^{8,9}

REFERENCES

- (1) Wu, F.; Li, N.; Su, Y.; Shou, H.; Bao, L.; Yang, W.; Zhang, L.; An, R.; Chen, S. *Adv. Mater.* **2013**, *25* (27), 3722.
- (2) Noh, H.-J.; Youn, S.; Yoon, C. S.; Sun, Y.-K. *J. of Power Sources* **2013**, *233*, 121.
- (3) Kim, J.-M.; Chang, S.-M.; Chang, J. H.; Kim, W.-S. *Colloids and Surf., A: Physicochemical and Engineering Aspects* **2011**, *384* (1–3), 31.
- (4) “USABC Goals for Advanced Batteries for EVs - CY 2020 Commercialization.” http://www.uscar.org/guest/article_view.php?articles_id=85.
- (5) Thangadurai, V.; Narayanan, S.; Pinzaru, D. *Chem. Soc. Rev.* **2014**, *43* (13), 4714.
- (6) Kim, J. G.; Son, B.; Mukherjee, S.; Schuppert, N.; Bates, A.; Kwon, O.; Choi, M. J.; Chung, H. Y.; Park, S. *J. of Power Sources* **2015**, *282*, 299.
- (7) Whiteley, J. M.; Woo, J. H.; Hu, E.; Nam, K.-W.; Lee, S.-H. *J. Electrochem. Soc.* **2014**, *161* (12), A1812.
- (8) Kuhn, A.; Gerbig, O.; Zhu, C.; Falkenberg, F.; Maier, J.; V. Lotsch, B. *Phys. Chem. Chem. Phys.* **2014**, *16* (28), 14669.
- (9) Wang, Y.; Richards, W. D.; Ong, S. P.; Miara, L. J.; Kim, J. C.; Mo, Y.; Ceder, G. *Nat. Mater.* **2015**, *14* (10), 1026.